

WEATHER ON SUBSTELLAR WORLDS: A STUDY OF CLOUDS, VARIABILITY
AND BINARITY AT THE L/T TRANSITION

by

Jacqueline Marie Radigan

A thesis submitted in conformity with the requirements
for the degree of Doctor of Philosophy
Graduate Department of Astronomy & Astrophysics
University of Toronto

Copyright © 2013 by Jacqueline Marie Radigan

Abstract

Weather on Substellar Worlds: A Study of Clouds, Variability and Binarity at the L/T
Transition

Jacqueline Marie Radigan

Doctor of Philosophy

Graduate Department of Astronomy & Astrophysics

University of Toronto

2013

A study of clouds and variability in brown dwarf atmospheres is presented, with a focus on understanding the mechanism by which condensate clouds are dissipated at the transition between L and T spectral types. The results of a large *J*-band variability survey of over 60 mid-L to T dwarfs, and related observations are presented. We find statistically significant evidence (at the 95% confidence level) for an increase in large amplitude variability (peak to peak variations larger than 2%) within the L/T transition (L9-T3.5 spectral types), suggesting that the disruption of dust clouds by weather phenomena may contribute to the rapid decline in condensate opacity and *J*-band brightening observed to occur in this regime. Alternatively, the large amplitude variability observed could be the result of increasing contrast between discrete cloud features and the underlying atmosphere, rather than the development of cloud holes. We highlight the discovery of a T dwarf with 26% variability, and provide a detailed comparison with atmosphere models in order to infer the nature of cloud features responsible. Results are consistent with both the presence of thick storm features or cloud holes in our target's atmosphere, but are inconsistent with the presence of magnetic spots. Supporting work related to clouds in L dwarf atmospheres, and the L/T transition binary fraction is presented. From studying an unusually blue L-dwarf companion to a nearby M-dwarf star we infer that thin or patchy condensate clouds,

rather than low metallicity and/or high surface gravity, are most likely responsible for its peculiar colors. The discovery of significant variability for a different blue L dwarf in our large variability survey provides further evidence for this hypothesis. Finally, combining our own high contrast imaging observations for 8 L/T transition targets with previous results we infer a resolved L/T transition binary fraction of $14_{-6}^{+7}\%$, consistent with that inferred for the general brown dwarf population. This latter result suggests that the L/T transition sample is not highly contaminated by unresolved multiples.

“Then you’re in the world again. At night, on a cold hill, taking
the telescope apart.”

-Louise Glück (a line from Telescope)

Acknowledgements

I would like to acknowledge financial support in my final three years in the form of a Vanier Canada Graduate Scholarship from the Natural Sciences and Engineering Research Council of Canada.

There are a number of people from the Department of Astronomy at the University of Toronto who have provided invaluable support along the way. I extend sincere thanks to my thesis advisor, Prof. Ray Jayawardhana, for providing encouragement, guidance, and a sense of perspective throughout my graduate career. I am indebted to Prof. David Lafrenière for early scientific mentorship. I am also grateful for the time, input and support of my thesis committee members Prof. Peter Martin and Prof. Yanqin Wu, as well as my first year project advisor, Prof. Marten van Kerkwijk. A big thank you goes to the wonderful administrative staff who have kept my head attached over the years, particularly Marc Goodman and Angie Ho. I am grateful for the camaraderie and friendship of other students and fellows (you know who you are) who brought a much needed levity to my time at Toronto.

I could not have managed without the boundless love, support and cheerleading of my family. Mom, Dad, Christopher, Grandmaman: knowing I always have a safe place to come home to has given me the courage to pursue life's adventures and challenges wherever they may lead.

Last but not least, to Jens: thanks for sticking it out with me, partner.

Contents

1	Introduction	1
1.1	Cloudy Brown Dwarfs	2
1.2	The L/T Transition	4
1.3	Previous Variability Searches	8
1.3.1	Red Optical Variability	9
1.3.2	NIR Variability Studies	11
1.4	Chapter Descriptions	12
2	An Unusually Blue Companion to a Nearby L-Dwarf	15
2.1	Overview	16
2.2	Introduction	16
2.3	Discovery and Observations	18
2.4	Physical Properties	21
2.4.1	The primary: G 203-50	23
2.4.2	The Companion: 2MASS J17114559+4028578	25
2.5	Discussion	28
2.5.1	The blue NIR colors of 2M1711+4028	28
2.5.2	Formation of G 203-50AB	31
2.5.3	Search Sensitivity	32
2.6	Summary and Outlook	34

3	Large Amplitude Variations of an L/T Transition Brown Dwarf	36
3.1	Chapter Overview	37
3.2	Introduction	37
3.3	Observations and Data Reduction	39
3.3.1	LCO Observations	39
3.3.2	Reduction and Processing of WIRC data	42
3.3.3	OMM Observations	47
3.3.4	Reduction of CPAPIR data	47
3.3.5	Photometric Calibration	47
3.4	Results and Analysis	50
3.4.1	The Reduced Light Curves	50
3.4.2	Rotation and Longer Timescale Trends	53
3.4.3	Possible long-term variability	60
3.5	Physical Properties	61
3.5.1	Binarity?	62
3.5.2	Model Fits to the NIR SED	64
3.6	Modeling Variability due to Heterogeneous Surface Features	68
3.6.1	A specific variability model for 2M2139	72
3.6.2	Comparison to SIMP0136	81
3.6.3	The need for self-consistent 3D model atmospheres	82
3.7	Discussion	85
3.7.1	Origin of the Observed Variability	85
3.7.2	Clouds versus Magnetic Spots	85
3.7.3	The L/T Transition	89
3.8	Conclusions	91

4	Binarity at the L/T Transition	95
4.1	Overview	96
4.2	Introduction	97
4.3	Observations and Data Reduction	99
4.3.1	Target Selection	99
4.3.2	NIRC2 Observations of L/T transition dwarfs	101
4.3.3	OSIRIS spectroscopy of the 2M0838+15 system	104
4.4	2M0838+15 ABC: Discovery of a Visual Triple T-Dwarf System	110
4.4.1	Analysis of the NIRC2 images: binary system properties and component fluxes	110
4.4.2	Common Proper Motion	113
4.4.3	System and Component Properties Inferred from Empirical Trends and Evolutionary Models	118
4.5	Search for companions and sensitivity limits	124
4.5.1	The binary fraction of our sample	127
4.6	Binary statistics in the L/T transition	127
4.6.1	The L9-T4 binary frequency	127
4.7	Discussion and Conclusions	136
4.7.1	2M0838+15ABC: A benchmark triple of early T-dwarfs	136
4.7.2	Formation and Dynamical Stability of 2M0838+15	138
4.7.3	Binarity at the L/T transition	142
5	A J-band Variability Survey of Brown Dwarfs	145
5.1	Overview	145
5.2	Observations	146
5.2.1	Target Sample and Observing Strategy	147
5.2.2	Las Campanas Observations	148
5.2.3	CFHT/WIRCam Observations and Data Reduction	150

5.3	Light Curve Analysis	151
5.3.1	Search Sensitivity: Empirical Detection Limits for Variability . .	153
5.3.2	Detections of Variability	155
5.4	Survey Detection Limits and Completeness	159
5.4.1	Recovery Rates of Simulated Signals	159
5.5	Variability Statistics	165
5.5.1	Testing the cloud “hole” hypothesis: does variability increase at the L/T Transition?	167
5.6	The Frequency of Variability at the L/T Transition	169
5.7	Discussion and Conclusions	173
6	Summary, Conclusions & Future Work	185
6.1	Summary and Conclusions	185
	Appendices	190
A	Chapter 3 Appendix	191
A.1	Relative Flux Calibration of SpeX Prism Library Spectra and Synthetic 2MASS Colors	191
A.2	Models for 2M2139’s Variability at Additional Epochs	193
B	Chapter 4 Appendix	196
B.1	The Empirical Flux Ratio Distribution of Resolved L and T Dwarf Binaries	196
C	Chapter 5 Appendix	200
C.1	Detrended lightcurves for all targets	200
C.2	Lomb-Scargle Periodograms for all targets	265
	Bibliography	273

List of Tables

2.1	Physical properties of the components of G 203-50AB	22
2.2	System properties of G 203-50AB	23
2.3	Spectral indices measured for 2M1711+2048	28
3.1	Observing Log	40
3.2	Reference stars used for differential photometry	45
3.3	Light Curve Properties	59
3.4	Target Properties	63
4.1	Targets	100
4.2	Observations	106
4.3	MCMC PSF Fitting Parameters	114
4.4	2M0838+15 ABC System Properties	115
4.5	2M0838+15 ABC Component Properties	116
4.6	The Composite L9-T4 Sample	131
4.6	The Composite L9-T4 Sample	132
5.1	Observing Log	175
5.1	Observing Log	176
5.1	Observing Log	177
5.1	Observing Log	178
5.1	Observing Log	179
5.2	Target Information	180

5.2	Target Information	181
5.2	Target Information	182
5.2	Target Information	183
5.3	Detections	184
B.1	Flux ratios of resolved binaries	198
B.1	Flux ratios of resolved binaries	199

List of Figures

1.1	Cooling and condensation curves for BD atmospheres from Chabrier et al. (2000) and Burrows et al. (2006)	3
1.2	A NIR spectral sequence for L and T dwarfs from Geballe et al. (2002)	5
1.3	A NIR color magnitude diagram and M_J vs spectral type for L and T dwarfs from Dupuy & Liu (2012)	6
1.4	A toy model of fractional cloud coverage across the L/T transition from Burgasser et al. (2002)	7
1.5	Example of a flux reversal binary from Looper et al. (2008).	8
1.6	Variability of the T2.5 dwarf SIMP 0136 from Artigau et al. (2009)	12
1.7	Summary of previous NIR photometric monitoring surveys of field L and T dwarfs	13
2.1	Proper motions of all sources within $10'$ of G 203-50	21
2.2	Spectrum of G 203-50	26
2.3	Spectrum of 2M1711+4028	29
2.4	Spectral comparison of 2M1711+4028, 2MASS J22244381-015852, and 2MASS J15074769-1627386	31
2.5	Separation versus total mass for known binaries	33
3.1	Stacked and mosaicked WIRC J band image of the field surrounding 2M2139	46

3.2	An example of raw and detrended lightcurves for 2M2139 and reference stars	46
3.3	Reduced light curves for 2M2139 obtained from 21-24 Sep 2009	49
3.4	Unbinned interleaved J (black), H (blue), and K_s (red) photometric sequences from 26, 30 Sep 2009 and 01 Oct 2009 epochs	52
3.5	Best-fitting round, two-spot model to the J -band light curves from 21 and 23 Sep 2009	55
3.6	Lomb-Scargle Periodogram of light curves spanning 21 Sep 2009 to 01 Oct 2009.	56
3.7	Light curves spanning 01 Aug 2009 to 08 Nov 2009 shown on a common flux scale	57
3.8	Light Curves for 2M2139 spanning 21 Sep 2009 to 01 Oct 2009 phased to over-constrained periods of 7.723 hr and 15.446 hr	58
3.9	Model fits to 2M2139 's NIR spectrum	66
3.10	Model amplitude ratios A_{K_s}/A_J and A_H/A_J as a function of temperature contrast ΔT	73
3.11	Same as figure 3.10, with $a = 0.2$, and including comparisons to the cloudy/clear and SETTL/COND models of Burrows et al. (2006) and Allard et al. (2001; 2003)	74
3.12	Simultaneous fits to both the NIR spectrum and photometric variability of 2M2139	75
3.13	The importance of simultaneously modeling both the NIR spectrum and color variability: an example using SIMP 0136	80
3.14	Temperature of the $\tau = 2/3$ surface as a function of wavelength for a cloudy model with and without condensate opacity	84
3.15	Secondary Roche Lobe radius as a function of mass ratio, q , assuming an orbital period of 15.44 hr	89

3.16	Color-magnitude diagram in the MKO filter system for M, L, and T dwarfs with measured parallaxes	92
4.1	Unresolved SpeX spectrum of the 2M0838+15ABC system	102
4.2	Reduced J , H , and K_s band cutouts of the 2M0838+15ABC system.	102
4.3	Postage stamps (K_s band) of all targets observed with NIRC2.	105
4.4	Resolved OSIRIS H and K_s spectra of the A and BC components	109
4.5	A series of 41×41 pixel surface plots demonstrating our PSF fitting of the 2M0838+15 BC system	116
4.6	An example of parameter distributions returned by our MCMC PSF fitting of the BC components	117
4.7	Spectral decomposition of the 2M0838+15 ABC components using templates from the SpeX prism library	121
4.8	Surface gravities and effective temperatures for the 2M0838+15 ABC components inferred using empirical trends and evolutionary models	125
4.9	K -band detection limits as a function of binary separation and contrast, ΔK	128
4.10	Probability distribution for the volume-bias corrected L9-T4 binary frequency at projected separations $\gtrsim 1 - 2.5$ AU	135
4.11	NIR $J - K_s$ colors as a function of spectral type for field BDs	139
4.12	Color magnitude diagrams showing the <i>relative</i> positions of the 2M0838+15 A, B and C components inferred from resolved photometry of the system	140
4.13	Binding energy as a function of total mass for stellar and VLM binary systems	143
5.1	Peak power in a Lomb-Scargle periodogram relative to the 0.01 FAP power for 742 reference stars	155

5.2	<i>Left</i> :Light curve for a significantly variable target, binned to a 10 min cadence. <i>Right</i> :Lomb-Scargle Periodogram for the detrended target light curve (solid black line) and those of reference stars observed simultaneously (solid grey lines).	159
5.3	As in figure 5.2.	159
5.4	As in figure 5.2.	159
5.5	As in figure 5.2.	160
5.6	As in figure 5.2.	160
5.7	As in figure 5.2.	160
5.8	As in figure 5.2.	161
5.9	Recovery rates of simulated sinusoidal signals as a function of amplitude and period	162
5.10	Lognormal period distributions used to asses the survey completeness	164
5.11	Simulated distribution for the geometric amplitude dilution factor $\alpha = A(i, \lambda) / A(90, 0)$	165
5.12	Survey completeness to sinusoidal variability signals as a function of peak-to-peak amplitude for the “short” and “long” period distributions	166
5.13	$J - K_s$ color as a function of spectral type for survey targets	168
5.14	Probability distributions for the observed frequencies of high amplitude (>2% peak-to-peak) variability for objects inside and out of the L/T transition	169
A.1	Comparison between 2MASS photometry and synthetic 2MASS colors derived from SpeX prism spectra for all L and T dwarfs in the SpeX prism library	192
A.2	Same as figure 3.12, but with amplitude ratios constrained using data from the 26 Sep 2009 epoch	194
A.3	Same as figure 3.12, but with amplitude ratios constrained using data from the 01 Oct 2009 epoch	195

B.1	The distribution of flux ratios for resolved L and T dwarf binaries in table B.1	197
C.1	Detrended Target Lightcurves	202
C.2	Detrended Target Lightcurves	203
C.3	Detrended Target Lightcurves	204
C.4	Detrended Target Lightcurves	205
C.5	Detrended Target Lightcurves	206
C.6	Detrended Target Lightcurves	207
C.7	Detrended Target Lightcurves	208
C.8	Detrended Target Lightcurves	209
C.9	Detrended Target Lightcurves	210
C.10	Detrended Target Lightcurves	211
C.11	Detrended Target Lightcurves	212
C.12	Detrended Target Lightcurves	213
C.13	Detrended Target Lightcurves	214
C.14	Detrended Target Lightcurves	215
C.15	Detrended Target Lightcurves	216
C.16	Detrended Target Lightcurves	217
C.17	Detrended Target Lightcurves	218
C.18	Detrended Target Lightcurves	219
C.19	Detrended Target Lightcurves	220
C.20	Detrended Target Lightcurves	221
C.21	Detrended Target Lightcurves	222
C.22	Detrended Target Lightcurves	223
C.23	Detrended Target Lightcurves	224
C.24	Detrended Target Lightcurves	225
C.25	Detrended Target Lightcurves	226

C.26 Detrended Target Lightcurves	227
C.27 Detrended Target Lightcurves	228
C.28 Detrended Target Lightcurves	229
C.29 Detrended Target Lightcurves	230
C.30 Detrended Target Lightcurves	231
C.31 Detrended Target Lightcurves	232
C.32 Detrended Target Lightcurves	233
C.33 Detrended Target Lightcurves	234
C.34 Detrended Target Lightcurves	235
C.35 Detrended Target Lightcurves	236
C.36 Detrended Target Lightcurves	237
C.37 Detrended Target Lightcurves	238
C.38 Detrended Target Lightcurves	239
C.39 Detrended Target Lightcurves	240
C.40 Detrended Target Lightcurves	241
C.41 Detrended Target Lightcurves	242
C.42 Detrended Target Lightcurves	243
C.43 Detrended Target Lightcurves	244
C.44 Detrended Target Lightcurves	245
C.45 Detrended Target Lightcurves	246
C.46 Detrended Target Lightcurves	247
C.47 Detrended Target Lightcurves	248
C.48 Detrended Target Lightcurves	249
C.49 Detrended Target Lightcurves	250
C.50 Detrended Target Lightcurves	251
C.51 Detrended Target Lightcurves	252
C.52 Detrended Target Lightcurves	253
C.53 Detrended Target Lightcurves	254

C.54 Detrended Target Lightcurves	255
C.55 Detrended Target Lightcurves	256
C.56 Detrended Target Lightcurves	257
C.57 Detrended Target Lightcurves	258
C.58 Detrended Target Lightcurves	259
C.59 Detrended Target Lightcurves	260
C.60 Detrended Target Lightcurves	261
C.61 Detrended Target Lightcurves	262
C.62 Detrended Target Lightcurves	263
C.63 Detrended Target Lightcurves	264
C.64 LS Periodograms of Target Light Curves	266
C.65 LS Periodograms of Target Light Curves	267
C.66 LS Periodograms of Target Light Curves	268
C.67 LS Periodograms of Target Light Curves	269
C.68 LS Periodograms of Target Light Curves	270
C.69 LS Periodograms of Target Light Curves	271
C.70 LS Periodograms of Target Light Curves	272
C.71 LS Periodograms of Target Light Curves	273

Chapter 1

Introduction

Figures 1.1-1.6 have been reproduced or adapted from third party publications in the *Astrophysical Journal* (Chabrier et al. 2000; Burrows et al. 2006; Geballe et al. 2002; Dupuy & Liu 2012; Burgasser et al. 2002; Looper et al. 2008; Artigau et al. 2009) with permission of the respective authors. Reproduced by permission of the AAS.

With observed temperatures ranging from $\sim 2200\text{--}300\text{ K}$, field brown dwarfs (BDs) with L and T spectral types possess the coolest atmospheres currently available to direct and detailed study, and thus constitute important precursors to investigating directly imaged extra-solar giant planet atmospheres. At these cool temperatures, an understanding of atmospheric condensates—which affect luminosities, radii, cooling histories, and spectral morphologies—is essential to deriving correct physical properties for both cool BDs and giant planets (e.g. Marley et al. 2002; Burrows et al. 2011). Our current understanding of ultracool atmospheres, including the formation and sedimentation of condensate clouds, has developed based on comparisons of detailed atmosphere models to observations of hundreds of L and T dwarfs identified in the solar neighborhood (e.g., Cushing et al. 2008; Stephens et al. 2009; Witte et al. 2011). Nonetheless, fundamental questions remain concerning the most basic properties of condensates, including their vertical and horizontal distributions, how these evolve as a function of effective temperature, and the role of secondary parameters such as gravity, metallicity, convection, and rotation in determining their properties.

This present work attempts to provide insight into the unsolved problem of cloud dissipation across the the L-dwarf/T-dwarf transition, with a focus on the role of cloud heterogeneities and variability, or what could be referred to in the broadest terms as “weather” (chapters 3 and 5). The closely related problems of dust clouds in L dwarfs and the L/T transition binary fraction are explored in chapters 2 and 4. Relevant background information on the role of condensate clouds in BD atmospheres, the L/T transition, and the history of variability searches is provided below.

1.1 Cloudy Brown Dwarfs

Brown dwarfs are the lowest mass products of the star formation process, ranging from ~ 75 to a few Jupiter masses. Unlike for stars their low masses result in core temperatures insufficient for stable hydrogen burning, and they spend their lives

simply cooling (Burrows et al. 1997; Chabrier et al. 2000). Below temperatures of ~ 2200 K, temperatures and pressures within in their photospheres begin to intersect with the condensation curves of various refractory species (figure 1.1)—including iron, silicates, and metal oxide compounds—collectively referred to as dust (Burrows & Sharp 1999; Lodders 1999). While the clouds themselves have a grey opacity and are largely featureless, their presence is indirectly inferred from the disappearance of strong molecular absorbers seen in the red optical spectral of M dwarfs such as TiO, VO, and CaH as they condense out of the gaseous phase (e.g. Kirkpatrick et al. 1999).

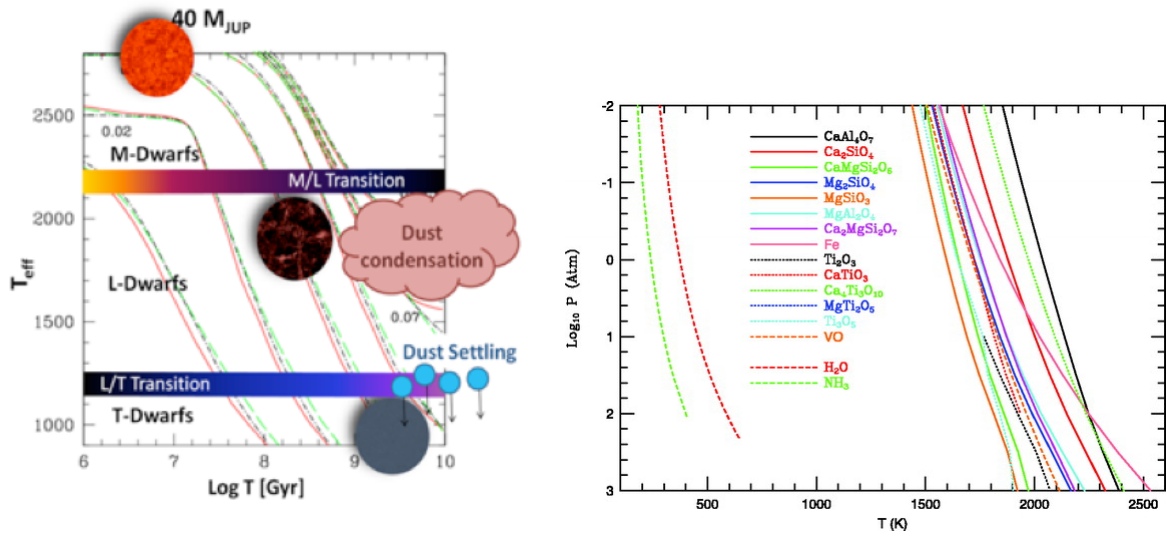


Figure 1.1: *Left*: Cartoon of the cooling history for a $40 M_{JUP}$ BD, based on cooling curves of Chabrier et al. (2000). After the first tens to hundreds of Myr, most BDs have cooled below the bottom of the main sequence. Dust condenses at ~ 2500 K and clouds thicken throughout the L spectral sequence. At cooler temperatures ($\lesssim 1200$ K) condensates are no longer supported in the upper atmosphere and settle out below the photosphere *Right*: Condensation curves for various refractory species expected to condense in BD atmospheres from Burrows et al. (2006).

In the near-infrared (NIR; wherein the peak energy is emitted), L dwarf SEDs are shaped by strong H_2O absorption bands at 1.4 and $1.9 \mu\text{m}$ that become deeper with spectral type (Leggett et al. 2001a; Reid et al. 2001a; Geballe et al. 2002). Dust clouds are also a major source of opacity in the NIR, causing L dwarf SEDs to become

progressively redder with increasing spectral type. The reddening is due to backwarming of the upper atmosphere, and the re-radiation of this energy by the cloud layer. At these stages BD spectra deviate significantly from blackbodies. A NIR LT spectral sequence from Geballe et al. (2002) is shown in figure 1.2.

At even cooler temperatures (~ 1200 K) dust condensates gravitationally settle below the photosphere (Allard et al. 2001; Tsuji 2002), and effectively disappear from view. The sedimentation of photospheric condensates coincides with the onset of molecular CH_4 absorption at 1.6 and $2.2 \mu\text{m}$ (H and K bands), marking the beginning of the T spectral class (?). The suppression of H and K band fluxes by CH_4 and H_2 opacity, combined with the disappearance of dust clouds leads to a dramatic blueward evolution of a BD's spectral energy distribution for T spectral types (figure 1.3).

1.2 The L/T Transition

While the the L spectral sequence is characterized by the formation and thickening of condensates with decreasing effective temperature, the L/T transition ($\sim \text{L8-T5}$ spectral types) is a sequence in decreasing condensate opacity at a near constant effective temperature (Golimowski et al. 2004; Stephens et al. 2009).

On a NIR color magnitude diagram (CMD) L dwarfs become progressively redder throughout most of the L spectral sequence due to an increasing photospheric dust opacity (figure 1.3). The L/T transition is evident on the CMD as an abrupt blue-ward shift in $J - K_s$ color by ~ 2 mag, accompanied by a brightening in the J -band of up to ~ 1 mag (Vrba et al. 2004; Zapatero Osorio et al. 2007; Faherty et al. 2012; Dupuy & Liu 2012).

This brightening in the J -band and abrupt turnaround in color was not foreseen: cloud models generally predict a much more gradual change in cloud properties over a wider range of effective temperatures (e.g. Tsuji & Nakajima 2003; Marley et al. 2002; Allard et al. 2003), and hence monotonically decreasing in J band fluxes.

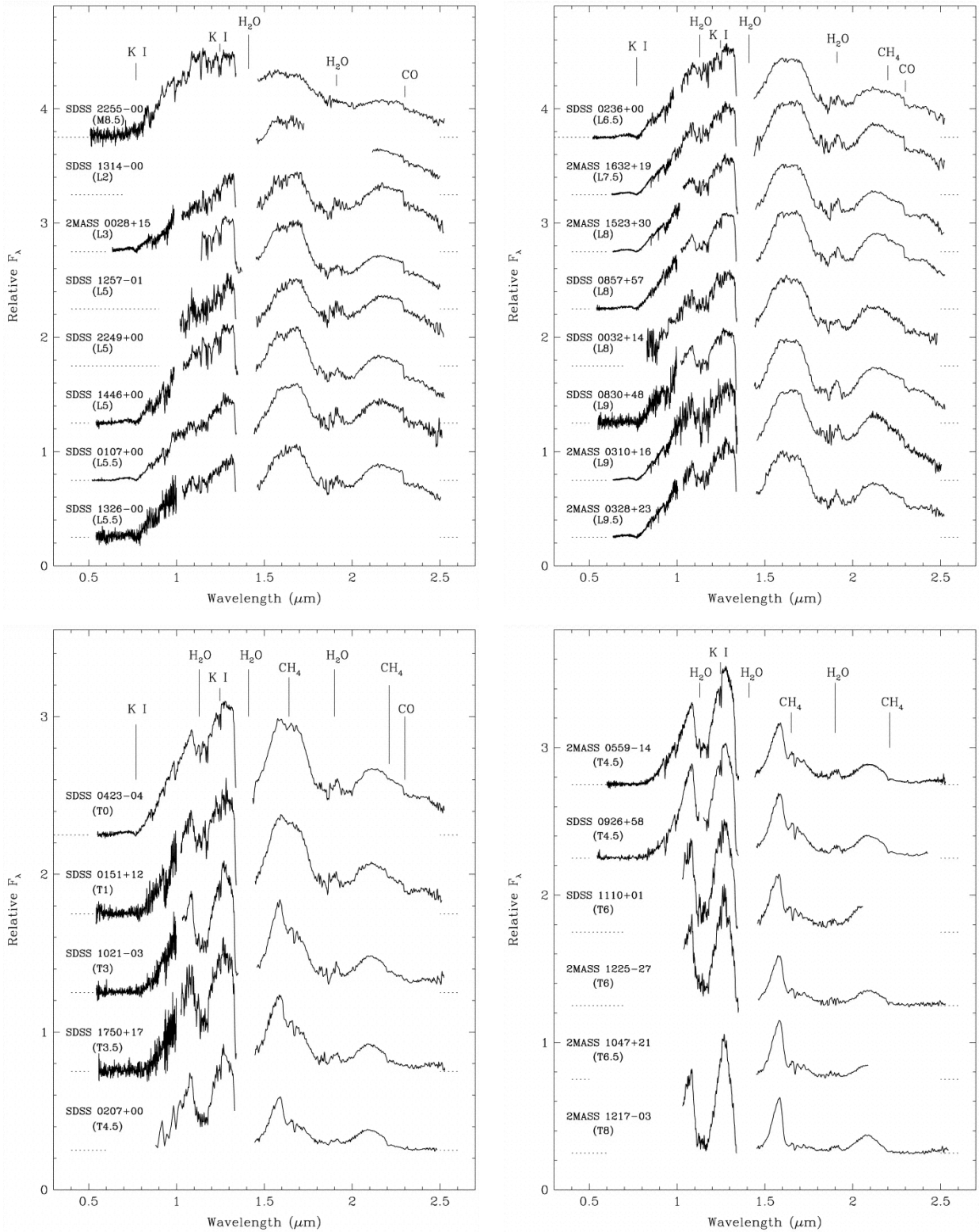


Figure 1.2: A NIR spectral sequence for L and T dwarfs from Geballe et al. (2002)

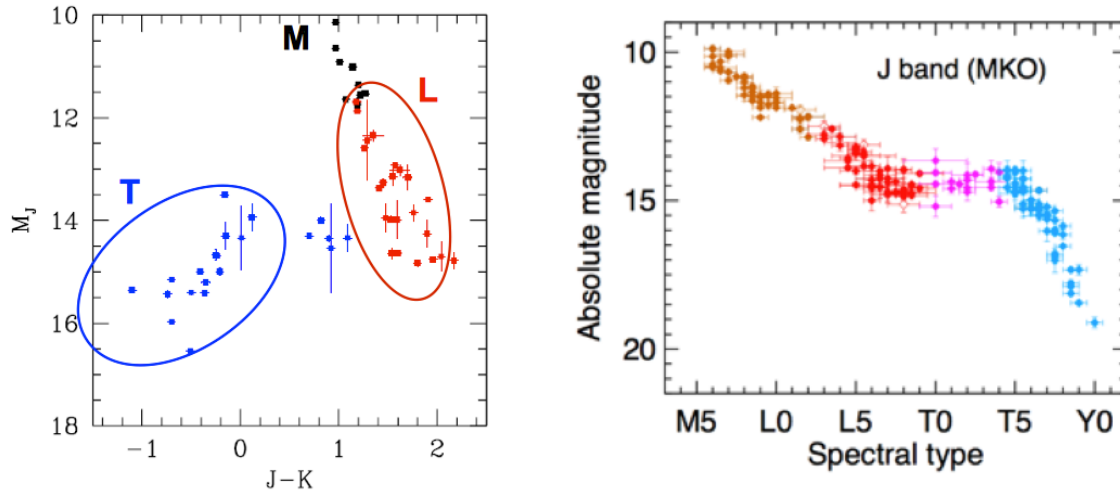


Figure 1.3: *Left:* A NIR color magnitude diagram of M (black points), L (red points), and T (blue points) dwarfs, constructed using parallax data compiled by S. K. Legget. *Right:* Absolute J magnitudes as a function of spectral type for BDs with measured parallaxes from (Dupuy & Liu 2012). J band brightening is apparent for L8-T5 spectral types.

Various ideas have been put forward to explain the L/T transition including the sudden rain-out of condensates (or equivalently an evolving sedimentation efficiency for dust grains) (Knapp et al. 2004; Saumon & Marley 2008), or the development of holes in the cloud layer (Ackerman & Marley 2001; Burgasser et al. 2002). In the latter case, the L/T transition represents a sequence in fractional cloud coverage, ranging from 100% cloud coverage for late-L dwarfs to 0% coverage for mid-T dwarfs (figure 1.4). According to toy models, both scenarios can reproduce main features of the transition such as J -band brightening with increasing spectral type, or the re-emergence of molecular FeH in early T dwarfs, which becomes depleted above the cloud layer due to condensate formation. However, neither idea has been modeled in detail as a physical process: both simply represent requirements that, if satisfied, could reproduce the observed behavior of BDs on a color-magnitude diagram. In this respect, the “cloud hole hypothesis” is attractive due to its ability to make testable predictions: cloud structures, if possessing large enough azimuthal asymmetries,

should give rise to photometric variability on rotational timescales.

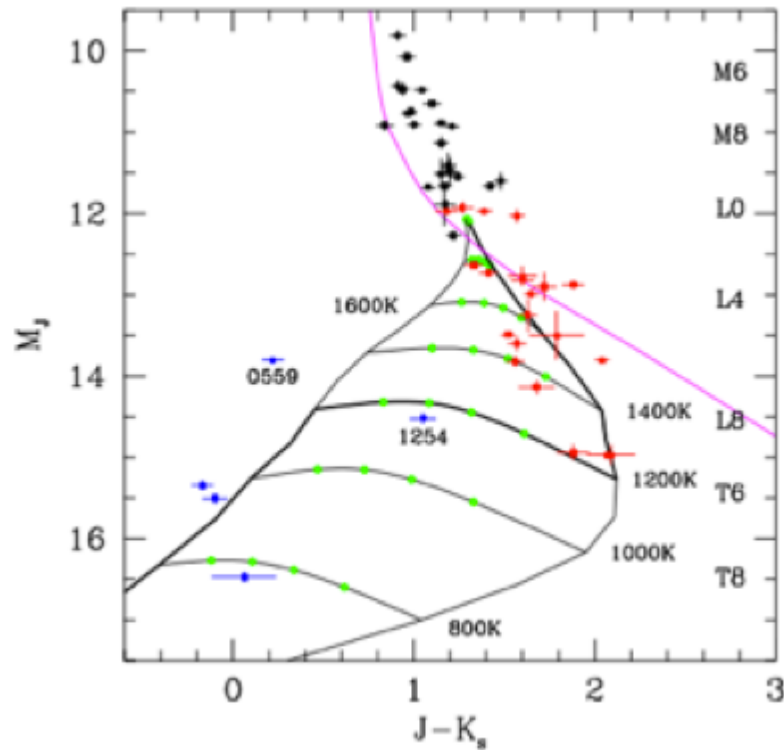


Figure 1.4: NIR color magnitude diagram from Burgasser et al. (2002), with cloud models overplotted. The pink line is the DUSTY models of Chabrier et al. (2000) wherein condensates extend to the top of the atmosphere, in chemical and phase equilibrium with the gas, and without any sedimentation. The leftmost diagonal solid black line is the “clear” model wherein the formation of condensates contribute to the chemical depletion of refractory elements, but the actual dust grains are assumed to immediately settle out of the photosphere, and hence do not contribute to the opacity (Burrows & Sharp 1999). The rightmost curved solid line is the “cloudy” model of Ackerman & Marley (2001); Marley et al. (2002) wherein the physical thickness of the cloud layer is parameterized and controlled by a cloud sedimentation efficiency parameter, f_{sed} , and allows the cloud layer to evolve as a function of effective temperature. The horizontal lines connecting the cloudy and clear models are sequences in fractional cloud coverage moving from 100% to 0% cloud coverage from right to left.

There are alternative theories that suggest the brightening is not an intrinsic evolutionary feature. For instance, Tsuji & Nakajima (2003) propose a Unified Cloudy Model (UCM) where the brightening observed on a color magnitude diagram does not reflect an evolutionary sequence, but rather the fact that populations of BDs

with different ages and surface gravities evolve across the L/T transition at different brightnesses. In addition, due to a relative scarcity of objects with \sim L9-T3 spectral types, it has been suggested that a high fraction of objects in this regime are binaries, which could explain why some appear brighter (e.g. Burgasser 2007). While it is possible that the latter two theories contribute to some extent, the discovery of several flux-reversal binaries wherein the later type component is brighter in the J band (and fainter in H and K_s) provide strong evidence that J -band brightening *is* an intrinsic evolutionary feature (figure 1.5; Looper et al. 2008).

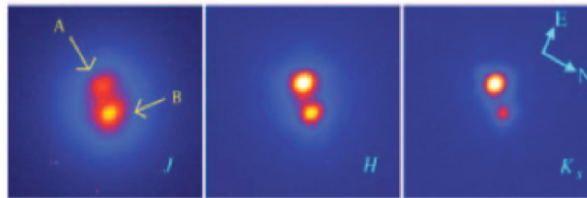


Figure 1.5: Example of a flux reversal binary from Looper et al. (2008) wherein the later type component is brighter in the J band, providing evidence that J -band brightening is an intrinsic feature of the L/T transition.

1.3 Previous Variability Searches

The combination of condensate clouds and rapid rotation has long motivated searches for weather phenomena in ultracool (late-M, L and T) dwarf atmospheres. In our own Solar System, condensate clouds on Jupiter form a stable pattern of bands, gaps, and cyclonic storm features. It has been a matter of considerable debate as to whether clouds in ultracool dwarf atmospheres ever form similar structures, or whether they remain more-or-less homogeneously distributed. Although their surfaces cannot be resolved directly, cloud structure in ultracool dwarfs can be probed indirectly via photometric or spectroscopic monitoring, on roughly rotational timescales in the case of quasi-stable features that co-rotate with the ultracool dwarf.

The first observations of this kind were performed by Tinney & Tolley (1999), who obtained time-resolved differential measurements in and out of a prominent red-optical TiO feature for two ultracool dwarfs. These authors found evidence of 40 mmag variability at the 2σ level for the young M9 BD LP 944-27, on a timescale consistent with the object's rotation period as inferred from $v \sin i$. Whether the variability of LP 944-27 originated from magnetic spots in which dust condensation may also be enhanced, the interplay between condensates and atmospheric dynamics (i.e. weather), or a combination of both still remains an open question. Subsequent observations of LP 944-20 have revealed X-ray flaring (Rutledge et al. 2000) as well as quiescent and flaring radio emission (Berger et al. 2001) indicating the LP 944-20 is magnetically active.

Since the first study, considerable effort has been made toward studying ultracool dwarf variability through time-resolved photometry at both red optical (Bailer-Jones & Mundt 1999; 2001; Martín et al. 2001; Clarke et al. 2002a;b; Gelino et al. 2002; Koen 2003; 2004; 2005a;b; 2006; Maiti et al. 2005; Littlefair et al. 2006; Rockenfeller et al. 2006; Maiti 2007; Littlefair et al. 2008) and infrared wavelengths (Artigau et al. 2003; Bailer-Jones & Lamm 2003; Enoch et al. 2003; Koen et al. 2004; 2005; Morales-Calderón et al. 2006; Lane et al. 2007; Clarke et al. 2008; Artigau et al. 2009). In addition, time-resolved spectroscopy has been performed for a few bright targets in the red optical (Bailer-Jones & Mundt 1999) and near infrared (Nakajima et al. 2000; Bailer-Jones 2002; Clarke et al. 2003; Bailer-Jones 2008; Goldman et al. 2008; Guenther et al. 2009).

1.3.1 Red Optical Variability

Observations in the red optical have targeted mainly late-M to early-L dwarfs, due to a significant drop-off in optical flux for later type dwarfs. In the *I*-band, a rather high fraction of early L-dwarfs show some statistical evidence for variability (as high as 30-80%; Bailer-Jones & Mundt 2001; Gelino et al. 2002; Koen 2003; 2004; 2005a;b),

although the fraction for which periodic variability has been claimed is at the lower end of this range ($\sim 30\%$). Typical peak-to-peak amplitudes of periodic variables are of the order of a few percent, and are often comparable to the photometric noise level. Complicating the interpretation of these results is that many of the claimed periodicities are inconsistent with rotation periods based on $v \sin i$ measurements (Kirkpatrick et al. 1999; Mohanty & Basri 2003; Bailer-Jones 2004; Zapatero Osorio et al. 2006; Reiners & Basri 2008).

For example, a 13.3 hr period found by Bailer-Jones & Mundt (2001) for the the L5 dwarf SDSSp J053951.99-005902.0 is deemed implausible as the rotation period based on a measurement of $v \sin i = 32 \pm 4$ by Zapatero Osorio et al. (2006). Another example is the 31 hr period for the L0.5 binary 2MASSI J0746425+200032 AB ($v \sin i = 27 \pm 3$; Bailer-Jones 2004) found by Gelino et al. (2002). For several L dwarfs there appears to be more than one timescale attached to their periodic behavior either concurrently (Koen 2005a), or over multiple epochs Bailer-Jones & Mundt (2001). It has been suggested that the rapid evolution of surface features (e.g. clouds) on rotational timescales could mask true rotation periods, or that the differential rotation of surface features could lead to more complex periodicities. No clear trends pertaining to $H\alpha$, $v \sin i$, spectral type or color seem to distinguish variable versus non-variable L-dwarfs.

Nonetheless, there are cases where optical periods can be matched to periodic radio pulsation (Lane et al. 2007) or periodic variations in $H\alpha$ (Clarke et al. 2003), and likely correspond to rotation periods. Recent work by Harding et al. (2011) shows that periodic radio, $H\alpha$, and broadband optical variability are correlated for some radio emitting late-M and early L-dwarfs, suggesting a link between magnetic activity and broadband variability in these objects. Thus, based on red-optical studies, variability in late-M, and early-L dwarfs is relatively common and may be related to magnetic spot activity, dust meteorology, or a combination of both.

1.3.2 NIR Variability Studies

While optical studies have been confined to early spectral types, the L/T transition is one of the most interesting regimes to test for cloud related variability and weather due to the ability of cloud holes to explain observed properties of the transition (e.g. as discussed in section 1.2). Due to a strong drop off in optical flux with increasing spectral type, a move to NIR wavelengths is required (wherein late-L and T-dwarfs are brightest).

Since the atmospheres of late-L and T dwarfs are increasingly neutral, they are less likely to support cool magnetic spots (Gelino et al. 2002; Mohanty et al. 2002), making the interpretation of detected variability in this regime less ambiguous. However, in contrast to optical surveys, ultracool dwarf variability at near and mid infrared wavelengths (e.g. Enoch et al. 2003; Koen et al. 2004; 2005; Morales-Calderón et al. 2006; Goldman et al. 2008; Bailer-Jones 2008; Clarke et al. 2008) appears to be rare (at least at similar amplitudes). In a study of 18 L and T dwarfs, Koen (2004) found no significant evidence of variability in the J band above the ~ 20 mmag level nor in the H or K_s bands above ~ 40 mmag. A further study focussing on known I -band variables (Koen et al. 2005) failed to detect any variability in the near infrared (NIR) J , H , and K_s bands in any of these same objects. In contrast, Enoch et al. (2003) monitored 9 objects with L2-T5 spectral types in the K_s band and claim large-amplitude periodic variability (0.1-0.4 mag) for 3 objects in their sample. However, these detections, which should have been straightforward to follow up with larger telescopes have not been repeated at later epochs.

While detections at the level claimed by Enoch et al. (2003) have not been reported since, recent results from high-precision NIR monitoring provide some evidence for lower-amplitude variability in the NIR. In a survey of 8 late-L and T dwarfs in the J band, Clarke et al. (2008) claim periodic variability for 2 of 7 late-L and T dwarfs monitored with amplitudes of 15 and 8 mmag and periods of 1.4 hr and

2 hr respectively (figure 1.6). Most recently, in a single targeted study, Artigau et al. (2009) found the T2.5 dwarf, SIMP0136 (Artigau et al. 2006), to be variable with a peak-to-peak amplitude of ~ 50 mmag in J and a period of 2.4 hr (a $10\text{-}\sigma$ detection). The high significance, repeatability and multi-band detections for SIMP0136 represents a breakthrough in comparison to previous work. Notably, SIMP0136 falls directly within the L/T transition regime.

Previous variability surveys *at NIR wavelengths* are summarized in figure 1.7. Although there has been significant previous work on ultra cool dwarf variability in general, it is clear that comparatively little attention has been paid to the L/T transition region.

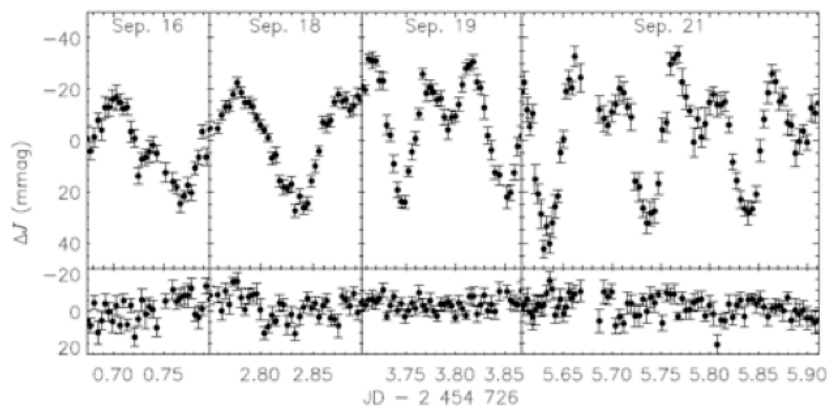


Figure 1.6: Variability of the T2.5 dwarf SIMP 0136 from Artigau et al. (2009).

1.4 Chapter Descriptions

The present work explores whether cloud heterogeneities can explain puzzling features of the L/T transition or peculiar L dwarfs. Chapter 2, which is reported first in chronological order, and which can be credited with inspiring the direction of this Thesis, describes the discovery of an unusually blue L-dwarf companion to an ordinary M-dwarf primary, for which thin or patchy condensates may explain its unusual

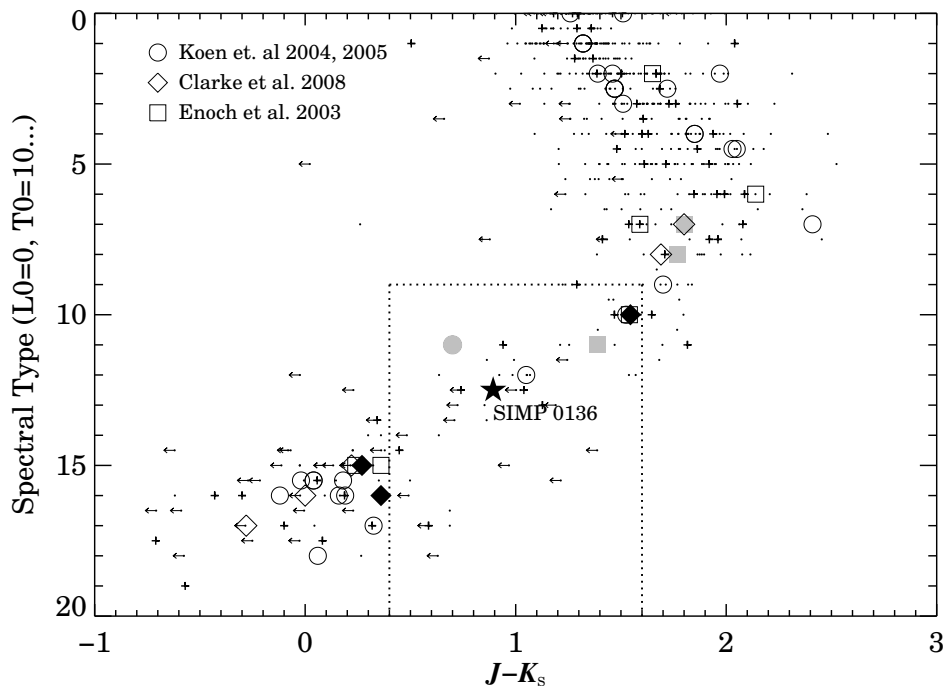


Figure 1.7: Summary of previous NIR photometric monitoring surveys of field L and T dwarfs. Spectral type versus $J - K_s$ color is plotted as black dots for all L and T dwarfs in the DwarfArchives (<http://DwarfArchives.org>, Maintained by Chris Gelino, Davy Kirkpatrick and Adam Burgasser) that have J -band detections in the Two Micron All Sky Survey (2MASS; Skrutskie et al. 2006). Known binaries are marked with crosses, and objects that have no K_s -band detection in 2MASS are marked with left-pointing arrows. A rough outline of the L/T transition regime (based on intermediate $J - K_s$ colors) is shown with dotted lines. Overplotted on the overall population are results from the JHK_s -band variability survey of Koen et al. (2004; 2005), the J -band variability survey of Clarke et al. (2008) and the K_s -band survey of Enoch et al. (2003) (we note that this latter study should be viewed cautiously, due to large photometric uncertainties, and hence lower sensitivities compared to other work). Detection limits for different targets vary widely, but are generally $\lesssim 20$ mmag (peak-to-peak) in the J -band. Open symbols represent null or inconclusive results (possible detections that were not ascribed high significance by their respective authors were interpreted here as null results; please refer to the references provided for a more complete picture). Filled symbols represent claimed detections of periodic variability in the J -band (black fill) and K_s -band (grey fill). The J -band detection of 50 mmag variability for SIMP0136 by Artigau et al. (2009) is shown as a filled star.

colors. Chapter 3 outlines the discovery of a T2.5 dwarf that varies with a peak-to-peak amplitude as high as 26% in the *J* band, including a detailed comparison with atmosphere models. In chapter 4 there is a brief reprieve from cloud variability, where focus is shifted to the L/T transition binary fraction (a possible source of contamination in the variability survey). Finally, Chapter 5 describes the culmination of this work: a large variability survey of L and T dwarfs, in search of evidence for patchy clouds.

Chapter 2

An Unusually Blue Companion to a Nearby L-Dwarf

Contents of this chapter have been published in the *Astrophysical Journal*: **Radigan, J., Lafrenière, D., Jayawardhana, R., & Doyon, R.** *Discovery of a Wide Substellar Companion to a Nearby Low-Mass Star*. 2008, *ApJ*, 689, 471. Reproduced by permission of the AAS. I wrote the paper, developed the software used to cross-match the 2MASS and SDSS catalogs, and led the analysis and interpretation of the data, under the supervision of R. Jayawardhana. The SpeX spectrum and Subaru adaptive optics images were obtained and reduced by D. Lafrenière.

2.1 Overview

We report the discovery of a wide (135 ± 25 AU), unusually blue L5 companion 2MASS J17114559+4028578 to the nearby M4.5 dwarf G 203-50 as a result of a targeted search for common proper motion pairs in the Sloan Digital Sky Survey and the Two Micron All Sky Survey. Adaptive Optics imaging with Subaru indicates that neither component is a nearly equal mass binary with separation $> 0.18''$, and places limits on the existence of additional faint companions. Examination of TiO and CaH features in the primary's spectrum are consistent with solar metallicity and provide no evidence that G 203-50 is metal poor. We estimate an age for the primary of 1-5 Gyr based on activity. Assuming coevality of the companion, its age, gravity and metallicity can be constrained from properties of the primary, making it a suitable benchmark object for the calibration of evolutionary models and for determining the atmospheric properties of peculiar blue L dwarfs. The low total mass ($M_{tot} \sim 0.21 M_{\odot}$), intermediate mass ratio ($q = 0.45 \pm 0.14$), and wide separation of this system demonstrate that the star formation process is capable of forming wide, weakly bound binary systems with low mass and BD components. Based on the sensitivity of our search we find that no more than 2.2% of early-to-mid M dwarfs ($9.0 < M_V < 13.0$) have wide substellar companions with $m > 0.06 M_{\odot}$.

2.2 Introduction

Although star birth is a complex process, the observation of binary systems—frequencies, mass ratios, and separations—can provide insight into the formation process as well as constraints for theoretical models. The formation of brown dwarfs (BDs) is particularly challenging since their masses are an order of magnitude smaller than the typical Jeans mass in molecular clouds.

Whether BDs form similarly to their more massive stellar counterparts or require

additional mechanisms is currently an open question. The answer may lie in the multiplicity properties of these substellar objects. Whereas free-floating BDs are observed in abundance, finding BDs as companions to stars has proved more difficult. A “brown dwarf desert” ($\lesssim 0.5\%$ companion fraction) is observed at close separations (< 3 AU) to main sequence stars, in comparison to a significant number of both planetary and stellar mass companions seen at similar separations (Marcy & Butler 2000). It has recently been determined that this desert does not extend out to larger separations for solar analogs (F,G,K stars), $\sim 7\%$ of which are found to harbor substellar companions at separations greater than 30 AU (Metchev & Hillenbrand 2005). However, searches for substellar companions to M dwarfs at large separations ($\gtrsim 40$ AU) have yielded mostly null results (e.g. Allen & Reid 2008; McCarthy & Zuckerman 2004; Hinz et al. 2002; Daemgen et al. 2007) or sparse results (e.g. Oppenheimer et al. 2001). There are only 5 known BD companions to stellar M dwarf primaries at separations greater than 40AU: TWA 5b,c (Lowrance et al. 1999), G 196-3B (Rebolo et al. 1998), GJ 1001B (EROS Collaboration et al. 1999), Gl 229B (Nakajima et al. 1995), and LP 261-75B (Burgasser et al. 2005; Reid et al. 2006). For thoroughness we note that the L2.5 companion GJ 618.1B (Wilson et al. 2001) may also fall into this category, however it is more likely stellar. In the VLM regime ($M_1 < 0.1 M_\odot$) surveys have found that no more than $\sim 1\%$ of stars have wide companions, including stellar ones (Burgasser et al. 2007). Additionally, VLM binaries are found to be on average 10-20 times more tightly bound than their stellar counterparts, hinting that disruptive dynamical interactions may play an important role in their formation (Close et al. 2003). These observations have been cited as evidence in favor of the ejection hypothesis (Reipurth & Clarke 2001; Bate & Bonnell 2005) where BDs and VLM stars are thought to be stellar embryos formed by the fragmentation of a more massive pre-stellar core, then prematurely ejected from their birth environments. However, BD companions to more massive stars do not tend to form harder binaries than stellar systems of similar total mass (e.g.

Reid et al. 2001c; Metchev & Hillenbrand 2005). While this is potentially evidence that BDs can form similarly to stars via turbulent fragmentation within molecular clouds (Padoan & Nordlund 2002), it is also consistent with simulations of disk instabilities (e.g. Stamatellos et al. 2007; Boss 2000), which are capable of producing substellar companions around more massive primaries.

While a significant fraction of solar mass stars may retain wide BD companions, this does not seem to hold true for lower mass stars. As a result, very few wide BD companions to low mass stars are known. The discovery and characterization of these systems, especially in the intermediate range between the solar analog and VLM regimes, will help complete the emerging picture of BD multiplicity at wide separations. Additionally, wide BD companions to stars make suitable “benchmark” objects, as their properties can be inferred from those of the primary (Pinfield et al. 2006). This is important for the calibration of BD evolutionary models, which requires independent age estimates.

Here we present the discovery of a wide substellar companion to a nearby M4.5 star. The search, discovery and followup observations are outlined in §2.3, while the physical properties of the system and its components are given in §2.4. In §2.5 we discuss the companion’s unusual NIR colors, possible formation scenarios, and the sensitivity of our search. Given a space density for M dwarfs we make a crude estimate of how rare such systems may be. A brief summary and outlook are presented in §2.6.

2.3 Discovery and Observations

The binary G 203-50 / 2MASS J17114559+4028578 (G 203-50AB hereafter) was found in a cross-match of the SDSS DR6 Photoprimary Catalogue (Adelman-McCarthy et al. 2008) and 2MASS Point Source Catalogue (Skrutskie et al. 2006) in which we searched for common proper motion pairs containing at least one VLM or BD component. The cross-correlation of catalogues, calculation of proper motions, and the identification of

co-moving stars was done in parallel for 4 deg^2 sections of the sky at a time, spanning the contiguous region of the SDSS Legacy survey in the northern galactic cap. We made preliminary cuts to include only 2MASS sources with $S/N > 5$ in at least one band (J, H, or K) and not flagged as minor planets, and SDSS sources that were not classified as “sky pointings” or electronic ghosts. For every 2MASS source the closest SDSS match was found and proper motion vectors with uncertainties were computed. A cut was made in order to select only stars that had moved at the 3σ level compared to all other stars within the area. Stars within $120''$ of one another with proper motion amplitudes agreeing within 2σ and proper motion components agreeing within 1σ in one of RA and DEC, were flagged as potential binaries. We applied a color cut of $z' - J > 2.5$ for at least one component to the proper-motion-selected sample in order to search for BD companions. Finally all candidates were examined visually to eliminate artifacts and spurious matches. Of all candidate systems, G 203-50AB stood out as harboring a very red companion with $z' - J \approx 2.9$. Although at first glance the companion passed our color cuts, the quoted z' error of ± 2 magnitudes rendered this color meaningless. Fortunately the primary was of known spectral type and absolute magnitude $M_J = 9.34 \pm 0.18$ (Reid et al. 2003), yielding $M_J = 13.3$ for the secondary, assuming it to be at the same distance as the primary. Average absolute magnitudes as a function of spectral type (Dahn et al. 2002) suggested that the companion was indeed a mid-L dwarf.

As a verification of the system’s physical association we have plotted the proper motions of G 203-50AB along with all other stars within $10'$ of the primary. Figure 2.1 clearly shows G 203-50AB as a co-moving pair.

In order to establish a spectral type for the companion we obtained an infrared spectrum ($R \sim 750$) of 2MASS J17114559+4028578 (2M1711+4028 hereafter) on 2008 Feb 28 using the SpeX Medium-Resolution Spectrograph (Rayner et al. 2003) at NASA’s Infrared Telescope Facility (IRTF). Observations were made in short wavelength (0.8

to $2.5 \mu\text{m}$) cross-dispersed mode with the $0.8''$ slit and the seeing was $0.7''$ - $0.9''$. We obtained eight 180 s exposures arranged in two ABBA nod patterns with a nod step of $7''$ along the slit. For telluric and instrumental transmission correction, the A0 star HD165029 was observed immediately after the target at the same airmass. Flat-fielding, background subtraction, spectrum extraction, wavelength calibration, order merging and telluric correction were done using SpeXtool (Cushing et al. 2004; Vacca et al. 2003). No scaling was applied to the cross-dispersed spectrum when merging the orders. The spectrum is presented and analyzed in §2.4.2.

To constrain the possible binary nature of the primary and the companion, adaptive optics imaging observations of the system were obtained on 2008 July 8 at the Subaru telescope (open use program S08A-074). The observations were made with the AO36 adaptive optics system (Takami et al. 2004) and the CIAO near-infrared camera (Murakawa et al. 2004). The primary star G 203-50 was used for wave front sensing. Five exposures of $7 \text{ s} \times 3$ co-additions were obtained in K_s over five dither positions. The images were reduced in a standard manner. A sky frame was obtained as the median of the five images after masking the regions dominated by the signal from the target. After subtraction of this sky frame, the images were divided by a normalized dome flat image and bad pixels were replaced by a median over their neighbors. All images were finally co-aligned, flux-normalized, and co-added. Owing to the faint R -band magnitude of the target star, the adaptive optics correction achieved is rather poor, with a PSF FWHM of $0.18''$. Visual inspection of the adaptive optics images indicates that neither the primary nor the companion is a nearly equal-mass binary with a separation of $\sim 0.18''$ or larger. Subtraction of a properly shifted and scaled version of the primary star PSF from that of the companion confirms that conclusion as this operation leaves no obvious residual. Our adaptive optics images also provide constraints on the existence of additional, fainter companions in the system. The detection limits achieved indicate that the primary has no other companion with

$\Delta K_s < 4.3$, 7.0 and 7.8 mag at separation greater than $0.5''$, $1''$ and $2''$ respectively. Similarly, the secondary has no companion with $\Delta K_s < 4.3$ above $0.5''$.

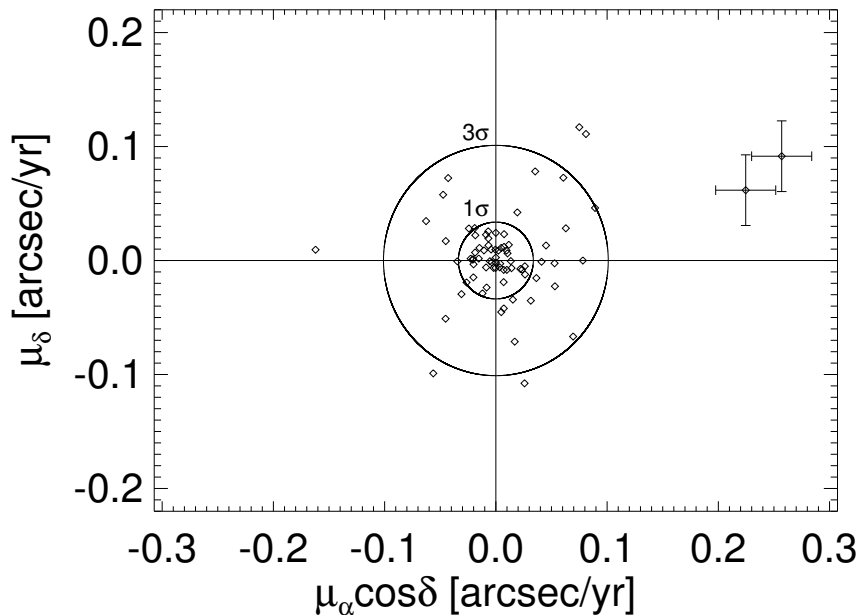


Figure 2.1: Proper motions of all sources within $10'$ of G 203-50. Circles indicate the 1σ and 3σ dispersions. G203-50 and 2M1711+4028 are displayed with error bars based on the 1σ dispersions along each axis, which dominates over the astrometric errors quoted by the individual catalogues. 2MASS and SDSS observations of this system are separated by a baseline of 6.0959 years.

2.4 Physical Properties

A summary of observational and physical properties of the system is given in tables 1 and 2. Proper motions for each component, in a reference frame defined by the median proper motion of all background stars within $10'$, were found and averaged to give a mean system proper motion of 242 ± 15 mas yr^{-1} in right ascension and 77 ± 17 mas yr^{-1} in declination. This is in good agreement with the proper motion tabulated for G203-50 of 250.5 ± 5.5 mas yr^{-1} and 84.2 ± 5.5 mas yr^{-1} in the Revised NLTT catalogue (Salim & Gould 2003).

Table 2.1. Physical properties of the components of G 203-50AB

Quantity	A	B
Designation	G 203-50	2MASS J17114559+4028578
$\mu_\alpha \cos \delta$ (mas yr ⁻¹)	229 ± 43	256 ± 36
μ_δ (mas yr ⁻¹)	61 ± 49	92 ± 43
2MASS J (mag)	11.074 ± 0.016	15.00 ± 0.06
2MASS M_J (mag)	9.34 ± 0.44 ^a	13.5 ^{+0.7b} _{-0.5}
$J - K_s$	0.80	1.28 ^c
$J - H$	0.51	0.79 ^c
$H - K_s$	0.29	0.49 ^c
d	22.2 ± 4.5	20.0 ± 6.3
Spectral type	M4.5 ^d	L5 ⁺² _{-1.5}
T_{eff} (K)	3114 ± 125	1700 ⁺²¹⁰ ₋₂₅₀
Mass (M_\odot)	0.146 ± 0.031	0.066 ^{+0.008} _{-0.015}
$H\alpha$ EW (Å)	3.8 ± 0.5	–
TiO5 ^d	0.34	–
CaOH ^d	0.32	–
CaH2 ^d	0.35	–
CaH3 ^d	0.60	–

^aBased on TiO5, CaOH, and CaH2 spectral indices (Reid et al. 2003)

^bBased on average absolute magnitudes by spectral type, see Dahn et al. (2002)

^csynthetic colors computed from the spectrum of 2M1711+4028 using relative spectral response curves and zero-magnitude fluxes given in Cohen et al. (2003)

^dSpectral type and indices from Reid et al. (2003)

Table 2.2. System properties of G 203-50AB

Quantity	Value
Distance (pc) ^a	21.2 ± 3.9
Angular separation (")	6.40 ± 0.02
Physical Separation (AU)	135 ± 25
$\mu_{\alpha \cos \delta}$ (mas yr ⁻¹) ^a	242 ± 15
μ_{δ} (mas yr ⁻¹) ^a	77 ± 17
Total mass (M_{\odot})	0.212 ± 0.032
Mass ratio	0.45 ± 0.14
Binding energy (erg)	$12.6 \pm 3.8 \times 10^{-41}$

^amean quantities of the components

2.4.1 The primary: G 203-50

G 203-50 has been assigned a spectral type of M4.5 and an absolute magnitude of $M_J = 9.34 \pm 0.18$ ¹ by Reid et al. (2003). The spectral type was assigned based on the TiO5 spectral index (Cruz & Reid 2002), while the absolute J magnitude is derived from polynomial fits to the TiO5, CaOH, and CaH2 spectral indices as a function of absolute J magnitude for M dwarfs with trigonometric parallaxes (Cruz & Reid 2002). We have verified the spectral type by comparison of G 203-50's spectrum (courtesy of Neill Reid) with reference spectra from Kirkpatrick et al. (1991) using standard spectra made available online by Kelle Cruz², and Pickles (1998). The spectrum of G 203-50 is shown alongside the M4.5 spectral standard Gl 83.1 in figure 2.2.

¹errors were not provided with the cataloged data, but we have inferred them from the quoted error in photometric distance

²http://www.astro.caltech.edu/~kelle/M_standards/

Since the absolute J magnitude is derived from spectral indices which may vary continuously between spectral types, it is in principle more precise than a magnitude derived based on the average value for all members of a given subtype. However, the absolute J magnitude provided by Reid et al. (2003) seems to have unrealistically low errors, given the large spread in absolute magnitude for mid-M spectral types (e.g. see figure 4 of Cruz & Reid 2002). As a sanity check we did a SIMBAD search yielding 45 M4.5 dwarfs with measured parallaxes and J band fluxes. The distribution of absolute J magnitudes has a median value of 9.0, and a standard deviation of 0.44. Therefore we choose to adopt a more conservative error estimate of 0.44 magnitudes.

Using $M_J = 9.34 \pm 0.44$, the corresponding photometric distance is 22.2 ± 4.5 pc. Assuming an age > 500 Myr we derived a mass of $0.146 \pm 0.031 M_\odot$ using the empirical mass-luminosity relationship of Delfosse et al. (2000), also in agreement with the models of Baraffe et al. (1998).

The spectrum of G 203-50 shows moderate $H\alpha$ emission. We measured the $H\alpha$ equivalent width (EW) to be $3.8 \pm 0.5 \text{ \AA}$ with errors stemming from a high sensitivity to the regions chosen to fit the pseudo-continuum on either side of the line. We used a cubic polynomial to fit the pseudo-continuum regions from 6544.3-6551.9 \AA and from 6576.6-6582.3 \AA . The relationship between $H\alpha$ activity and age becomes degenerate for low mass dwarfs (Zuckerman & Song 2004) making it difficult to draw firm conclusions about the age of G203-50. However, the activity lifetime of M stars in terms of $H\alpha$ emission has recently been constrained using a sample of 38000 M dwarfs from SDSS Data Release 5 (West et al. 2008). The activity lifetime for M4 and M5 stars respectively is found to be 4.5 and 7 Gyr. Considering that G 203-50 is more active than the majority of M dwarfs of similar spectral type (Reid et al. 2003, e.g.) it is reasonable to infer that it is not near the end of its active phase. Nor does G 203-50 display signs of extreme youth, as it has no associated x-ray source in ROSAT. Therefore we tentatively estimate the age of G 203-50 to be between 1 and 5 Gyr.

Based on the metallicity scale of Gizis (1997) the TiO5 and CaH2 indices of G 203-50 are consistent with solar metallicity, indicating $[M/H] > -1.0$. We measured the metallicity index of Lépine et al. (2007) to be $\zeta_{\text{TiO}/\text{CaH}} = 0.95$, where solar metallicity is represented by $\zeta_{\text{TiO}/\text{CaH}} = 1$, and metal poor stars have $\zeta_{\text{TiO}/\text{CaH}} < 0.825$. Our own fits of model spectra in the 6200-7300 Å region verify these results. We fit the NextGen99 model atmospheres (Hauschildt et al. 1999) to G 203-50's spectrum in the region of TiO and CaH bands of 6200-7300 Å. We used a grid of models with $3000 \text{ K} < T_{\text{eff}} < 3300 \text{ K}$ in steps of 100K, $4.5 < \log g < 5.5$ in steps of 0.5 dex, and $-2.0 < [M/H] < 0.0$ in steps of 0.5 dex. These parameter ranges were chosen based on values of $T_{\text{eff}} = 3114 \pm 125$ and $\log g = 5.14 \pm 0.05$ computed from the evolutionary models of Baraffe et al. (1998) using the 1-5 Gyr isochrones. In each case the templates were convolved with a gaussian with a FWHM equal to the instrumental resolution (~ 5.5 Å) of G 203-50's spectrum and then interpolated onto the data. As noted by Lépine et al. (2007), none of the model spectra were good fits, with the CaH band consistently appearing too strong relative to TiO. However, as expected the best fitting model spectra were those with solar metallicity, with the fit becoming progressively worse for decreasing $[M/H]$. Therefore we find no evidence to suggest that G 203-50 is metal poor. A higher resolution spectrum is required to determine the metallicity more precisely (for example, using the method of Bean et al. 2006, accurate to ~ 0.1 dex).

2.4.2 The Companion: 2MASS J17114559+4028578

Using reference spectra from the IRTF (maintained by John Rayner), SpeX Prism (maintained by Adam Burgasser), CGS4 (Leggett et al. 2001b), and NIRSPEC (McLean et al. 2003) spectral libraries, we determined the best fitting spectral type for the companion to be L5 (see figure 2.3). However, other reasonable matches were found from L3.5 to L6.5. We also measured spectral indices defined by Geballe et al.

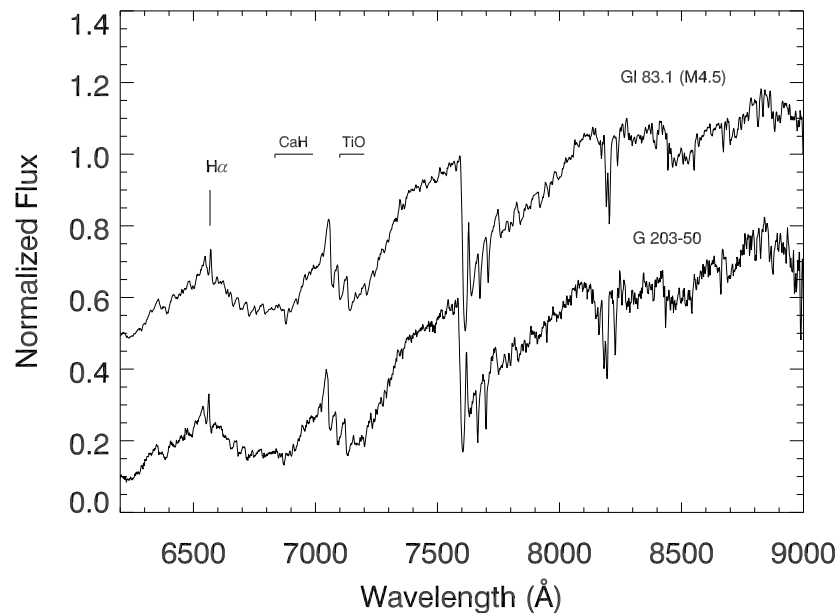


Figure 2.2: Spectrum of G 203-50 (Reid et al. 2003), plotted alongside the M4.5 spectral standard Gl 83.1 for comparison.

(2002), Tokunaga & Kobayashi (1999), Reid et al. (2001b), and McLean et al. (2003). The indices are presented in table 2.3, yielding spectral types from L4.5 to L8. We calculated synthetic 2MASS colors of $J - K_s = 1.28$, $J - H = 0.79$ and $H - K_s = 0.49$ from the spectrum³ of 2M1711+4028 using the relative spectral response curves and zero-magnitude fluxes given in Cohen et al. (2003). These NIR colors make 2M1711+4028 unusually blue for a mid-late L dwarf (Cushing et al. 2008). The large range in spectral type implied by the spectral indices, and the unusually blue NIR colors of 2M1711+4028 likely have a common origin. Several instances of anomalously blue L dwarfs have been previously noted (e.g. Knapp et al. 2004; Burgasser et al. 2008), where the optical spectra appear normal, but the NIR colors are much bluer than average. These blue L dwarfs are characterized by enhanced H₂O absorption

³the quoted 2MASS J , H , and K_s magnitudes are flagged as being biased by the nearby primary, however our derived colors agree with the former to within 0.1 mag

bands and diminished CO, giving the appearance of a later spectral type in the NIR, while J and K band features such as FeH are more consistent with an earlier optical classification (see §2.5.1 for further discussion). Similarly for 2M1711+4028, the strong H₂O indices predict spectral types from L6.5 to L8 while z-FeH and J-FeH indices predict types <L6 and the K1 (not to be confused with K I) index predicts a spectral type of L4.5. This is consistent with the two best matching reference spectra: the relatively blue L dwarfs SDSSp J05395199-0059020 (Fan et al. 2000) and 2MASS J15074769-1627386 (Reid et al. 2000), both of which have optical spectral types of L5, and the latter of which is an optical spectral standard. Considering all of our measurements, we have assigned a NIR spectral type of $L5_{-1.5}^{+2}$ to 2M1711+4028, with our choice being most strongly influenced by the best fitting reference spectra. The error bars span the entire range of reasonable spectral types based on template fitting and spectral indices, excluding the H₂O indices.

Using the absolute magnitude-spectral type relationship provided by Dahn et al. (2002) an absolute magnitude of $13.5_{-0.5}^{+0.7}$ is found for the secondary, corresponding to a distance of 20.0 ± 6.3 pc. This is consistent with the distance of 22.2 ± 4.5 pc derived for the primary. The average distance for the system is 21.2 ± 3.9 pc. We find an effective temperature of 1700_{-250}^{+210} K based on the spectral type-effective temperature relationship of Golimowski et al. (2004). Using the DUSTY model isochrones for 1 and 5 Gyr (Chabrier et al. 2000), we derive a mass of $0.066_{-0.015}^{+0.008} M_{\odot}$. The quoted uncertainty takes into account the 1σ uncertainty in T_{eff} as well as the age interval. While our upper limit of $0.074 M_{\odot}$ straddles the stellar-substellar boundary, this is the most conservative estimate, allowing for a very broad range in spectral types. We conclude that 2M1711+4028 is most likely substellar, an issue which can be resolved in the future by obtaining an optical spectrum in order to further constrain its spectral type.

Based on 2MASS and SDSS astrometry 2M1711+4028 is separated from G 203-50 by

Table 2.3. Spectral indices measured for 2M1711+2048

Index	Value	Spectral Type	Reference
H2O 1.5 μm	1.73	L8	1
CH4 2.2 μm	1.09	L7	1
K1	0.33	L4.5	2
H2O ^A	0.49	L7.5	3
H2O ^B	0.60	L6	3
H2O A	0.45	L7	4
H2O B	0.76	L5.5	4
J-FeH	0.81	<L6	4
z-FeH	0.46	<L6	4

References. — (1)Geballe et al. (2002); (2)Tokunaga & Kobayashi (1999); (3)Reid et al. (2001b); (4)McLean et al. (2003)

a mean angular separation of $6.47'' \pm 0.14''$, in agreement with the angular separation measured from the adaptive optics images of $6.40'' \pm 0.02''$ at $234.1^\circ \pm 0.2^\circ$. This corresponds to a projected separation of 135 ± 25 AU, at the average system distance.

2.5 Discussion

2.5.1 The blue NIR colors of 2M1711+4028

The NIR colors of mid-late L dwarfs vary significantly within a single spectral type. For L5 dwarfs there is a spread of ~ 0.7 magnitudes in $J - K_s$ (Kirkpatrick 2008;

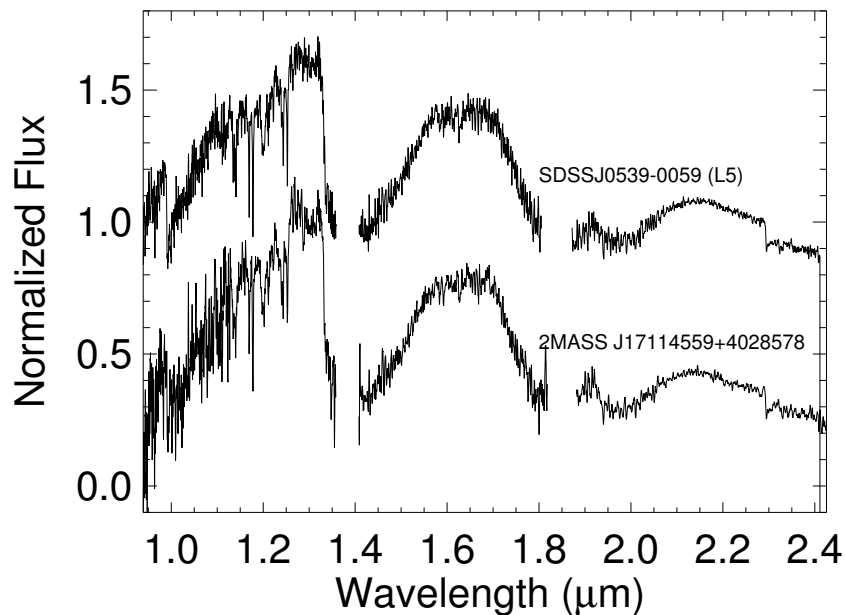


Figure 2.3: Spectrum of 2M1711+4028 obtained at IRTF using the SpeX Medium-Resolution Spectrograph. The spectrum is plotted alongside the L5 dwarf SDSSp J05395199-0059020 (Fan et al. 2000), from the IRTF Spectral Library. Both spectra are normalized in 1.27-1.33 μm and offset for clarity.

Cushing et al. 2008). Although surface gravity and metallicity play a role, comparison of atmospheric models to actual spectra (e.g. Knapp et al. 2004; Cushing et al. 2008; Burgasser et al. 2008) suggests that large variations in the NIR colors of L dwarfs are primarily related to the properties of condensate clouds in their atmospheres, with unusually red SEDs arising from thick clouds and blue ones from thin or large-grained clouds. Common to the known peculiar blue L dwarfs is exaggerated H₂O absorption and diminished CO, as seen in the spectrum of 2M1711+4028. As discussed in §2.4.2 the discrepancy between the late-type H₂O indices and the earlier type FeH and K1 indices, along with its unusually blue NIR colors are indications that 2M1711+4028 falls into this category. For comparison we overplot 2M1711+4028’s spectrum with the spectra of the very red L4.5 dwarf 2MASS J22244381-0158521 (Kirkpatrick et al. 2000), and the relatively blue L5 optical standard 2MASS J15074769-1627386 (see

figure 2.4). All spectra agree reasonably well in the J-band but diverge significantly at H and K, which may indicate differing properties of condensate clouds in their atmospheres. As a member of a wide binary system the surface gravity and metallicity of 2M1711+4028 can be constrained from properties of the primary, yielding an excellent laboratory for studying BD atmospheres. The estimated age of 1-5 Gyr for the G 203-50 primary implies a relatively high surface gravity for the companion, possibly contributing to its blue NIR colors. However surface gravity alone does not seem to be sufficient in explaining the NIR colors of peculiar blue L dwarfs (Burgasser et al. 2008). Additionally, the primary shows no signs of being metal poor, lending support to the hypothesis that unusually blue NIR colors can be primarily attributed to cloud properties. Higher resolution spectroscopy of the primary and a more precise determination of the metallicity is required in order to confirm this conclusion.

Another potential cause of unusually blue NIR colors is unresolved binarity. This may explain the slight onset of CH₄ absorption at 2.2 μm in the spectrum of 2M1711+4028. At least one of the known peculiar blue L dwarfs, 2MASS J08053189+4812330 (Burgasser et al. 2007) is thought to be an unresolved binary with L4.5 and T5 components. However, this system exhibits a pronounced dip in the 1.6 μm CH₄ feature due to the peaked shape of the T dwarf's SED, whereas the spectrum of 2M1711+4028 is relatively flat in that region. Furthermore, the SED and colors of our companion are very similar to that of another blue L4.5 dwarf, 2MASS J11263991-5003550 (2M1126-5003 hereafter), discussed at length by Burgasser et al. (2008). By constructing composite spectra using published L and T dwarf spectra from the SpeX prism library, Burgasser et al. (2008) determined that no reasonable composite spectrum could be found that matched that of 2M1126-5003 in both the optical and NIR. Without an optical spectrum for 2M1711+4028 we are limited in the conclusions we can draw, but its similarities to 2M1126-5003 may suggest that 2M1711+4028 is a single BD. Our AO images support this conclusion, indicating that the BD is not a near-equal mass binary

with separation $> 0.18''$.

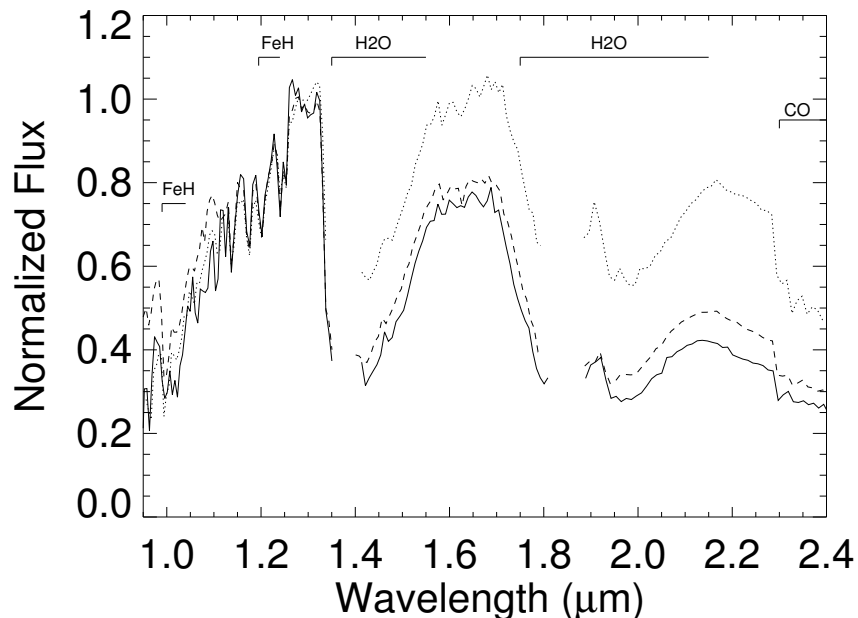


Figure 2.4: Spectrum of blue ($J - K_s = 1.28$) L dwarf 2M1711+4028 (solid line, this paper) overplotted with spectrum of relatively red ($J - K_s = 2.05$) L4.5 dwarf 2MASS J22244381-0158521 (top dotted line, Kirkpatrick et al. 2000) and relatively blue ($J - K_s = 1.52$) L5 optical standard 2MASS J15074769-1627386 (dashed line, Reid et al. 2000). Both comparison spectra are from the IRTF Spectral Library. All spectra are normalized in 1.27-1.29 μm . They have been rebinned to a lower resolution for clarity.

2.5.2 Formation of G 203-50AB

With a total mass of $\sim 0.21 M_\odot$ G 203-50AB is slightly more massive than the rare wide VLM binaries, but much less massive than the solar analogues around which BDs are routinely found at wide separations (see §2.2, and figure 2.5). It is therefore of interest to consider how G 203-50AB may have formed. Could the secondary have formed through gravitational instability in a disk around the primary? Given the mass ratio of $q=0.45$, that would imply a $M_{\text{disk}} > 0.45M_*$, whereas typical disks around low-mass stars contain a few percent of M_* at ~ 1 Myr (Scholz et al. 2006). Since it

is unlikely that the entire disk would end up in the companion, the total disk mass, even in a conservative estimate, would have to be larger than the primary's own mass to start with. Thus, we conclude that formation of 2M1711+4028 in a protostellar disk around G 203-50 is implausible.

On the other hand, gravitational fragmentation of prestellar cores appears to be capable of forming a wide variety of binary systems, depending on the size, mass and angular momentum of the core (e.g. Bate 2000). However, simulations usually have some difficulty producing binary stars with low component masses and wide separations (e.g. Bate et al. 2003; Goodwin et al. 2004). Some theoretical models invoke ejection from the parent cloud to halt further accretion that would otherwise lead to higher masses. Given its projected separation of 135 ± 25 AU, the G 203-50AB binary has a binding energy of $12.6 \pm 3.8 \times 10^{-41}$ erg, placing it below the empirical "minimum" noted by Close et al. (2003) and Burgasser et al. (2007). Thus, it is unlikely to have survived such an ejection. We suggest that G 203-50AB most likely formed via fragmentation of an isolated core and did not suffer strong dynamical interactions during the birth process or subsequently.

2.5.3 Search Sensitivity

In order to assess the sensitivity of our search we simulated proper motion distributions of M dwarfs distributed uniformly in a spherical volume out to 25 pc, with tangential space velocities drawn from the distribution of Schmidt et al. (2007). To be sensitive to a particular M dwarf primary, its displacement between the 2MASS and SDSS surveys had to be greater than the 3σ dispersion of all other stars in the 4 deg^2 section of the sky in which it was found. For each such section of the sky, the time baseline between the surveys was computed and used to determine the minimum proper motion required for a detection. We assumed that the population of M dwarfs within 25 pc was uniformly distributed and assigned equal weight to each 4 deg^2

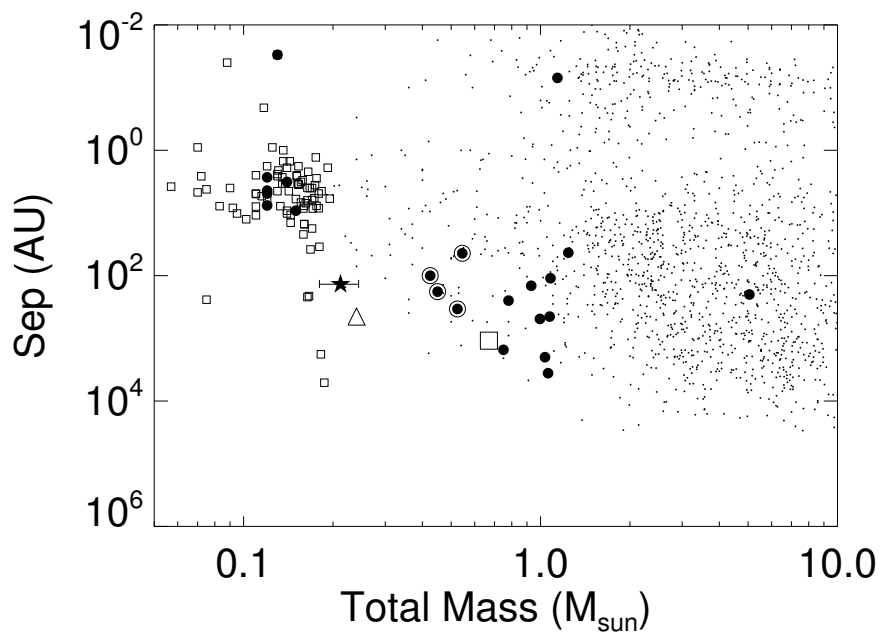


Figure 2.5: Separation versus total system mass for known binary systems. Stellar binaries (dots) are from Tokovinin (1997); Fischer & Marcy (1992); Reid & Gizis (1997b); Close et al. (1990); VLM binaries (open squares) are from the VLM binary archive, maintained by Nick Siegler (vlmbinaries.org); BD-stellar binaries (filled circles) are from Reid et al. (2001c); Metchev & Hillenbrand (2005). G 203-50AB (star symbol) falls in between the VLM and solar analogue regimes, and appears to be more loosely bound than most systems of similar mass. BD-stellar systems with M-dwarf primaries from Reid et al. (2001c) have been circled. The large triangle and square are BD-M dwarf systems from Wilson et al. (2001) and Reid et al. (2006).

area of the sky. Using the simulated proper motion distributions the fraction of M dwarfs whose proper motions we could have measured was determined for each section of the sky, giving an average fraction of 0.58. Adopting an M dwarf space density ($9.0 < M_V < 13.0$ or roughly M0.5-M5.5) of $283.37 \times 10^{-4} \text{ pc}^{-3}$ (Reid et al. 2002), and given a search area of 7668 deg^2 of the sky, we should have been sensitive to approximately 201 ± 12 early-mid M dwarfs within 25 pc.

Although in some cases we were able to recover binary systems with separations $< 4''$, we conservatively put a lower limit of $6''$ on our sensitivity, ensuring that

components are well separated. The upper limit for separation is set by our search radius, which extended to $120''$. These limits correspond to projected separations of 30-600 AU at 5 pc and 150-3000 AU at 25 pc. Our sensitivity to companions around each star was dictated by the mean 2MASS J-band limiting magnitude (S/N=10) of ~ 16.5 , corresponding to a minimum mass of $\sim 0.06 M_{\odot}$ at 25 pc, assuming an age of 1-5 Gyr. Other factors preventing us from finding companions include poor astrometry due to saturation of the primary, or low S/N of the secondary. To estimate the number of binaries missed we used SIMBAD and DwarfArchives⁴ to compile a list of 31 M-dwarfs and 38 BDs with previously measured proper motions large enough to pass our cuts, and tested whether we could measure the same proper motions using SDSS and 2MASS astrometry. We found that 91% of the time for M dwarfs, and 79% of the time for BDs our measured proper motions agreed with the previously measured ones, using the same criteria as our matching algorithm described in §2.3. Therefore, we should have been capable of identifying approximately 72% of binaries with sufficiently high proper motions. Correspondingly we adjust our sensitivity to $\sim 145 \pm 9$ M dwarfs. Adopting Poisson uncertainties on a 1σ confidence interval for our single detection ($= 1_{-0.8}^{+2.3}$) we roughly estimate that $0.7_{-0.6}^{+1.5}\%$ of early-mid M dwarfs have substellar companions with masses greater than $\sim 0.06 M_{\odot}$, at separations above ~ 120 AU.

2.6 Summary and Outlook

Above we have outlined our discovery of a wide, unusually blue, L5 companion to the nearby M4.5 dwarf G 203-50. Since BDs cool with time, it is not possible to infer their masses from observed luminosities. In order to break this degeneracy, the age (or an age indicator such as gravity) of the BD must be known. Even so, determining

⁴<http://dwarfarchives.org>

the mass of a BD requires accurate evolutionary models. In order to constrain these models we must rely on a handful of BDs for which independent age estimates can be obtained. Our companion, 2M1711+4028 falls into this category, as its age can be constrained from the age of the primary. With an angular separation of over $6''$ the components of G 203-50AB are well separated, allowing the primary and secondary to be studied independently. At a distance of only ~ 21 pc, the parallax can be measured relatively easily, providing a more precise determination of distance and luminosity. Assuming an age of 1-5 Gyr, 2M1711+4028 is older than most BDs with independent age estimates (e.g. those found in star forming regions) and can therefore provide an anchor point in a poorly constrained mass-age regime. Furthermore, as an unusually blue L dwarf in the NIR, 2M1711+4028 provides a unique opportunity for studying the relative importance of gravity, metallicity and cloud properties in determining the NIR colors of L dwarfs.

With a total mass falling between the solar mass and VLM regimes, G 203-50AB also has an important bearing on star formation theory. Based on the large mass ratio between the system components, we rule out formation of the companion in the disk of the primary. Instead we suggest that this weakly bound binary formed via the fragmentation of an isolated core, and did not suffer disruptive dynamical interactions. Statistically we put an upper limit of 2.2% on the wide companion fraction for BD companions with $m > 0.06 M_{\odot}$ around early-to-mid M dwarfs.

In order to better constrain the properties of this unique system we recommend that future observations of G 203-50AB include: a parallax measurement to resolve uncertainties over the distance and absolute magnitude of G 203-50; a high resolution spectrum of G 203-50 in order to determine the metallicity more precisely; an optical spectrum for 2M1711+4028 to determine an optical spectral type; and time series spectra to check for spectroscopic binarity.

Chapter 3

Large Amplitude Variations of an L/T Transition Brown Dwarf

Contents of this chapter have been published in the *Astrophysical Journal*: **Radigan, J., Jayawardhana, R., Lafrenière, D., Artigau, E., Saumon, D. & Marley, M.** *Large-amplitude Variations of an L/T Transition Brown Dwarf: Multi-wavelength Observations of Patchy, High-contrast Cloud Features.* 2012, *ApJ*, 750, 105. Reproduced by permission of the AAS.

I wrote the paper, did the majority of observing, reduced the light curve data, and led the analysis and interpretation of the results, under the supervision of R. Jayawardhana. D. Lafrenière also did some of the observing, and reduced archival HST adaptive optics images. Theoretical atmosphere models used were provided by M. Marley and D. Saumon.

3.1 Chapter Overview

We present multiple-epoch photometric monitoring in the J , H , and K_s bands of the T1.5 dwarf 2MASS J21392676+0220226 (2M2139), revealing persistent, periodic ($P = 7.721 \pm 0.005$ hr) variability with a peak-to-peak amplitude as high as 26% in the J -band. The light curve shape varies on a timescale of days, suggesting that evolving atmospheric cloud features are responsible. Using interpolations between model atmospheres with differing cloud thicknesses to represent a heterogeneous surface, we find that the multi-wavelength variations and the near-infrared spectrum of 2M2139 can be reproduced by either (1) cool, thick cloud features sitting above a thinner cloud layer, or (2) warm regions of low condensate opacity in an otherwise cloudy atmosphere, possibly indicating the presence of holes or breaks in the cloud layer. We find that temperature contrasts between thick and thin cloud patches must be greater than 175 K and as high as 425 K. We also consider whether the observed variability could arise from an interacting binary system, but this scenario is ruled out. 2M2139 joins the T2.5 dwarf SIMP0136 discovered by Artigau and coworkers as the second L/T transition brown dwarf to display large-amplitude variability on rotational timescales, suggesting that the fragmentation of dust clouds at the L/T transition may contribute to the abrupt decline in condensate opacity and J -band brightening observed to occur over this regime.

3.2 Introduction

The combination of condensate clouds and rapid rotation has long-motivated searches for cloud and weather-related variability of ultracool dwarfs (e.g. Tinney & Tolley 1999). Observations in the red optical (Bailer-Jones & Mundt 2001; Gelino et al. 2002; Koen 2003; 2004; 2005a;b) have targeted mainly late-M and early-L dwarfs due to a drop-off in optical flux for later spectral types. Evidence for periodic variability

is found for $\sim 30\%$ of early-type objects monitored in the I -band with peak-to-peak amplitudes of a few percent. However, it is unclear whether modulation is the result of magnetic spots, dust clouds or a combination of both. In order to study variability at the L/T transition, a move to infrared wavelengths wherein late-L and T dwarfs are bright is required.

Since the atmospheres of late-L and T dwarfs are increasingly neutral, they are less likely to support cool magnetic spots (Gelino et al. 2002; Mohanty et al. 2002), making the interpretation of detected variability in this regime less ambiguous. However, in contrast to optical surveys, ultracool dwarf variability at near and mid infrared wavelengths (e.g. Enoch et al. 2003; Koen et al. 2004; 2005; Morales-Calderón et al. 2006; Goldman et al. 2008; Bailer-Jones 2008; Clarke et al. 2008) appears to be rare (at least at similar amplitudes). In a study of 18 L and T dwarfs, Koen (2004) found no significant evidence of variability in the J band above the ~ 20 mmag level nor in the H or K_s bands above ~ 40 mmag. A further study focussing on known I -band variables (Koen et al. 2005) failed to detect any variability in the near infrared (NIR) J , H , and K_s bands in any of these same objects. In contrast, Enoch et al. (2003) monitored 9 objects with L2-T5 spectral types in the K_s band and claim large-amplitude periodic variability (0.1-0.4 mag) for 3 objects in their sample. However, these detections have not been repeated at later epochs, and their amplitudes are only $\sim 1-3$ times the reported photometric precision.

While detections at the level claimed by Enoch et al. (2003) have not been reported since, recent results from high-precision NIR monitoring provide some evidence for lower-amplitude variability in the NIR. In a survey of 8 late-L and T dwarfs in the J band, Clarke et al. (2008) claim periodic variability for 2 of 7 late-L and T dwarfs monitored with amplitudes of 15 and 8 mmag and periods of 1.4 hr and 2 hr respectively. Most recently, in a single targeted study, Artigau et al. (2009) found the T2.5 dwarf, SIMP0136 (Artigau et al. 2006), to be variable with a peak-to-

peak amplitude of ~ 50 mmag in J and a period of 2.3 hr (a $10\text{-}\sigma$ detection). The high significance, repeatability and multi-band detections for SIMP0136 represents a breakthrough in comparison to previous work. Notably, SIMP0136 falls directly within the L/T transition regime.

Here we present continuous photometric monitoring in the J , H , and K_s bands of the T1.5 dwarf 2MASS J21392676+0220226 (Reid et al. 2008, 2M2139 hereafter) using the Wide Field Infrared Camera on the DuPont 2.5-m telescope at Las Campanas. 2M2139 is the most variable BD to date, and was discovered in our large J -band monitoring program for weather-related variability of cool BDs (Radigan et al., in preparation). In §3.3 we describe the observations and data reduction, and in §3.4 we present and analyze the reduced light curves. In §3.5 we present an overview of 2M2139's physical properties based on existing archival data. In §3.6 we attempt to model the observed multi-band variability using linear combinations of 1-dimensional cloudy and clear atmosphere models. In §3.7 we discuss our results and possible origins of the observed variability. Finally, in §3.8 we give a brief summary of our conclusions and suggestions on how to proceed.

3.3 Observations and Data Reduction

3.3.1 LCO Observations

Observations of 2M2139 were made using the Wide Field Infrared Camera (WIRC; Persson et al. 2002) on the Du Pont 2.5 m telescope at Las Campanas, as part of a large survey for J -band variability of cool BDs (Radigan et al., in prep). The camera consists of 4 HAWAII-I arrays, each with a $3.2'$ field of view and a pixel scale of $0.2''$. The camera is intended as a wide-field survey camera, with $3'$ gaps between detectors. We have not used it as such, choosing to position our target consistently on the south-west array, which we determined to be the least noisy of the four chips. New

Table 3.1. Observing Log

Date ^a	Instr. ^b	Filter	UT Start ^c	Length (hr)	t _{exp} (s)	N _{exp}	Notes
01 Aug 2009	WIRC	J	00h19m	3.1	40	140	Clear at start with light clouds after 1.5 hr, 0.7'' seeing
21 Sep 2009	WIRC	J	00h14m	5.12	60	255	Clear with occasional passing light cloud, 0.7'' seeing
22 Sep 2009	WIRC	K _s	23h53m	5.48	20	412	Clear with occasional passing light cloud, 0.8'' seeing
23 Sep 2009	WIRC	J	23h29m	5.99	60	260	Clear with occasional passing light cloud, 0.7'' seeing
24 Sep 2009	WIRC	H	23h25m	6.01	20	498	Clear with occasional passing light cloud, 0.7'' seeing
26 Sep 2009	WIRC	J,H,K _s	23h45m	5.58	45,20,20	91,130,132	Clear, 1.5'' seeing
30 Sep 2009	WIRC	J,H,K _s	23h40m	4.81	45,20,20	82,110,114	Clear at start becoming cloudy after first 4.1 hr, 1.2'' seeing
01 Oct 2009	WIRC	J,H,K _s	23h46m	5.11	45,20,20	77,104,110	Clear, 1.1'' seeing
08 Nov 2009	CPAPIR	J	22h37m	4.37	21.6	387	Clear, 1.5-2'' seeing

^aDates correspond to the local day at the beginning of the night.

^bWIRC observations were conducted on the LCO 2.5-m telescope, and CPAPIR on the OMM 1.6-m telescope

^cUT Start time may be +1 day ahead of the local date.

J-band filters closely matching the Mauna Kea Observatory (MKO) system (Tokunaga & Vacca 2005) were purchased and installed for our survey in order to minimize the effects of differential atmospheric extinction, by cutting off time-variable telluric water absorption bands red-ward of $1.35 \mu\text{m}$ (e.g, Artigau 2006).

2M2139 was first monitored in the *J* band on 01 Aug 2009 for 2.5 hours. An analysis of its light curve revealed a 90 mmag increase in brightness over this time span. This prompted us to follow-up with longer photometric sequences in *J*, *H*, and *K_s* bands on the four consecutive nights of 21-24 Sep 2009. In order to obtain near-simultaneous photometry in multiple bandpasses, additional photometric sequences alternating between *J*, *H*, and *K_s* bands every ~ 20 min were obtained on 26 Sep 2009, 30 Sep 2009, and 01 Oct 2009. A log of all observations is provided in Table 3.1.

All observations except those of 21 Sep 2009 were made using a random dither pattern wherein the telescope was offset by at least $3''$ (15 pixels) after each exposure, and all pointings were contained in a $15''$ (75 pixels) square box. Individual exposure times in *J* were 40 s (09 Aug 2009), 45 s (26 Sep 2009, 3 Sep 2009, 01 Oct 2009), or 60 s (23 Sep 2009). Exposures were read out using correlated double sampling. Along with telescope offsets this resulted in effective cadences of 62 s, 68 s, and 82 s respectively for the listed exposure times. For the *H*- and *K_s*-bands we used individual exposure times of 20 s throughout, resulting in an effective cadence of 42 s.

The *J*-band observations of 21 Sep 2009 employed a staring strategy, in which the target centroid was kept fixed on the same pixel throughout the sequence. This was accomplished using an *IDL* routine to stream the incoming science images onto a standard laptop and compute real-time guiding corrections. An alert was sounded, and manual closed-loop corrections to the guide-camera reference position were made each time the target strayed by more than 0.5 pixels from its initial position (approximately once every 5-15 minutes). Without telescope offsets the efficiency of staring observations is significantly increased. Individual exposures of 60 s were used,

resulting in a cadence of 67 s. Nine-point dither sequences for the purpose of rough sky subtraction and centroiding were made at the beginning, middle and end of the 5.12 hr observation.

For each sequence, dome-flats (lamp on and off) and dark frames corresponding to each exposure time were taken either on the afternoon preceding, or the morning following each observation.

3.3.2 Reduction and Processing of WIRC data

All raw images were corrected for non-linearity using a detector response curve measured on 27 Jul 2009. Calibration images were median-combined to create high signal-to-noise dark and flat-field frames. The dark-current contribution was then subtracted from all other images. For the dithered sequences, a running sky frame was computed by median combining the 11(7) $J(HK)$ -band images that were (i) taken closest in time to, and (ii) were spatially offset by at least $6''$ (30 pixels) from the image being reduced. After an initial first-pass reduction, stars were identified from the stacked field, and then masked for the second pass so as not to bias the median-combined sky frames. After sky subtraction, pixel-to-pixel variations in quantum efficiency were removed by dividing the resultant image by the flat-field. Bad pixels identified from the flat-field or pixels having more than 35000 counts ($>3\%$ non-linear) were flagged. Except for sky subtraction, reduction of the non-dithered staring sequence is almost identical to the procedure described above. In this case the sky frames were constructed by median combining the 9-point dither sequences taken before and after staring, linearly interpolating between them in time, and scaling to the 3σ -clipped median of each science image. Since immediate background levels are also subtracted using aperture photometry, the primary motivation of sky subtraction for the staring sequence is to achieve better centroiding of the target and reference PSFs. For all reductions and analyses we considered only the south-west array of the

WIRC camera.

Relative Differential Photometry

For each monitoring sequence, aperture photometry was performed on 2M2139 and a set of reference stars in 2M2139's the field of view, using a circular aperture of 1.5 times the median full width at half maximum (FWHM) of all stars in each image. A large aperture was chosen to decrease the systematic effects of slightly elongated PSFs on our photometry which occasionally occur due to a gradual degradation of the telescope focus during long sequences. Residual sky levels in the vicinity of each star were measured inside an annulus centered on each source of inner radius 3.7 times the FWHM and a width of 11 pixels. Flux measurements in which a flagged pixel fell inside the aperture were set to an error value and disregarded in the light curve analysis.

The raw light curves display fluctuations in brightness due to changing atmospheric transparency, airmass, and residual instrumental effects throughout the night. To a very good approximation these changes are common to all stars, and can be removed. First, the raw light curves of all stars were converted from absolute to relative fluxes via division by their median brightness. Next, for each reference star a calibration curve was created by median combining the light curves of all other reference stars (excluding that of the target and star in question). The raw light curve of each reference star was then divided by the corresponding calibration curve to obtain a corrected light curve. The standard deviations of the corrected light curves for each reference star (σ) were then measured. This process was repeated multiple times, using an iterative approach where only reference stars with $\sigma < 15$ mmag in J and < 25 mmag in H and K_s were kept.¹ This process was terminated (usually after the second iteration) when the number of good calibration stars no longer changed.

¹For the observations of 30 Sep 2009 these criteria were relaxed to $\sigma < 20$ mmag in J and < 30 mmag in K_s , and for the observations of 01 Oct 2009 they were relaxed to $\sigma < 30$ mmag in K_s .

A calibration curve for 2M2139 was then computed using this subset of high signal-to-noise (S/N) references, less a comparison star of similar brightness. Figure 3.1 shows a stacked and mosaicked image of the field with reference stars labelled by letter. Details (identifiers and magnitudes) of the reference and comparison stars used to calibrate each set of observations are provided in table 3.2. We note that on some nights otherwise high S/N reference stars were excluded due to consistently falling on bad pixels, saturation, or contamination from a faint nearby source in poor seeing conditions (e.g. star E). While it would be optimal to use a common set of reference stars throughout, we find that the shape and amplitude of our final light curves are independent of our choice of reference stars. For most of our observations star *B* from figure 3.1 was chosen as the comparison, with the exception of 01 Aug 2009 when it didn't fall in the field of view and we used star *I* instead.

Detrended light curves for 2M2139 and the comparison star were obtained by dividing their raw fluxes by the final calibration curve. An example of raw and detrended light curves for the reference stars and target, as well as light curve standard deviations as a function of star brightness for the 23 Sep 2009 epoch are shown in figure 3.2. Detrended J , H and K_s light curves for 2M2139 and the comparison star for the consecutive nights of 21-24 Sep 2009 are displayed in figure 3.3.

In addition, light curve properties for all epochs including amplitudes, and standard deviations for the target (σ_t) and comparison star (σ_c) are provided in table 3.3. Since the light curves for 2M2139 show large trends, σ_t is obtained by taking the standard deviation of 2M2139's light curve subtracted by a shifted version (by one element) of itself, and then divided by $\sqrt{2}$. For the epochs where we cycled through the J , H , and K_s filters, large time gaps exist in the sequence for any given filter, necessitating a different method for obtaining σ_t . Thus for these sequences we took σ_t to be the average of the standard deviations obtained for individual ~ 20 min segments in a given filter.

Table 3.2. Reference stars used for differential photometry

2MASS ID	Letter ID ^a	J	$J-K_s$	Epochs used ^b
J21392216+0220185	A	15.51	0.65	2,4,9
J21392311+0222009	B	14.46	0.64	2-9 ^c
J21392542+0222102	C	12.98	0.48	1-3,5-9
J21392392+0222383	D	15.22	0.93	2-5,6-7(J, H only),8-9
J21392228+0223082	E	14.26	0.64	2,4-7
J21392465+0223140	F	14.63	0.92	2-9
J21393173+0222126	G	11.48	0.37	3,5-9
J21393318+0222356	H	15.40	0.52	1
J21393533+0220584	I	13.50	0.36	1 ^c
J21393502+0220466	J	15.33	0.59	1
J21393596+0220488	K	15.65	0.59	1

^aStars are labelled by letter in figure 3.1.

^bEpochs from table 3.1 are numbered chronologically from 1-9.

^cComparison star

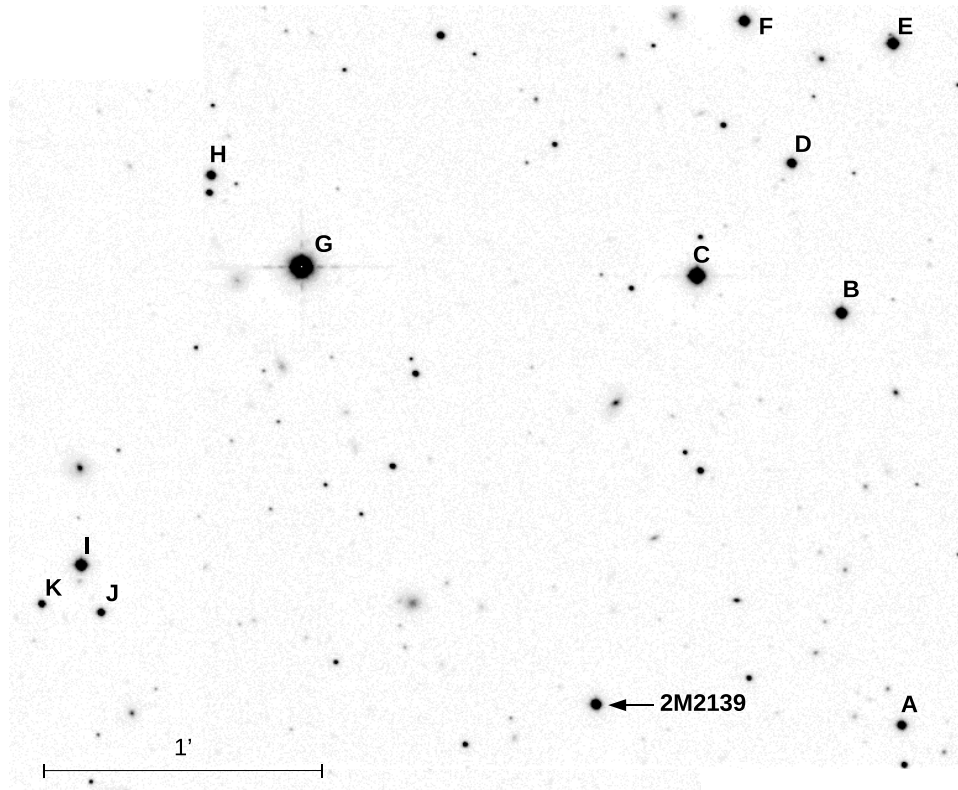


Figure 3.1: Stacked and mosaicked WIRC J band image of the field surrounding 2M2139 . The target and reference stars used for differential photometry are labeled, with details provided in table 3.2.

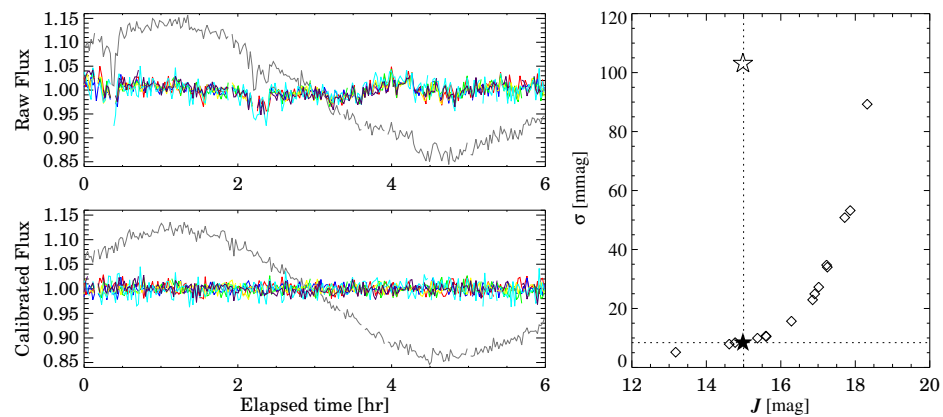


Figure 3.2: *Left*: An example of raw (top) and detrended (bottom) lightcurves for 2M2139 (grey lines) and reference stars (colored lines) for a photometric sequence taken on 23 Sep 2009. *Right*: Standard deviations of the detrended light curves for all stars on the chip as a function of J magnitude. 2M2139 is shown as an open star symbol.

3.3.3 OMM Observations

Due to the evolving nature of the light curve, the target was observed again on the night of 08 Nov 2009 using the Observatoire du Mont Mégantic 1.6-m telescope and the Camera PANoramic Proche Infra-Rouge (CPAPIR, Artigau et al. 2004). The camera has a 30' field of view with a pixel scale of 0.89". As with our WIRC observations, an MKO *J* filter was employed. Observations commenced at an airmass of 1.39 and concluded at an airmass of 2.35. Random dithers were made between each exposure, always keeping the target within 1' of the central position. A single co-addition with an exposure time of 21.6 s was used for all science frames, resulting in a median cadence of 38 s.

3.3.4 Reduction of CPAPIR data

The raw CPAPIR images were processed using the CPAPIR pipeline. A running median sky image were constructed by taking the median of the 11 frames centered on the frame of interest after masking bright field stars identified in the Two Micron All Sky Survey (2MASS; Skrutskie et al. 2006) . After sky subtraction, images are divided by a flat field image constructed from on/off dome images. The Poisson noise associated with the flat field is $\sim 0.2\%$ per pixel and a negligible contributor to the overall error budget. Aperture photometry was performed in a similar manner to the WIRC images, but using an aperture size of 1 FWHM, and an annulus of inner radius 3.5 FWHM, and 11 pixel width.

3.3.5 Photometric Calibration

In addition to the relative photometry, all light curves were flux-calibrated against the 2MASS catalog using references identified in figure 3.1. While the WIRC *H* and *K_s* filters are similar to those from 2MASS, the MKO *J* filter installed for our survey

is significantly narrower than the 2MASS J filter. Because we do not have enough reference stars to derive robust color-dependent corrections between our MKO J filter and 2MASS J filter, we first converted 2MASS J magnitudes of the reference stars to MKO magnitudes according to the color-dependent transformations provided by Leggett et al. (2006).

The 2MASS catalog magnitudes, corrected for our filter system, were then converted to counts (multiplied by some arbitrary factor) and a linear fit between the catalog and measured counts was performed. The quality of the photometric calibration was determined from the slope error for each linear fit, and found to be accurate among reference stars at the 1-2% level.

In figures we have opted to plot light curves in units of relative flux as opposed to magnitudes. The reference magnitudes corresponding to relative fluxes of 1 are given by $J_{MKO}=14.75$, $H=14.11$, and $K_s=13.59$. The chosen reference magnitudes correspond to the median magnitudes measured in each bandpass for the near-simultaneous JHK_s sequence of 26 Sep 2009, where the light curves were observed to have similar amplitudes in all bandpasses.

In addition to placing all light curves on a common flux scale, the photometric calibration allows us to compare the magnitudes and colors derived here with archival data from 2MASS and the SpeX Prism Library². In the SpeX Prism Library there are two low resolution NIR spectra ($R\sim 120$) for 2M2139, obtained in 2003 and 2004 by Burgasser et al. (2006a). The SpeX Prism Library, while not able to provide absolute photometry, allows us to derive colors for 2M2139 at additional epochs. When synthetic 2MASS colors for M, L and T dwarfs from the SpeX Prism Library are compared to their 2MASS values, the match is surprisingly good, with a standard deviation similar to the reported photometric errors from the 2MASS catalog. For L and T dwarfs no significant systematic trends exist as a function spectral type, whereas

²<http://pono.ucsd.edu/~adam/browndwarfs/spexprism/>

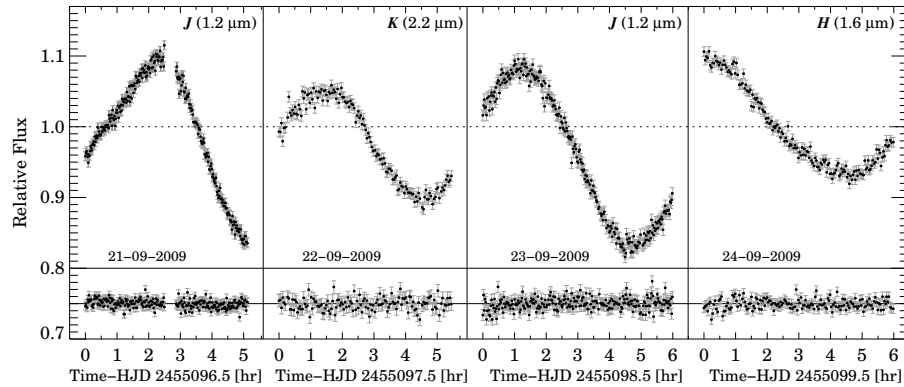


Figure 3.3: Reduced light curves for 2M2139 obtained from 21-24 Sep 2009 (top) and a comparison star of similar brightness (bottom). Vertical lines separate observations on different nights. The given dates correspond to the beginning of each observing night. The J -band data points show unbinned 60 s exposures, while the H and K_s data points show 20 s exposures binned by a factor of 3.

we find the synthetic $J - K_s$ colors of M dwarfs to be on average slightly bluer than values derived in 2MASS. We present a comparison between 2MASS and synthetic SpeX colors in Appendix A.1.

Finally, for a proper comparison between WIRC, 2MASS, and SpeX (synthetic 2MASS) photometry, we have converted WIRC magnitudes derived for 2M2139 to the 2MASS system. Correction terms between the two filter systems were computed directly from 2M2139’s NIR spectrum using 2MASS and WIRC filter plus system transmission curves and a Kurucz model Vega spectrum as a zero-magnitude flux reference (Kurucz 1979; 1993). Recall that for reference stars corrections between J filters were accounted for in advance by our conversion of 2MASS to MKO J magnitudes, while H and K_s band corrections are generally negligible. Magnitudes and colors measured for 2M2139 from WIRC, 2MASS and SpeX epochs, as well as correction terms specific to 2M2139 used to convert between WIRC and 2MASS filter systems, are provided in table 3.4.

3.4 Results and Analysis

3.4.1 The Reduced Light Curves

Full J , H , and K_s light curves from the adjacent nights of 21-24 Sep 2009 are shown in figure 3.3. These epochs encompass the largest variability observed for 2M2139 with peak-to-peak amplitudes of 26% in J , 17% in H and 16% in K_s . Peak-to-peak amplitudes are measured directly as the maximum change in brightness, divided by the mid-brightness. We note that the H -band variation may be slightly larger since its global maximum is not entirely captured.

The near-simultaneous J , H , and K_s light curves taken on 26 Sep 2009, 30 Sep 2009, and 01 Oct 2009 are shown in figure 3.4. Unbinned data are shown in the top panel, while in the middle panel the data have been binned to one data point per filter change (6 exposures per epoch in J , and 10 in H and K_s , less exposures discarded due to bad pixels). Error estimates for the unbinned data points are given by the standard deviation of all measurements in a continuous segment at a given filter position, while the binned data points were assigned uncertainties of $1/\sqrt{N}$ times lower, where N is the number of binned exposures at a given filter position. Relative amplitudes of variability in the different bands were measured by assuming all light curves to have the same functional form, but with differing amplitudes. For this purpose we used the J -band light curves as templates, linearly interpolating between binned data points. Scaled versions of the J -band templates were then fit to the H and K_s light curves using a simple weighted linear regression. The best-fit solutions (which we will refer to as the H and K_s band templates) are overplotted on the data in figure 3.4. We find amplitude ratios of $A_H/A_J = \{0.91 \pm 0.07, 0.84 \pm 0.08, 0.91 \pm 0.15\}$ and $A_{K_s}/A_J = \{0.83 \pm 0.08, 0.59 \pm 0.07, 0.45 \pm 0.11\}$ for the earliest to latest epoch respectively. Here, A_i represents a peak-to-peak amplitude of photometric variability in a bandpass i given by the absolute change in brightness divided by the

mid-brightness. Uncertainties for the amplitude ratios were determined by repeating the above procedure on a set of 1000 simulated light curves. The simulated light curves were obtained from sampling the J , H , and K_s band templates at the times of our binned data points in figure 3.4. A random noise component was added to each point, drawn from a gaussian distribution with a standard deviation equal to the 1σ uncertainty corresponding to that data point. In practice we found that the fits between the H and K_s light curves and scaled J -band templates produced reduced χ^2 values from 1.4-3, and we therefore scaled the width of the random error component to achieve a reduced $\chi^2 \sim 1$ in comparison to the best-fit templates. Measured light curve amplitudes and ratios for the different epochs are tabulated in table 3.3.

The results from the near-simultaneous sequences are somewhat surprising. The light curves from the consecutive nights of Sep 21-24, where observations were made in a single but different band each night (figure 3.3), would have led us to conclude that variations in the H and K_s bands are only 50-60% of those in J . However, amplitude ratios measured from the first near-simultaneous sequence on 26 Sep 2009 appear close to unity. Upon repeating the near-simultaneous measurements at two subsequent epochs we continued to find $A_H/A_J \gtrsim 0.84$, while we found A_{K_s}/A_J as low as 0.45 in the latter epoch. Our data may hint at amplitude ratios that are themselves variable, as amplitude ratios from the first and last epoch with simultaneous JHK_s data are incompatible at the 2σ level. In addition, none of the peak to peak amplitudes measured for the simultaneous JHK_s light curves (irrespective of bandpass) are as large as the lowest amplitudes measured from the single-band consecutive night sequences of 21-24 Sep 2009. Therefore, there is evidence that both amplitude ratios, as well as the overall amplitude may vary with either epoch, light curve phase, or a combination of both.

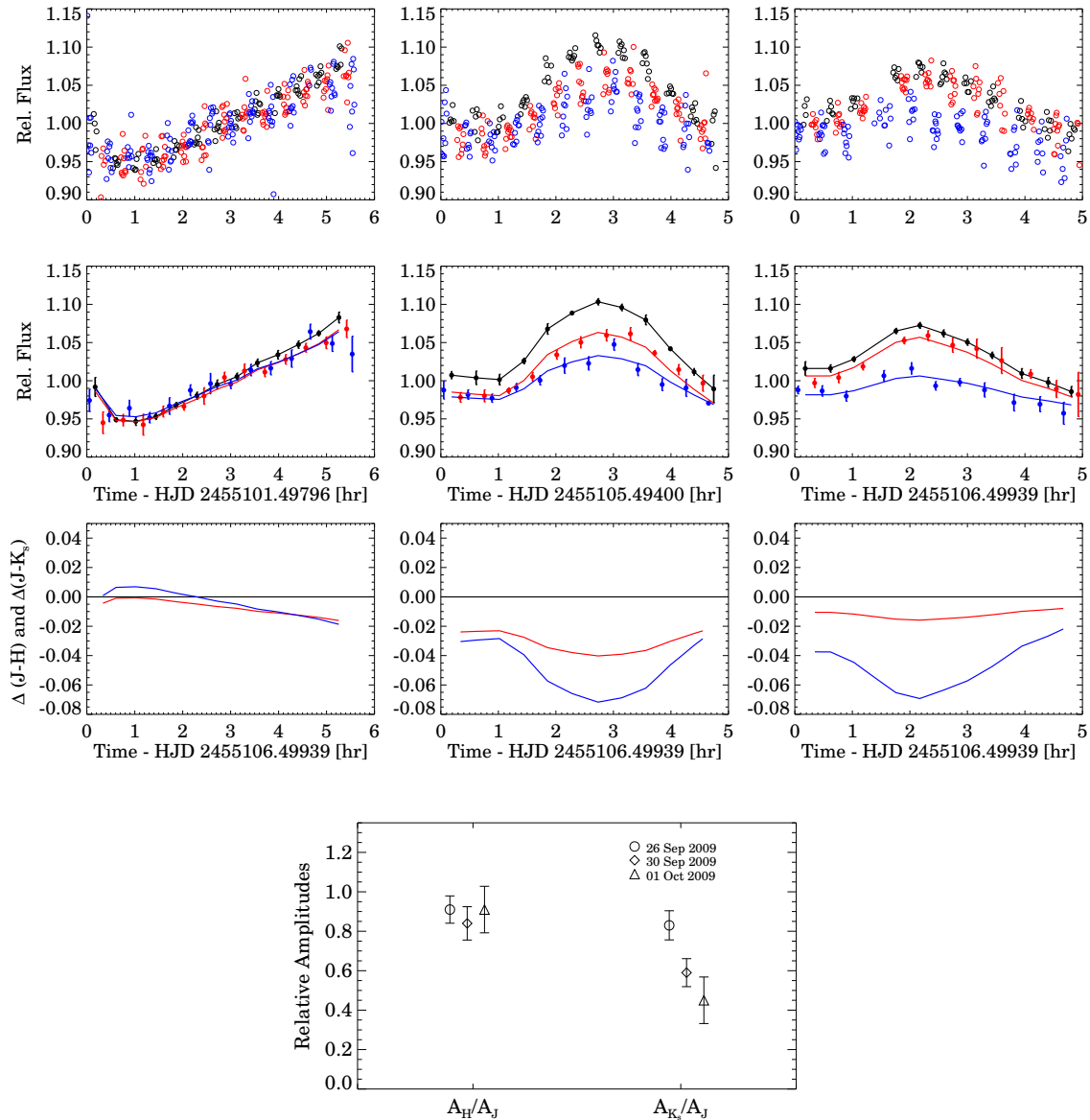


Figure 3.4: *Top row panels:* Unbinned interleaved J (black), H (blue), and K_s (red) photometric sequences from 26, 30 Sep 2009 and 01 Oct 2009 epochs. Unity corresponds to J_{MKO} , H , and K_s magnitudes of 14.75, 14.11, and 13.59 respectively. *Middle row panels:* Binned (see text for details) J , H , and K_s light curves, with same color scheme as above. Linear interpolations of the binned J band points are shown as black lines. Scaled, best-fitting versions of these J -band templates to the H and K_s light curves are shown as red and blue lines respectively. *Bottom row panels:* Changes in $J - H$ and $J - K_s$ colors, based on the scaled templates. *Bottom panel:* Amplitude ratios and uncertainties derived from Monte Carlo simulations for each of the three epochs.

3.4.2 Rotation and Longer Timescale Trends

While not strictly uniform from epoch to epoch, the variations exhibited by 2M2139 show a clear periodicity. Since the *J*-band light curves do not seem to have evolved significantly in shape from 21 Sep 2009 to 23 Sep 2009 we determined an approximate period by fitting a periodic function to these light curves. Since variations are not perfectly sinusoidal, we chose a round, non-overlapping, two-spot model (Dorren 1987) as our periodic function, and performed fitting using a Markov Chain Monte Carlo (e.g. Lewis & Bridle 2002) technique with a Metropolis Hastings algorithm (Metropolis et al. 1953; Hastings 1970) (figure 3.5). Using this method we determined a period of 7.721 ± 0.005 hr, with the quoted value and errors derived from the maximum likelihood and 67% credible regions of the posterior distribution of periods. The uncertainty is likely underestimated due to the implicit assumption that the light curve shape has not evolved between cycles used for fitting.

Two spots are required to fit the asymmetry in the light curve, which is hinted at from a secondary “bump” present at the beginning of the *J*-band light curve from 21 Sep 2009, and which also becomes apparent when observations are phased to the best-fit period.

In addition to fitting for the period, we also computed a Lomb-Scargle Periodogram (Scargle 1982; Horne & Baliunas 1986) of the *J*-band data spanning 21 Sep 2009 to 01 Oct 2009 (figure 3.6). In order not to favor epochs with more densely sampled data, all light curves were linearly resampled at 10-min spacing within each observing window. Despite falling close to the 8 hr sub-peak of the window function (which peaks at 24 hr), the strongest peak at 7.73 hr matches the 7.721 ± 0.005 hr recovered from our spot modeling.

We find that the uncertainty in the best-fit rotation period of 7.721 ± 0.005 hr gives us the freedom to phase the Aug 2009 light curves with those from Sep 2009, but there is no single period that can accommodate all epochs spanning Aug 2009 - Nov 2009.

As an example of this, all light curves (presented on a common flux scale) are shown in figure 3.7, phased to an over-constrained period of 7.723 hr. In fine-tuning the period to precisely 7.723 hr, we have arbitrarily chosen to phase the earlier (Aug 2009) observations with those from Sep 2009 in order to illustrate the resultant mismatch in phases for the later (Nov 2009) epoch. However, given the lack of a common phasing across all epochs, there is no reason to expect the 01 Aug 2009 observations to be in phase with the middle epochs. Thus, while we have used a period of precisely $P = 7.723$ hr in our figures, it should be understood that this is illustrative, and that the actual periodicity cannot be constrained beyond 7.721 ± 0.005 hr from our observations.

While the maxima and minima of the light curves spanning 21 September 2009 to October 01 2009 appear roughly synchronized with a 7.723 hr period, there are large differences in amplitude, and more subtle differences in light curve shape from epoch to epoch.

There is a marked decrease in the observed light curve amplitudes between the 23 Sep 2009 and 26 Sep 2009 epochs. While this may indicate short timescale evolution of cloud features, it is also consistent with a more stable, double-peaked light curve with a period of $2 \times 7.72 = 15.44$ hr such that the higher-amplitude variations observed on 21 Sep 2009 and 23 Sep 2009 sample a different phase of the light curve than the lower-amplitude variations observed at subsequent epochs. This possibility is illustrated in figure 3.8 where light curves spanning 21 Sep 2009 to 01 Oct 2009 are shown phased to both 7.723 hr and 15.446 hr (once again, over-constrained) periods. For the case where $P = 15.446$ hr, overall changes in light curve shape and amplitude, although still apparent, are less pronounced. A period of 15.44 hr would make 2M2139 a somewhat slow rotator in comparison to other ultracool dwarfs with $v \sin i$ measurements, which have inferred periods ranging from ~ 2 -12 hr (e.g. Reiners & Basri 2008).

There appears to be some phase coherence on a timescale of days to weeks,

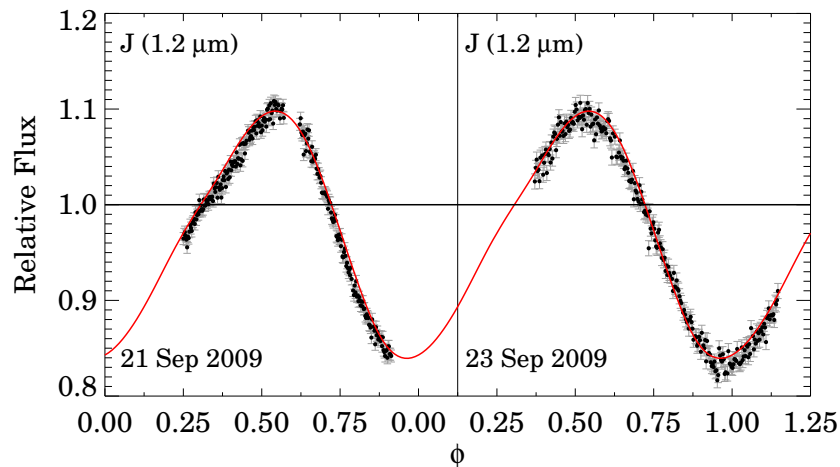


Figure 3.5: *Top*: Best-fitting round, two-spot model (red curve, $P=7.721$ hr) to the J -band light curves from 21 and 23 Sep 2009 (data points).

suggesting that we are observing cloud features that persist at least this long. Over months the phase coherence is lost, which may indicate evolution of the cloud coverage or the dissipation and formation of new features. An intriguing possibility is that the long-timescale evolution of the light curve is caused by the differential rotation of a storm system with respect to cloud features at different latitudes (e.g. Artigau et al. 2009). The light minimum of the last epoch (8 Nov 2009) is approximately 3 hr ahead of the continuous J -band sequence from 23 Sep 2009, which could imply a differential rotation of ~ 3 degrees per day or wind speeds of ~ 45 m s $^{-1}$ during that time period (approximately half of that on Jupiter). We note that this estimate relies on our over-constrained period of 7.723 hr which was obtained by assuming a *constant* phase for the Aug through Oct epochs, which may not be realistic. Long term monitoring of 2M2139 should be able to verify the existence of a persistent, differentially rotating feature.

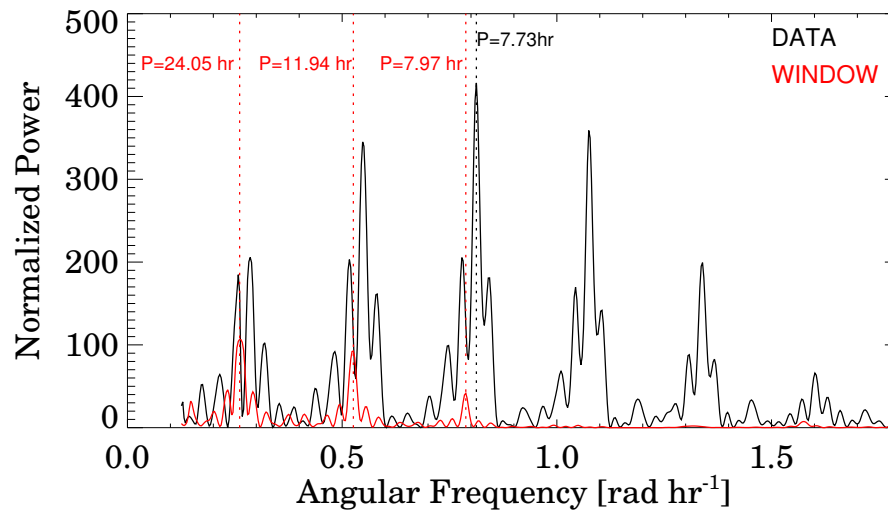


Figure 3.6: Lomb-Scargle Periodogram (black line) of light curves spanning 21 Sep 2009 to 01 Oct 2009. The power corresponding to a false alarm probability of 0.003 is ~ 4 , falling well below any peaks in the periodogram. The scaled window function (red line) shows a main peak at 24 hr corresponding to the spacing of our nightly observations, with additional peaks at 12 hr, 8 hr, etc. The strongest data peak at 7.73 hr matches the 7.721 ± 0.005 hr value recovered from fitting a periodic function to the light curve (see figure 3.5).

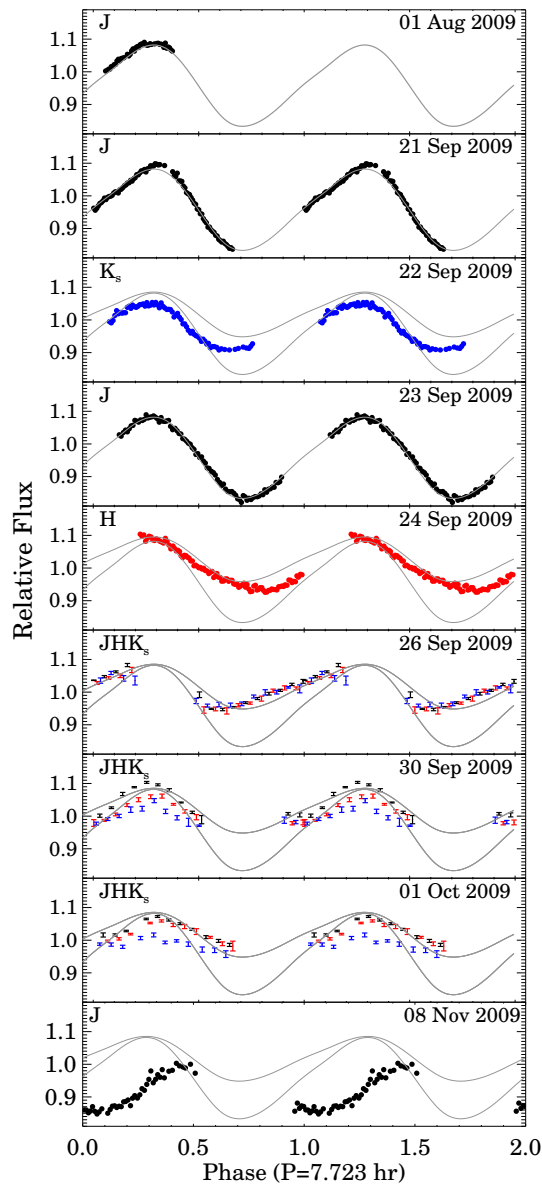


Figure 3.7: J (black) H (red), and K_s (blue) light curves spanning 01 Aug 2009 to 08 Nov 2009 shown on a common flux scale where unity corresponds to J_{MKO} , H , and K_s magnitudes of 14.75, 14.11, and 13.59 respectively. The data have been phased to an over-constrained period of 7.723 hr (see text for the explanation). For clarity, the data have been binned by factors of 3 (WIRC J -band sequences), 7 (CPAPIR J -band sequence in bottom panel), and 5 (H and K_s sequences). The interleaved JHK_s sequences are binned as in figure 3.4. The best-fitting two-spot model from figure 3.5 is overplotted (solid grey lines) to highlight deviations from the original light curve shape as a function of time. The same model, with the amplitude scaled by 55%, is also overplotted on the lower amplitude sequences as a visual aid.

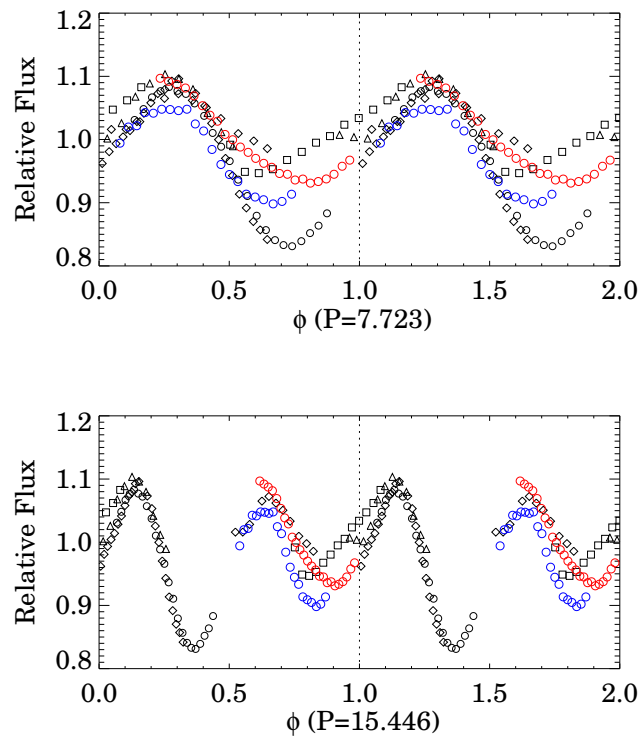


Figure 3.8: Light Curves for 2M2139 spanning 21 Sep 2009 to 01 Oct 2009 phased to over-constrained (see text for explanation) periods of 7.723 hr (top) and 15.446 hr (bottom). Black, red and blue points represent J , H , and K_s band data respectively. Different symbols of the same color differentiate different epochs. The data have been binned for clarity. Unity corresponds to J_{MKO} , H , and K_s magnitudes of 14.75, 14.11, and 13.59 respectively.

Table 3.3. Light Curve Properties

Epoch ^a	Filter	A^b	A_H/A_J	A_{K_s}/A_J	σ_t	σ_c
01 Aug 2008	<i>J</i>	0.080	-	-	0.0072	0.0056
21 Sep 2009	<i>J</i>	0.260	-	-	0.0067	0.0051
22 Sep 2009	<i>K_s</i>	0.156	-	-	0.0145	0.0156
23 Sep 2009	<i>J</i>	0.262	-	-	0.0079	0.0070
24 Sep 2009	H	0.166	-	-	0.0124	0.0119
26 Sep 2009	<i>J (H,K_s)</i>	0.134 (0.123, 0.111)	0.91±0.07	0.83±0.08	0.0092 (0.0159,0.0186)	0.0088 (0.0136,0.0236)
30 Sep 2009	<i>J (H,K_s)</i>	0.109 (0.092, 0.064)	0.84±0.08	0.59±0.07	0.0107 (0.0154,0.0201)	0.0107 (0.0132,0.0227)
01 Oct 2009	<i>J (H,K_s)</i>	0.084 (0.077, 0.038)	0.91±0.15	0.45±0.11	0.0088 (0.0142,0.0175)	0.0076 (0.0116,0.0188)
08 Nov 2009	<i>J</i>	0.152	-	-	0.0391	0.0232

^a As in table 3.1, dates correspond to the local day at the beginning of the night.

^b Peak-to-peak amplitudes are measured as the absolute change in flux, divided by the mid-flux and correspond to the filter(s) indicated in the second column.

3.4.3 Possible long-term variability

From comparing our WIRC photometry to that from 2MASS (both on the 2MASS photometric system, see table 3.4), we find 2M2139 to be significantly bluer ($J - K_s = 1.26 - 1.34$) at the time of the WIRC observations than reported by 2MASS ($J - K_s = 1.67 \pm 0.07$). We can estimate 2M2139's maximum change in $J - K_s$ color within the time spanned by our WIRC observations by making the conservative assumption of $A_{K_s} / A_J = 0.45$ (see figure 3.4 and table 3.3). This amplitude ratio, the lowest in our data, can be used to infer a maximum $\Delta(J - K_s)$ of 0.15 mag for the full range of J band variability observed ($A_J = 0.26$). Therefore, there is no way to reconcile the 2MASS catalog color of $J - K_s = 1.67 \pm 0.07$ with that observed by WIRC, unless large systematic errors exist in our photometric calibration. Fortunately, NIR spectra for 2M2139 from the SpeX Prism Library provides two additional epochs which we can compare to WIRC and 2MASS photometry. Synthetic 2MASS colors of $J - K_s = 1.32 \pm 0.083$ and 1.36 ± 0.080 were found for the 2003 and 2004 SpeX epochs respectively, in agreement with the WIRC photometry. It is interesting to note that compared to 198 other L and T dwarfs for which we have also measured synthetic SpeX photometry (see Appendix A.1), 2M2139's large offset between 2MASS and SpeX colors makes it a 4σ outlier. Thus it may have been possible to identify this target's variability well in advance of our observations. It is also notable that there is no apparent increase in scatter between 2MASS and SpeX photometry across the L/T transition, with a few other less extreme outliers occurring at earlier spectral types. These additional outliers should be followed up, although it appears that variability on the scale observed for 2M2139 is quite rare.

Thus, if the 2MASS epoch can be trusted, there is evidence that the entire range of 2M2139's variability is larger than captured by our observations. We note that there is no reason to suspect an error in the 2MASS colors, as catalog magnitudes derived from profile fitting agree well with those from aperture photometry, and

the 2MASS J , H , and K_s observations are simultaneous. Furthermore, according to our WIRC photometry the noted blueward shift in $J - K_s$ since the 2MASS epoch is almost entirely attributable to a brightening in the J -band, accompanied by a plateau or possible dimming in the K_s band. If real, this long-term trend of anti-correlated behavior in J and K_s is qualitatively different than the highly correlated variability we observed over short timescales.

3.5 Physical Properties

The physical properties of 2M2139 derived here and elsewhere are presented in table 3.4. 2M2139 is a cool field BD with an optical spectral type of T0 determined by Reid et al. (2008), and a NIR spectral type of T1.5 from Burgasser et al. (2006a). The NIR spectra ($R \sim 120$) from Burgasser et al. (2006a) were taken with the Medium Resolution Near Infrared Spectrograph (SpeX) at the NASA's InfraRed Telescope Facility (IRTF), and are available online from the SpeX Prism Library. There is no parallax data available for this target at this time, and given its unique variability (and hence potentially unique atmospheric characteristics) it is unclear to what degree standard relationships between spectral type, absolute magnitude and temperature may apply. For field BDs (~ 3 Gyr) with measured parallaxes and estimated bolometric luminosities it has been shown that effective temperatures plateau or slightly decrease from ~ 1400 - 1200 K across the L/T transition (\sim L7-T4 SpTs; Golimowski et al. 2004; Stephens et al. 2009). The scatter about this temperature is reported as ~ 100 K. Using the relationship provided by Stephens et al. (2009) we derive $T_{eff} = 1270 \pm 100$ K for a T1.5 spectral type. However, the temperature of the L/T transition also shows some dependence on gravity (e.g. Metchev & Hillenbrand 2006; Leggett et al. 2008; Stephens et al. 2009), and this temperature could be lower if 2M2139 is moderately young.

If we assume 2M2139 to have an age/mass typical of field T dwarfs, an absolute magnitude and distance can be determined from empirical relationships. Using the

spectral type versus MKO K magnitude relation given by Marocco et al. (2010), excluding known binaries and using a NIR spectral type of T1.5, we find an absolute magnitude of $M_K = 13.35 \pm 0.25$ mag. The error bar reflects the coefficient uncertainties of the polynomial fit provided by Marocco et al. (2010), but neglects intrinsic scatter of the sample about the relation. This intrinsic scatter is estimated by Liu et al. (2006) to be ~ 0.39 mag, and we therefore adopt this larger uncertainty hereafter. Assuming 2M2139 is a single object, this corresponds to a distance of $11.6_{-1.9}^{+2.3}$ pc, where we have used the 2MASS K_s magnitude of 13.58 mag, first converted to an MKO K magnitude using the relationship provided by Stephens & Leggett (2004), to obtain the distance modulus. Our distance estimate is notably closer than that of 18.8 pc cataloged by Looper et al. (2007) using the MKO-J relationship of Liu et al. (2006).

3.5.1 Binarity?

Burgasser et al. (2010) have suggested that 2M2139 is a binary candidate since a composite spectral template consisting of $L8.5 \pm 0.7$ and $T4.5 \pm 1.5$ components provide a significantly better fit to its NIR spectrum than any single template. For example, pronounced CH_4 absorption is present at $1.2 \mu\text{m}$, but is weak or absent in H and K_s . One way to reproduce this mismatch is with the addition of a late T companion with highly suppressed H and K_s fluxes; this would enhance the height of the J -band peak, while having a much smaller effect on the H and K band SEDs. However, even this composite match fails to reproduce the relative strength of CH_4 absorption in the J , H and K_s bands, leading the authors to conclude that if a binary, the components “may themselves have unusual properties.” Given the unique variability of 2M2139 reported in the present work, its peculiar NIR spectrum may be the result of an uncommonly heterogeneous atmosphere, rather than binarity.

2MJ2139 was observed on 2006 June 23 using HST/NICMOS with the NIC1 camera

Table 3.4. Target Properties

Quantity	Value or Range	Data Ref.	Source
Identifier	J21392676+0220226	2MASS ^a	2
α (J2000)	21 ^h 39 ^m 26 ^s .76	2MASS ^a	2
δ (J2000)	+02 ^d 20'22".6	2MASS ^a	2
Optical SpT	T0	–	3
NIR SpT	T1.5	–	4
Period	7.721±0.005 hr	–	1
T_{eff} (3 Gyr)	1270 ± 100 K ^e	–	1
$M_{K,MKO}$ (3 Gyr)	13.35 ± 0.25 ^f	–	1
d	11.6 ^{+2.3} _{-1.9} pc ^f	–	1
J	15.26±0.049		
H	14.16±0.053	2MASS ^a	2
K_s	13.58±0.045		
$J - K_s$	1.67±0.066		
$J - K_s$	1.32±0.07		
$J - H$	0.89±0.07		
$\Delta J_{(2M-MKO)}$	0.183	SpeX ^b	1
$\Delta H_{(2M-WIRC)}$	-0.065		
$\Delta K_s_{(2M-WIRC)}$	-0.016		
J_{MKO}	14.66-14.96 ^c		
J	14.84-15.14 ^c		
H	14.00-14.18 ^c	WIRC	1
K_s	13.54-13.71 ^c		
$J - K_s$	1.26-1.34 ^d		

^a2MASS Point Source Catalog, the epoch is JD 2451741.8470 (16 Jul 2000)

^bSynthetic photometry using 2M2139's NIR spectrum (Burgasser et al. 2006a) from the SpeX Prism Library. Note that the closely agreeing 2003 and 2004 epochs have been averaged.

^cRanges span the entire set of WIRC observations (i.e. all epochs) presented here.

^dRanges correspond only to epochs where near-simultaneous JHK_s photometry is available.

^eDerived from the empirical relation of Stephens et al. (2009)

^fDerived from the empirical relation of Marocco et al. (2010)

Note. — References refer to (1)This paper, (2)Skrutskie et al. (2006), (3)Reid et al. (2008), (4)Burgasser et al. (2006a)

(43 mas pixel⁻¹) and the F170M and F110W filters (HST program ID 10143). We analyzed these data to put constraints on the binarity of this brown dwarf. For point-spread function (PSF) fitting and subtraction, we used both a model PSF generated with the TinyTim³ software (Krist 1993) as well as the image of another brown dwarf (2MJ0257-3105) observed with the same settings only two days later as part of the same program. The latter reference PSF provided a noticeably better fit to the image of 2MJ2139+02 than the former, although in both cases the subtraction left no significant residuals. Thus the data provide no indication of binarity. By introducing fake binary companions of various contrasts and separations in the images and repeating the reference PSF fitting, we can rule out the presence of a binary companion with contrasts of 0, 1, 2, and 3 mag at separations larger than 0.055'', 0.065'', 0.08'' and 0.13'', respectively. These limits correspond to physical separations between 0.66-1.56 AU at a distance of 12 pc.

Given the apparent proximity of this source, future parallax measurements should provide more stringent constraints on its distance, absolute magnitude, and potential binarity.

3.5.2 Model Fits to the NIR SED

Detailed atmosphere models including the effects of dust condensation and settling can be used to explore atmospheric properties of field BDs including effective temperature, gravity, metallicity, vertical mixing (via departures from chemical equilibrium), and condensate clouds (e.g. Cushing et al. 2008; Stephens et al. 2009; Witte et al. 2011). However, certain issues with atmosphere models are well documented. For instance, studies of benchmark objects—those with known masses (e.g. Dupuy et al. 2011), and/or ages (Leggett et al. 2008)—have demonstrated that effective temperatures determined from model atmosphere fitting can differ by up to a few hundred degrees

³<http://www.stsci.edu/hst/observatory/focus/TinyTim>

compared to those derived from evolutionary models. Second, low-gravity L dwarfs (Faherty et al. 2011, submitted) and directly imaged planets (e.g. Bowler et al. 2010; Skemer et al. 2011) have been found to be less luminous than “normal” field BDs of a given spectral type. This latter observation is surprising as lower gravity objects are expected to be larger in radius, and hence brighter. The ability of low gravity atmospheres to retain a thicker and higher cloud layer, high metallicity, and/or non-equilibrium chemistry may be responsible (e.g. Barman et al. 2011), and highlights that significant interdependencies between effective temperature, condensate properties, surface gravity, and other secondary parameters may exist.

In addition to known problems, it is unclear whether standard 1D models are appropriate for 2M2139 as it’s large variability indicates a heterogeneous surface. Nonetheless, we have performed fits of 1D model atmospheres to 2M2139’s NIR spectrum in order to determine the general properties required to reproduce its spectrum in a manner consistent with other studies. Also, in the following section we model 2M2139’s variability and NIR spectrum simultaneously using linear combinations of 1D cloudy and clear model atmospheres. Thus, the single spectral fits performed here will serve as a reference to which hybrid cloudy/clear models can be compared.

The Atmosphere Models

The model spectra employed here have been calculated for solar metallicity and chemical equilibrium, for simplicity allowing only effective temperature (T_{eff}), surface gravity ($\log g$) and cloud sedimentation efficiency (f_{sed}) to vary. The f_{sed} parameter describes the efficiency of condensate sedimentation within the atmosphere, according to the cloud model of Ackerman & Marley (2001), which has been successfully used to reproduce observations of a wide range of cloudy BDs (e.g. Cushing et al. 2008; Stephens et al. 2009) as well as Jupiter. Large values of f_{sed} correspond to more efficient particle growth, resulting in larger particle sizes that more efficiently rain

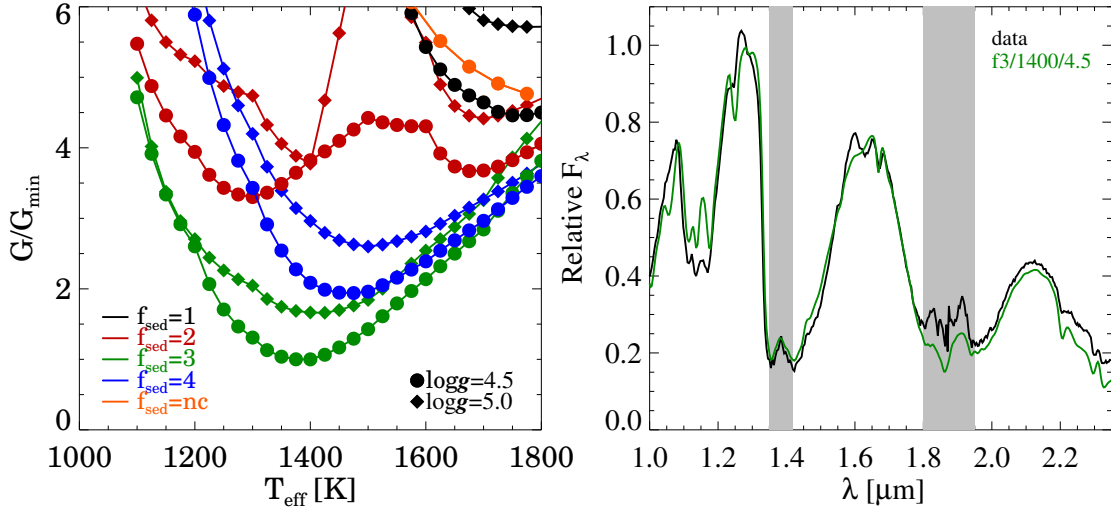


Figure 3.9: *Left panel:* The weighted χ^2 statistic G (normalized to its overall minimum value, G_{min}) for a series of different f_{sed} , $\log g$, and T_{eff} . *Right panel:* The model spectrum corresponding to the minimum G statistic (green line) is shown overplotted on the data (black line). Regions of high telluric absorption which have been omitted from the fit are shown in grey.

out of the atmosphere and consequently lower opacity cloud decks. Our model grid was calculated for $500 \text{ K} < T_{eff} < 2000 \text{ K}$ in steps of 100 K, $\log g = \{4.5, 5.0\}$, and $f_{sed} = \{1, 2, 3, 4, nc\}$, where ‘nc’ denotes a cloudless model. Although the models were calculated with 100 K spacing, we have linearly interpolated between them to obtain a finer sampling in T_{eff} of 25 K.

Fitting procedure

For each model in our grid we computed a weighted χ^2 statistic, following a modified version of the procedure described by Cushing et al. (2008), and given by

$$G = \sum_i w(\lambda_i) \left(\frac{F(\lambda_i) - cM(\lambda_i; T_{eff}, \log g, f_{sed})}{\sigma_i} \right)^2 \quad (3.1)$$

where $F(\lambda_i)$ is the observed spectrum, and $M(\lambda_i; T_{eff}, \log g, f_{sed})$ is the model, scaled by a constant factor $c \equiv (R/d)^2$ that minimizes G , where R is the BD radius and d is its distance. All model spectra were smoothed to replicate the average resolution of

2M2139's spectrum over the wavelength region of interest ($R \sim 100$), via convolution with a Gaussian. Due to unequal spacing of the data, the fit is weighted by $w(\lambda_i) = \Delta\lambda_i$, where $\Delta\lambda_i$ is the width of wavelength bin i . Fitting was performed over the wavelength intervals of 1.0-1.35 μm , 1.42-1.8 μm , and 1.95-2.35 μm , avoiding regions of high telluric water absorption. Due to uncertainties in molecular band strengths and opacities, as well as the complexity of condensate cloud physics, the models are generally incomplete and can disagree with the observations at a level significantly greater than the measurement uncertainties associated with the data. Thus we have chosen to set all $\sigma_i = 1$, so as not to bias a particular wavelength regime based on their measurement uncertainties. This is equivalent to including a constant uncertainty term for each wavelength bin in order to account for model incompleteness. Since this constant term is much larger than the measurement uncertainty for any given wavelength bin included in the fit, the σ_i become essentially constant.

In figure 3.9 we plot the G statistic (normalized by its absolute minimum value across all models tested, G_{min}) for various values of f_{sed} and $\log g = \{4.5, 5.0\}$ as a function of effective temperature. We find the best fit corresponds to $\log g = 4.5$, $f_{sed}=3$ and $T_{eff}=1400$ K. While an effective temperature of 1400 K is consistent with the range of L/T transition temperatures found by Golimowski et al. (2004) and Stephens et al. (2009), a surface gravity of $\log g=4.5$ would then imply a rather young age of 100 Myr and mass of $\sim 20 M_{Jup}$ (Saumon & Marley 2008). It is interesting to note that the K band portion of 2M2139's SED has been reported as a best match to that of the low gravity directly imaged planet HR8799 b (Barman et al. 2011). However, model fits to the low resolution NIR spectra of field BDs do not strongly constrain surface gravity, and can yield values of $\log g$ differing by up to 1.0 dex when different wavelength regimes are used for fitting (Cushing et al. 2008). In addition, according to Cushing et al. (2008) a value of $\log g = 4.5$ derived from spectral fitting is not particularly unusual for a field BD, even when evolutionary sequences predict higher surface

gravities ($\log g > 5$) for the same objects. Thus, it would be premature to conclude anything about 2M2139 's age and gravity based on model fits alone, especially since there is no additional evidence for youth. With this in mind, it may be more likely that interdependencies between surface gravity and other physical parameters such as cloud thickness and/or metallicity (despite being assigned independent model parameters) lead to the latter being mimicked by the former in spectral models. For the purpose of this paper we continue to use the $\log g = 4.5$ models to describe 2M2139 's atmosphere, but caution that the physical interpretation of the gravity parameter is unclear. The analysis presented here and in subsequent sections is not strongly affected by this choice of model surface gravity, other than providing an optimal fit to 2M2139 's NIR SED. Specifically, trends pertaining to photometric variability in the following sections are qualitatively similar for different surface gravities. Furthermore, from figure 3.9, T_{eff} appears roughly independent of $\log g$, but depends strongly on f_{sed} . Thus, while $\log g$ is poorly constrained by the models, it is only of secondary importance to our analysis in comparison to the cloud thickness parameter, f_{sed} .

3.6 Modeling Variability due to Heterogeneous Surface Features

While we discuss alternative explanations for 2M2139's variability in the discussion section, here we construct a simple model for the observed variability, assuming that heterogeneous surface features are responsible. We envision a scenario where "spots" or cloud features remain approximately static in the BD's rotating frame over a single rotation, and variability arises due to rotational modulation. We consider a simple model where the BD surface is composed of two types of regions differing in temperature and/or cloud properties, possessing surface fluxes \mathcal{F}_1 and \mathcal{F}_2 . At a given snapshot in time the total flux from the BD, \mathcal{F} , is given by a linear combination

of \mathcal{F}_1 and \mathcal{F}_2 weighted by their relative filling fractions over the BD's visible disc. The peak-to-peak amplitude of variability that an observer would detect in a given bandpass due to a change in these filling factors can be expressed as

$$A = \frac{(1-a-\Delta a)\mathcal{F}_1 + (a+\Delta a)\mathcal{F}_2 - (1-a)\mathcal{F}_1 - a\mathcal{F}_2}{0.5[(1-a-\Delta a)\mathcal{F}_1 + (a+\Delta a)\mathcal{F}_2 + (1-a)\mathcal{F}_1 + a\mathcal{F}_2]} \quad (3.2)$$

$$= \frac{\Delta a}{\alpha + \mathcal{F}_1/\Delta\mathcal{F}} \quad (3.3)$$

where $A = \Delta\mathcal{F}/\mathcal{F}$ is the change in flux divided by the mid-brightness flux. The parameter a is the minimum filling factor of the \mathcal{F}_2 regions, Δa is the change in filling factor, and $\Delta\mathcal{F} = \mathcal{F}_2 - \mathcal{F}_1$. The parameter $\alpha = a + 0.5\Delta a$ corresponds to the filling factor of the \mathcal{F}_2 regions at mid-brightness.

Synthetic photon fluxes \mathcal{F}_2 and \mathcal{F}_1 for use in equation 3.3 were computed from the 1D model spectra integrated over the WIRC system plus filter transmission curves. For this purpose we used the models of Saumon & Marley (2008) described above with solar metallicity, $\log g = 4.5$, and a range of values in f_{sed} and T_{eff} . We also experimented with different $\log g$ values, but found them to be a poor match to 2M2139's NIR spectrum, and hence only present the optimal case where $\log g = 4.5$ here. In general, $\mathcal{F}_1 = \mathcal{F}_1[T_1, f_{\text{sed}1}]$ and $\mathcal{F}_2 = \mathcal{F}_2[T_1 + \Delta T, f_{\text{sed}2}]$ so that each region is characterized by a distinct effective temperature and cloud sedimentation efficiency. As a matter of convention we will always choose $f_{\text{sed}1} \leq f_{\text{sed}2}$, such that the \mathcal{F}_1 regions have higher condensate opacity. The parameter T_1 represents the effective temperature of the \mathcal{F}_1 regions, while $T_1 + \Delta T$ is the effective temperature of the less cloudy \mathcal{F}_2 regions. For a given combination of T_1 , ΔT , $f_{\text{sed}1}$, $f_{\text{sed}2}$, a and Δa , fluxes can then be determined from 1D model atmosphere grids, and the resultant variability computed via equation 3.3. We caution that, in general, 1D models with different effective temperatures and vertical distributions of dust condensates have different underlying pressure-temperature profiles, and thus interpolations between them cannot be made in a self-consistent way. Nonetheless, in the absence of 3D models, it is instructive

to use 1D models as a guide, understanding their drawbacks. Limitations of our modeling approach are discussed further in section 3.6.3.

Using equation 3.3 we computed A_{K_s}/A_J and A_H/A_J as a function of ΔT for a variety of combinations of f_{sed1} and f_{sed2} . The various combinations can be broadly divided into two main cases, which we specify for later reference:

Case A Case A corresponds to an atmosphere with heterogeneous cloud features, where $f_{\text{sed1}} \neq f_{\text{sed2}}$. This case could describe an atmosphere composed of clouds and clearings, or more generally regions of differing condensate opacities. This picture of a brown dwarf with spatially variable cloudiness is motivated by the cloud fragmentation hypothesis of the L/T transition (Ackerman & Marley 2001; Burgasser et al. 2002), discussed in the introduction.

Case B Case B corresponds to a uniformly cloudy atmosphere where $f_{\text{sed1}} = f_{\text{sed2}}$, with heterogeneities in temperature only. This case may approximate the presence of cool or hot magnetically induced spots. We have not modeled hot or cool spots in a uniformly *clear* atmosphere because the red $J - K_s$ color of 2M2139 is incompatible with cloud-free models and precludes this scenario. For this case we have chosen to consider only $f_{\text{sed1}} = f_{\text{sed2}} = 3$ based on the best-fitting 1D model atmosphere for 2M2139 (figure 3.9).

For each pairing of model grids specified by $f_{\text{sed1}} = \{1, 2, 3\}$ and $f_{\text{sed2}} = \{3, 4, \text{nc}\}$ we used equation 3.3 to compute (i) A_{K_s}/A_J and A_H/A_J as a function of ΔT , and (ii) the corresponding change in filling factor, Δa required to produce the maximum observed variability of $A_J = 0.26$. Results for a representative selection of these pairings are shown in figure 3.10 for values of $T_1 = 1100$ K and 1400 K; a reasonable range for 2M2139. Results are plotted for both $a = 0.2$ and $a = 0.6$ in order to demonstrate a weak dependence of our result on the minimum filling factor. Note that the overall effective temperature can be much greater than T_1 when $\Delta T > 0$, as warm regions

quickly dominate the total flux. Although it is not clear a priori what appropriate values of T_1 should be, 1400 K represents a reasonable upper limit when $\Delta T > 0$, since it coincides with both our model fitting in section 3.5.2 and the upper limit of the L/T transition temperature found by Stephens et al. (2009). The lower value of $T_1=1100$ K is shown to be appropriate in the following section.

For comparison, figure 3.11 compares results for case *A* from different model atmosphere groups, including the cloudy and clear models of Burrows et al. (2006) and the SETTL and COND models of Allard et al. (2001; 2003).

Our figures 3.10-3.11 recover trends previously discussed by Artigau et al. (2009). Namely, cool or hot spots within a cloudy atmosphere (case *B*) produce amplitude ratios A_{K_s}/A_J exclusively > 1 , whereas warm regions of low-condensate opacity (case *A*) yield $0 \lesssim A_{K_s}/A_J \lesssim 1$ for $\Delta T \gtrsim 100$ K. The observed amplitude ratios for 2M2139 are positive and consistently < 1 and therefore inconsistent with the presence of magnetic spots. Rather, our modeling supports an interpretation of patchy clouds, wherein regions of lower condensate opacity are warmer.

As seen in figures 3.10-3.11, a variety of model combinations for case *A* are able to reproduce observations, with differing requirements for ΔT and Δa . In general, models where the difference between $f_{\text{sed}1}$ and $f_{\text{sed}2}$ is small require lower temperature contrasts but slightly larger changes in filling factor to model the observations. Increasing the parameter a yields large amplitude ratios for a given temperature contrast ΔT , but also requires a larger Δa . In all cases temperature contrasts $\gtrsim 150$ K are required to model the observed amplitude ratios, with some model combinations requiring temperature contrasts in excess of 400 K. The SETTL/COND and cloudy/clear models of Allard et al. (2003) and Burrows et al. (2006) are equally able to reproduce the photometric variations, requiring somewhat lower temperature contrasts when $T_1 \lesssim 1200$ K. While the variety of models and parameters capable of reproducing the photometric data appears large, in the following section we use

2M2139's NIR spectrum as an additional constraint to significantly reduce the span of good solutions.

3.6.1 A specific variability model for 2M2139

The modeling of photometric variations alone, as done in the previous section, ignores additional information about 2M2139's spectral energy distribution that can further constrain the nature of the variability. In addition, it has been previously noted (e.g. Burrows et al. 2006), that the same models capable of reproducing observed changes in broadband colors do not necessarily reproduce the NIR spectra of L/T transition dwarfs.

For combinations of $f_{\text{sed1}} = \{1, 2, 3\}$ and $f_{\text{sed2}} = \{3, 4, \text{nc}\}$ and $\log g = 4.5$, we searched for combinations of T_1 , ΔT , a , and Δa capable of reproducing *both the NIR SED and observed variations* of 2M2139. We have restricted ourselves to the region of parameter space where $\Delta T > 0$ corresponding to the upper right quadrant in figure 3.10. We systematically examined a grid of hybrid models with $T_1 = 800 - 1600$ K and $\Delta T = 0 - 700$ K in steps of 25 K. Our warmest model has $T_{\text{eff}} = 2100$ K, and therefore our grid is incomplete for regions where $T_1 + \Delta T > 2100$ K. We note that all original spectra were computed with 100 K spacing, and we have linearly interpolated between models to obtain our finer sampling. At each grid point:

1. A parameter α (corresponding to the mid-brightness filling factor, $a+0.5\Delta a$) was uniquely determined by fitting a hybrid model given by

$$M(\lambda) = (1 - \alpha)\mathcal{F}_1[\lambda; T_1, f_{\text{sed1}}] + \alpha\mathcal{F}_2[\lambda; T_1 + \Delta T, f_{\text{sed2}}] \quad (3.4)$$

to 2M2139's NIR spectrum, using a procedure identical to the one used for spectral fitting in section 3.5.2 (see equation 3.1). We note that in the above

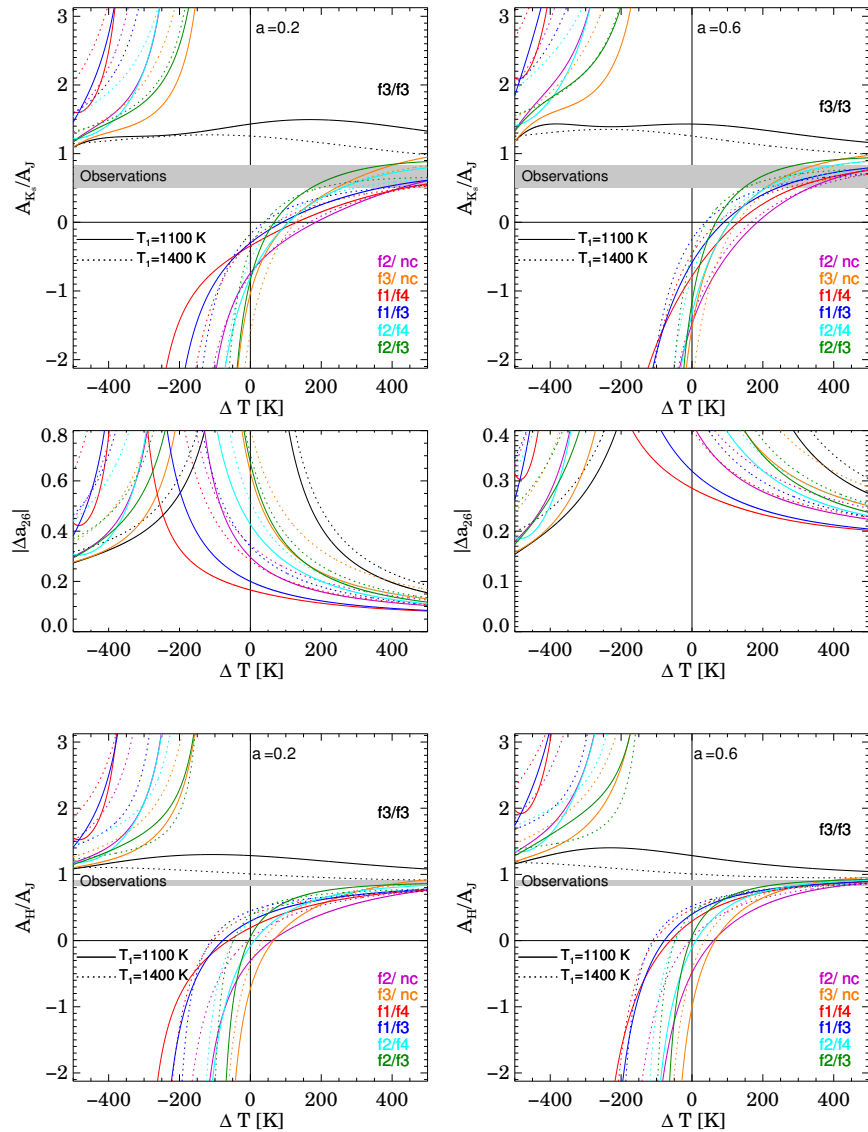


Figure 3.10: *Top*: Model amplitude ratios A_{K_s}/A_J for a BD with a heterogeneous surface as a function of the temperature contrast between surface elements, ΔT . Amplitude ratios were computed from equation 3.3, using a variety of cloudy and clear model fluxes ($\mathcal{F}_1[f_{\text{sed}1}, T_1]$ and $\mathcal{F}_2[f_{\text{sed}2}, T_2 + \Delta T]$) from Saumon & Marley (2008), indicated by color in the plot legend. Here we have used the shorthand of f_{n1}/f_{n2} to denote $f_{\text{sed}1} = n_1/f_{\text{sed}2} = n_2$, and “nc” for the cloud-free model. For all cases curves are plotted for constant $T_1=1100$ K (solid lines) and $T_1=1400$ K (dotted lines). Colored lines correspond to case A (heterogeneous clouds) while the black lines correspond to case B (cool/hot spots). The left and right panels demonstrate a weak dependence on the initial filling fraction of the \mathcal{F}_2 regions, with $a=0.2$ (left) and $a=0.6$ (right). *Middle*: For each curve in the above panel, the corresponding change in filling factor, Δa , required to produce the maximum observed variability for 2M2139 of $A_J = 0.26$, is shown. *Bottom*: Same as the top panels but for A_H/A_J (Δa_{26} remains unchanged from the upper panel).

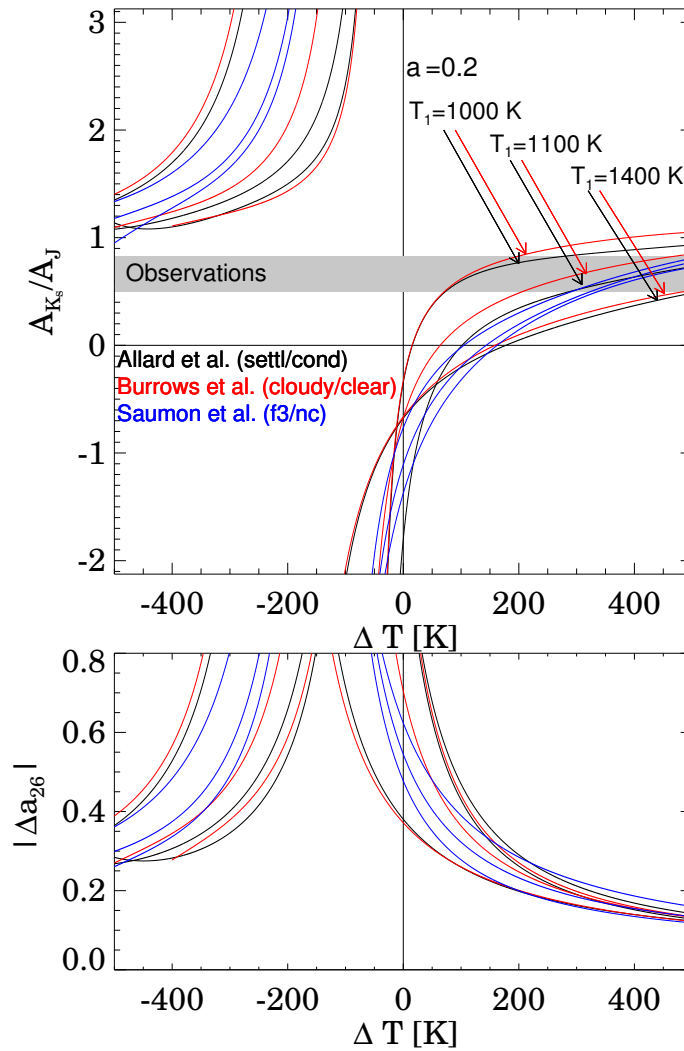


Figure 3.11: Same as figure 3.10, with $a = 0.2$, and including comparisons to the cloudy/clear and SETTL/COND models of Burrows et al. (2006) and Allard et al. (2001; 2003) (see the main text for more detail). For each set of models the three curves correspond to fixed values of $T_1=1100$ K, 1200 K, and 1400 K.

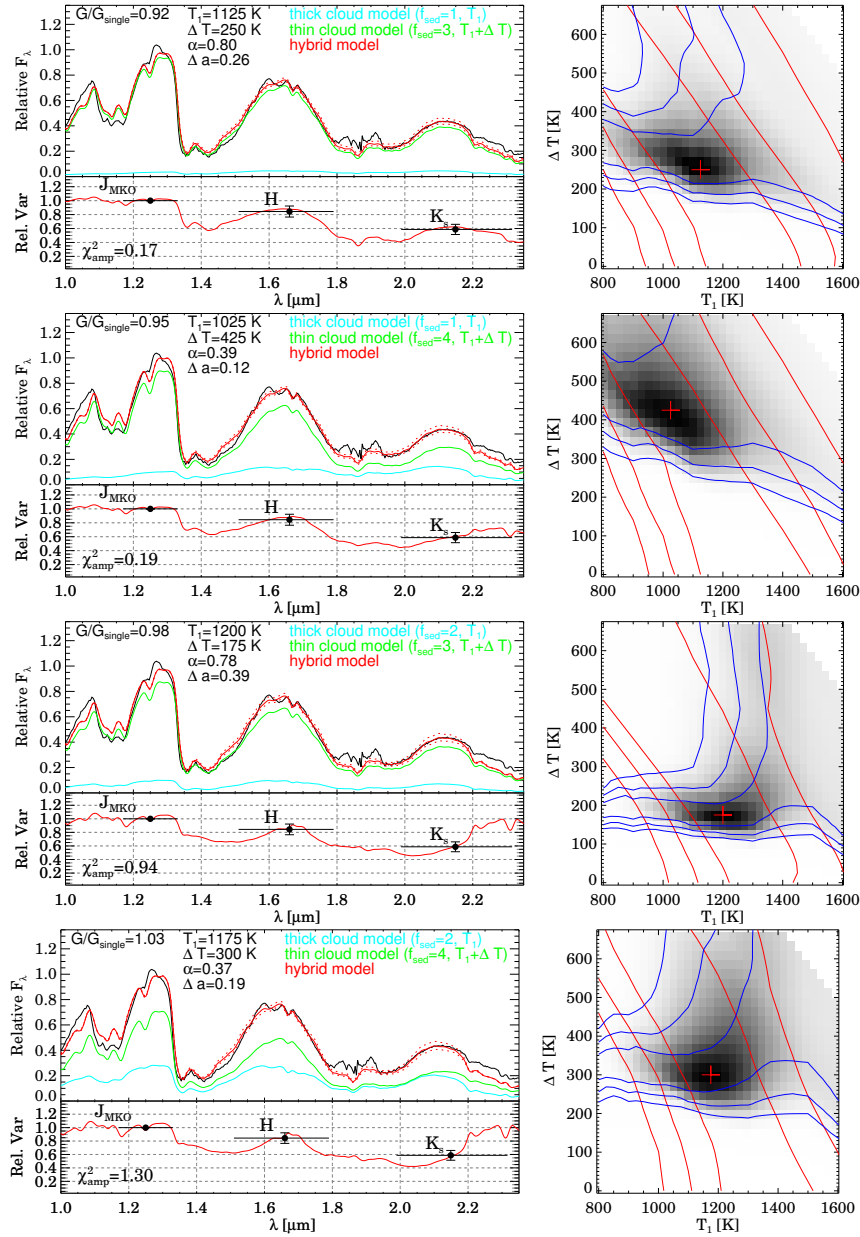


Figure 3.12: Simultaneous fits to both the NIR spectrum (black line) and photometric variability (black data points) of 2M2139 for the four model combinations where $f_{\text{sed}1} = \{1, 2\}$ and $f_{\text{sed}2} = \{3, 4\}$ (see text for explanation). *Right*: Contours in the T_1 - ΔT plane for $\Delta\chi_{\text{amp}}^2$ (blue) and for $4\Delta G/G_{\text{single}}$ (red), corresponding to levels of $\{2.3, 6.2, 11.8\}$, where the Δ indicates differences in G and χ_{amp}^2 from their minimum values on the grid. A red cross marks the combination of T_1 and ΔT (for which α and Δa are also uniquely determined) where $\chi_{\text{amp}}^2 + 4G/G_{\text{single}}$ is a minimum. The shaded map shows the exponential of $-(\chi_{\text{amp}}^2 + 4G/G_{\text{single}})/2$ with square-root scaling to emphasize the tails of the distribution. *Left*: The hybrid model spectrum at mid-light (red solid line), corresponding to the best-fit parameters marked by the red cross on the right. The model is a linear combination of cloudy (cyan line) and less-cloudy (green line) surfaces, where the filling fraction of less-cloudy regions varies by an amount Δa . Dotted red lines show the hybrid model at maximum and minimum light, assuming $A_J=0.26$, and normalized over the 1.23 to 1.25 μm range. The bottom left panel shows the relative variations that would result for the best-fitting model as a function of wavelength, normalized to the J band. The observed amplitude ratios and their errors are overplotted for comparison, and χ_{amp}^2 for the best fit is specified.

equation we have used \mathcal{F}_1 and \mathcal{F}_2 to represent model fluxes as a function of wavelength, instead of integrated over a given bandpass as before. The minimum weighted χ^2 statistic, G , associated with each grid point was recorded.

2. We solved for a and Δa by inputting $a = \alpha - 0.5\Delta a$ and $A_J=0.26$ into equation 3.3, where we have chosen to set A_J to the maximum observed variability.⁴ In some cases Δa derived from the best spectral fit was unphysical (e.g. $a + \Delta a > 1$), and in these cases we systematically varied our fit parameter α until we found the lowest- G fit that also satisfied the physical condition that $a + \Delta a \leq 1$.
3. We computed model amplitude ratios A_{K_s}/A_J and A_H/A_J by inputting parameters a , $\mathcal{F}_1[T_1]$, and $\mathcal{F}_2[T_1 + \Delta T]$ into equation 3.3. A χ^2 statistic for the amplitude ratios given by $\chi_{\text{amp}}^2 = [(A_H/A_J - x)^2/\sigma_x^2 + (A_{K_s}/A_J - y)^2/\sigma_y^2]$ was recorded, where x and y are the observed amplitude ratios, and σ_x and σ_y their uncertainties (see table 3.3).

According to the above procedure (repeated separately for various combinations of f_{sed1} and f_{sed2}), G and χ_{amp}^2 were determined for every grid point in the T_1 - ΔT plane, allowing us to identify regions of parameter space capable of reproducing both the NIR spectrum and broadband variability of 2M2139.

We obtained best-fit parameters by determining where $\chi_{\text{amp}}^2 + 4G/G_{\text{single}}$ was a minimum on our grid. Here, G_{single} corresponds to the best-fitting single (non-hybrid) spectral model found in section 3.5.2. We note that the G values have $N - 3$ degrees of freedom (dof; where $N = 304$ is the number of data points used for fitting) and have been scaled such that $G_{\text{single}} = \text{dof}$. If we were to minimize $\chi_{\text{amp}}^2 + G$, the best-fit parameters would be strongly dominated by the spectral fit, which uses significantly more data points (however, due to model incompleteness and highly correlated

⁴When α is fixed, Δa is linear in A_J , and therefore the Δa corresponding to smaller overall amplitudes can be easily inferred.

residuals this increase in data points does not result in proportionately more precise parameters). Instead, we have used our prior knowledge of the observed spectrum to impose a more broad constraint, allowing a wide range of “credible” spectral templates and eliminating obvious mismatches. In practice, we found that scaling G by $4/G_{\text{single}}$ assigns a reasonable weight to the spectral fit (e.g., see figures 3.12 and 3.13).

We found only a few combinations of f_{sed1} and f_{sed2} that were capable of reproducing the photometric variations, while at the same time providing a reasonable spectral match. Those where cool, high condensate opacity regions are represented by $f_{\text{sed1}} = \{1,2\}$ and warm, lower condensate opacity regions are represented by $f_{\text{sed2}} = \{3,4\}$ generally provide good fits to the data, with the $f_{\text{sed1}} = 1/f_{\text{sed2}} = 3$ combination providing the best fit. These four model scenarios, and corresponding best-fit parameters, are shown in figure 3.12, fitted to the simultaneous JHK_s photometric data from 30 Sep 2009. Shown are contours for $4G/G_{\text{single}}$ and χ_{amp}^2 in the T_1 - ΔT plane. The hybrid model spectrum corresponding to the best-fit parameters, as well as the resultant variability as a function of wavelength are also shown. We have chosen to show fits to the A_H/A_J and A_{K_s}/A_J amplitude ratios from 30 Sep 2009 as the amplitude ratios measured on this date are approximately intermediate to those measured in the other two epochs for which we have simultaneous JHK_s light curves. We have opted not to average the amplitude ratios over all epochs since the measurements are incompatible at the 2σ level and may represent different cloud configurations. In particular, the near-unity amplitude ratios from 26 Sep 2009 are challenging to fit, and strongly bias the averaged values. Rather, we provide best-fit contours and spectra corresponding to the other two epochs in Appendix A.2.

Depending on the combination of f_{sed1} and f_{sed2} we infer temperature contrasts of $\Delta T=175$ - 425 K between thick and thin cloud regions, and changes in filling factor of $\Delta a=0.12$ - 0.39 (see figure 3.12).

Rather than an atmosphere composed of clouds and clearings, our observations are best reproduced by one possessing regions of differing cloud opacity. For the best-fitting pairing of $f_{\text{sed1}} = 1/f_{\text{sed2}} = 3$ shown in figure 3.12 (and similarly for the $f_{\text{sed1}} = 2/f_{\text{sed2}} = 3$ combination) the data can be described by an atmosphere composed primarily of $f_{\text{sed2}} = 3$ regions (67% -93% coverage over the visible disc as a function of phase) with cooler, thicker cloud patches ($f_{\text{sed1}} = 1$) covering the remainder of the surface (7%-33%). The thick cloud patches have a temperature of $T_1=1125$ K, while the thinner cloud patches are $\Delta T = 250$ K warmer. Physically, this model could indicate condensate clouds that form in at least two distinct layers at different depths in the atmosphere. Such layers could arise due to compositional stratification of condensates (e.g. Lodders & Fegley 2006), or from complex atmospheric dynamics. Long-lived cyclonic storm systems and transient high altitude clouds are seen in the atmospheres of the Solar System gas giants (e.g. Smith et al. 1989; Vasavada et al. 1998), and it is possible that similar features exist in the atmosphere of 2M2139. Since small spatial scales will tend to be averaged out in the disc-integrated light, the large amplitude of our observations (and the corresponding large azimuthal asymmetry in modeled cloud coverage) is most consistent with the presence of sizable cloud features. If the observed variations were attributed to a single high-altitude storm, it would have to occupy 26% of the visible disc in order to produce $A_J = 0.26$.

Alternatively, for the next-best-fitting $f_{\text{sed1}} = 1/f_{\text{sed2}} = 4$ model also shown in figure 3.12 (and similarly for the $f_{\text{sed1}} = 2/f_{\text{sed2}} = 4$ combination) the data can be described by an atmosphere composed primarily of cloudy $f_{\text{sed1}} = 1$ regions with $T_1=1025$ K (67%-55% coverage as a function of time) interspersed with warmer regions of lower condensate opacity ($f_{\text{sed2}} = 4$). In this case a much higher temperature contrast of $\Delta T = 425$ K, and a correspondingly smaller change in filling factor affecting only 12% of the visible disc are required. This scenario is closer to the picture of an atmosphere covered by cloudy and clear regions that might naively be

expected based on theories of cloud fragmentation at the L/T transition. However, it is notable that we are unable to find solutions where $f_{\text{sed}2} = 'nc'$ to represent the data, indicating that the modeled “clearings” must retain some degree of condensate opacity (i.e. $f_{\text{sed}2} = 4$). For an atmosphere with a same T-P profile throughout and where temperature decreases monotonically as a function of altitude (as is expected for isolated BDs), this large temperature contrast is an indication that thick cloud patches extended to higher, cooler regions of the atmosphere.

For the best-fitting hybrid spectra, the normalizing constant $c = (R/d)^2$ in Eq. 3.1, along with a BD radius of $R = 0.13 R_{\odot}$ obtained from the evolution models of Saumon & Marley (2008) yield spectroscopic distances ranging from 15.7-18.5 pc, which are larger than the 11.6 pc distance derived earlier from the empirical *K*-band relationship of Marocco et al. (2010). If we instead assume a higher gravity of $\log g = 5.0$ at odds with the best-fitting spectral models, we find $R = 0.1 R_{\odot}$ and obtain distances of 13.8-14.1 pc, which are closer to the empirical estimate.

We also attempted the above analysis using the SETTL/COND and cloudy/clear model combinations of Allard et al. (2003) and Burrows et al. (2006), however we were unsuccessful in simultaneously reproducing the NIR SED and photometric variations of 2M2139 using these models. This is not surprising given that we find no good solutions with $f_{\text{sed}2} = 'nc'$ (truly condensate-free regions) using the models of Saumon & Marley (2008).

Finally, we should note that in finding the best hybrid models, we have assumed that our target’s observed spectrum corresponds to its mid-brightness state. This is a reasonable approximation, as synthetic colors derived from 2M2139’s NIR spectrum are consistent with $J - K_s$ and $J - H$ colors measured for this target at the time of the WIRC observations. In figure 3.12 we display the model maximum and minimum light spectra in addition to the best-fitting mid-brightness spectrum, all normalized to the *J* band, in order to demonstrate that differences between the three are minimal.

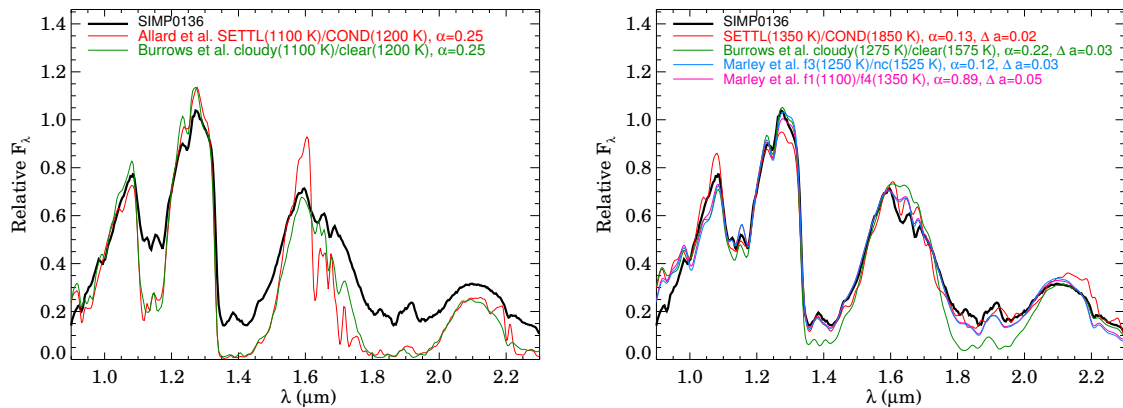


Figure 3.13: The NIR spectrum of SIMP0136 (Burgasser et al. 2006a), with hybrid model spectra (linear combinations of cloudy and clear models) used to model its photometric variability overplotted (similar to the left panel of figure 3.12). The filling fractions and effective temperatures of the models used to form each hybrid spectrum are shown in the legend. *Left*: Hybrid model spectra obtained by setting $T_1 + \Delta T = 1200$ K a priori, and modeling only photometric variations as done by Artigau et al. (2009) (see text for more detail). *Right*: Hybrid model spectra corresponding to our simultaneous modeling of the photometric variations *and* NIR spectrum of SIMP0136. Red and green lines correspond to the same model sets as in the left panel, but with filling fractions and temperature contrasts that better reproduce SIMP0136’s NIR spectrum as well as its photometric variability of $A_{K_s} / A_J = 0.48$. Blue and pink lines correspond to models of Saumon & Marley (2008) where $f_{\text{sed}1} = 1 / f_{\text{sed}2} = 4$ and $f_{\text{sed}1} = f_4 / f_{\text{sed}2} = \text{‘nc’}$ respectively.

Even when the absolute variability amplitudes are large and differ as a function of wavelength ($A_J = 0.26$, $A_{K_s} / A_J = 0.45\text{--}0.83$), changes to the shape of a normalized spectrum are barely perceptible by eye. Accordingly, the assumption that the observed spectrum corresponds to mid-brightness does not significantly impact our results. In contrast, the obvious spectral mismatch that results from fitting models to photometric variations alone, without using a spectral constraint, is illustrated in figure 3.13 for SIMP 0136.

3.6.2 Comparison to SIMP0136

Here we apply our variability model to SIMP0136, the other known example of a quasi-periodic variable T-dwarf. Artigau et al. (2009) modeled the variations of SIMP0136 ($A_{K_s}/A_J \sim 0.48$ and $A_J \sim 0.05$ mag) using 1D cloudy and clear model atmospheres and an interpolation scheme equivalent to our equation 3.3. While we have used primarily the models of Saumon & Marley (2008), Artigau et al. (2009) used combinations of cloudy and clear models from 3 different groups: the SETTL and COND models of Allard et al. (2001; 2003) and the cloudy and clear models of Burrows et al. (2006), as well as those from Tsuji & Nakajima (2003). They found that a temperature contrast of $\Delta T \sim 100$ K between clear and cloudy regions and $\Delta a \sim 0.15$ can reproduce the J and K_s variability of SIMP0136, with good agreement between all model sets. However, we find that the model spectra corresponding to this result ($T_1=1100$ K, $\Delta T=100$ K, $a=0.25$) provide a poor match to SIMP0136's NIR spectrum (figure 3.13), demonstrating that models capable of reproducing changes in broadband colors do not necessarily yield good spectral matches.

In order to make a fair comparison between 2M2139 and SIMP0136 we have repeated our above analysis for SIMP0136, relying on the amplitudes of variability reported by Artigau et al. (2009) and SIMP0136's NIR spectrum from Burgasser et al. (2006a). We find that the variability and NIR spectrum of SIMP0136 can be well-reproduced by a wide range models, including those where $f_{\text{sed1}} = \{1, 2, 3\}$ and $f_{\text{sed2}} = 4$, as well as those where $f_{\text{sed1}} = \{3, 4\}$ and $f_{\text{sed2}} = \text{nc}$. These solutions require temperature contrasts ranging from ~ 75 K for the $f_{\text{sed1}} = 3/f_{\text{sed2}} = 4$ pairing to ~ 275 K for the $f_{\text{sed1}} = 3/f_{\text{sed2}} = \text{nc}$ pairing, and require changes in filling factor affecting 3% to 15% of the visible disc. We also repeated our analysis using the SETTL/COND models of Allard et al. (2003) and cloudy/clear models of Burrows et al. (2006). For these latter models we found poor overlap between parameters capable of simultaneously reproducing the observed photometric variations and SIMP0136's NIR spectrum,

with optimal temperature contrasts occurring for $\Delta T=500$ K and 300 K respectively, and significantly poorer spectral fits. A selection of best-fitting hybrid spectra for SIMP0136 from different model groups is shown in figure 3.13.

In general, we find that our results agree qualitatively with those of Artigau et al. (2009). However, for the sake of comparison, we find that temperature contrasts required to model the observed $A_{K_s}/A_J \sim 0.48$ for SIMP 0136 are at least 2-3 times higher (and changes in filling factor smaller) than previously inferred if a spectral constraint is imposed.

3.6.3 The need for self-consistent 3D model atmospheres

Due to the lack of self-consistent 3D models our above modeling approach is necessarily data-driven as opposed to physically motivated. The drawback is that combinations of independent 1D atmosphere models may possess incompatible T-P profiles, and we are therefore not guaranteed to arrive at physically plausible configurations (see the discussion within Marley et al. 2010). This leads us to question whether the high temperature contrasts derived above, and in particular $\Delta T \gtrsim 300$ K in several cases, are physically reasonable.

Figure 3.14 shows the temperature of the $\tau = 2/3$ surface as a function of wavelength for a model with $f_{\text{sed}} = 2$, $\log g = 4.5$ and $T_{\text{eff}}=1000$ K, with and without condensate opacity. Both models share the same T-P profile, but in the latter condensate opacity has been switched off. The cloud-free $\tau = 2/3$ surface occurs at higher temperatures, indicating that photons emerge from deeper atmospheric layers in the absence of condensate opacity. The temperature contrast between the cloudy and cloud-free “photospheres” is as high as 600 K in the J band, and therefore the large temperature contrasts required to model our observations are not unreasonable. However, the relative contrasts in the J and K_s bands appear problematic; in the K_s band the contrast between the cloudy and cloud-free $\tau = 2/3$ surface has dropped

to only ~ 100 K. Thus, in the K_s band, one does not look much deeper into the atmosphere even if cloud opacity is removed. This is mainly due to an increased gaseous opacity from collision induced absorption by H_2 molecules (CIA) at these wavelengths, causing the gaseous (cloud-free) photosphere to occur at higher altitudes, and hence cooler temperatures. This structure of the cloudy model poses a problem if we wish to reproduce the large observed amplitude ratios of $A_{K_s} / A_J \gtrsim 0.45$, as it requires the K_s band flux within clear regions to be larger than allowed by the T-P profile of the cloudy model. Of course, this assumes that the T-P structure of the upper atmosphere is identical within cloudy and clear regions, which need not be the case.

The above results suggest that conclusions drawn from linear combinations of 1D atmosphere models must be viewed with caution, and highlights the need for self-consistent 3D modeling, including the effects of atmospheric circulation. Recent progress in this direction has been made by Marley et al. (2010), who have calculated a set of self-consistent patchy cloud models of the L/T transition, where cloudy and clear regions share a common T-P profile. These models continue to use the cloud model of Ackerman & Marley (2001) to describe cloudy regions and contain an additional parameter h , which specifies the fractional coverage of “holes”, or cloud-free regions in the atmosphere. However, these models predict negative A_{K_s} / A_J (i.e. anti-correlated amplitudes), inconsistent with those observed for 2M2139. Since the Marley et al. (2010) models assume a common T-P profile within cloudy and clear regions, this may indicate that the T-P profiles diverge in a real atmosphere. Alternatively, our modeling in the previous section demonstrates that the best fits to the data derive from models in which the lowest condensate opacity surface elements are not truly condensate-free (i.e. $f_{\text{sed}} = 4$), which may also account for part of the discrepancy between the data and models from Marley et al. (2010).

There are several possible explanations for the mismatch between self-consistent models and the K_s band data. A larger than expected contrast between cloudy and

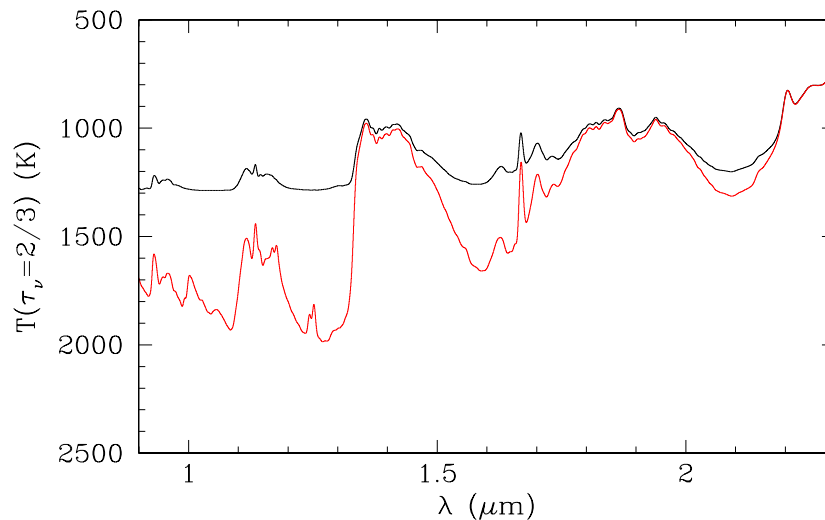


Figure 3.14: Temperature of the $\tau = 2/3$ surface as a function of wavelength for a model with $f_{\text{sed}} = 2$, $\log g = 4.5$, and $T_{\text{eff}} = 1000$ K, with (black line) and without (red line) condensate opacity, courtesy of Dr. Didier Saumon (Saumon & Marley 2008).

clear regions in the K_s band could suggest thick, high-altitude dust clouds, or weaker than expected H_2 CIA, possibly the result of high metallicity. Alternatively, the T-P structure of a partially cloudy atmosphere may itself be horizontally inhomogeneous within the photosphere, requiring a fully 3D hydrodynamical treatment to model. In addition, there is always the possibility that different types of cloud heterogeneities than envisioned here, or a completely different mechanism may be responsible for the variability of 2M2139. Assuming that the variability is indeed the result of heterogeneous clouds, these observations can be used to guide future modeling efforts.

3.7 Discussion

3.7.1 Origin of the Observed Variability

While heterogeneous clouds is our preferred explanation for the observed variability, and the scenario we have modeled in depth, it is worth exploring whether other mechanisms could be responsible.

3.7.2 Clouds versus Magnetic Spots

The asymmetric and evolving light curve shape of 2M2139, with periodic behavior on a rotation timescale, is the typical signature of surface spots. As noted earlier, the derived 7.721 ± 0.005 hr periodicity would be consistent with rotation rates of ultracool dwarfs (~ 2 -12 hrs Reiners & Basri 2008) inferred from $v \sin i$ data, whereas a double-peaked light curve with a 15.44 hr period would correspond to a slower rotator (this is not inconsistent with $v \sin i$ data, as observations are biased against such slow rotators). The nature of the surface features responsible is not immediately clear. For stars, cool magnetic spots are a common source of variability, related to the suppression of convective heat flux within magnetic flux tubes that penetrate the stellar photosphere. However, estimates of magnetic Reynolds numbers in cool dwarf atmospheres (Gelino et al. 2002; Mohanty et al. 2002), predict weak coupling between the gas and magnetic field, with magnetic Reynolds numbers of $R_m \sim 0.01$ - 10^{-6} throughout the photospheres of late-L and T type BDs. It is unknown to what extent cooling in deeper, ionized layers might carry through to the photosphere. From an empirical standpoint, only a small fraction of late-M dwarfs display variability due to magnetic spots, and typical photometric amplitudes are $< 5\%$ (e.g. Terndrup et al. 1999; Scholz & Eislöffel 2004; Scholz et al. 2009). Thus, if magnetic in origin, the NIR variability of 2M2139 would be an order of magnitude larger than what is typical of late M-dwarfs.

Alternatively, condensate clouds in rapidly rotating BD atmospheres may form discrete cloud features, similar to the banding and cyclonic storms observed on Jupiter. At wavelengths where the gaseous opacity is low (e.g. in the NIR 1-2 μm regime between water absorption bands), the flux emitted from ‘holes’ or clearings in the cloud layer may emerge from atmospheric depths hundreds of degrees hotter than the opaque cloud layer (e.g. figure 3.14). Such large temperature contrasts would provide a natural explanation for large-amplitude variability in the *J* and *H* bands, and somewhat smaller variability in *K_s*. On Jupiter, regions of low condensate opacity are visible as bright hot spots at 5 μm , where an analogous gaseous opacity window exists. By conducting synthetic photometry on resolved images of Jupiter, Gelino & Marley (2000) determined that the contrast between cloud features and hot spots in Jupiter’s atmosphere may lead to variability as high as 20% at 5 μm over a single rotation, with variations strongly correlated with the position of the Great Red Spot, a high altitude anti-cyclone. Thus Jupiter may prove to be the closest astrophysical analog for 2M2139’s unique variability, with both warm clearings and a high-altitude storm feature contributing to variations.

Finally, the modeling presented here (§3.6, figures 3.10-3.11) strongly supports the heterogeneous clouds interpretation — rather than magnetically induced cool or hot spots — as it reproduced the observations best. Since magnetic structures and clouds would be effectively decoupled, the magnetic spot model would correspond to the case B we have investigated (uniformly cloudy atmosphere with spatial variations in T_{eff} only), which we found cannot explain the observations. This is of course consistent with the fact that clouds are known to occur in BD atmospheres while magnetic spots are very unlikely in these cool atmospheres.

At this point we cannot distinguish between a scenario where a high altitude cloud or storm feature is responsible over a scenario where the atmosphere is composed primarily of broken clouds and clearings. Further monitoring, and improved atmo-

sphere models where heterogeneities are represented in a more physically consistent way will be required to confirm this result.

Could the variability of 2M2139 be related to binarity?

Given 2M2139's potentially double-peaked light curve, and similar amplitudes of variations observed in J , H , and K_s bands in at least one epoch (see figure 3.8) we consider here whether the observed variability could arise from an eclipsing binary system. Since the continuous shape of the light curve is inconsistent with that of a detached binary system (there is no flat out-of-transit region), a semi-detached configuration would be required. In addition, subtle changes in the light curve shape from night to night, as well as the overall light curve asymmetry would require an extra variable component, such as a hot-spot due to mass transfer. The requirement that one component fill its Roche Lobe allows us to place constraints on the range of primary and secondary masses and ages that could form a semi-detached system. For a given primary mass, M_1 , and mass ratio $q = M_2/M_1$ (where $M_2 < M_1$), the Roche Lobe size of the secondary can be computed via the formula of Eggleton (1983) given by $R_L/a = 0.49q^{-2/3}/(0.6q^{-2/3} + \ln[1 + q^{-1/3}])$. The separation, a , is determined from Kepler's law assuming a period of 15.44 hr, corresponding to a double-peaked light curve. The secondary Roche Lobe sizes can then be compared to typical BD radii from evolutionary models. In figure 3.15 we show the secondary Roche Lobe size as a function of mass ratio for primary masses of 10, 30 and 60 $M_{Jupiter}$. For comparison we over-plot typical secondary BD radii from evolutionary models, assuming a primary effective temperature of ~ 1300 K (note that the system age is fixed from the combination of primary mass and effective temperature, yielding approximate ages of 20 Myr, 280 Myr, and 1.8 Gyr from lowest to highest primary mass). The system parameters for which secondary Roche Lobe filling may occur are limited. We find that Roche Lobe sizes are much larger than typical secondary radii

for almost all primary masses and mass ratios. This scenario is possible only for low primary masses ($M_1 < 10 M_{Jup}$) and low mass ratios ($q < 0.05 - 0.1$), such that a semi-detached binary with a 15.44 hr period would have to be a young (< 20 Myr), double planetary-mass system. For more typical BD masses and ages, the binary components should remain detached, and unable to produce the observed light curve.

Phase variations (i.e. from the day/night side contrast of an irradiated companion) in non-eclipsing systems can also produce periodic variations. However, intrinsic phase variations of an irradiated companion would be washed out by the brighter primary, resulting in much lower levels of variability than observed for 2M2139.

A further problem with the binary scenario is that multi-epoch observations spanning Aug 2009 to Nov 2009 cannot be phased together, requiring either the Aug 2009 or Nov 2009 epoch to be offset in phase from the other epochs. The timing of both epochs has been verified in the acquisition time-stamps as well as manual log books, and phasing all epochs together would require both to be in error—an occurrence we deem to be extremely unlikely. In order to produce a large offset in the expected eclipse timings by natural means, a moderately elliptical, precessing orbit is required ($e \gtrsim 0.15$, e.g. Ragozzine & Wolf (2009)). This could potentially be achieved if the system is undergoing Kozai oscillations (Kozai 1962) due to the presence of a third body in a highly inclined orbit to the inner pair. However, in order for the precession timescale to be sufficiently fast (e.g. months) such a third perturber would closely approach or exceed the criterion for dynamical instability given by Eggleton & Kiseleva (1995). Furthermore, the effects of tidal friction between the inner pair would act to suppress Kozai cycles over time and circularize the inner orbit (e.g. Fabrycky & Tremaine 2007), making it increasingly unlikely to observe a system in this configuration.

Based on the above considerations we feel we can reasonably exclude an eclipsing binary as the source of 2M2139's variability.

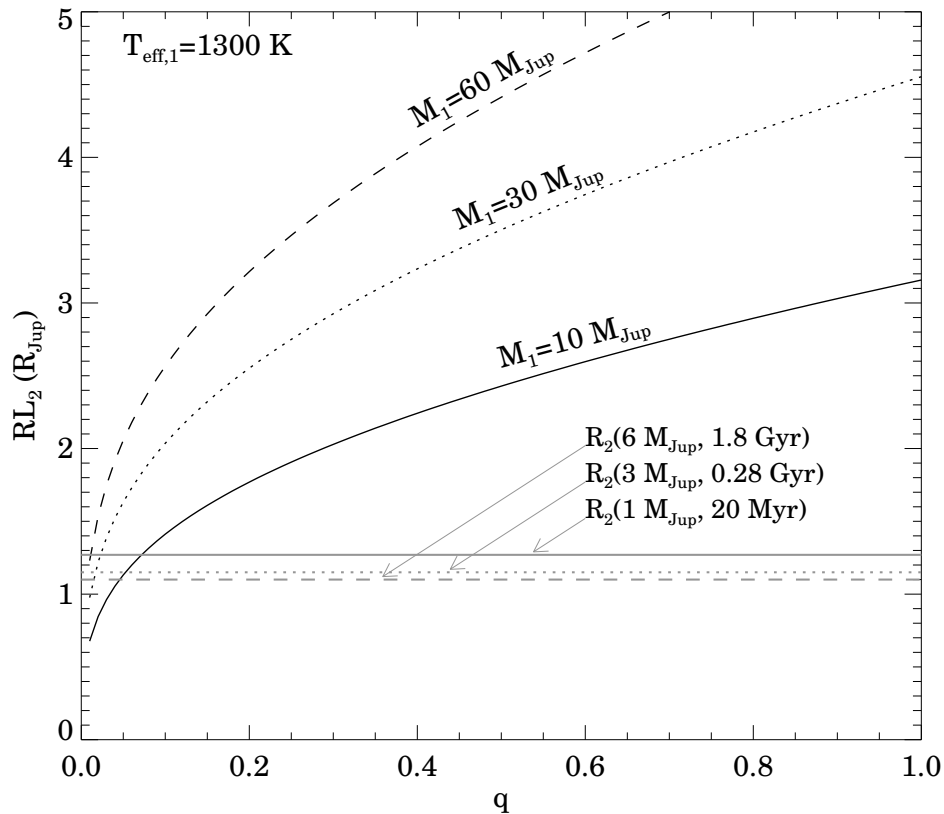


Figure 3.15: Secondary Roche lobe radius as a function of mass ratio, q , for primary masses of 10, 30, and $60 M_{Jup}$, assuming an orbital period of 15.44 hr (black lines). Secondary radii determined from evolutionary models for fixed $q = 0.1$, and assuming a primary effective temperature of 1300 K are overplotted (grey lines).

Alternatively, like Jupiter, BDs are expected to have large magnetic fields. Thus it is conceivable that some sort of magnetic interaction between a close binary pair is possible without requiring physical Roche lobe filling. However, such a scenario does not naturally explain a double-peaked light curve, and its ability to produce significant and highly contrasting photospheric features is unclear.

3.7.3 The L/T Transition

2M2139 joins SIMP0136 as the second known cool BD to display *persistent and significant* quasi-periodic variability in the NIR, with amplitudes well above the level of photon noise and systematic errors. With spectral types of T1.5 and T2.5, and

NIR colors of $J - K_s = 1.3$ and $J - K_s = 0.98$, both BDs fall squarely within the L/T transition regime (see figure 3.16). Although a larger sample is needed, observations of 2M2139 and SIMP0136 suggest that large amplitude NIR variability may be more common at the L/T transition, consistent with the cloud fragmentation hypothesis of Ackerman & Marley (2001) and Burgasser et al. (2002). In addition, the positions of SIMP0136 and 2M2139 on the color-magnitude diagram — within the L/T transition regime where the cloud opacity decreases significantly — provides further rationale to prefer heterogeneous clouds as the mechanism for the observed variability.

Overplotted on the color magnitude diagram in figure 3.16 are vectors showing the direction of observed variability for 2M2139 and SIMP 0136. Rather than tracing the approximate evolution of field BDs across the L/T transition, the vectors point upward of the transition path, rising much more steeply in M_J with decreasing $J - K$. This difference reflects the fact that evolution across the L/T transition occurs over astronomical timescales, over which a significant amount of heat is lost from the upper atmosphere as the higher temperature T-P profile below a cloudy atmosphere evolves toward the lower temperatures under a clear atmosphere (e.g. Saumon & Marley 2008). When we observe variability due to clouds and clearings at a snapshot in time we see underlying clear patches that are warmer than the integrated effective temperature of the atmosphere, and hence warmer than the atmosphere of a more evolved cloud-free T-dwarf of the same effective temperature. Therefore, the direction of the L/T transition path is determined by both decreasing cloud coverage and a loss of entropy from the upper photosphere that occurs over astronomical timescales, while the direction of the instantaneous variability vector traces only changes in cloud coverage.

While heterogeneous clouds appear to be the most likely explanation for our observations, the physical mechanism by which clouds may fragment at the L/T transition remains unknown. One possibility is that as clouds form progressively lower

in the atmosphere as the BD cools, eventually the entire vertical extent of the cloud is found within the dynamic troposphere which is more subject to local variations in updrafts and downdrafts arising from convection. These localized weather patterns are better able to disrupt the cloud than when the BD is warmer and a substantial fraction of the cloud opacity is found within the relatively quiescent stratosphere. While weather remains a poorly understood phenomenon even among the planets in our own Solar System, BDs represent a simplified case where atmospheric dynamics result primarily as a consequence of rapid rotation and internal heat, without the complication of external forcing due to irradiation from a parent star. Thus future observations of weather in BD atmospheres may provide a novel opportunity to study atmospheric circulation and cloud meteorology in a higher gravity regime, never before probed.

3.8 Conclusions

We have reported the unique, large-amplitude quasi-periodic variability of the cool L/T transition BD 2M2139. Our major findings and conclusions are summarized here.

1. *Variability* We have observed 2M2139 to be highly variable in the NIR over 9 separate epochs spanning 100 days, with an amplitude as high as 26% in the *J*-band. Measured amplitude ratios range from $A_J/A_H = 0.84 - 0.91$ and $A_{K_s}/A_J = 0.45 - 0.83$, with uncertainties of $\pm 0.07-0.15$. It remains unclear whether these variations in relative amplitude from epoch to epoch are intrinsic, or reflect hidden measurement uncertainties. Disagreement at the 2σ level between epochs suggests the former. In addition to the short timescale variability, comparison with 2MASS photometry hints that there may be a longer-term (10 yr) variation that consists mainly of a brightening in the *J*-band.

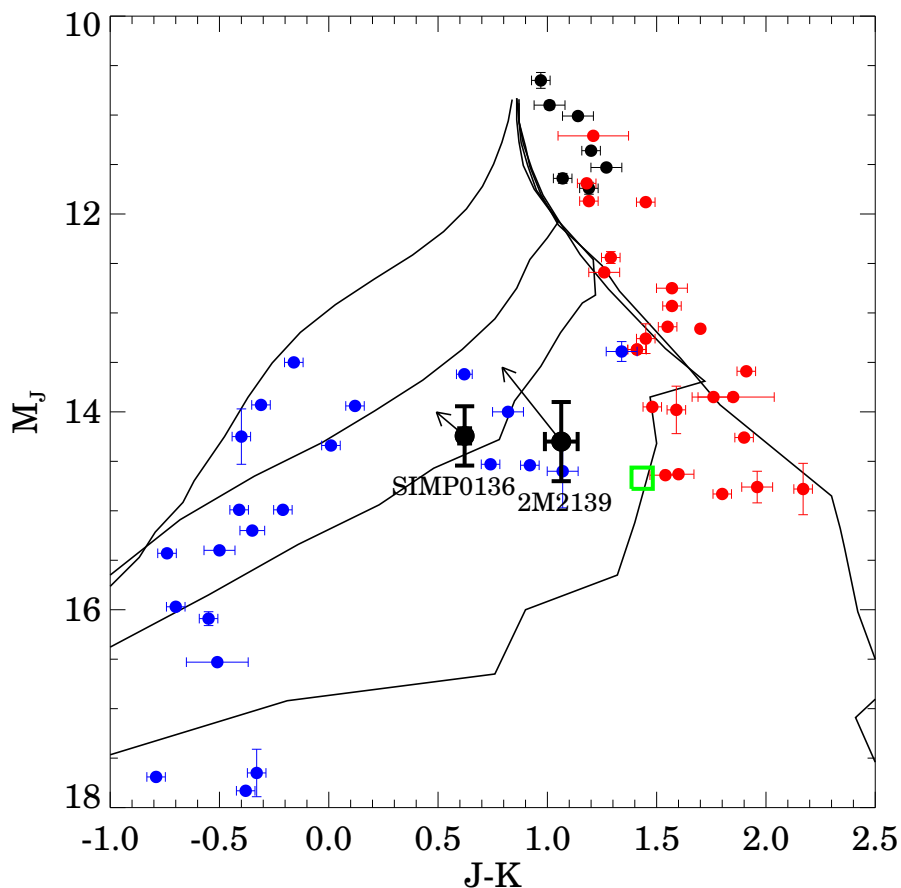


Figure 3.16: Color-magnitude diagram in the MKO filter system for M, L, and T dwarfs with measured parallaxes (black, blue and red points respectively) from the compilation of S. K. Leggett. The approximate positions of SIMP0136 and 2M2139 are overplotted based on spectroscopic parallaxes as opposed to real ones. The $J - K_s$ color of 2M2139 (converted to the MKO system) is based on the colors derived from WIRC and SpeX epochs (see table 3.4), as opposed to 2MASS. The approximate position of 2M2139 on the color magnitude diagram based on its 2MASS color (also converted to the MKO system) is shown as a green square (its absolute magnitude was determined *relative to* the WIRC/SpeX epochs, as the empirical relations for determining absolute magnitude have not changed). Solid black lines from right to left indicate the $f_{\text{sed}} = 1, 2, 3, 4$, and nc model colors respectively for $\log g = 5.0$. Although we have used spectral models with $\log g = 4.5$ throughout, a value of $\log g = 5.0$ is more appropriate for comparison with the population of field BDs (in addition, see the discussion in section 3.5.2 about choices of $\log g$ values). Arrows depict the vector direction of the variability observed for 2M2139 (this paper, averaged from the 3 epochs in figure 3.4) and reported for SIMP 0136 (Artigau et al. 2009), both magnified in amplitude by a factor of 3.

2. *Periodicity* We have measured a minimum period of 7.721 ± 0.005 hr for 2M2139. It is also possible that the light curve is double-peaked with a period of $2 \times 7.72 = 15.44$ hr. In the latter case, the period would be somewhat larger than the 2-12 hr periods typical of field BDs.

3. *Time Evolution of the Light Curve* Despite a clear periodicity, the light curve shape changes from night to night, and we cannot simultaneously phase our earliest and latest epochs with the middle ones, indicating substantial evolution of cloud features on timescales of weeks to months, with more subtle changes occurring on a timescale of days. The differential rotation of a storm feature is a possible explanation for the longer timescale evolution observed.

4. *Modeling variability due to patchy clouds* We have searched for linear combinations of 1D atmosphere models differing in temperature and condensate properties, that can simultaneously reproduce the observed multi-band variability and the NIR spectrum of 2M2139. Using the models of Saumon & Marley (2008) we found that the observations can be reproduced by a heterogeneous surface wherein regions of higher condensate opacity ($f_{\text{sed}}=1$ or $f_{\text{sed}}=2$) are cooler, and regions of lower condensate opacity ($f_{\text{sed}} = 3$ or $f_{\text{sed}} = 4$) are warmer (by ~ 175 - 425 K). The best-fitting model suggests that cool, thick cloud features— for instance one or more storms systems occupying 25% of 2M2139’s visible disc —may be responsible. Alternatively, the data is also well-reproduced by a model where atmospheric heterogeneities consist of warm clearings in a cloudy atmosphere, however “clear” regions must retain some degree of cloud opacity (i.e. $f_{\text{sed}}=4$). The large temperature contrast required between thin and thick cloud patches may suggest that the thick clouds extend to higher altitudes in the atmosphere. We reiterate that these results should be viewed cautiously, as

interpolations between independent 1D models do not necessarily result in physically plausible configurations.

5. Origin of Variability The continuous, asymmetric, and evolving nature of the light curve strongly suggests that atmospheric cloud features are responsible for 2M2139's variability. Due to 2M2139's (i) status as an L/T transition BD and the expectation of patchy clouds in this regime, (ii) cool, neutral photosphere, and (iii) our modeling of the observations we have argued that surface features responsible are heterogeneous clouds rather than magnetically induced spots. We have also considered that 2M2139 may be an interacting binary, but have ruled out this scenario.

6. The L/T Transition Both 2M2139 and SIMP0136, the two known examples of BDs that display large-amplitude, persistent variability in the NIR, have colors and spectral types falling directly within the L/T transition, suggesting that variability in this regime may be higher-amplitude and/or more frequent. These results therefore provide empirical support for the idea that the fragmentation of dust clouds can explain observed properties of the L/T transition.

Looking forward, long term monitoring of this target both photometrically and spectroscopically, and over a broader wavelength regime, should reveal the true nature of its variability. In addition, a parallax measurement and high resolution spectrum will be essential in order to better constrain 2M2139's absolute magnitude and physical properties.

Chapter 4

Binarity at the L/T Transition

Contents of this chapter have been submitted to the *Astrophysical Journal*: **Radigan, J., Jayawardhana, R., Lafrenière, D., Dupuy, T., Liu, M., & Scholz, A.** *Binarity at the L/T Transition and the Discovery of a Visual T-Dwarf Triple System*, 2012. I wrote the paper, and did the majority of observing, data reduction, analysis, and interpretation, under the supervision of R. Jayawardhana. Second epoch NIRC2 observations of the resolved triple T-dwarf system were obtained and reduced by T. Dupuy and M. Liu. The spectrum of probable K giant star BD+211974 (used for telluric corrections) was obtained and reduced by Aleks Scholz.

4.1 Overview

We present new high contrast imaging of 8 L/T transition brown dwarfs using the NIRC2 camera on the Keck II telescope. One of our targets, the T3.5 dwarf 2MASS 0838+15, was resolved into a hierarchical triple with projected separations of 2.45 ± 0.5 AU and 27 ± 5 AU for the BC and A(BC) components respectively. Resolved OSIRIS spectroscopy of the A(BC) components confirm that all system members are T dwarfs. Using resolved photometry to perform a spectral decomposition we infer spectral types of $T3 \pm 0.5$, $T3 \pm 0.5$, and $T4.5 \pm 0.5$ for the A, B, and C components respectively. The uniformly brighter primary has a bluer $J - K_s$ color than the next faintest component, which may reflect earlier evolution across the L/T transition for objects with higher surface gravity, or alternatively divergent cloud properties amongst components. Relying on empirical trends and evolutionary models we infer a total system mass of $0.034\text{-}0.104 M_\odot$ for the BC components at ages of 0.3-3 Gyr, which would imply a period of 12-21 yr assuming the system semi-major axis to be similar to its projection. We also infer differences in effective temperatures and surface gravities between components of no more than ~ 150 K and ~ 0.1 dex. Given the similar physical properties of the components, the 2M0838+15 system provides a controlled sample for constraining the relative roles of effective temperature, surface gravity, and dust clouds in the poorly understood L/T transition regime where evolving condensate properties are thought to play a significant role in the evolution from late-L to early-T spectral types. Combining our imaging survey results with previous work we find an observed binary fraction of 4/18 or $22_{-8}^{+10}\%$ for unresolved spectral types of L9-T4 at separations $\gtrsim 0.05 - 0.07''$. This translates into a volume-corrected frequency of $14_{-5}^{+7}\%$ using an empirically determined correction factor of $\alpha = 1.8$. While this frequency is only slightly larger than values of $\sim 9\text{-}13\%$ reported outside the transition, it represents an increase by a factor of 2 over the binary fraction of an equivalent L9-T4 sample selected from primary rather than unresolved spectral types ($7_{-4}^{+6}\%$). Thus while our

data hints at a higher binary fraction for unresolved L9-T4 spectral types, this increase is not yet statistically significant, and a larger sample is required to settle the issue.

4.2 Introduction

The L/T transition, roughly spanning L8-T5 spectral types, is characterized by dramatic spectral evolution at near-infrared wavelengths at a near-constant effective temperature of ~ 1200 K (Golimowski et al. 2004; Stephens et al. 2009). Rather than following a sequence in effective temperature, evolution across the L/T transition follows the disappearance of condensate clouds from brown dwarf photospheres as heavy dust grains subject to diminishing pressure-support gravitationally settle faster than they can be replenished (e.g. Ackerman & Marley 2001; Tsuji 2002; Marley et al. 2002; Allard et al. 2003; Woitke & Helling 2003). As condensate opacity declines, the $\tau = 2/3$ surface moves to deeper, warmer atmospheric layers. The resulting constancy in the L/T transition effective temperature reflects a balance between opposing phenomena: cooling of the atmosphere is roughly offset by its increasing transparency to deeper layers (Saumon & Marley 2008). This effect is seen most clearly in at wavelengths $\sim 1 \mu\text{m}$ (*Y* and *J*-bands) which are particularly sensitive to condensate opacity. From L8-T5 spectral types the $1 \mu\text{m}$ flux increases by a factor as high as ~ 2.5 , (“*J*-band brightening”; Dahn et al. 2002; Vrba et al. 2004; Dupuy & Liu 2012; Faherty et al. 2012), as the dust opacity declines.

The processes governing the dissipation and settling of condensates across the L/T transition remains poorly understood, with models generally predicting a much more gradual change in cloud properties over a wider range of effective temperatures (e.g. Tsuji & Nakajima 2003; Marley et al. 2002; Allard et al. 2003). It is debated as to what extent the rapid decrease in cloud opacity is due to global changes in cloud thickness and position, changing grain properties, increasing rates of grain sedimentation, or a decreasing cloud filling fraction over the brown dwarf’s surface (e.g. Burrows et al.

2006; Saumon & Marley 2008; Burgasser et al. 2002). Recent observations of the highly variable L/T transition dwarfs SIMP0136 (Artigau et al. 2009) and 2M2139+02 (Radigan et al. 2012) suggest that heterogeneous cloud cover may indeed contribute to the declining condensate opacity in this regime.

Multiple systems have already played an important role in testing formation, atmosphere and evolutionary models for very low mass (VLM, $M_1 \lesssim 0.1 M_\odot$) and substellar objects in general (e.g. Stassun et al. 2007; Burgasser et al. 2007; Liu et al. 2010; Dupuy & Liu 2012). When attempting to understand the L/T transition, multiple systems are important in two major ways. First, it has been suggested that there could be an unusually high binary fraction in this regime (\sim L9-T4 spectral types). According to a population synthesis of Burgasser (2007), this hypothesized increase reflects a dip in the luminosity function of bonafide single brown dwarfs at these spectral types (e.g. due to rapid evolution through this regime), in contrast to a roughly constant luminosity function for unresolved binaries whose integrated light spectral types mimic those of true transition objects. Thus multiplicity searches at the L/T transition are important in order to determine the degree of binary contamination, and to identify contaminants. Second, if L/T transition binaries are resolved into constituent parts in or straddling the L/T transition, they can provide strong tests of models where two free parameters, the age and metallicity of the system, are fixed. For instance, the identification of “flux-reversal” binaries wherein the secondary component is brighter than the primary in the J band have provided direct evidence that this brightening is a real evolutionary feature associated with the disappearance of dust clouds (e.g.Looper et al. 2008). Furthermore, in cases where masses can be constrained from visual orbits these systems can act as gravity benchmarks which will further our understanding of the dependence of cloud properties on surface gravity.

Here we present high contrast imaging observations of 8 brown dwarfs occupying the sparsely populated late-L/T transition, designed to search for hitherto undetected

multiples. One object, the T3.5 dwarf 2M0838+15, was resolved into a triple system. This discovery constitutes the first hierarchal triple T-dwarf ever reported, as well as the first brown dwarf visual triple system. In section 4.3 we describe our target sample including the discovery of 2M0838+15, our observations and data reduction. In section 4.4 we analyze the resolved NIRC2 images and OSIRIS spectroscopy of the newly resolved 2M0838+15 ABC system. In section 4.3.2 we describe the search for companions and detection limits around our entire sample. In section 4.6 we combine our results with those from previous surveys to infer a binary fraction for L9-T4 spectral types, and to test whether there is a statistically significant increase in binary frequencies inside the L/T transition. In section 4.7 we summarize our major findings and discuss our results in the context of the L/T transition and substellar formation models.

4.3 Observations and Data Reduction

Here we present high contrast imaging observations of 8 L/T transition brown dwarfs (BDs) using the NIRC2 camera on the Keck telescope obtained on 2010 Jan 8. One target in our sample was resolved into a triple system, for which we obtained follow up imaging with NIRC2 on 22 March 2010 and partially resolved spectroscopy using OSIRIS on 2011 Dec 03. These three data sets are described in the following subsections.

4.3.1 Target Selection

Details for our NIRC2 imaging targets are provided in table 4.1. The targets were selected to overlap with an L/T transition sample of brown dwarfs targeted for variability monitoring (Radigan et al. 2011) where possible, while gaps in our program were filled by additional targets with late-L and T spectral types that were observable

Table 4.1. Targets

Target ID	SpT	J	H	K _s	J-K _s	Reference(s) ^a
2MASS J01191207+2403317	T2	17.0	16.0	1.0	31.6 ± 6.6	1
2MASS J02474978-1631132	T2	17.2	16.2	15.6	1.57	1
2MASS J03284265+2302051	L8	16.7	15.6	14.9	1.8	2, 4
2MASS J03510423+4810477	T1	16.5	15.6	15.0	1.50	1
2MASS J06020638+4043588	T4.5	15.5	15.6	15.2	0.37	3
2MASS J07420130+2055198	T5	16.2	15.9	16.2 ^a	0.00	4, 5
2MASS J07584037+3247245	T2	15.0	14.1	13.9	1.07	4, 5
2MASS J08381155+1511155	T3	16.65	16.21	16.2	0.45	6, 7

^aDiscovery reference as well as the NIR spectral type reference is different from the former.

^bundetected in 2MASS, derived from spectrum

References. — (1)Chiu et al. (2006) (2)Kirkpatrick et al. (2000) (3)Looper et al. (2007) (4)Knapp et al. (2004) (5)Burgasser et al. (2006a) (6)Aberasturi et al. (2011) (7)This paper

at low airmass at the time of our observations. Objects were further culled based on not having previously been targeted by a high resolution imaging survey, and possessing a suitable tip-tilt stars within 50". One object fulfilling these criteria was an unpublished T dwarf, 2MASS J0838+15, whose discovery and spectral confirmation is described in the following subsection.

Discovery and Spectral Confirmation of 2M0838+15

The early T dwarf 2M0838+15 was discovered in 2008 from our own proper motion cross-match of 2MASS and SDSS catalogs (described in Radigan et al. 2008), but re-

mained unreported. This source was independently discovered as a T-dwarf candidate in a crossmatch of 2MASS and WISE by Aberasturi et al. (2011).

We obtained spectral confirmation for 2M0838+15 on 2008 March 01 using the SpeX Medium-Resolution Spectrograph (Rayner et al. 2003) at NASA’s Infrared Telescope Facility (IRTF). Observations were made in the short slit (15'') prism mode (0.8-2.5 μm), with a 0.5'' slit. The seeing was 0.8''-0.9''. We obtained ten 180 s exposures consisting of 5 AB pairs with a nod step of 7'' along the slit. For telluric and instrumental transmission correction the A0V star HD 79108 was observed immediately after the target at a similar air mass. Flat-fielding, background subtraction, spectrum extraction, wavelength calibration, and telluric correction were done using Spextool (Cushing et al. 2004; Vacca et al. 2003).

The unresolved spectrum for 2M2139 is presented in figure 4.1. Based on least squares fitting of spectral templates in the SpeX Prism Library to our data we derive a spectral type of $T3.5 \pm 0.5$ for the unresolved source.

Due to its status as an L/T transition object without previously reported high contrast imaging observations, 2M0838+15 was included in our LGS AO mini-survey of L/T transition BDs, described above in section 4.3.2. Images obtained using the NIRC2 camera during the observations of 2010 January 08 revealed this source to be a hierarchal triple (figure 4.2) consisting of a widely separated A(BC) pair ($\sim 0.5''$), with the BC component being further resolved into a tight double ($\sim 0.05''$).

4.3.2 NIRC2 Observations of L/T transition dwarfs

Observations of 8 L/T transition BDs (see table 4.1) were obtained in the first half of the night of 2010 Jan 8 using the NIRC2 narrow camera on the Keck II telescope. Due to the lack of bright natural guide stars within 20'' of our targets, the laser guid star and off axis tip-tilt (TT) star were used for adaptive optics (AO) corrections. For each target we obtained 3 or more dithered images in the K_s band. We used a 3-point

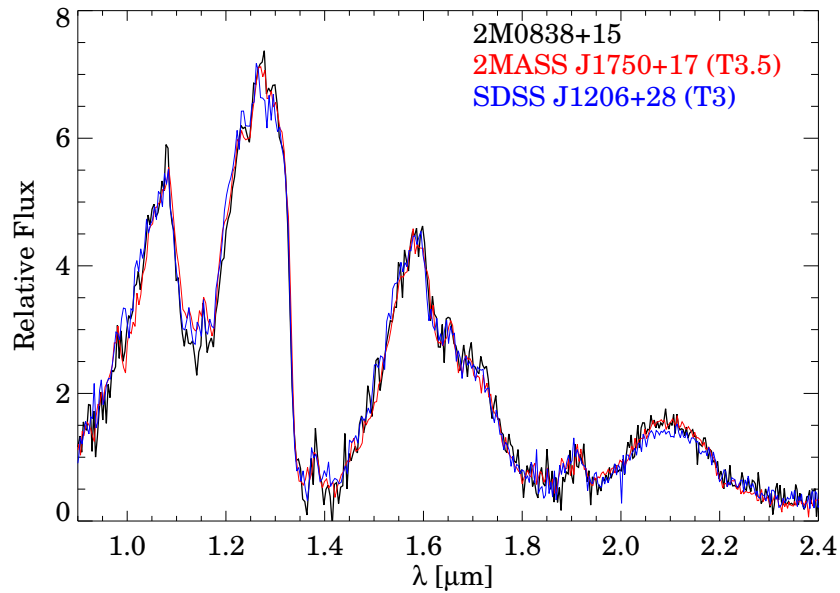


Figure 4.1: Unresolved JHK spectrum of the 2M0838+15ABC system (black line), obtained using SpeX at the IRTF. The best-fitting template for the SpeX Prism Library, the T3.5 dwarf SDSSp J175032.96+175903.9 (Geballe et al. 2002; Burgasser et al. 2006a), is over plotted as a spectral type reference (red). The next best fitting template, the T3 dwarf SDSS J120602.51+281328.7 (Chiu et al. 2006) is also shown.

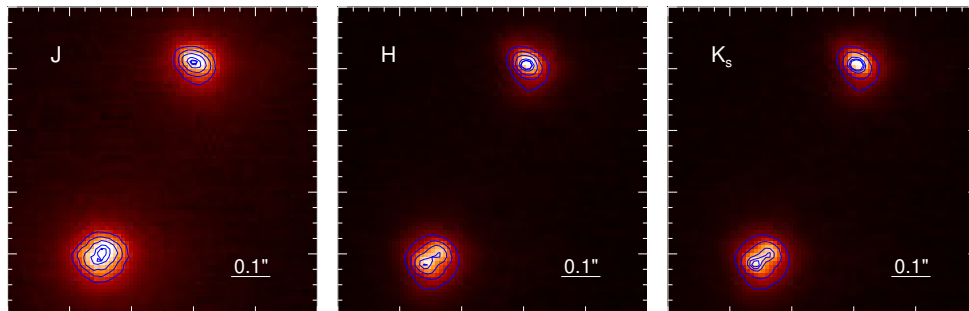


Figure 4.2: Reduced J , H , and K_s band cutouts (from left to right) of the 2M0838+15ABC system.

dither pattern, offsetting targets $\pm 2.5''$ from the center of the array in both x - and y - directions, excluding the bottom-left quadrant of the array which is significantly noisier than the others. Although highly varying from target to target the median FWHM and Strehl ratios achieved in the K_s band were $0.073''$ and 0.19 respectively. Some targets were also observed in the J and H bands but with lower image quality. Here, we only present multi-band data for the lone target in our sample that was resolved into a multiple system. Details pertaining to observations of individual targets including airmass, exposure times, number of exposures, average FWHM and Strehl ratios, and TT star magnitudes and separations are provided in table 4.2.

For calibration purposes ten to fifteen dome flat fields (with the lamp on and off) for each bandpass were taken in the early evening before sunset. Dark frames were obtained the afternoon after the observations for all but the longest exposure times (180 s and 210 s). For exposure times without corresponding dark frames the longest exposure (120 s) dark frames were simply scaled. The dark frames for each exposure time were median combined to form master dark frames for each exposure time. A master dark of the appropriate exposure time was then subtracted from all other science images. The flat field frames for a given filter were median combined and the resultant lamp-off frames subtracted from the lamp-on frames to obtain a single high-signal-to-noise flat field for each filter. All science images were divided by the flat field to correct for pixel-to-pixel variations in quantum efficiency. For each science image of a given target in a given bandpass a sky frame was obtained by averaging together all other exposures wherein the target did not fall in the same quadrant of the array. The iterative ($3\text{-}\sigma$ clipped) median of each sky frame was scaled to match the iterative median of the corresponding science frame in the target quadrant. The scaled sky frames were then subtracted from the science frames. A bad pixel mask was constructed by identifying hot pixels in the dark frames and dead pixels in the flat field frames. Additional bad pixels missed by this method were manually flagged. Bad

pixels located more than 2 FWHM away from the target were corrected by replacing their value with that of a 5×5 pixel median filtered image. Bad pixels falling within 2 FWHM of the target were interpolated using a second order surface interpolation of neighboring pixels. All pixel interpolations in the vicinity of our targets were also examined by eye. In addition to retaining the reduced individual exposures, all science images for a given filter and target were positionally cross-correlated against one another to determine relative sub-pixel offsets, interpolated onto a common grid, and stacked. Individual exposures with the narrowest FWHMs were used to search for close companions as described in section 4.5, while the stacked images were used to place limits on the presence of well-separated faint companions.

Reduced images of our targets are shown in figure 4.3. One of eight targets, the T3.5 dwarf 2M0838+15, was resolved into a multiple system. Images obtained revealed this source to be a hierarchal triple consisting of a widely separated A(BC) pair ($\sim 0.5''$), with the BC component being further resolved into a tight double ($\sim 0.05''$). Examples of reduced and sky-subtracted J , H , and K_s images of the 2M0838+15 ABC system are shown in figure 4.2. We analyze these images to obtain fluxes and system parameters in section 4.4.1

4.3.3 OSIRIS spectroscopy of the 2M0838+15 system

Spatially resolved spectra of the the 2M0838+15 components were obtained on 2011 Dec 03 in the latter half of the night using the OSIRIS integral field unit on the Keck II telescope. Conditions were partially cloudy. The extinction only dropped below 1 mag, permitting operation of the laser, in the latter quarter of the night. The star USNO-A2.0 050-05806001, located $51.1''$ away, was used for TT corrections, and fell in a good, non-vignetted region of the guide camera field of view when the 2M0838+15 A(BC) system was aligned along the long axis of the OSIRIS spectrograph (a position angle of 19 on the sky). We had originally planned to use the finest $0.1''$ plate scale

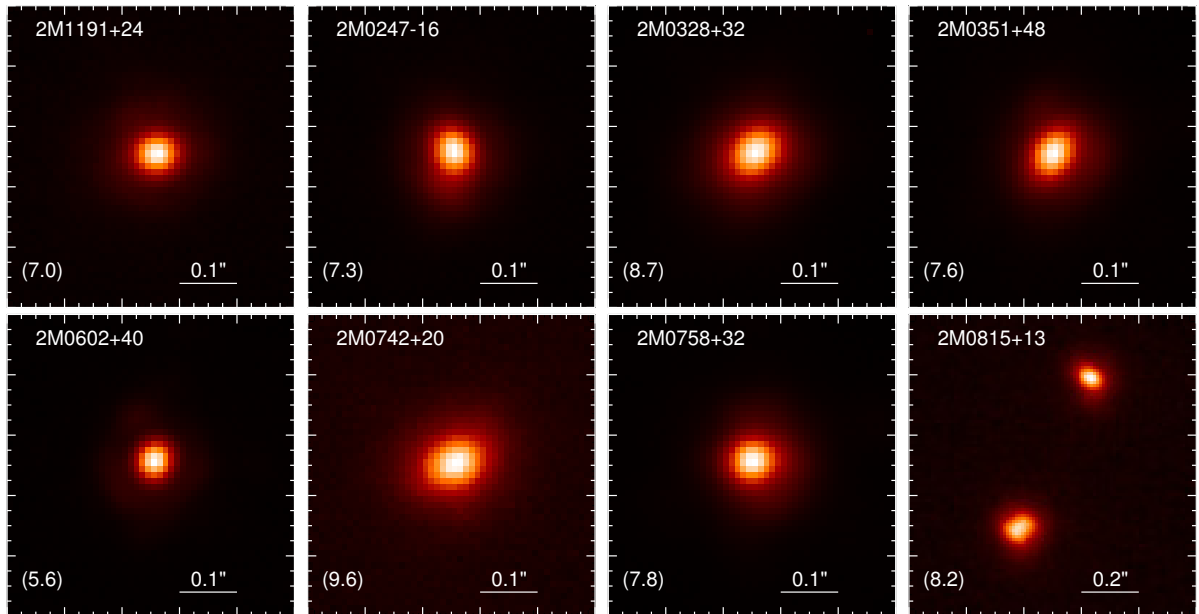


Figure 4.3: Postage stamps (K_s band) of all targets observed with NIRC2. In several cases the PSF is elongated in the direction of the TT star. Only a single target 2M0838+15 was resolved into a multiple system (bottom right). The camera position angle on the sky is 45.7° .

Table 4.2. Observations

Target	SpT	Filter	N_{exp}	t_{exp} (s)	airmass ^a	FWHM (")	Strehl	TT R Mag ^b	TT Sep ^c
2M0119+24	T2	K_s	3	120	1.03	0.065	0.23	16.0	9.0
2M0247-16	T2	K_s	5	80	1.24	0.073	0.19	13.8	45.7
2M0328+23	L8	K_s	6	100	1.01	0.085	0.15	16.9	61.2
2M0351+48	T1	K_s	5	80	1.15	0.077	0.17	10.0	55.0
2M0602+40	T4.5	K_s	3	60	1.1	0.056	0.31	10.6	50.9
2M0742+20	T5	K_s	2	80	1.16	0.087	0.17	16.0	38.2
2M0758+32	T2	K_s	6	30	1.13	0.075	0.20	15.9	40.9
2M0838+15	T3.5	K_s	4	120	1.18	0.081	0.25	12.6	51.1
2M0838+15	T3.5	J	4	210	1.13	0.106	0.05	12.6	51.1
2M0838+15	T3.5	H	4	180	1.10	0.083	0.13	12.6	51.1

^aAir mass at the start of the observation

^bR magnitude of the tip-tilt star

^cAngular distance between the target and tip-tilt star

and obtain blank sky frames for sky subtraction. However, because of time lost due to clouds in the first half of our run, we instead opted to use the $0.35''$ plate scale which provided a slightly larger field of view and increased efficiency by allowing us to dither on-chip rather than requiring separate blank sky frames. We obtained two AB pairs of spectra in the *H*-band with 15 minute and 5 minute exposures respectively, and one AB pair of *K*-band spectra with 6 min exposures.

We observed the A0V star HD64586 and a probable K giant star BD+211974 for telluric correction before (*H*-band only) and after (*H* and *K* bands) the science observations, at similar airmass. Due to bad weather and initial problems acquiring the science target, observations of the first telluric occurred over 2 hours ahead of the science exposures. Unfortunately although our second telluric BD+211974 is listed in SIMBAD as an A0V star, we discovered upon obtaining a spectrum that it is more likely an M or K giant with strong CO absorption features in the *K* band (although relatively featureless in *H*). In order to use BD+211974 for telluric correction, knowledge of its intrinsic spectrum is required. To this end we obtained a spectrum of BD+211974 using SpeX at the IRTF in short wavelength cross dispersed mode on 9 Jun 2012, using the A0V star HD79108 for telluric correction. The spectrum was reduced using SpeXtool (Cushing et al. 2004; Vacca et al. 2003).

The raw spectra were sky subtracted in AB pairs, wavelength calibrated and converted into 3D data cubes (2 spatial directions plus wavelength) using the OSIRIS data reduction pipeline (DRP) with the latest rectification matrices available (2010 July). The pipeline also corrects for bias variations between detector output channels, crosstalk, electronic glitches, and attempts cosmic ray removal. 1-D spectra were extracted from the reduced data cubes by via aperture photometry on the individual wavelength slices. A circular aperture of 2.5 pixel radius centered on each of the A and BC components was used. Residual sky levels were measured in annuli of 6 and 9 pixel inner and outer radii. Extraction of the brighter standard star spectra

were conducted using a larger 4-pixel radius aperture, and residual sky levels were found to be negligible. For the A0V star HD64586 we used the XtellCorr software package described in Vacca et al. (2003) to obtain our telluric spectrum (including scaled hydrogen line removal, and division of the spectrum by a Vega template). For the giant star BD+211974 we determined a telluric correction by dividing our non-corrected OSIRIS spectrum of BD+211974 by the fully corrected (i.e. intrinsic) SpeX spectrum. In the K band BD+211974 is our only option for telluric correction, while in the H band both HD64586 and BD+211974 were available. When applied to the H band science data, we found that the latter provided a slightly cleaner correction and was thus adopted in our final reduction. We verified the DRP wavelength solution by comparing a sky spectrum to a database of OH lines and found it to be good to within $\sim 10 \text{ \AA}$, which is more than sufficient for our purposes.

The resultant H and K spectra for the A and BC components, in units of relative F_λ are shown in figure 4.4. Relative scaling of the A and BC contributions was achieved using our resolved NIRC2 photometry, while scaling between H and K bands was determined using our IRTF spectrum of the unresolved 2M0838+15 system. The final spectra are sampled with two bins per resolution element at a native resolution of $R \sim 3800$, but have been binned (using an error-weighted mean) by a factor of 7 to increase the signal to noise. The K band spectrum of component A has a very low signal to noise and we were unable to extract a clean spectrum free of systematic wiggles. Thus we only show a rough SED for this component, in $0.03 \mu\text{m}$ bins. For reference we have overplotted the unresolved IRTF spectrum, and find it is reasonably well reproduced by the A+BC OSIRIS spectra. Given the near equal luminosity and colors of the BC components, this result confirms that all 3 constituents of the 2M0838+15 system are T-dwarfs.

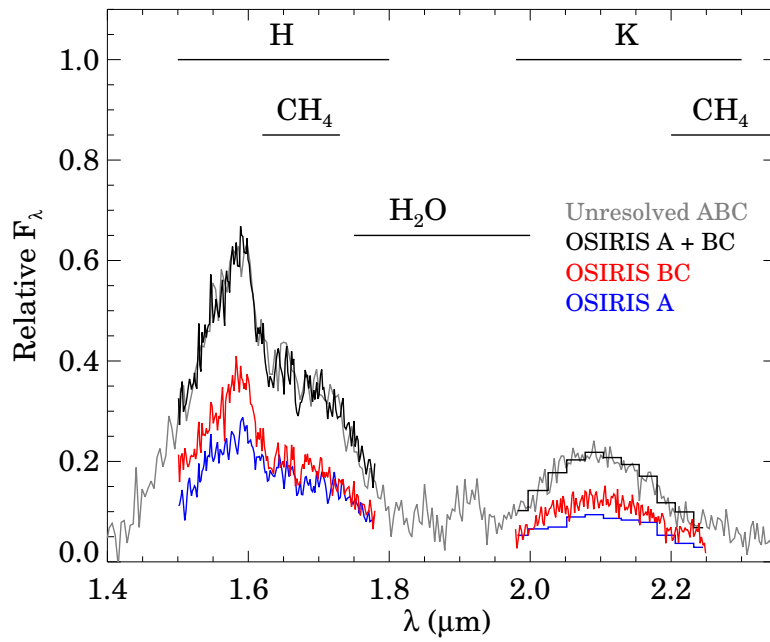


Figure 4.4: Resolved H and K_s spectra of the A (blue line) and BC (red line) components obtained using the OSIRIS spectrograph on the Keck II telescope. The sum of the A and BC contributions is plotted as a black line. The unresolved SpeX spectrum is shown for reference in grey and was used to scale the relative H and K_s contributions.

4.4 2M0838+15 ABC: Discovery of a Visual Triple T-Dwarf System

4.4.1 Analysis of the NIRC2 images: binary system properties and component fluxes

Binary parameters for the tight BC components were determined by fitting a double PSF model (using component A as a single PSF reference) to the data. Our model consisted of 9 parameters: two specifying the pixel position of component B relative to component A, x_B and y_B ; two specifying the angular separation and position angle of component C from component B, ρ_{BC} and θ_{BC} ; two specifying the fluxes of the B and C components with respect to component A, F_B/F_A and F_C/F_A ; and three parameters defining a plane $c_0 + c_1x + c_2y$ to account for a sloping background due to the tail of component A. Fitting was performed in a 27 pixel box centered on components BC. Given a set of 9 model parameters, scaled and shifted versions of component A were interpolated onto the data grid using IDL's cubic interpolation routine (which approximates interpolation with a sinc function), and then added to the background sloping plane. We adopted the NIRC2 plate scale of $0.009963''\text{pix}^{-1}$ and 0.13 deg offset in position angle found by Ghez et al. (2008) in order to convert pixel coordinates to angular separations and position angles. The images were not corrected for distortion before fitting. Based on distortion corrections provided by (Yelda et al. 2010) the differential distortion at distances similar to the BC component separation is ~ 0.2 mas, and across our entire fitting box is < 1 mas.

MCMC Parameter Estimation

Bayesian parameter estimation for our model was accomplished using a Markov Chain Monte Carlo (MCMC) integrator (e.g., Lewis & Bridle 2002). A Markov Chain provides

an efficient way of exploring a multidimensional parameter space, with the desirable property of returning samples that approximate the true posterior distribution of each parameter, marginalized over all other parameters. We used a Metropolis-Hastings algorithm (Metropolis et al. 1953; Hastings 1970) which takes steps through the model parameter space, Θ , drawn from some “proposal” distribution, wherein any proposed step $\Theta_k \rightarrow \Theta'_{k+1}$ is accepted or rejected (with the current parameters retained) based on the relative probabilities of the current and proposed parameters. This ratio can be inferred from Bayes law as:

$$\frac{P(\Theta'_{k+1}|\text{data})}{P(\Theta_k|\text{data})} = \frac{P(\text{data}|\Theta'_{k+1})P(\Theta'_{k+1})}{P(\text{data}|\Theta_k)P(\Theta_k)} \quad (4.1)$$

where $P(\text{data}|\Theta)$ is the likelihood function and $P(\Theta)$ is our prior distribution for parameters Θ . If the above ratio is greater than a random number generated from a uniform distribution on the interval $[0,1]$ then the step is accepted, otherwise it is rejected and the original parameters retained. Thus steps that improve the fit are accepted 100% of the time, while steps resulting in a poorer fit are accepted some of the time, preventing the chain from becoming stuck in a local minimum. Each proposed step was drawn from a multivariate Gaussian proposal distribution with covariance approximating that of the posterior distribution we wished to sample. The desired covariance of the proposal distribution was determined empirically from a short “test” run containing $n/10$ steps or samples, before starting a longer integration with the full n steps.

Treating each pixel in our fitting box as an independent measurement with Gaussian errors the likelihood function is given by

$$P(\text{data}|\Theta_k) \propto \prod_{i=0}^N \exp\left(-\frac{[N_i - M_i(\Theta_k)]^2}{2\sigma_i^2}\right) = e^{-\chi_k^2/2} \quad (4.2)$$

where N_i and M_i are the actual and modeled counts in pixel i . The error contribution to each bin was determined to be $\sigma_i = \sqrt{\sigma_b^2 + N_i/G}$, where σ_b is the “background”

standard deviation of the reduced and sky subtracted image (i.e. in a region without an astronomical source). The term $\sqrt{N_i/G}$ is the poisson noise from astronomical sources, where N_i is the number of counts (ADU) in bin i of the sky subtracted image and $G = 4e^- \text{ADU}^{-1}$ is the detector gain. The σ_i were scaled by a constant factor, a , in order to achieve a reduced $\chi^2 \approx 1$ between the best fitting model and data. Rather than fixing a , we include it as a model parameter, where it is naturally marginalized over by the MCMC integrator. The inclusion of a as a parameter yields a modified likelihood function given by¹:

$$P(\text{data}|\Theta_k) \propto \frac{1}{a_k^N} e^{-\chi_k^2/2a_k^2} \quad (4.3)$$

We have adopted uniform priors for all model parameters ($P(\Theta) \propto 1$), but note that our results are unchanged by adopting a Jeffreys prior of $P(\Theta) \propto 1/\Theta$ for scale parameters a , F_B/F_A , F_C/F_A , c_1 and c_2 . We found good convergence of the MCMC chains—indicated by the repeatability of our results for different choices of starting parameters—for runs with at least $n = 10^5$ steps. The results presented here use $n = 10^6$ steps, where the first 10% of points have been discarded as a burn-in period.

MCMC Results

MCMC fitting of the BC components was performed for each individual exposure taken in the J , H and K_s bands. An example of the reference PSF (component A), data (components BC), best-fitting model, and residuals for a single image is shown in figure 4.5. In all cases subtraction of the best fitting model from the data leaves no significant residuals above the noise level. An example of probability distributions of model parameters obtained from our MCMC is shown in figure 4.6. For each

¹In practice we compute the natural *logarithm* of the likelihood function in order to avoid working with very large numbers, before finally exponentiating the difference between two log-likelihoods in the application of equation 4.1.

image analyzed most probable values for parameters ρ_{BC} , θ_{BC} , F_B/F_A , and F_C/F_A , and corresponding 68% and 95% credible are given in table 4.4.1.

Parameters ρ_{BC} and θ_{BC} obtained in all three bandpasses agree, with the exception of two *J* band images where the BC components are not well resolved ($\rho_{BC} < 0.5$ FWHM). The image-to-image RMS deviations of parameters sometimes exceed the width of the 68% credible intervals derived by up to a factor of two. This scatter reflects, in part, uncharacterized systematic differences between images not accounted for in our MCMC analysis. We obtain final estimates of parameters by averaging the results found for individual images, and choose to adopt the RMS of all measurements as a realistic estimate of random and systematic uncertainties (rather than dividing the RMS by \sqrt{N} , which assumes noise is random and gaussian).

Averaging the results from all images (excluding the two *J* band images where $\rho_{BC} < 0.5$ FWHM) we find a binary separation of $\rho_{BC} = 50.0 \pm 0.7$ mas and a position angle of $\theta_{BC} = -7^\circ \pm 2^\circ$, with quoted uncertainties corresponding to the standard deviation of the 11 measurements. For the A(BC) system parameters we determined the average *x*- and *y*-pixel offsets between component A and the midpoint of the BC system in each image, corrected for distortion using the pixel offsets provided by Yelda et al. (2010), and then multiplied by the plate scale. Averaging results from all images we find a separation and position angle of $\rho_{A(BC)} = 549 \pm 1$ mas and $\theta_{A(BC)} = 18.8^\circ \pm 0.1^\circ$. Relative fluxes of the A, B, and C components were determined in a similar fashion and then converted to relative magnitudes. The resultant system and component properties are provided in tables 4.4 and 4.5 respectively.

4.4.2 Common Proper Motion

On 2010 March 22 followup images of the 2M0838+15 system were obtained in the *H* and *CH₄s* (methane) filters using the NIRC2 narrow camera. Observing conditions were partially cloudy, the image FWHM was large (0.12''), and the BC components

Table 4.3. MCMC PSF Fitting Parameters

Filter	No.	FWHM (mas)	Strehl	Sep (mas)			PA (deg)			F_B/F_A			F_C/F_A		
				ML	68% CI	95% CI	ML	68% CI	95% CI	ML	68% CI	95% CI	ML	68% CI	95% CI
<i>H</i>	1	97.9	0.096	49.3	[48.7,49.8]	[48.2,50.4]	-10.37	[-9.5,-11.2]	[-8.6,-11.2]	0.729	[0.702, 0.759]	[0.702, 0.759]	0.656	[0.641,0.669]	[0.626,0.683]
<i>H</i>	2	86.3	0.129	50.5	[50.1,50.8]	[49.7,51.2]	-5.37	[-4.8,-6.2]	[-4.1,-7.0]	0.722	[0.704, 0.741]	[0.704, 0.741]	0.654	[0.645,0.663]	[0.635,0.673]
<i>H</i>	3	79.5	0.123	50.1	[49.8,50.4]	[49.5,50.7]	-6.77	[-6.5,-7.6]	[-6.0,-8.1]	0.729	[0.714, 0.744]	[0.714, 0.744]	0.663	[0.655, 0.67]	[0.647,0.677]
<i>H</i>	4	66.6	0.172	50.1	[49.8,50.4]	[49.5,50.7]	-6.77	[-6.3,-7.5]	[-5.7,-8.1]	0.73	[0.716, 0.745]	[0.716, 0.745]	0.647	[0.641,0.655]	[0.633,0.662]
<i>H</i>	5	72.8	0.146	50.2	[49.7,50.7]	[49.2,51.2]	-7.07	[-6.2,-8.1]	[-5.3,-9.1]	0.733	[0.721, 0.744]	[0.709, 0.755]	0.627	[0.616,0.638]	[0.605, 0.65]
<i>H</i>	6	94.6	0.095	50.3	[49.6,50.8]	[49.1,51.4]	-7.97	[-7.1,-9.2]	[-5.8,-10.3]	0.744	[0.729, 0.758]	[0.714, 0.773]	0.663	[0.648,0.677]	[0.634,0.693]
<i>K_s</i>	1	89.3	0.213	49.3	[48.5,50.0]	[47.6,50.8]	-8.57	[-7.3,-9.9]	[-5.9,-11.2]	0.705	[0.689, 0.721]	[0.673, 0.737]	0.624	[0.608, 0.64]	[0.591,0.657]
<i>K_s</i>	2	84.9	0.245	50.1	[50.2,51.7]	[49.4,52.5]	-3.87	[-2.6,-5.2]	[-1.2,-6.5]	0.729	[0.714, 0.745]	[0.698, 0.760]	0.577	[0.562,0.592]	[0.547,0.607]
<i>K_s</i>	3	73.7	0.302	51.0	[49.6,50.7]	[49.1,51.2]	-8.17	[-7.4,-9.0]	[-6.7,-9.9]	0.733	[0.722, 0.745]	[0.709, 0.756]	0.598	[0.586,0.609]	[0.575,0.621]
<i>K_s</i>	4	77.0	0.253	49.8	[50.4,51.7]	[49.7,52.3]	-6.57	[-5.3,-7.9]	[-3.7,-9.2]	0.742	[0.727, 0.757]	[0.712, 0.772]	0.592	[0.576,0.606]	[0.561,0.622]
<i>J</i>	1	112	0.032	48.2	[47.5,48.8]	[46.9,49.5]	-11.7	[-10.6,-12.9]	[-9.4,-14.1]	0.637	[0.618, 0.653]	[0.597,0.669]	0.715	[0.697,0.734]	[0.680,0.756]
<i>J</i>	1	81.1	0.061	49.8	[49.3,50.2]	[48.9,50.6]	-5.07	[-4.5,-5.9]	[-3.9,-7.0]	0.638	[0.628, 0.647]	[0.681,0.658]	0.714	[0.704,0.732]	[0.694,0.733]
<i>J</i>	1	109	0.041	49.0	[48.5,49.7]	[47.8,50.2]	-9.9	[-8.9,-11.0]	[-7.8,-12.2]	0.651	[0.637, 0.665]	[0.623,0.679]	0.721	[0.708,0.735]	[0.694,0.750]

Table 4.4. 2M0838+15 ABC System Properties

Parameter	Value	Reference
Identifier	J08381155+1511155	2
α (J2000)	08 ^h 38 ^m 11 ^s .55	2
δ (J2000)	+15 ^d 11'15".5	2
$\mu_\alpha \cos \delta$ (")	-0.121 \pm 0.031	3
μ_δ (")	-0.032 \pm 0.051	3
J	16.65 \pm 0.16	2
H	16.21 \pm 0.17	2
K _s ^d	16.20 \pm 0.20	1
J-K _s ^d	0.45 \pm 0.07	1
J-H ^d	0.51 \pm 0.07	1
NIR SpT ^b	T3.5	1
d (pc)	49 \pm 12	1
ρ_{BC} (mas)	50.0 \pm 0.7	1
θ_{BC} (deg)	-7 \pm 2	1
$\rho_{A(BC)}$ (mas)	548.6 \pm 1.2	1
$\theta_{A(BC)}$ (deg)	18.8 \pm 0.1	1
q _{AB} ^e	0.89 – 0.92	1
q _{(BC)A} ^e	0.56-0.57	1

^bUnresolved spectral type

^cSpectroscopic parallax

^dSynthetic 2MASS photometry from SpeX spectrum

^eRange or value provided spans values inferred for 0.3-3Gyr

References. — (1) This work; (2)2MASS Point Source Catalog (Skrutskie et al. 2006); (3)(Aberasturi et al. 2011)

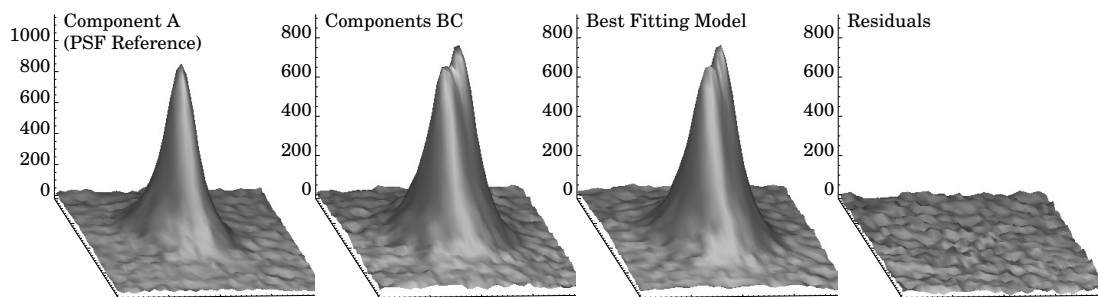


Figure 4.5: A series of 41×41 pixel surface plots demonstrating our PSF fitting of the 2M0838+15 BC system. An example fitting our double-PSF model (using component A as a PSF reference) to the tight BC system. From left to right: the “model” PSF (component A); the “data” (the BC components); the most probable double-PSF model found from our MCMC (a superposition of shifted and scaled versions of component A); and residuals between the data and model.

Table 4.5. 2M0838+15 ABC Component Properties

Parameter	A	B	C
NIR SpT	T3 \pm 0.5	T3 \pm 0.5	T4.5 \pm 0.5
J	17.57 \pm 0.16	18.01 \pm 0.16	17.95 \pm 0.16
H	17.10 \pm 0.17	17.43 \pm 0.18	17.78 \pm 0.18
K _s	17.11 \pm 0.28	17.46 \pm 0.20	17.67 \pm 0.20
J _{MKO}	17.31 \pm 0.16	17.78 \pm 0.16	17.65 \pm 0.16
ΔJ_{MKO}	...	0.47 \pm 0.04	0.38 \pm 0.04
ΔH	...	0.33 \pm 0.03	0.68 \pm 0.05
ΔK_s^a	...	0.35 \pm 0.02	0.56 \pm 0.04
M (3 Gyr, M_\odot)	0.060 \pm 0.009	0.054 \pm 0.008	0.050 \pm 0.008
M (300 Myr, M_\odot)	0.020 \pm 0.005	0.018 \pm 0.005	0.016 \pm 0.004

^aDifferential magnitude with respect to component A

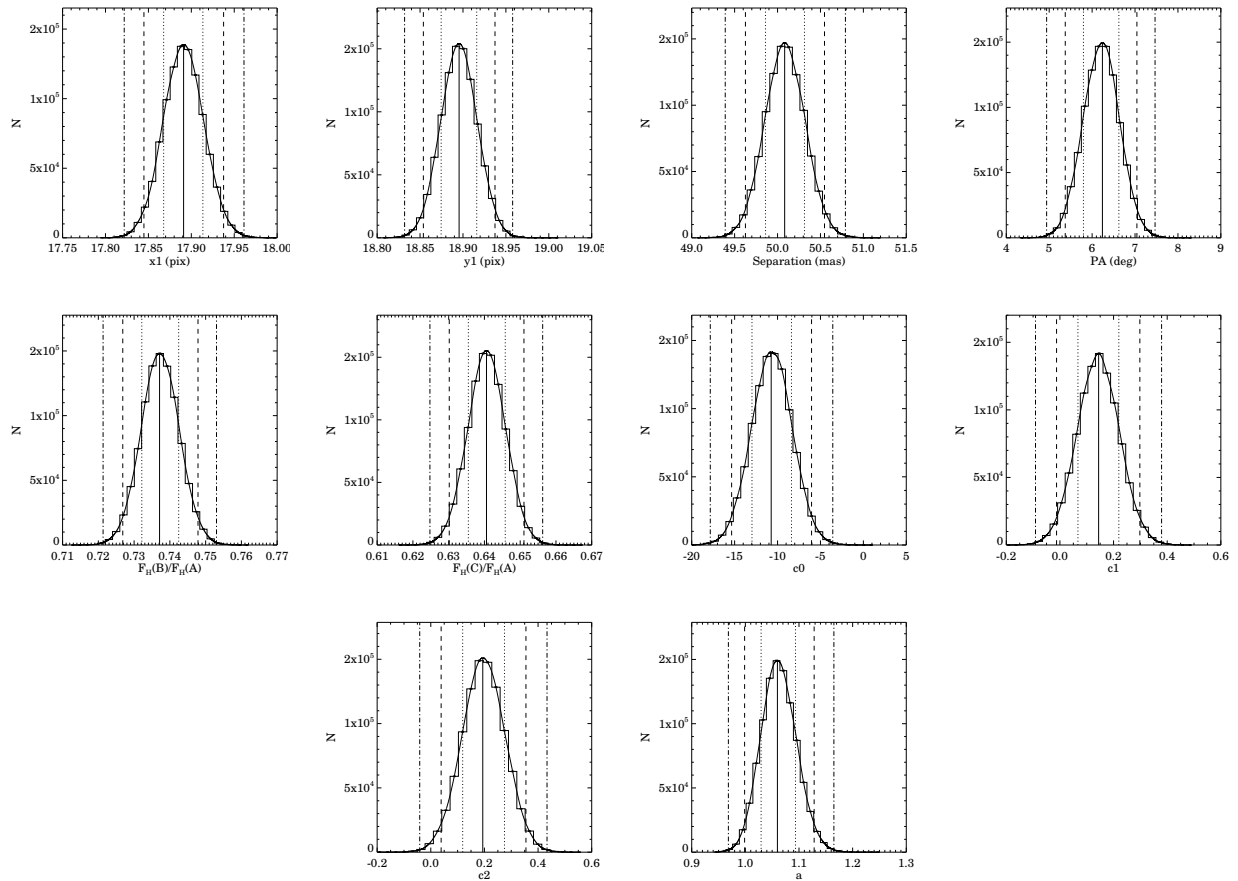


Figure 4.6: An example of parameter distributions returned by our MCMC PSF fitting of the BC components. The model and parameters used are described in the text. The distributions are shown as binned histograms, with a smooth cubic spline interpolation over plotted. Solid vertical lines indicate the most probable parameter values, while dotted, dashed, and dot-dashed lines indicate 68.2%, 95.4%, and 99.7% credible intervals respectively.

were not resolved. From fitting gaussian PSFs to these data, relative positions and fluxes were determined for the A(BC) components. We found the $(CH_4s - H)$ color of components A and BC to be indistinguishable within ± 0.05 mag (with uncertainties inferred from 6 and 5 dithered images in the CH_4s and H bands respectively), implying that the A and BC components have identical spectral types within ± 1 subtypes according to the spectral type versus $(CH_4s - H)$ relationship provided by Liu et al. (2008). This provided strong initial confirmation that the A(BC) components were both early-mid T-dwarfs.

The 73 day separation between the first and second epoch NIRC2 images allowed us to confirm the common proper motion of the A(BC) components. Based on 2MASS, SDSS and WISE epochs Aberasturi et al. (2011) determined a proper motion of $\mu = 0.13 \pm 0.06 \text{ mas yr}^{-1}$ for the unresolved 2M0838+15 system (see table 4.4), which would amount to a linear motion of $25 \pm 12 \text{ mas}$ between observations. We find the separation of the A(BC) components remains unchanged between 2010 Jan 08 ($548.6 \pm 1.2 \text{ mas}$) and 2010 March 22 ($549.0 \pm 1.6 \text{ mas}$) within a combined 2 mas uncertainty. This allows us to constrain the relative motions of the A(BC) components to within 10 mas yr^{-1} , or a tenth of the system common proper motion. Given their similar spectral types, proximity on the sky and shared proper motions within 10 mas yr^{-1} , the 2M0838+15 ABC components are almost certainly physically associated.

4.4.3 System and Component Properties Inferred from Empirical Trends and Evolutionary Models

Magnitudes and Colors

We used relative fluxes measured from our MCMC fitting, combined with 2MASS magnitudes to determine the individual magnitudes of the components. Since the

system is not detected in the 2MASS K_s band we derived a 2MASS K_s magnitude by computing a synthetic $J - K_s$ color of 0.45 ± 0.07 from the SpeX spectrum (e.g. Radigan et al. 2012), which implies a $K_s = 16.20 \pm 0.20$. The quoted uncertainty takes into account the relative component fluxes derived in section 4.4.1, the photometric error reported in the 2MASS catalog, and uncertainties in our synthetic SpeX photometry, propagating all errors in the standard way (using a linear approximation about mean values), and adding contributions from various sources in quadrature. Individual magnitudes and colors of the components are given in table 4.5.

Since we have determined relative component fluxes and magnitudes more precisely than system magnitudes reported in 2MASS, we include values and uncertainties for the differential magnitudes between components, ΔJ , ΔH , and ΔK_s in table 4.5.

Spectral Types

We determined spectral types for the A, B and C components using the resolved NIRC2 photometry and spectral templates of other field brown dwarfs from the SpeX Prism Library² to decompose our unresolved 2M0838+15 SpeX spectrum into its individual ABC components, described in detail below. We first decomposed the unresolved system into A and BC components, and then decomposed the best matching BC template into individual B and C components.

To perform the decomposition, we first identified all templates with spectral types of L0 in the SpeX prism library sharing the same apertural resolution ($R \sim 120$) as our 2M0838+15 ABC spectrum. Since the relative color between components is much better constrained than the system color we first identified all templates sharing the same $J - K_s$ color as component BC within 1σ uncertainties. We then looped over each BC-template, and identified templates for component A falling within the observed $\Delta(J - K_s) \pm \sigma_{\Delta(J - K_s)}$ and $\Delta(J - H) \pm \sigma_{\Delta(J - H)}$ between BC and A components. The

²Maintained by A. J. Burgasser, and located at <http://pono.ucsd.edu/~adam/browndwarfs/spexprism/library.html>

prospective BC and A templates were scaled to match the observed H -band fluxes of the BC and A components and added together to create a composite template. The composite templates were then interpolated onto the data and scaled in order to minimize $\chi^2 = \sum_i [(data_i - template_i)/error_i]^2$. We scaled the error contribution in order to achieve $\chi^2/dof = 1$ for the best fitting model. Results are shown in figure 4.7. Acceptable matches for the A(BC) components range from T3-T3.5 with the optimal match for component A being the T3 dwarf SDSS J120602.51+281328.7 (Chiu et al. 2006), and the optimal match for component B being the T3.5 dwarf SDSSp J175032.96+175903.9 (Geballe et al. 2002; Burgasser et al. 2006a). We therefore assign spectral types of $T3 \pm 0.5$ and $T3.5 \pm 0.5$ to the A and BC components respectively.

The BC components were decomposed in a similar manner starting from the optimal BC template spectrum of SDSSp J175032.96+175903.9. We found best fitting templates with T3 (SDSS J120602.51+281328.7; Chiu et al. 2006) and T4.5 (2MASS J12154432–3420591 Looper et al. 2007) spectral types for the B and C components respectively, and the range of acceptable matches is well described by assigning spectral types of $T3_{-1}^{+0.5}$ and $T4.5 \pm 0.5$ to the B and C components. The results of our spectral decomposition are shown in figure 4.7, and provide a reasonable match to the resolved OSIRIS A and BC spectra.

The similar spectral types found for the A and BC components are consistent with $(CH_4s - H)$ colors found in section 4.3.2, which indicate spectral types within ± 1 . In addition, the determined spectral types agree well with the combined light spectral type of T3.5. Due to the low SNR of the OSIRIS spectra, as well as sub-ideal sky subtraction and telluric correction we have not attempted to obtain spectral types by direct fits to these spectra, or from narrow band indices. In the future, higher SNR spectroscopy, possibly resolving all three components should be attempted.

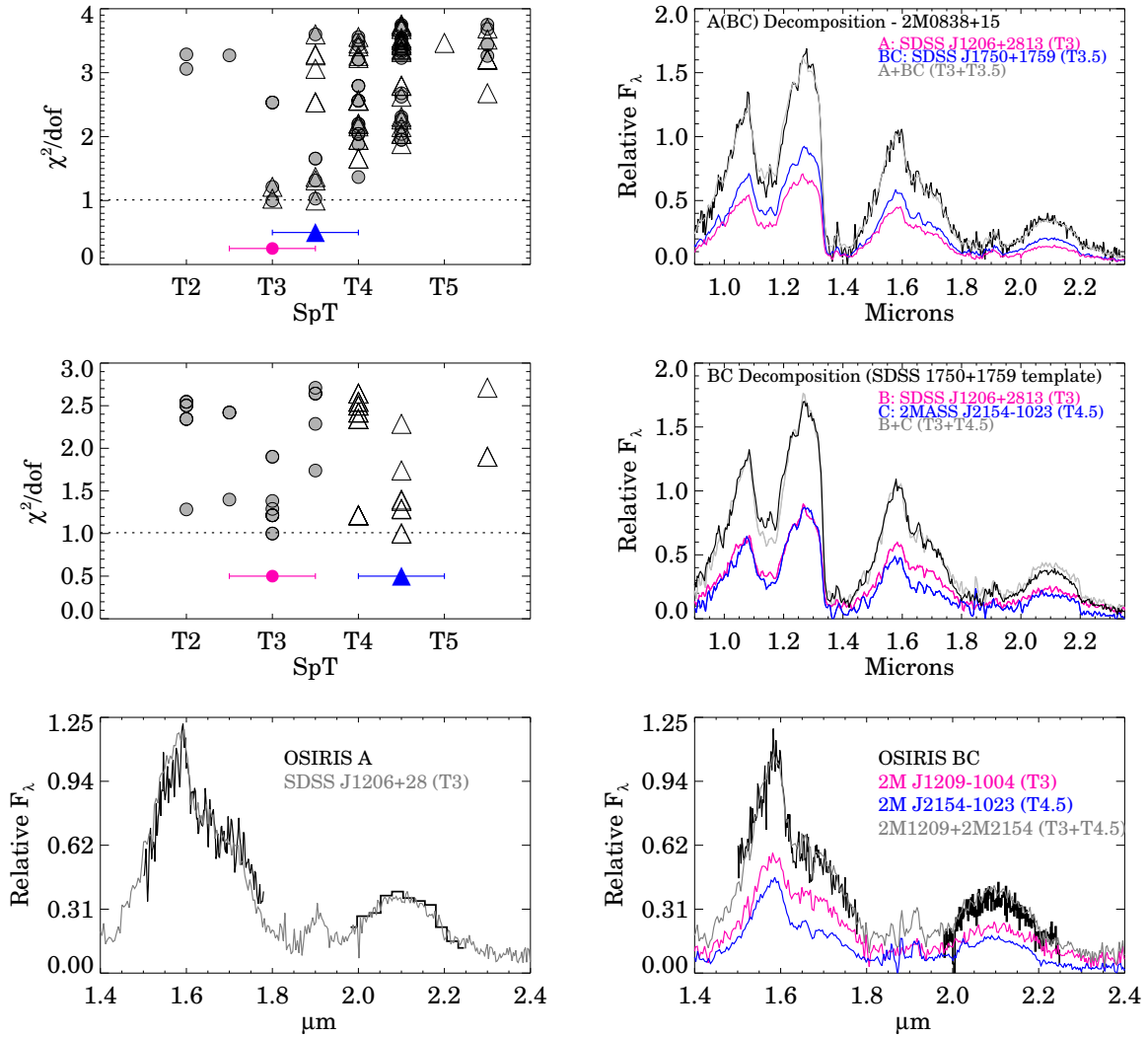


Figure 4.7: Top panel: Spectral typing of 2M0838+15A via least-squares fitting of spectral templates from the SpeX prism library. Scaled χ^2 values for each spectral fit as a function of spectral type are shown in the left panel, while the corresponding best-fitting templates ($\chi^2/\chi^2_{min} < 2$) are overplotted in grey. Although the low SNR K_s data for 2M0838+15 A is plotted for reference, it was not used in the fit. Middle panel: spectral decomposition of the BC components using composite spectral templates from the SpeX prism library as described in section 4.4.3. The reduced χ^2 values for each spectral fit as a function of B (filled circle) and C (open triangle) spectral types are shown in the left panel, while the best-fitting composite templates ($\chi^2/\chi^2_{min} < 1.5$) are overplotted in grey, with the individual B and C contributions shown in cyan and pink respectively. Bottom panel: Same as the middle panel but with relative spectral types shown on the left, and the more poorly fitting templates ($\chi^2/\chi^2_{min} > 1.5$) shown for comparison.

Absolute Magnitudes and Distance

Using the 2MASS M_{K_s} vs SpT relation of Dupuy & Liu (2012) and magnitudes and SpTs derived above for the ABC components, we calculated an absolute magnitude and distance modulus for the individual A, B and C components. We determined a mean distance modulus of 3.5 ± 0.5 , which implies a distance of 49 ± 12 pc. Distances inferred for the individual A, B and C components of 46, 54 and 47 pc agree within uncertainties, yet reflect the similar spectral types despite different brightnesses for the A and B components. Given uncertainties take into account uncertainties in the measured magnitudes and spectral types of the components, as well as intrinsic scatter of ~ 0.46 mag about the Dupuy et al. relationship.

At a distance of 49 pc and assuming the semi-major axes to be similar in length to their projections, the system would have physical separations of 2.45 ± 0.5 AU (BC) and 27 ± 5 AU (A[BC]) respectively.

Relative Masses, Effective Temperatures and Surface Gravities

Without an independent measurement of mass or age, evolutionary models are degenerate and prevent absolute physical properties from being inferred. However, assuming the components of the ABC system to be coeval we can infer relative properties for a reasonable range of ages. We estimated bolometric luminosities using the updated MKO-K band bolometric corrections provided by Liu et al. (2010), first converting 2MASS K_s magnitudes to MKO magnitudes using the the corrections as a function of spectral type provided by Stephens & Leggett (2004). The differences in bolometric corrections between components is small, with a maximum difference of 0.013 mag between components B and C. Thus relative bolometric luminosities inferred are dominated by the differences in K band magnitudes of the components rather than their bolometric corrections. This yielded bolometric luminosities of $\log L_A/L_\odot = -4.92 \pm 0.21$, $\Delta \log L_{B-A}/L_\odot = -0.15 \pm 0.03$, and $\Delta \log L_{C-A}/L_\odot =$

-0.23 ± 0.04 , where we have expressed the luminosities for the B and C components as differences relative to component A.

For a given system age these luminosity estimates can be converted to masses, effective temperatures, radii, and surface gravities via evolutionary models. We used the evolutionary models of Burrows et al. (1997) to infer masses, effective temperatures, and surface gravities at ages of 3 Gyr (typical for field brown dwarfs) and 300 Myr. For a 3 Gyr old system we find masses of 60, 54, and $50 \times 10^{-3} M_{\odot}$ with a systematic uncertainty of $\sim 15\%$ and relative uncertainties of $\sim 3\%$. For an age of 300 Myr we find masses of 20, 18 and $16 \times 10^{-3} M_{\odot}$ with a systematic uncertainty of $\sim 25\%$ and relative uncertainties of $\sim 5\%$. The largest source of uncertainty factoring into these calculations comes from the absolute magnitude determination.

In both cases the mass ratio of the BC components, q_{BC} is close to unity (0.92 for 3 Gyr and 0.89 for 300 Myr), which is typical for brown dwarf binaries which are found to have a mass ratio distribution peaking strongly at unity (e.g. Burgasser et al. 2007; Allen 2007). While the A(BC) mass ratio of ~ 0.57 would be atypically low compared to the majority of BD binaries, near-equal mass A, B, and C components for VLM triple systems are common (e.g Burgasser et al. 2012).

In order to estimate a range in surface gravities and temperatures spanned by the ABC components we have plotted inferred effective temperatures and surface gravities along a series of isochrones ranging from 300 Myr to 5 Gyr, shown in figure 4.8. For ages of 0.5-5 Gyr $d(\log g)/d(T_{\text{eff}})$ is approximately constant along isochrones, with the ABC components spanning a fairly narrow range in temperature (~ 150 K), and surface gravity (~ 0.1 dex) irrespective of age or mass.

Given the inferred system masses and a semi-major axis of 2.45 AU, the BC system would have a period ranging from ~ 12 yr (3 Gyr) to 21 yr (300 Myr). Thus a dynamical mass measurement of the BC components may be possible on a relatively short timescale, which should greatly constrain the system's position in figure 4.8.

In addition, efforts to obtain a parallax are ongoing, which will provide improved constraints on the system's absolute magnitude and bolometric luminosity.

4.5 Search for companions and sensitivity limits

Here we present our search for companions around the entire sample of 8 L/T transition objects observed with NIRC2 (section 4.5).

Each reduced image was carefully visually examined for companions. Only a single object, 2M0838+15, was resolved into a multiple system. Our sensitivity to companions was determined via simulations. For a given binary separation, ρ , and contrast, ΔK , we constructed 100 simulated binary pairs using a cutout of the observed target as a single PSF model, with randomized position angles. We then attempted to recover companions from the simulated images in the following way:

1. We iteratively measured the RMS background noise of the simulated image, σ .
2. We searched for point sources in the image using the IDL adapted version of the DAOPHOT `find` algorithm, setting a 5σ detection threshold.
3. If more than one source was detected by `find` we looped over each non-primary candidate source and applied additional criteria for a detection. Since the AO images have a noise profile that varies with radius from the central source, the background RMS noise was re-measured in an 0.9 FWHM wide annulus centered on the primary source and with a mid-radius corresponding to the distance to the candidate source. Sources with peak fluxes less than three times the noise within the annulus were discarded.
4. If only one source was initially detected, an additional search for close companions within a 1 FWHM radius from the central source was conducted. First,

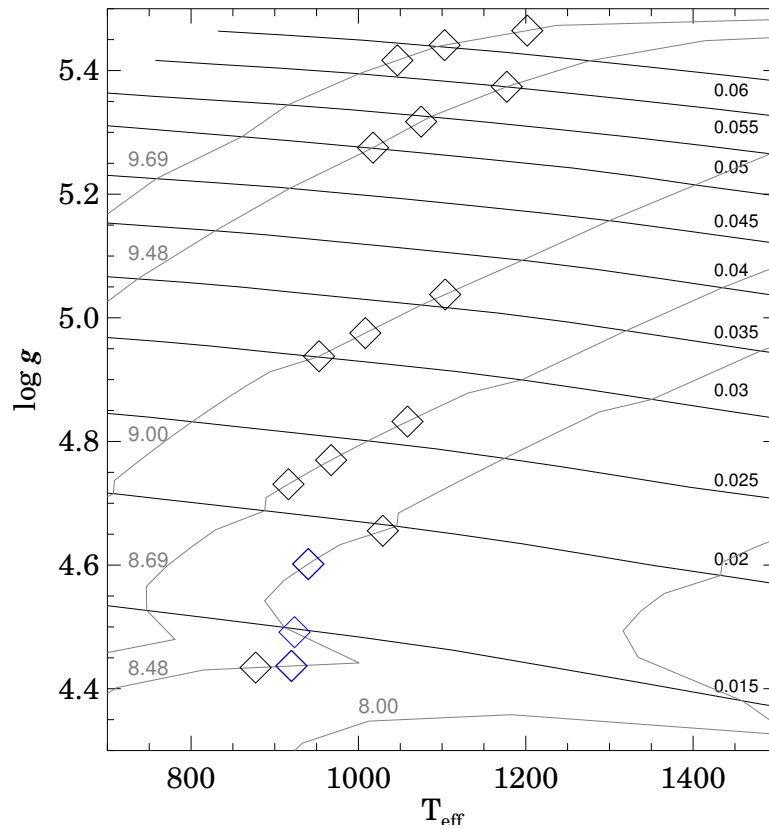


Figure 4.8: An example of the age-mass degeneracies typical for BD systems, with surface gravities and effective temperatures for the 2M0838+15 ABC components inferred using empirical trends and evolutionary models, are plotted (from left to right) along a series of isochrones ranging from 300 Myr to 5 Gyr. Isochrones (grey lines labeled with $\log t[\text{yr}]$) and lines of constant mass (black lines labeled in units of M_{\odot}) using the evolutionary models of Burrows et al. (1997) are overplotted. Non-singular solutions for component B are shown in blue. A dynamical mass for the BC system will constrain the system age, temperatures and surface gravities, and allow a direct comparison to model isochrones.

low frequency features were subtracted from the simulated image by subtracting a median-filtered image (wherein each pixel is replaced by the median of surrounding pixels in a box size of 1×1 FWHM rounded up to the nearest odd-integer number of pixels). We then repeated our search for additional sources using `find`. Potential detections within 1 FWHM of the primary source were further vetted by requiring them to have peak fluxes >0.15 times that of the primary (corresponding to roughly three times the largest residuals found when subtracting a gaussian PSF from our data) and that they are separated by more than 0.5 FWHM from the primary source.

The above criteria were fine-tuned and verified by visual inspection and consistently picked out only bonafide companions in our simulated datasets, while rejecting other point-source-like structures in the AO PSFs. Applied to the data, the above criteria successfully detects the close 2M0838+15BC pair in all our science images wherein $\rho_{BC} > 0.5$ FWHM, while assigning non-detections to the other sources in our sample. Our sensitivity to companions at a given separation is given by the recovery rate of simulated companions at a given separation, and is shown for each source in figure 4.9. We achieved the greatest sensitivity to close companions when using single science exposures with the narrowest FWHMs, while we were more sensitive to well-separated companions in the stacked science images. We therefore repeated our simulations for both individual and stacked images, retaining the highest companion recovery rate of the two cases.

Although varying from target to target we are sensitive to 95% of companions with $\Delta K < 1$ at innermost separations of 60-80 mas, and to companions with contrasts of $\Delta K < 3-4$ at separations $>100-200$ mas. The tight BC components of 2M0838+15 fall just inside this minimum separation where companions are routinely detectable. We easily resolve the BC pair due to the fact that the binary axis runs approximately perpendicular to the PSF elongation in the direction of the TT star. In other words

sensitivity is a function of position angle for elongated PSFs, and the 95% recovery rates reported reflect the least sensitive position angles.

4.5.1 The binary fraction of our sample

In our sample we resolved 1 of 8 targets into a multiple system (we do not count 2M0838+15 BC as an additional target). The probability of observing n multiples in our sample is given by the binomial distribution, $P(n|N = 8, \nu_{obs})$, where ν_{obs} is the observed binary frequency (uncorrected for observational biases), n is the number of binaries observed and N is the sample size. A Beta distribution for ν_{obs} is obtained by using Bayes Law to infer $P(\nu|n = 1, N = 8) \propto P(n = 1|N = 8, \nu_{obs})P(\nu_{obs})$, where we have assumed a flat (most ignorant) prior probability distribution of $P(\nu_{obs}) = 1$. From the posterior distribution we derive an observed multiple frequency of $12.5^{+13.4}_{-8.2}\%$ for our sample. The quoted uncertainties correspond to the 68% credible interval of the distribution of frequencies. For a non-symmetric distribution there are many ways to construct a credible interval about the maximum likelihood. Here we have constructed a “shortest” credible interval $[a, b]$, such that $P(a) = P(b)$, which is more informative than an equal-tail interval. Within the uncertainties, this result is consistent with those from other magnitude-limited studies which find uncorrected binary fractions of $\sim 17\text{-}20\%$ (e.g., Bouy et al. 2003; Gizis et al. 2003; Burgasser et al. 2003a; 2006a).

4.6 Binary statistics in the L/T transition

4.6.1 The L9-T4 binary frequency

In its broadest interpretation, the L/T transition may include $\sim L6\text{-}T5$ spectral types, over which a flattening in effective temperature occurs (e.g. Golimowski et al. 2004; Stephens et al. 2009). However, here we wish to focus more narrowly on L9-T4 spectral types, over which J-band brightening occurs. Since the J band represents a molecular

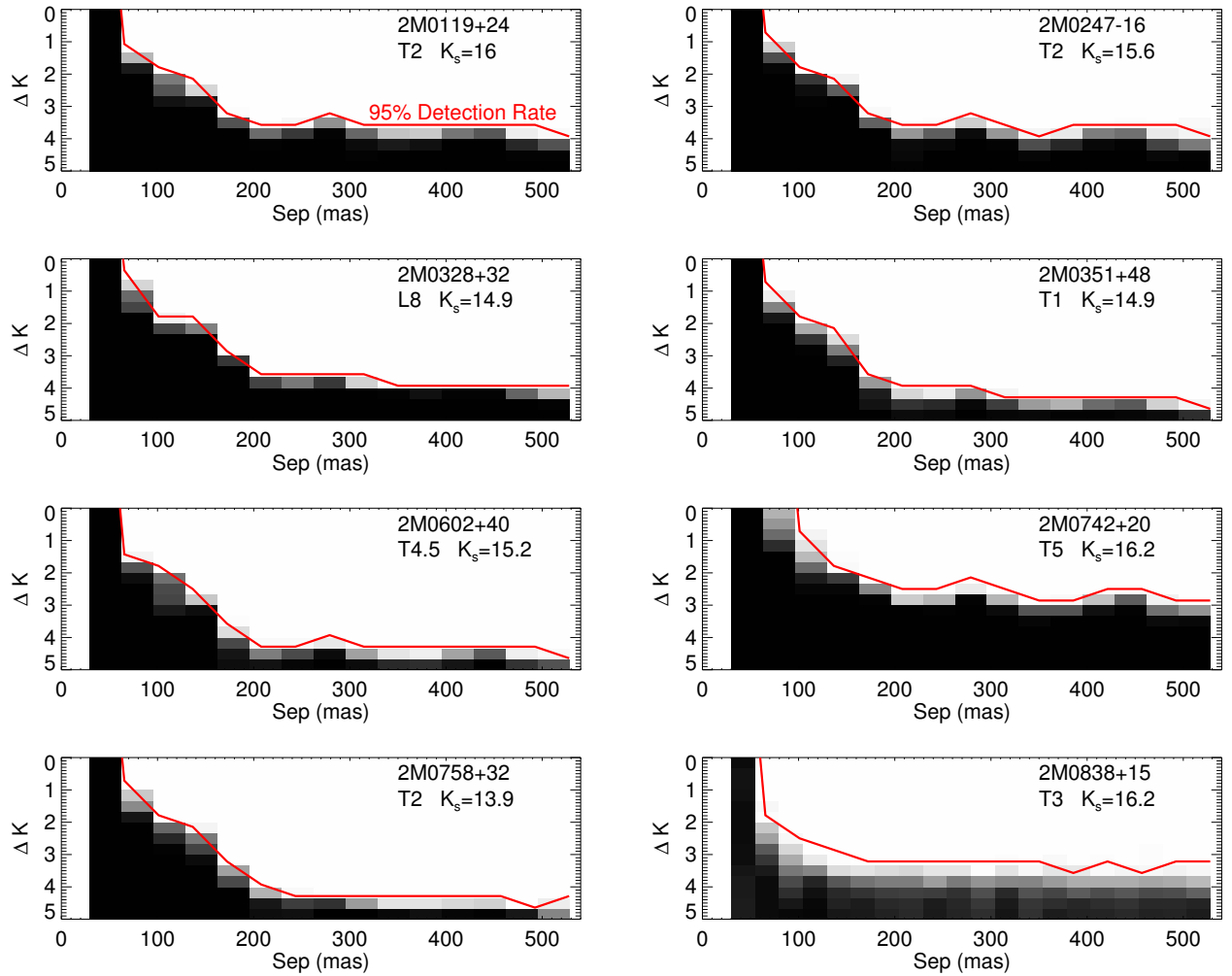


Figure 4.9: K -band detection limits as a function of binary separation and contrast, ΔK . Red lines indicate the 95% recovery rate of simulated companions. The shading depicts the recovery rate for any separation and contrast, linearly varying from a 0% percent (black) to 100% (white)

opacity window, the flux measured within it is particularly sensitive to condensate opacity. While a monotonic decrease in J band flux is observed for L0-L8 spectral types as well as for T5 spectral types onward, this trend is reversed over L8-T5 spectral types, and can be attributed to a decrease in condensate opacity over this range. Thus L9-T4 spectral types make up the evolutionary branch over which clouds are removed from the photosphere. We have chosen not to include the ends of this branch (L8 and T5 bins) so as not to contaminate the sample with objects of ambiguous membership. This region is also the sparsest region of the L/T transition, suggesting that brown dwarfs spend comparatively less time at these spectral types. Accordingly, this is precisely the regime where an overabundance of binaries is predicted (Burgasser 2007). Additionally, this is the spectral type range over which variability is expected due to heterogeneous cloud coverage (e.g. Burgasser et al. 2002; Radigan et al. 2012), and the level of binary contamination in this regime has important consequences for variability surveys (e.g. Clarke et al. 2008; Radigan et al. 2011).

Although small, our sample increases the number of objects observed with L9-T4 spectral types by 40%. If taken together with the L/T transition sample observed by Goldman et al. (2008), these more recent data nearly double the number of objects surveyed for multiplicity in this regime. Here we combine our data with the L/T transition survey of Goldman et al. (2008), T-dwarf surveys of Burgasser et al. (2003a; 2006a), and the combined L and T samples of Bouy et al. (2003) and Reid et al. (2006; 2008) to examine the binary frequency in the L/T transition.

The combined statistical sample

Although the surveys considered are a heterogeneous group, they are all sensitive to minimum angular separations of approximately $\gtrsim 0.05 - 0.07''$. In addition, ultra cool dwarf binaries tend to have flux ratios well above typical detection limits (except at small angular separations), implying that differing sensitivities to faint

companions among surveys does not strongly impact binary statistics (e.g. Burgasser et al. 2007; Allen 2007). To achieve consistency each target was cross-correlated with the DwarfArchives database of known L and T dwarfs to determine a homogeneous set of NIR spectral types and colors. Names, spectral types and $J - K_s$ colors of the combined sample are provided in table 4.6.

In total the combined sample consists of 19 objects including 2M0838+15 with NIR spectral types of L9-T4 (inclusive). However, as the only known higher order multiple in the sample, 2M0838+15 is significantly further away ($d \sim 50$ pc) than other objects of the sample ($d < 35$ pc) and likely biases the result. Rather than attempting a complete correction for higher order multiples we apply a 35 pc distance cut, which effectively removes 2M0838+15 from the targets considered, yielding a final sample size of 18.

Based on 4/18 detections in the L9-T4 sample, we computed $P(\nu_{obs}|n, N) \propto P(n|N, \nu_{obs})$ as in section 4.5.1, obtaining an observed binary fraction for the combined sample of $\nu_{obs} = 22^{+10}_{-8}\%$. This is on the high end, but comparable to other reported visual binary fractions for L and T dwarfs (subject to similar selection effects and observational constraints, and uncorrected for biases) previously discussed in section 4.5.1 (~ 17 -20%).

Table 4.6. The Composite L9-T4 Sample

2MASS ID	SpT ^a	J	$J - K_s$	$m - M$	d (pc)	θ (")	Δm	Ref ^b	Ref ^c
2MASS J01191207+2403317	T2	17.02 ± 0.18	1.00 ± 0.26	2.51 ± 0.50	31.8 ± 6.6^c	5	...
2MASS J01365662+0933473	T2.5	13.45 ± 0.03	0.89 ± 0.04	-1.07 ± 0.46	6.1 ± 1.3^c	4	...
2MASS J01514155+1244300	T1	16.57 ± 0.13	1.38 ± 0.23	1.92 ± 0.50	21.4 ± 1.5	2	2
2MASS J02474978-1631132	T2	17.19 ± 0.18	1.57 ± 0.27	2.11 ± 0.50	26.5 ± 5.5^c	5	...
2MASS J03284265+2302051	L9.5	16.69 ± 0.14	1.78 ± 0.18	1.97 ± 0.47	30.2 ± 3.8	1, 5	2
2MASS J03510423+4810477	T1	16.47 ± 0.13	1.47 ± 0.18	1.73 ± 0.48	22.2 ± 4.6^c	5	...
2MASS J04234858-0414035	T0	14.47 ± 0.03	1.54 ± 0.04	-0.12 ± 0.46	13.9 ± 0.2	0.164	F170M	2	3
2MASS J05185995-2828372	T1	15.98 ± 0.10	1.82 ± 0.12	0.90 ± 0.47	22.9 ± 0.4	0.051	F170M	2	3
2MASS J07584037+3247245	T2	14.95 ± 0.04	1.07 ± 0.07	0.38 ± 0.46	11.9 ± 2.5^c	5	...
2MASS J08371718-0000179	T1	17.10 ± 0.21	1.23 ± 0.30	2.61 ± 0.51	30 ± 12	2	2
2MASS J09083803+5032088	L9	14.55 ± 0.02	1.60 ± 0.04	0.10 ± 0.46	10.5 ± 2.2^c	6	...
2MASS J09201223+3517429	T0p	15.62 ± 0.06	1.65 ± 0.09	0.93 ± 0.46	29.1 ± 0.7	0.075	F814W	1	3
2MASS J10210969-0304197	T3	16.25 ± 0.09	1.13 ± 0.20	1.35 ± 0.49	33.4 ± 1.5	0.172	F170M	2	3
2MASS J12545393-0122474	T2	14.89 ± 0.04	1.05 ± 0.06	0.33 ± 0.46	11.8 ± 0.3	2	1
2MASS J14044941-3159329	T2.5	15.58 ± 0.06	1.04 ± 0.11	0.90 ± 0.47	23.8 ± 0.6	4	3

Table 4.6 (cont'd)

2MASS ID	SpT ^a	J	$J - K_s$	$m - M$	d (pc)	θ (")	Δm	Ref ^b	Ref ^c
2MASS J17503293+1759042	T3.5	16.34 ± 0.10	0.86 ± 0.21	1.54 ± 0.50	27.6 ± 3.5	2	2
2MASS J20474959-0718176	T0	16.95 ± 0.20	1.57 ± 0.28	2.33 ± 0.50	20.0 ± 3.2	4	4
2MASS J22541892+3123498	T4	15.26 ± 0.05	0.36 ± 0.15	0.80 ± 0.48	14.4 ± 3.0^c	2	...

^aUnresolved Spectral Type^bSurvey References^cParallax References. Distances without parallaxes are based on SpT vs absolute K_s magnitude relationship of Dupuy & Liu (2012).

Correcting for observational biases

In magnitude limited samples a Malmquist bias leads to binaries being sampled in a larger volume than singles. Here we follow the example of Burgasser et al. (2003a; 2006a) who provide an expression for the real binary frequency, ν , in terms of the observed frequency, ν_{obs} :

$$\nu = \frac{\nu_{obs}}{\alpha(1 - \nu_{obs}) + \nu_{obs}} \quad (4.4)$$

where α is the ratio of volume searched for binaries to that of the volume searched for single objects given by

$$\alpha = \frac{\int_0^1 (1 + \rho)^{3/2} f(\rho) d\rho}{\int_0^1 f(\rho) d\rho} \quad (4.5)$$

where $\rho = f_2/f_1$ is the flux ratio of components, $f(\rho)$ is the distribution of flux ratios. The limiting cases where $f(\rho)$ is flat and 100% peaked at unity yield values of $\alpha = 1.86$ and $\alpha = 2.82$ respectively, and typically an intermediate value is used. However, if we examine the distribution of flux ratios for all known ultracool binaries (see Appendix B) we find a broad distribution that peaks at $\sim 0.4 - 0.5$ with a negative skew, such that the mean flux ratio is slightly larger than this. Integrating over this distribution we obtain $\alpha = 1.87$, which is equivalent to the case where $f(\rho)$ is flat. As a check, the binaries in our sample have flux ratios (in their survey filter, see table 4.6) ranging from 0.39-0.46 which yield an average value of $(1 + \rho)^{3/2} = (d_{bin}/d_{single})^3$ of 1.7. As a compromise between the two values, we adopt a value of $\alpha = 1.8$ for our sample.

To correct for our greater sensitivity to binaries over single objects, we performed a change in variables from $\nu_{obs} \rightarrow \nu$:

$$P(\nu) = P(\nu_{obs}) \left| \frac{d\nu_{obs}}{d\nu} \right| \quad (4.6)$$

where a relationship between ν and ν_{obs} is given in equation 4.4.

From the resulting distribution we determined the most probable binary frequency and uncertainties corresponding to a 68% shortest credible interval (see figure 4.10). This yielded a resolved L9-T4 binary fraction of $14_{-5}^{+7}\%$ (at projected separations $\gtrsim 1 - 2.5$ AU). It is important to note that this is only the visual binary frequency for the stated detection limits and ignores the small-separation wing of the semi-major axis distribution. By some estimates spectroscopic binaries could be as numerous as resolved systems (Maxted & Jeffries 2005; Joergens 2008), increasing the total binary fraction by a factor of 2. However, if we consider only visual binaries there is another more subtle bias that arises due to counting remaining unresolved objects as singles in equation 4.4, which leads to a small underestimate of the resolved binary frequency (the search volume for single objects is over-corrected due to unresolved binary interlopers). The maximum effect of this bias can be determined by doubling the estimate for ν_{obs} in the denominator of equation 4.4. Doing so we find a binary fraction of 15%, which represents a negligible increase when compared to the larger counting errors from binomial statistics.

For comparison, the T-dwarf surveys of Burgasser et al. (2003a) and Burgasser et al. (2006a) found bias corrected binary fractions of $9_{-4}^{+15}\%$ and $12_{-4}^{+7}\%$ (but used a slightly larger value of $\alpha = 2.16$), while the late-M and L-dwarf surveys of Bouy et al. (2003) and Reid et al. (2008) found binary fractions of $\sim 10\%$ and $12_{-3}^{+5}\%$ respectively (the latter survey was volume-limited). While we find a slightly higher binary frequency from L9-T4 spectral types, it remains comparable to those reported by other surveys at the 1σ level.

It is nonetheless interesting to note that if we select the L9-T4 sample based on *primary* spectral types rather than unresolved system types the observed binary fraction drops to $2/16$ ($=12.5\%$), which translates into a bias-corrected frequency of $7_{-4}^{+6}\%$ or about half of the unresolved fraction (resolved spectral types of binaries for

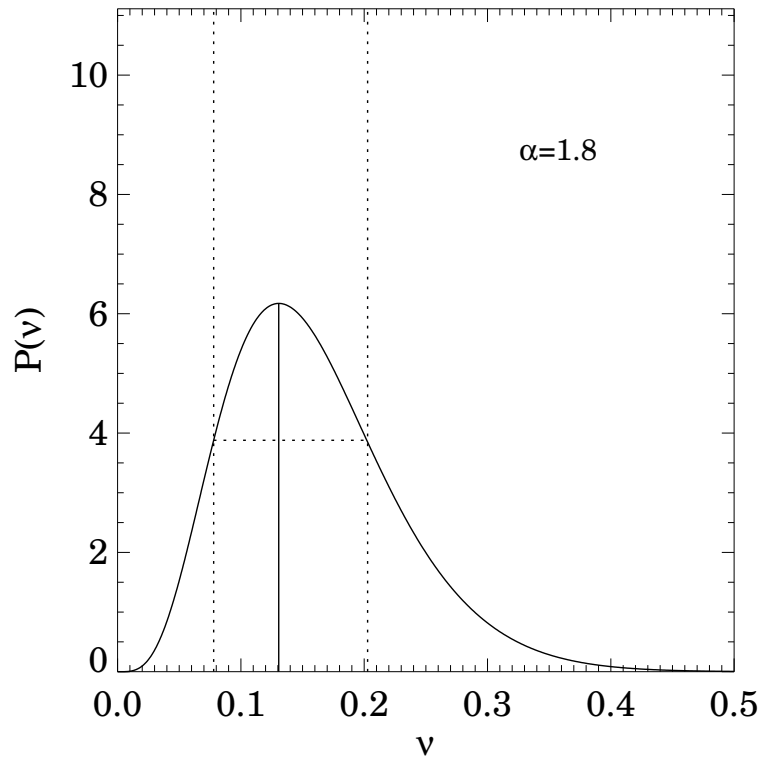


Figure 4.10: Probability distribution for the volume-bias corrected L9-T4 binary frequency at projected separations $\gtrsim 1 - 2.5$ AU. Dotted lines show the 68% credible region about the most probable value.

the surveys considered here are provided in table B.1). Thus even though we don't find a statistically significant increase in binary fraction for L9-T4 spectral types relative to other L and T dwarf samples, there is some evidence of a systematic increase in binary frequency between unresolved and primary spectral-type-selected samples by a factor of ~ 2 . This is consistent with the population synthesis of Burgasser (2007), which show that the binary frequency approximately doubles for unresolved L9-T4 dwarfs given a flat input distribution as a function of primary spectral type. In addition, we cannot rule out an L9-T4 binary frequency as high as 21% (the upper limit of our 68% credible interval), and it therefore remains possible that the unresolved binary frequency is much higher in the L/T transition. Clearly, a larger sample of L/T transition objects is needed to make progress.

4.7 Discussion and Conclusions

4.7.1 2M0838+15ABC: A benchmark triple of early T-dwarfs

We have presented resolved imaging and spectroscopy of the first triple T-dwarf system, 2M0838+15 ABC.

With a dynamical mass measurement possible for the BC components, 2M0838+15 ABC will serve as a benchmark system in the poorly contained L/T transition regime. Even without a dynamical mass, this system represents the largest homogeneous sample of early T-dwarfs to date, whose relative colors and spectral types can be used to test evolutionary models along a single isochrone.

The relative positions of the A, B and C components on a color-magnitude diagram are shown in figure 4.12. We find that component A, which is brightest in all three bandpasses, has a $J - K_s$ color intermediate to the fainter B and C components. This could reflect a sensitive dependence of the L/T transition effective temperature on surface gravity, with the slightly higher mass/gravity component A evolving across the transition at a systematically higher temperature and luminosity than the BC components. However, from figure 4.8 we find that this difference in surface gravity can be no more than ~ 0.1 dex for ages greater 300 Myr, which might suggest a different explanation.

Alternatively, different condensate cloud properties could explain differences in brightness between components A and B without the need to invoke differences in surface gravity. Observations of variable brown dwarfs have demonstrated that changes in cloud coverage at constant effective temperature, surface gravity, and empirical spectral type can lead to brightness variations as high as $\sim 26\%$ in the J band and $\sim 15\%$ in the K_s band (Artigau et al. 2009; Radigan et al. 2012). Thus rather than being more massive, it is possible that component A simply has thinner clouds and/or lower fractional coverage than components B and C.

It is generally true that BD binaries tend to have similar relative $J - K_s$ colors, with both components appearing red, average, or blue for their respective spectral types (figure 4.11). This color correlation is discussed by Artigau et al. (2011) in relation to an oddball T2.5/T4 binary, SIMP 1619+0313, whose components have surprisingly divergent colors, with the early type component appearing very blue, and the later type component appearing unusually red. Artigau et al. (2011) found that differing cloud coverage (93% for the later type component and 50% for the earlier type) provided a consistent explanation for this flux reversal at both far red and NIR wavelengths. Thus SIMP 1619+0313 AB and 2M0838+15 AB provide examples of coeval components within the L/T transition wherein the secondary appears fainter and redder. This is in contrast to typical L/T binaries wherein $J - K_s$ colors become progressively bluer with later spectral types, as is the case for 2M0838+15 BC. While differing degrees of dust cloud coverage can explain these reversals from the normal trend, it is unclear what leads to such different cloud properties in a minority of cases.

Assuming for now that 2M0838+15 does not vary in brightness, we explore the possibility that systematic differences in cloud properties between the A and BC components could be due to viewing geometry. For instance, if the tight BC components have spin axes that are aligned with each other but not with the wider component A, the difference in relative cloud properties may reflect pole-on versus edge-on orientations of banded clouds. There is some evidence both observationally (Hale 1994) and in hydrodynamic radiative simulations of star formation (Bate 2012) that close binary components (separation $\lesssim 30$ AU) have preferentially aligned spins on account of dissipative interactions during the formation process, while wider binaries and members of triple systems are more frequently misaligned. Given that all field brown dwarf binaries have small separations ($\lesssim 10-15$ AU) it is possible that the majority have aligned spins and hence correlated cloud coverage, while higher order multiples such as 2M0838+15 ABC are more likely to have a severely misaligned

component from three-body dynamics. However, recent observations by Konopacky et al. (2012) of 11 VLM binaries cast some doubt on this hypothesis. These authors find nearly half of their sample (5/11) have highly different $v \sin i$ (all with separations < 5 AU) which may indicate frequent spin mis-alignment in close VLM binaries (although this could also reflect intrinsically different rotation rates). Furthermore, it seems less likely that the more extreme properties of the SIMP1619+0313 AB components could be explained by viewing geometry, however it may be notable that with a projected separation of ~ 15.4 AU, SIMP 1619+0303 is one of the widest known BD field binaries.

Finally, it may be significant that both 2M0838+15 and SIMP 1629+1303 have $J - H$ colors that fall in the underpopulated “early/mid-T gap” discussed by Dupuy & Liu (2012), through which BDs evolve rapidly. Perhaps the rapid nature of evolution in this regime leads to a “spreading out” of evolutionary progress (i.e. in the dispersal of condensate clouds), leading to more divergent properties among coeval binary components in this region of color space.

4.7.2 Formation and Dynamical Stability of 2M0838+15

The 2M0838+15 ABC system stands out as the only known brown dwarf visual triple to date, and furthermore the only known brown dwarf triple system where all three components have been directly and conclusively detected. There are only two other examples of probable brown dwarf triple systems in the literature: Kelu-1 (Ruiz et al. 1997; Liu & Leggett 2005; Stumpf et al. 2008) and DENIS-P J020529.0-115925 (Delfosse et al. 1997; Koerner et al. 1999; Bouy et al. 2005), although in these cases the tertiary component remains unresolved and the ratios of inner-to-outer period and separation are unknown. There are a handful of VLM triples (7 known or suspected to date) discussed in Burgasser et al. (2012), and of these only two prove to be good analogs to 2M0838+15 ABC with near-equal component masses and relatively low

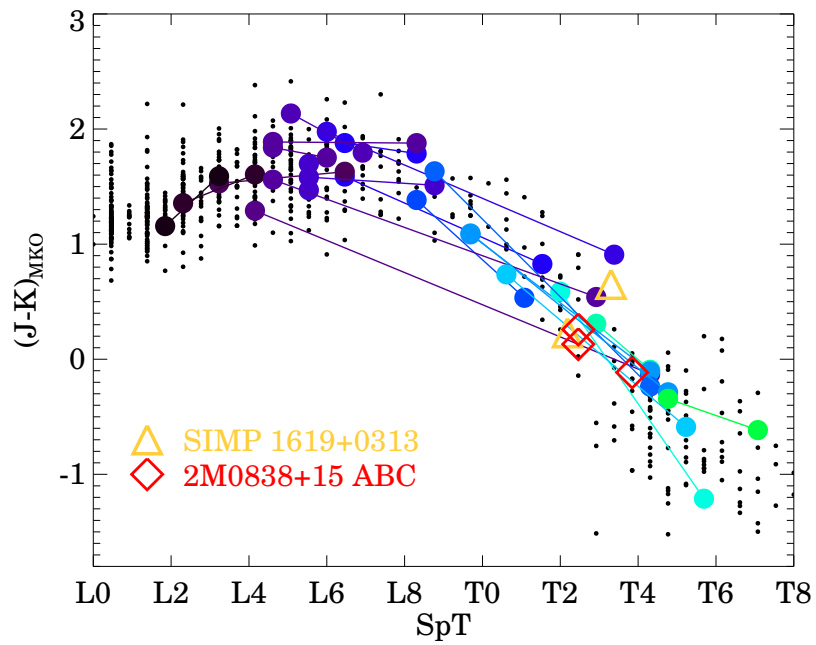


Figure 4.11: NIR $J - K_s$ colors as a function of spectral type for field BDs, color coded by primary spectral type for clarity (binaries are taken from the database of Dupuy & Liu (2012)). The 2M0838+15 ABC components are plotted as open diamonds, and the peculiar SIMP 1629+0313 system of Artigau et al. (2011) is plotted as yellow triangles. Uncertainties in the spectral types and colors of the ABC components are approximately reflected by the symbol size.

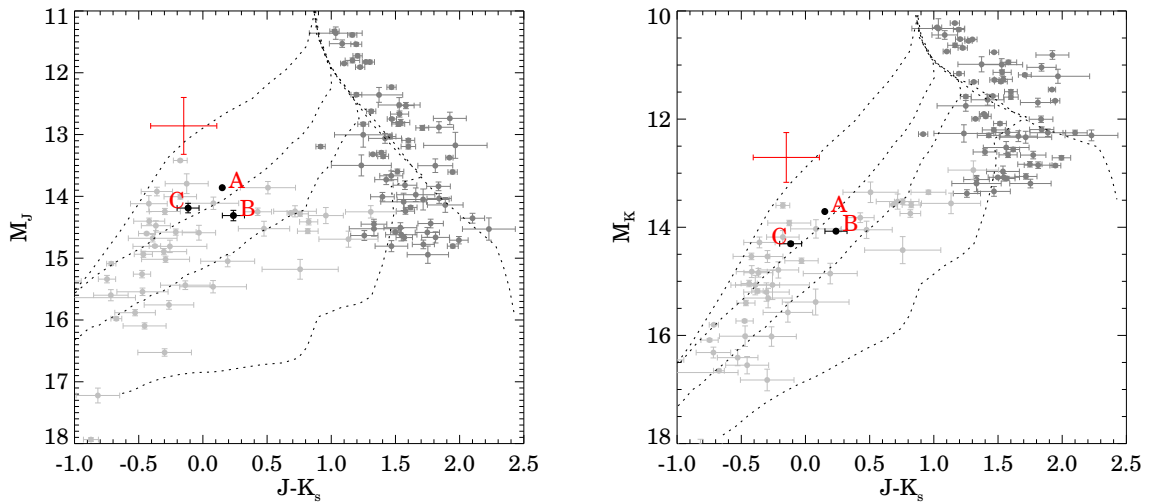


Figure 4.12: Color magnitude diagrams showing the *relative* positions of the 2M0838+15 A, B and C components inferred from resolved photometry of the system. Note that the absolute position along the vertical M_J and M_K axes of the 2M0838+15 system is not independently constrained. In each figure, a red error bar shows the systematic uncertainty in absolute magnitudes and colors for the 2M0838+15 system, while black error bars show relative errors of the B and C component magnitudes and colors with respect to component A.

ratios of outer-to-inner separations: (i) LP 714-37, an M5.5/(M8/M8.5) triple with similar component masses of 0.11, 0.09, and 0.08 M_{\odot} , and outer/inner separations of 33 AU/7 AU; (ii) LHS 1070 ABC, a (M5/M8.5/M9) triple with component masses of 0.12, 0.08, and 0.08 M_{\odot} and separations of 12 AU and 3.6 AU (Leinert et al. 2001; Seifahrt et al. 2008). The other known VLM triples have much larger inner-to-outer separation ratios ($\gtrsim 100$), which implies a multimodal distribution of inner-to-outer period ratios as is seen for higher mass triples (e.g. Tokovinin 2008).

Hydrodynamic simulations of fragmentation and subsequent evolution in a gas-rich environment (e.g. Bate et al. 2002b; Bate 2009; 2012) can form triples at separations smaller than the fragmentation scale ($\lesssim 100$ -1000 AU) and with preference for equal masses as a result of dissipative interactions with disks, and accretion. These simulations successfully produce VLM and brown dwarf triples with outer-to-inner separation ratios of ~ 10 -100. The role, if any, of subsequent dynamical interactions within a gas-free cluster is unclear. Simulations of gravitational interactions between small- N cluster members by Sterzik & Durisen (2003) can infrequently produce BD triples ($\sim 0.2\%$ of all triple systems), but this mechanism does not reproduce observed characteristics of higher mass triples (Tokovinin 2008) and therefore is unlikely a major determinant of stellar multiplicity properties in general. However, there is debate as to whether dynamical ejection (e.g. Reipurth & Clarke 2001; Bate et al. 2002a) of BD systems from the surrounding gas reservoir, while accretion is still ongoing, may be required to halt further growth and prevent proto-brown dwarfs from reaching stellar masses.

For an age of 3 Gyr we find an approximate binding energy of $\sim 20 \times 10^{41}$ erg, satisfying the minimum binding energy typically found for VLM binaries (e.g. Close et al. 2003; Burgasser et al. 2007). If this binding energy cut-off is the result of dynamical ejection then the 2M0838+15 ABC system is likely to have survived such an event. Alternatively, for an age of 300 Myr the system would have a binding energy

of $\sim 1.6 \times 10^{41}$ erg, well below the empirical minimum, and join only a handful of similarly weakly bound VLM and BD systems (see figure 4.13). This observation may favor an older age for the 2M0838+15 ABC. Thus for a ~ 3 Gyr age formation via turbulent fragmentation followed by ejection from its birth cloud may be a viable formation scenario for the 2M0838+15 ABC system.

With an inner-to-outer ratio of projected separations of ~ 10 , the 2M0838+15 ABC system currently satisfies the stability criterion suggested by Eggleton & Kiseleva (1995) of $Y_0 > 6.7$, where Y_0 denotes the ratio of inner binary apastron separation, versus the outer binary periastron separation. Due to projection effects the actual inner to outer separation ratios could be even larger than measured. Assuming that the outer to inner ratio of semi-major axes is close to the observed ratio of projected separations (~ 10) implies a period ratio of ~ 30 for the inner and outer orbits. In this case the empirical stability criterion of Tokovinin (2004), $P_{out}(1 - e_{out})^3 / P_{in} > 5$, is satisfied for outer eccentricities of $e_{out} \lesssim 0.45$. Thus current observations are consistent with the longterm stability of the 2M0832+15ABC system.

4.7.3 Binarity at the L/T transition

We have found a late-L/T transition binary frequency (L9-T4 spectral types, at observed separations $\gtrsim 0.05 - 0.07''$) of $14_{-6}^{+7}\%$. While this is slightly larger than reported frequencies outside of the transition (Burgasser et al. 2003a; 2006a; Reid et al. 2008; Bouy et al. 2003, $\sim 9-12\%$), it is not a statistically significant increase. This preliminary result provides an optimistic outlook for studies of L/T transition brown dwarfs: it suggests that this sample is not significantly contaminated (or at least not much more so than other ultracool dwarf populations) by binaries whose combined spectra mimic those of a bonafide L9-T4 dwarfs. On the other hand, we found the unresolved L9-T4 binary fraction to be double that of a primary-spectral-type-selected sample which may hint that the binary frequency does increase in this regime, and that the

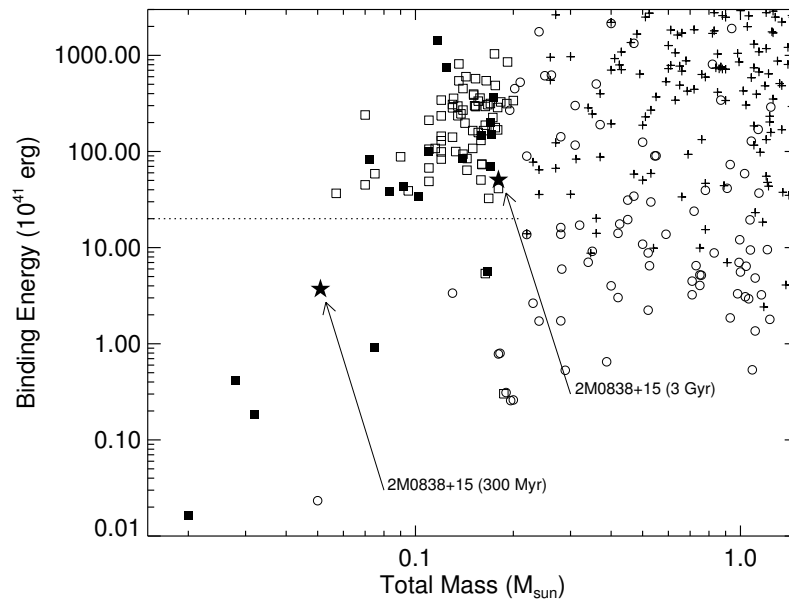


Figure 4.13: Binding energy as a function of total mass for stellar and VLM binary systems. The 2M0838+15 A(BC) system is plotted using a 5-point star. A dotted horizontal line makes the minimum binding energy cutoff of $\sim 20 \times 10^{41}$ erg observed for the majority of VLM binaries. Most of the other VLM binaries plotted (squares) are taken from the VLM Binary Archive, which is a compilation of data from 144 unique publications which can be accessed at vlmbinaries.org. Additional VLM systems, stellar binaries (crosses) and stellar primaries with VLM secondaries (open circles) are taken from Close et al. (1990); Fischer & Marcy (1992); Tokovinin (1997); Reid & Gizis (1997a;b); Reid et al. (2001c); Caballero et al. (2006); Daemgen et al. (2007); Kraus & Hillenbrand (2007); Radigan et al. (2008); Luhman et al. (2009); Faherty et al. (2010). Young/low-gravity systems are marked by filled circles and squares.

actual unresolved L9-T4 binary frequency could be on the high end of our inferred distribution for ν (e.g. $\sim 20\%$ at the 1σ upper limit). A larger sample will be required to resolve these contradictory indications.

Burgasser et al. (2010) asked the question of whether L/T transition binaries may be identified from their NIR spectra. This would be advantageous as it would allow us to improve our statistical studies and to identify binary contaminants in the L/T transition regime. The authors compared the NIR spectra of L/T transition dwarfs to a series of single and composite spectral templates and identified objects with spectral features common to known binaries as “strong” and “weak” binary candidates depending on the number of common traits. Our sample contained 2 “strong” binary candidates (2M0247+16 and 2M0351+48) and 2 “weak” binary candidates (2M0119+24 and 2M0758+32) suggested by Burgasser et al. (2010), and none were resolved into multiples. This result suggests that either (i) we cannot identify binaries reliably using spectral indices, or (ii) that the estimated number of binaries missed at low separations is significant. In all likelihood both of these explanations are partially true. In the first case, spectral irregularities in the candidate binaries must be caused by atypical atmospheric or physical properties, rather than binarity. This is likely the case for another strong candidate binary of Burgasser et al. (2010), 2M2139+02, which was found to have peculiar atmospheric characteristics (patchy clouds, and large-amplitude photometric variability; Radigan et al. 2012). Alternatively, the second explanation may find support in radial velocity surveys of VLM stars and BDs both in the field or in young clusters (e.g. Maxted & Jeffries 2005; Basri & Reiners 2006; Joergens 2008) which show that there may be just as many binaries at separations < 3 AU as found by direct imaging surveys. In this latter case the true L9-T4 binary frequency could be as high as $\sim 30\text{-}40\%$. Even so, this would imply that the majority ($\sim 2/3$) of objects in the late-L/T transition are single.

Chapter 5

A J-band Variability Survey of Brown Dwarfs

5.1 Overview

An outstanding issue in the understanding of ultracool dwarf atmospheres is the abrupt shift from red ($J - K \sim 2$) to blue ($J - K \sim 0$) near-infrared colors, accompanied by a J -band brightening, at the boundary between L and T spectral types, marking the transition from cloudy to cloud-free atmospheres. While current 1-dimensional cloud models generally fail to capture the main features of the transition, most notably the narrow temperature range over which it occurs, it has been hypothesized that a disruption of the cloud layer as it sits progressively lower in the photosphere could contribute to a more abrupt decrease in dust opacity in this regime. If present, such patchy cloud coverage should give rise to photometric variability on rotational timescales. Motivated in part by the recent discovery of ~ 50 mmag periodic variability of the T2.5 dwarf SIMP0136 by Artigau et al. 2009, we have undertaken the most comprehensive NIR variability survey of cool brown dwarfs (BDs) to date, designed to test for heterogeneous cloud coverage in a sample of BDs spanning mid-L to late-T spectral types. Here we describe our large J -band survey for variability of cool

BDs using the Wide Field Infrared Camera (WIRC) on the 2.5-m Du Pont telescope at Las Campanas, supplemented with additional observations of northern targets using the Wide-field InfraRed Camera (WIRCam) on the 3.6-m Canada-France-Hawaii Telescope. Our *J*-band search has targeted over 60 isolated BDs with high cadence, continuous photometric sequences over time baselines of ~ 1.5 -6 hr. Our data suggest that heterogeneous cloud features are responsible for variability in a subset of partially cloudy BDs spanning the transition between L and T spectral types (with an observed fraction of $23_{-8}^{+11}\%$ being variable). Based on our results we can claim with 95% confidence that high amplitude variability (peak-to-peak amplitudes $>2\%$) is more frequent inside the L/T transition. This work provides the first clear evidence for an increase in the frequency and/or amplitudes of photometric variability across the L/T transition, suggesting that heterogeneous clouds may explain the peculiar *J*-band brightening observed to occur with decreasing effective temperature in this regime. However, these observations could also be interpreted as an increasing *contrast* between pre-existing cloud features within the L/T transition, rather than the development of cloud holes. Future observations will be required to break degeneracies between these scenarios.

For additional introductory material, and a history of previous variability searches, see section 2.2.

5.2 Observations

The bulk of the present work was carried out over 60 nights (less time lost due to technical difficulties and poor weather) using WIRC at Las Campanas, with time divided into 5 12-night observing runs spanning July 2009 to May 2010. The northern subsample was observed in queue mode using WIRCam on CFHT in the 2009A semester.

5.2.1 Target Sample and Observing Strategy

Targets were selected to span mid-L to late-T spectral types, with special care taken to populate the L/T transition region of the color magnitude diagram. Known binaries were avoided when possible, although some were observed when there were no other suitable targets. From Las Campanas 57 unique targets were observed with $J < 17$ and $\delta < 15^\circ$. On a given night targets were selected based on opportunity (airmass < 1.5 for several hours), and a weighing of observing conditions and target brightness. The 5 CFHT queue targets consisted of reasonably bright L9-T5 targets with right ascensions ranging from 21h to 8hr, and $\delta > 15^\circ$.

Due to a long history of ambiguous results in BD variability monitoring (e.g., see section 1.3), the present work was designed to (i) survey an unprecedented number of objects allowing for robust statistical analysis, (ii) achieve improved photometric precisions of $\sim 1\%$, and (iii) better control for potentially confounding factors such as second order extinction and variable-phase light curves. In order to observe a large number of objects, each target was typically observed only once, and monitored continuously over a ~ 2 -5 hr interval with a 20-60 s cadence. Since ultra cool dwarfs are found to be rapid rotators with periods ranging from ~ 2 -10 hr (e.g., Reiners & Basri 2008), the chosen time baseline aims to cover a large fraction of a rotational period in order to detect rotationally modulated variability in a single epoch. Continuous, high cadence monitoring was chosen instead of a sparser time sampling over weeks or months because (i) it leads to more precise differential photometry, and (ii) the evolution of surface features (e.g., clouds) on a BD's surface may prevent observations taken over multiple epochs from being phased together in a coherent way. Finally, new J -band filters closely matching the Mauna Kea Observatory (MKO) system (Tokunaga & Vacca 2005), which cut off precipitable water vapor bands redward of $1.35 \mu\text{m}$ (e.g., Artigau et al. 2006), were purchased and installed on WIRC in order to minimize second order extinction effects (WIRCam on CFHT also uses an MKO J filter).

The final sample consists of 62 unique target light curves. Of these, 47 are longer than 3 hr in length and achieve (non-binned) precisions better than 2%, and binned precisions better than 1% (RMS of relative photometry). A log of all observations is provided in table 5.1, while target and detection information is provided in table 5.2.

5.2.2 Las Campanas Observations

Observations at Las Campanas utilized the NIR camera WIRC on the Du Pont 2.5 m telescope. The camera consists of 4 HAWAII-I arrays, each with a 3.2' field of view and a pixel scale of 0.2''. The camera is intended as a wide-field survey camera, with 3' gaps between detectors. We did not use it as such, choosing to position our targets consistently on the south-west array, which we determined (from dark and flat field data) to be the least noisy of the four chips. All exposures were read out using correlated double sampling with a pixel-to-pixel full frame reset-preread-read-read sequence. Observations were obtained either in staring mode or by using a random dither pattern confined to a $\sim 15''$ radius on the detector. Both staring, and the use of a localized random dither pattern (rather than a wide N-point pattern) minimize the movement of stars on the detector, which serves to minimize position-dependent systematics such as residual flat-fielding errors. For each sequence, dome-flats (lamp on and off) and dark frames corresponding to each exposure time were taken either on the afternoon preceding, or the morning following each observation. On several occasions we obtained twilight flat field frames, but did not find them to be an improvement over the dome flat fields. For most observations dome-flats (lamp on and off) and dark frames corresponding to each exposure time were taken either on the afternoon preceding, or the morning following each observation.

Staring observations

For staring observations the target centroid is kept fixed on the same pixel throughout the sequence. This was accomplished using an *IDL* routine to stream the incoming science images onto a standard laptop and compute real-time guiding corrections. An alert was sounded, and manual closed-loop corrections to the guide-camera reference position were made each time the target strayed by more than 0.5 pixels from its initial position (approximately once every 5-15 minutes). Without telescope offsets the efficiency of staring observations is significantly increased. Individual exposures of 20-60 s were used depending on target brightness, resulting in a cadence of 27-67 s. Nine-point dither sequences for the purpose of rough sky subtraction and centroiding were made at the beginning, end (and sometimes middle for long observations) of each contiguous staring sequence. Staring observations were preferred in more crowded fields, and in poor seeing conditions.

Dithered observations

For targets significantly fainter than the sky, and in very good seeing conditions dithered observations were preferred. A random dither pattern within a fixed radius (or sometimes box) was employed wherein the telescope was offset by at least 3'' (15 pixels) after each exposure. All pointings were typically contained in a 15'' (75 pixels) diameter circle or box, although slow drifts in pointing over long sequences sometimes caused the center of the dither pattern to drift.

Reduction of WIRC Data

All raw images were dark subtracted (the dark current is negligible, and this mostly removes a drifting bias; in fact, our dark frames often record low *negative* counts), and corrected for non linearity using a linearity sequence of dome flats obtained on 27 Jul 2009, iteratively solving for the original (i.e., non-subtracted) counts since

detector reset in the first and second CDS reads. Dome flat fields (constructed from median combined and differenced lamp-on and lamp-off images) were used to correct for inter-pixel variations in quantum efficiency. For dithered sequences, a running sky frame was subtracted from all science images. Faint stars were identified in an initial first-pass reduction, and subsequently masked for the second pass so as not to bias the sky frames. Hot or dead pixels, as well as pixels having more than 35,000 counts ($>3\%$ non-linear) were flagged. Isolated bad pixels were interpolated over using a gaussian fitting function in the vicinity of the bad pixel with the IDL Astronomy Library routine MASKINTERP. Except for sky subtraction, reduction of the staring sequences is almost identical to the procedure described above, however in these cases sky frames obtained before and after the staring sequence were used for sky subtraction.

For each monitoring sequence, aperture photometry was performed on the target and a set of reference stars, using a circular aperture of radius 1.5 times the median full width at half maximum (FWHM) of all stars in each image. Residual sky levels in the vicinity of each star were measured inside an annulus centered on each source. There are typically several good reference stars in the $3.2' \times 3.2'$ WIRC field of view and many more in the WIRCam field of view which can be used for relative photometry. Details of the light curve analysis are given in section 5.3.

5.2.3 CFHT/WIRCam Observations and Data Reduction

Observations of 5 targets were carried out in queue mode using WIRCam on the 3.6-m CFHT during the 2009A semester. Photometric conditions, low airmass ($<1.5-1.7$), and seeing better than $\sim 1''$ (for in-focus sequences) were provided as observing constraints. A staring strategy was employed with a small defocus for bright targets (SDSS J075840.33+324723.4, and 2MASSI J2254188+312349). Exposure times ranged from 15 to 40 seconds depending on target brightness. In-focus sky sequences using a

9-pt dither pattern and identical exposure times were taken before and after staring. The raw data were automatically processed by the 'Iwi processing pipeline. Manual sky subtraction was performed using the processed but pre-sky-subtracted data products. Sky images were median combined to create sky frames. Either a single sky frame or an interpolation in time between before and after sky frames was scaled and subtracted from all science images. With a $20' \times 20'$ field of view, and pixel scale of $0.3'' \text{ pix}^{-1}$, WIRCam typically provides many tens of similar-brightness reference stars for differential photometry.

5.3 Light Curve Analysis

The raw light curves display fluctuations in brightness due to changing atmospheric transparency, seeing, airmass, and residual instrumental effects throughout the night. To first order these changes are common to all stars, and can be removed. First, the raw light curves of all stars were converted from absolute to relative fluxes via division by their median brightness. Next, for each reference star a calibration curve was created by median combining the light curves of all other reference stars (excluding that of the target and star in question). The raw light curve of each reference star was then divided by the corresponding calibration curve to obtain a corrected light curve.

For each normalized and corrected light curve the standard deviation, σ , was determined using the IDL `ROBUST_SIGMA` routine which calculates an outlier-resistant standard deviation as outlined in Beers et al. (1990). While for flat light curves σ is a measure of the noise, for variable light curves it measures both noise and intrinsic variations. We therefore measure a second quantity σ_{pt} , which is the standard deviation of the light curve subtracted from a shifted version of itself, $f_{i+1} - f_i$, divided by $\sqrt{2}$. We refer to this latter measurement as the point-to-point noise, which is not sensitive to low frequency trends, and provides a better estimate of the noise for variable light curves.

Next, poor quality or low signal-to-noise reference stars were eliminated if any of the following conditions were met: (i) $\sigma > 1.5\times$ that of the target star, (ii) σ values that represent a 3-sigma departure compared to a smooth fit to the σ vs. magnitude trend of all stars on the chip (see figures C.1-C.63), (iii) a large number of non-linear or bad pixels (more than 4 non-linear pixels or 1 interpolated pixel on average in the photometry aperture), (iv) having failed flux extraction in over 25% of images, or (v) having an extended PSF compared to other stars in the frame (e.g., a galaxy or double star). This procedure is designed to eliminate both intrinsically variable sources and sources that fall on unusually noisy regions of the array (i.e., on a hot/cold pixel that was not flagged, or with a bright nearby neighbor). The bulk properties of reference star light curves are discussed in detail in section 5.3.1. This subset of good, high-signal-to-noise references, less the star in question, are then used to re-calibrate each raw light curve.

In the last step, a detrending procedure is applied that attempts to remove residual trends in the corrected light curves. A simple plane fit to the corrected flux vector, \mathbf{f} , in the form of $\mathbf{f}(\mathbf{u}, \mathbf{v}) = p_0 + p_1\mathbf{u} + p_2\mathbf{v}$ is largely successful in removing residual trends, where the vectors \mathbf{u} and \mathbf{v} correspond to the seeing (median FWHM of stellar PSFs in a given image) and first-order variations (i.e., the calibration curve) respectively. With only three free parameters in the fit, this method successfully removes systematic trends correlated with seeing or first-order variations common to all stars on the chip, without significantly impacting the recovery of intrinsic variability signals. The light curve is further fit to a second order polynomial in x and y pixel position. While there is some degree of correlation between flux and position for some targets, the positional detrending provides only a marginal improvement for most light curves.

This vetting and detrending procedure is repeated for successive iterations until the number of good reference stars stabilizes (typically 1-3 iterations). The target and all other stars are calibrated and detrended a last time, using the final stable set of

“good” reference stars to create calibration curves (always omitting the target and star in question from its own curve in order to maintain independence between the calibration curve and corrected fluxes). This procedure typically yields 3-10 good reference light curves with low RMS deviations and no other identifiable problems.

Detrended light curves for each target and up to 7 reference light curves with σ values closest to the target are shown in figures C.1-C.63. The reference stars displayed are automatically selected from the set of reference light curves used for calibration, without manual interference, and do not represent the best quality or highest signal to noise light curves obtained. Also shown are diagnostic plots of how the sky brightness, seeing, first-order (common to all stars) variations, and airmass change as a function of time throughout each sequence. For WIRC targets an image of the field of view is shown, and reference stars labelled by number. The WIRC reference stars have been positionally matched to the 2MASS catalog, and J-K colors for the reference stars are identified. There is no evidence for significant correlations between 2nd-order trends and reference star color and/or airmass in the WIRC dataset.

5.3.1 Search Sensitivity: Empirical Detection Limits for Variability

The problem of detecting arbitrary variability in a light curve with both random and systematic noise contributions is challenging. Furthermore, not all trends in the data are evidence of intrinsic variability: it is common for the fully reduced reference star light curves to possess low-level residual systematic trends at the $\sim 0.5-1\%$ level. The frequency and strength of instrumental trends in the data must be characterized in order to assess detection limits for intrinsic variability.

Properties of 742 Reference Star Lightcurves

In order to determine empirical detection limits for intrinsic variability, a library of reference star light curves was assembled from 70 WIRC observing sequences (not

all of unique targets). Light curves with: (i) more than 4 non-linear pixels on average in the photometry aperture, (ii) more than 1 interpolated pixel on average in the photometry aperture were flagged and excluded. Furthermore, we only considered light curves for which $\sigma < 0.04$.

Structure in the reference light curves was examined by computing power spectra, using the Lomb-Scargle method (Scargle 1982; Horne & Baliunas 1986). For each light curve a 0.01 false alarm probability (FAP) was determined from 1000 simulated light curves. The simulated light curves were produced by randomly permuting the indices of the original light curves. The LS periodogram was computed for a minimum period of 15 minutes up to a maximum period of twice the observation baseline. While the maximum period that can be detected corresponds to the observation length, the LS periodogram is still sensitive to the presence of lower frequency power, even if a period can not be determined. For example, linear trends show up as broad low frequency power. For each reference light curve the peak power in the LS periodogram and the 0.01 FAP were determined. The ratio of peak power to the 0.01 FAP level is shown in figure 5.1 as a function of the relative light curve point-to-point RMS, σ_{pt} .

For 3.6% of reference star light curves the ratio of peak power to the 0.01 FAP level is >1 . Unfortunately we have no way of determining whether this power in the LS periodogram reflects intrinsic variability or residual systematic trends. Alternatively 99% of reference stars have peak power to 0.01 FAP ratios <1.4 . We therefore adopt a detection threshold of 1.4 times the 0.01 FAP derived from simulations, which should conservatively yield a false positive rate of $<1\%$. We find similar results for 84 reference stars observed with WIRCam where $\sigma_{pt} > 0.0075$, also shown in figure 5.1. However, for $\sigma_{pt} < 0.0075$, a large fraction of the WIRCam stars show evidence of low amplitude trends, and a detection threshold of 3-4 times the 0.01 FAP level is more appropriate. We have only two target light curves in this regime, and for both their ratios of peak power to the 0.01 FAP is < 1 . The ratio of peak power to the 0.01 FAP

for BD targets is over plotted in figure 5.1 for comparison. It is immediately clear that the BD light curves are significantly more variable than those of the reference stars. Furthermore, our variability diagnostic of peak power that is 1.4 times larger than the white-noise 0.01 FAP is in good agreement with a by-eye assessment of the light curves (figures C.12,C.17,C.22, and C.44).

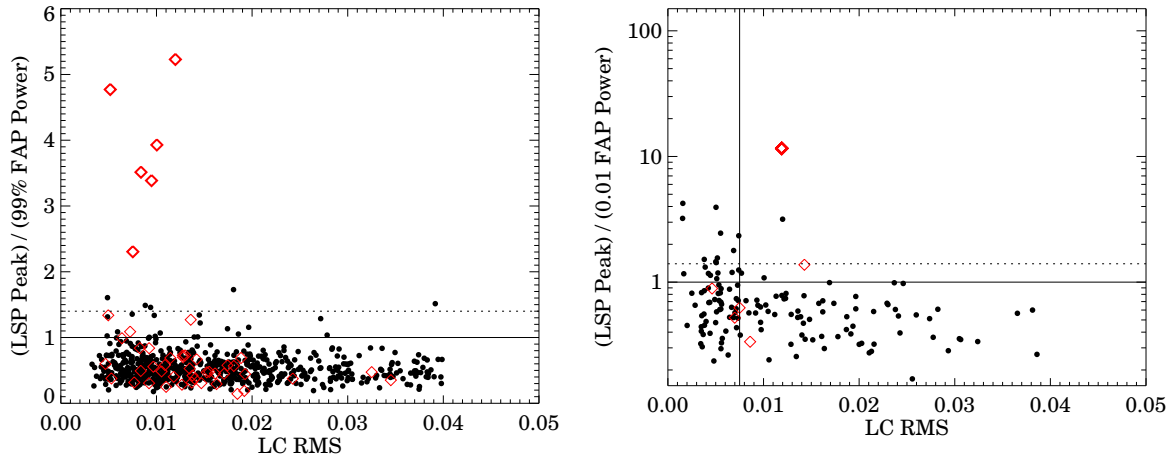


Figure 5.1: Peak power in a Lomb-Scargle periodogram relative to the 0.01 FAP power for 742 reference stars (black points) observed with WIRC (left) and 142 reference stars observed with WIRCam (right). The ratio of peak power to 0.01 FAP level is over plotted for BD targets as red diamonds. Horizontal lines are plotted for ratios of 1 and 1.4 as a visual aid. The vertical line in the right panel corresponds to $\sigma_{pt}=0.0075$. To the left of this line the detection threshold increases from 1.4.

5.3.2 Detections of Variability

Here we define β to be the peak power in an LS Periodogram, divided by the 0.01 FAP determined from simulations. In the previous section we empirically determined that $\beta > 1.4$ less than 1% of the time for (presumably non-variable) reference stars. This limit is conservative because some reference stars may in fact be intrinsically variable. The β values for the target light curve are provided in table 5.2. We consider detections to be significant when $\beta > 1.4$, corresponding to a 99% probability of being real. Targets for which $1 < \beta < 1.4$ are noted as marginal detections. Four

targets: 2M0423, DEN0817, 2M0559, and SDSS1416 have been flagged for quality and would not have passed our cuts of inclusion in the reference star library used to determine the false-positive rate. The binary 2M0423 is flagged as having on average two interpolated pixels in the photometry aperture while the other targets are flagged for having more than 4 non-linear pixels in the PSF core (> 8000 counts). All four of these targets have low-level trends in their light curves that produce significant power in their LS periodograms. However, due to quality flags, these detections are not reliable, and are excluded from our statistical sample (similarly flagged reference stars also show a much larger incidence of variability).

The targets for which we have detected variability are listed in table 5.3. Light curves and LS periodograms for variable targets are shown in figures 5.2-5.8. We find that for highly variable targets, the light curve detrending procedure can remove some degree of the intrinsic signal, and introduce spurious features. This occurs because the procedure attempts to detrend any coincidental correlation between the intrinsic signal and other observables. Figures 5.2-5.8 therefore show *non-detrended* versions of the light curves, as opposed to the detrended versions that are used to assess detections (found in appendix C.1). While it is certainly a worry that the detrending procedure might erase variability signals entirely, upon examining both normal and detrended versions of our light curves we find this is not the case. Furthermore both normal and detrended versions of all light curves have been examined by eye. In general, intrinsic variability should not correlate well with common first order variations or seeing. Furthermore, if we were to detect a variability signal strongly correlated with either, to the point of being erased by detrending, we would question the significance of that detection. Thus our procedure implicitly assigns lower significance to detections that are correlated with other observables. The influence of the detrending procedure on signal recovery is quantified in section 5.4.

We find significant evidence of variability ($\beta > 1.4$) for 7 targets in our statistical

sample. Each is briefly described in the following sections.

SIMP J013656.57+093347.3

The T2.5 dwarf SIMP J013656.57+093347.3 (Artigau et al. 2006) was previously found to be variable with a peak to peak amplitude as high as 8% by Artigau et al. (2009) and with a period of 2.4 hr. It's light curve is known to change in amplitude and shape from epoch to epoch. The observations from Las Campanas captured an amplitude of only 3%.

SDSS J075840.33+324723.4

Variability of SDSS J075840.33+324723.4 (Knapp et al. 2004) is presented for the first time here. The peak to peak amplitude is measured to be 4.5%. We point out that SDSS J075840.33+324723.4 is a suspected strong binary candidate of Burgasser et al. (2010), however Keck AO imaging presented in chapter 4 does not find any companions with $\Delta K > 1(3)$ at separations $>0.06''(0.2'')$. The variability of this target has subsequently been confirmed by Spitzer (PID:80123, PI:Radigan) where a period of ~ 5 hr was found.

2MASS J11263991-5003550

The target 2MASS J11263991-5003550 (Folkes et al. 2007) is a peculiar L dwarf with $J - K_s$ colors that are unusually blue for its spectral type, most likely the result of thin, large-grained condensates (Burgasser et al. 2008). Given the variability presented here we suggest that the blue colors observed are due to patchy clouds. A tentative period of ~ 3.7 hr is inferred from the LS periodogram of this target's light curve. The variability has been confirmed at two subsequent epochs.

SIMP J162918.41+033537.0

The target SIMP J162918.41+033537.0 is an unpublished T2.5 dwarf discovered in the SIMP proper motion survey (Artigau et al., in prep). In a 4 hr observation we

measured peak-to-peak variations of 3%. The full amplitude is likely larger, since our observation encompasses only the trough of the light curve. The variability of this object was been confirmed at subsequent ground based epochs where a *J* band amplitude as high as 5% was found. It has also been observed with Spitzer (PID:80123, PI:Radigan), where a period of ~ 6 hr was found.

2MASS J21392676+0220226

The target 2MASS J21392676+0220226 (Reid et al. 2008) was observed to vary by 9% in a 2.5 hr observation. Subsequent observations of this target presented in chapter 3 reveal a *J* band peak-to-peak amplitude as high as 26%. This is the largest variability reported for a BD to date.

2MASS J22282889-4310262

Variability of 2MASS J22282889-4310262 (Burgasser et al. 2003b) was first detected by Clarke et al. (2008) who find a peak-to-peak *J* band amplitude of 15 mmag and a period of 1.4 hr. We confirm this result, measuring a peak-to-peak amplitude of 14 mmag and a period of 1.43 ± 0.02 hr based on a sinusoidal fit to this target's light curve over 4 continuous periods.

2MASS J18283572-4849046

Although 2MASS J18283572-4849046 has peak power in its LS periodogram above our detection threshold, the detection is considered tentative. Other reference stars in close proximity to the target show similar trends as can be seen from figure C.56. We expect ~ 0.57 false positives in our sample, so it would not be unreasonable to find a single questionable detection.

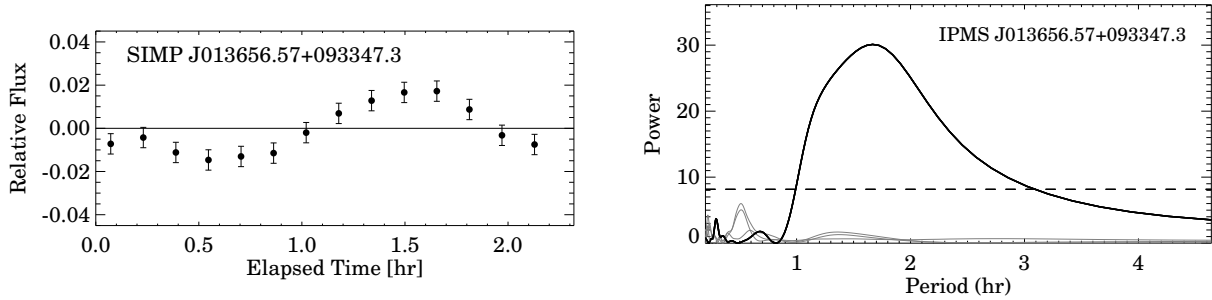


Figure 5.2: *Left*: Light curve for a significantly variable target, binned to a 10 min cadence. *Right*: Lomb-Scargle Periodogram for the detrended target light curve (solid black line) and those of reference stars observed simultaneously (solid grey lines).

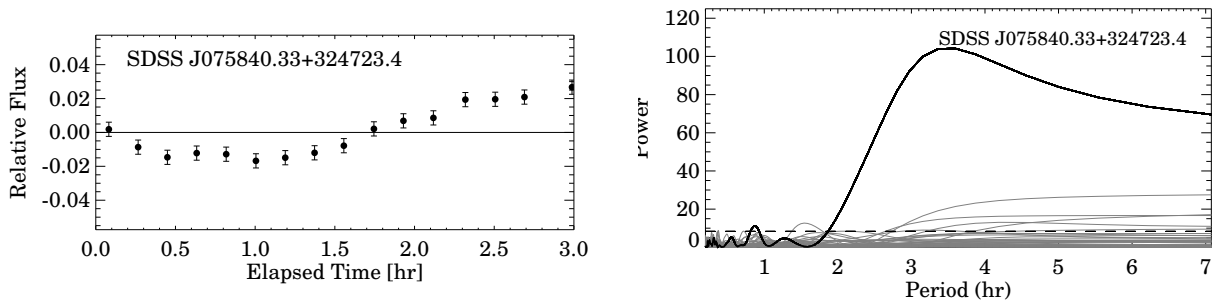


Figure 5.3: As in figure 5.2.

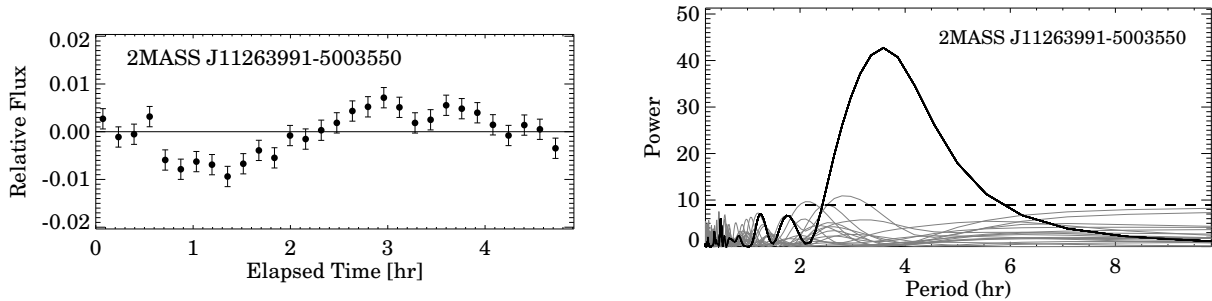


Figure 5.4: As in figure 5.2.

5.4 Survey Detection Limits and Completeness

5.4.1 Recovery Rates of Simulated Signals

In order to determine our completeness to intrinsic variability signals we injected sinusoidal signals of amplitude A , period P , and random phase into our library of

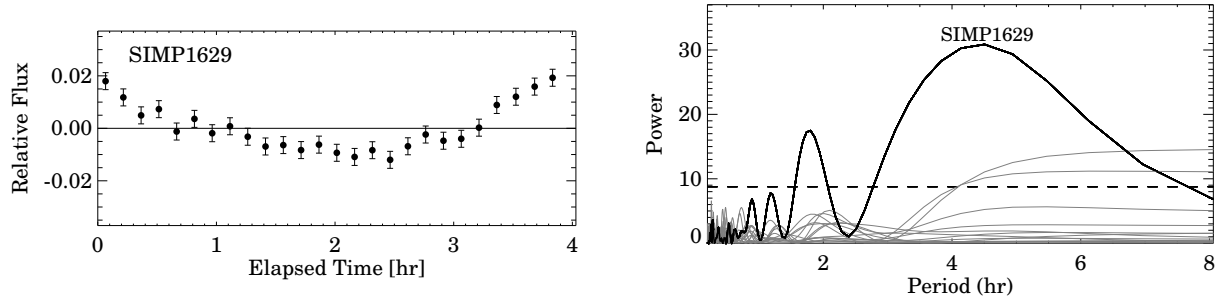


Figure 5.5: As in figure 5.2.

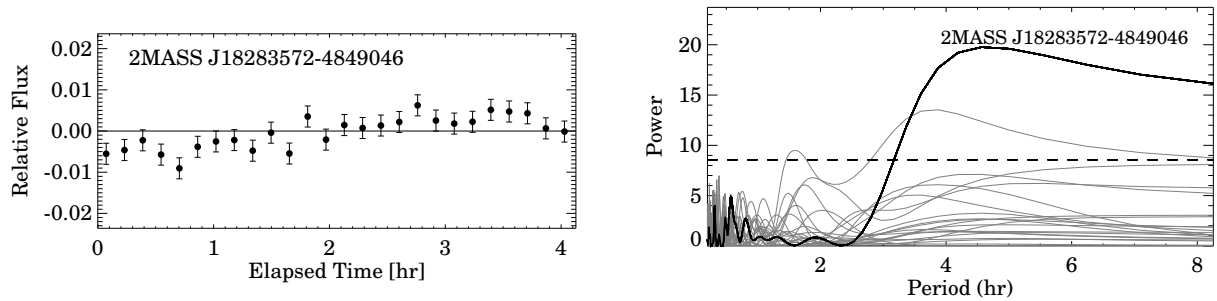


Figure 5.6: As in figure 5.2.

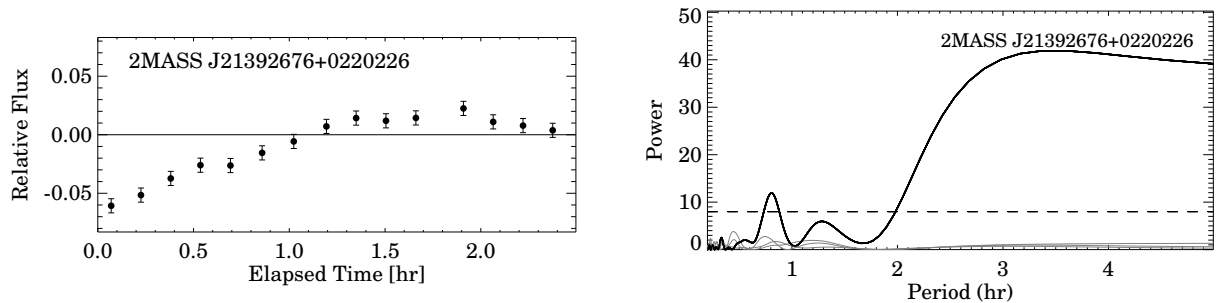


Figure 5.7: As in figure 5.2.

reference star light curves. After injecting the signal, the light curves were detrended as in section 5.3 in order to account for any diminishment of intrinsic signals from this procedure. The LS periodogram of the light curve was then computed, and the ratio of peak power to the 0.01 FAP determined. A detection was counted when this ratio was >1.4 . This procedure was completed for a grid of peak-to-peak amplitudes ranging from 1%-10%, and periods ranging from 2.5 to 20 hr with 10 and 8 grid points

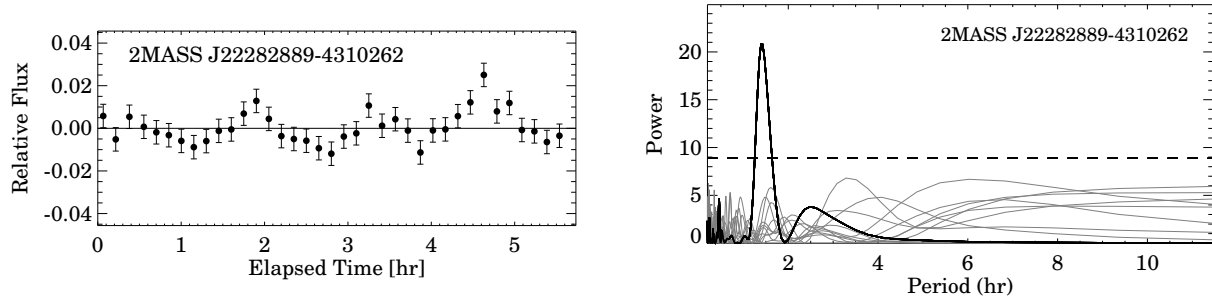


Figure 5.8: As in figure 5.2.

respectively.

Recovery rates for the injected variable signals were then determined as a function of observed light curve properties:

- $\sigma_a = \sigma_{pt} \sqrt{\delta t / 67s}$ where σ_{pt} is an estimate of the point-to-point noise in the reference light curve, and δt is the average cadence of the observation. Since not all sequences use the same exposure times, σ_a is the noise estimate *adjusted* for a 67 s cadence.
- the observation time baseline, Δt

For every point on the grid of amplitudes and periods we divided the simulated light curves into 4 bins in Δt centered on 1.75, 3., 4.25, and 5.5 hr (we seldom have an observing sequence longer than 5.5 hr). For each bin in Δt we determined the detection fraction as a function of σ_a . This was done for 20 points in σ_a ranging from 0.01 to 0.1 using a sliding bin of width 0.02. To further smooth over noise we then fit the detection fraction with a 3rd order polynomial in σ_a . All fits were visually verified. This procedure yielded a 4-dimensional grid in A , P , σ_a , and Δt , varying smoothly (and for the most part monotonically) in all dimensions. Thus, the recovery fraction of a given signal in a given light curve, denoted here as $f_{det}(\sigma_a, \Delta t; A, P)$, is given from a 4-dimensional linear interpolation on this grid.

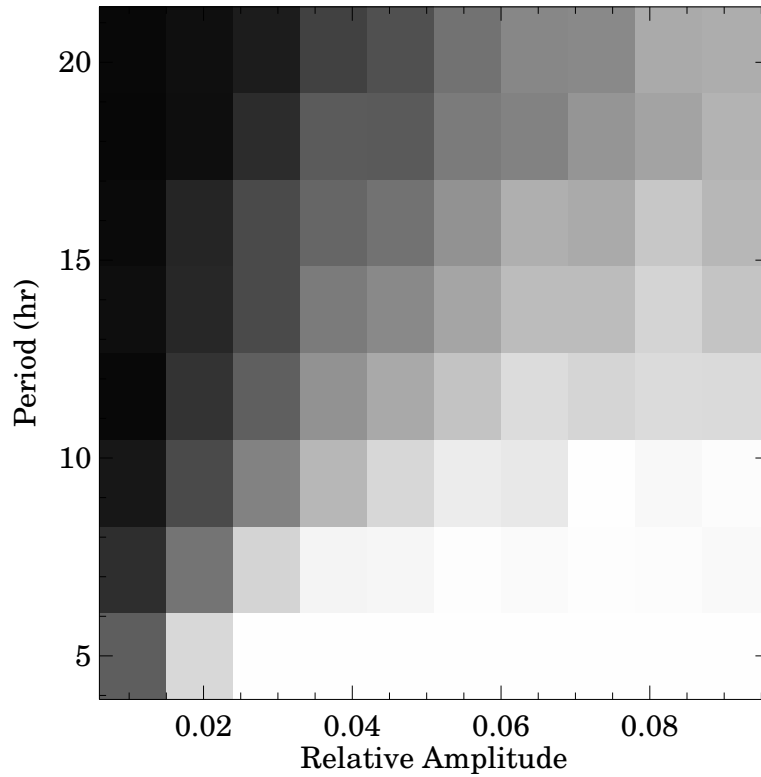


Figure 5.9: Recovery rates of simulated sinusoidal signals as a function of amplitude and period. This slice in the 4-dimensional grid corresponds to a light curve with $\sigma_a = 0.015$, and a time baseline of 3.5 hr. The shading varies linearly from recovery rates of 0% (black) to 100% (white).

Rotation Periods

In addition to the instrumental detection limits, the period distribution will affect the recovery rate of variable signals. For a single BD target our sensitivity to a particular variability amplitude is given by

$$f_{\text{sens}}[\sigma_a, \Delta t; A] = \int_0^{\infty} f_{\text{det}}[\sigma_a, \Delta t; A, P] f(P) dP \quad (5.1)$$

where $f(P)$ is the distribution of periods for our sample. The overall survey completeness to variability signals of a given amplitude is then given by

$$F_{\text{sens}}(A) = \frac{1}{N} \sum_{i=1}^N f_{\text{sens}}[\sigma_{a,i}, \Delta t_i; A] \quad (5.2)$$

where N are the number of targets surveyed, and $\{\sigma_{a,i}, \Delta t_i\}$ are the parameters describing the light curve of target i .

Previous $v \sin i$ studies of L and T dwarfs provide some clue as to the the period distribution $f(P)$. We find that a lognormal period distribution given by

$$f(P) = \frac{1}{P\sigma\sqrt{2\pi}} e^{-\frac{(\ln P - \mu)^2}{2\sigma^2}} \quad (5.3)$$

and with parameters $\sigma = 0.45$ and $\mu = 1.4$ provides a reasonable match to L and T dwarf $v \sin i$ data from Reiners & Basri (2008) and Zapatero Osorio et al. (2006) (assuming random spin orientations and Jupiter size radii for their targets). However, the possible 15.7 hr period for the highly variable T-dwarf 2M2139 (see chapter 3) would be highly unlikely given this distribution. We therefore consider a second period distribution given by $\mu = 2.2$ and $\sigma = 0.8$, with a tail extending to longer periods and truncated at 24 hr. Both period distributions are plotted in figure 5.10.

Stellar Inclination and Spot Latitudes

The distribution of inclinations for our targets will also affect our completeness. For example, no variability is expected from a pole-on target. However, lower inclinations do not give rise to smaller variability in general. If non-axisymmetric cloud or hole features are not equatorial, the maximum amplitudes will occur for $i < 90^\circ$. Without any knowledge of the cloud surface distribution, we assume here that cloud features (or asymmetries) are equally likely at any position on a spherical surface, as well as random spin orientations for our targets. Under these assumptions we estimated a distribution $f(\alpha)$ where $\alpha = A(i, \lambda)/A(90^\circ, 0^\circ)$ is a geometric dilution factor that gives the distribution of amplitudes observed for a spot feature with a maximum amplitude $A_0 = A(90^\circ, 0^\circ)$.

We estimated $f(\alpha)$ by using the round spot model of Dorren (1987) (with zero limb darkening) to simulate light curves with various spot latitudes and stellar inclinations.

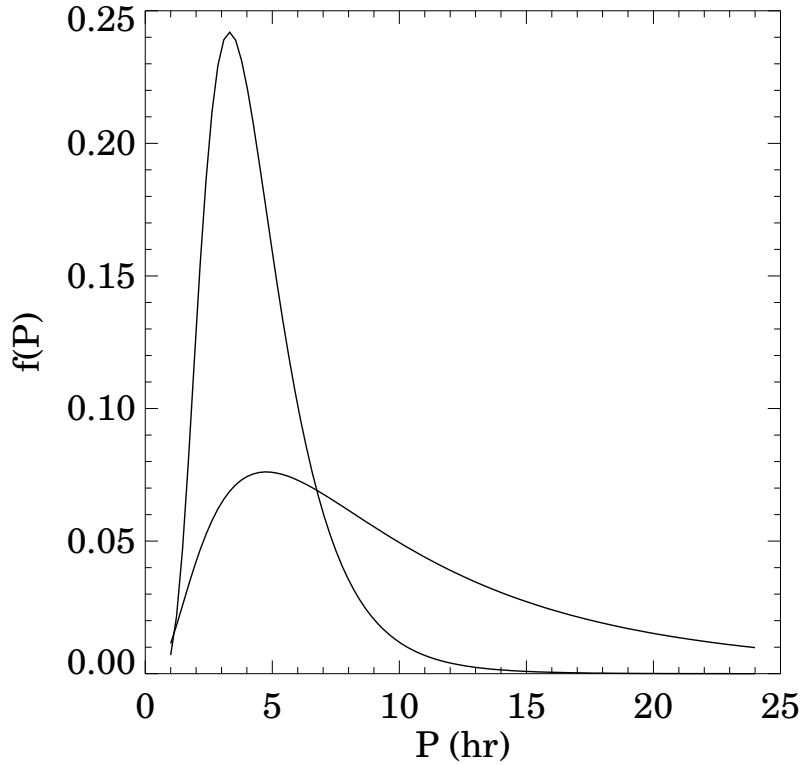


Figure 5.10: Lognormal period distributions used to assess the survey completeness. The “short” period distribution is based on a comparison to $v \sin i$ measurements by Reiners & Basri (2008) at Zapatero Osorio et al. (2006). The “long” tail period distribution is motivated by the possible 15.4 hr period detected for 2M2139 in chapter 3.

In each case we simulated a single spot of 10° radius with inclinations and latitudes drawn from distributions $f(i) \propto \sin i$ and $f(\lambda) \propto \cos \lambda$, with inclinations ranging from $0^\circ \rightarrow 90^\circ$ and latitudes spanning $-90^\circ \rightarrow 90^\circ$. For each simulated light curve the amplitude was measured, and normalized by A_0 .

Integrating over $f(\alpha)$ as well as $f(P)$ we obtain an expression for our completeness to targets with “virtual” amplitudes A_0 :

$$f_{\text{sens}}^0[\sigma_a, \Delta t; A_0] = \int_0^\infty \int_0^\infty f_{\text{det}}[\sigma_b, \Delta t; \alpha A_0, P] f(P) dP f(\alpha) d(\alpha) \quad (5.4)$$

Similarly, the overall survey completeness to targets with surface features *capable* of producing a maximum variability of A_0 for $\lambda = 0^\circ$ and $i = 90^\circ$ is

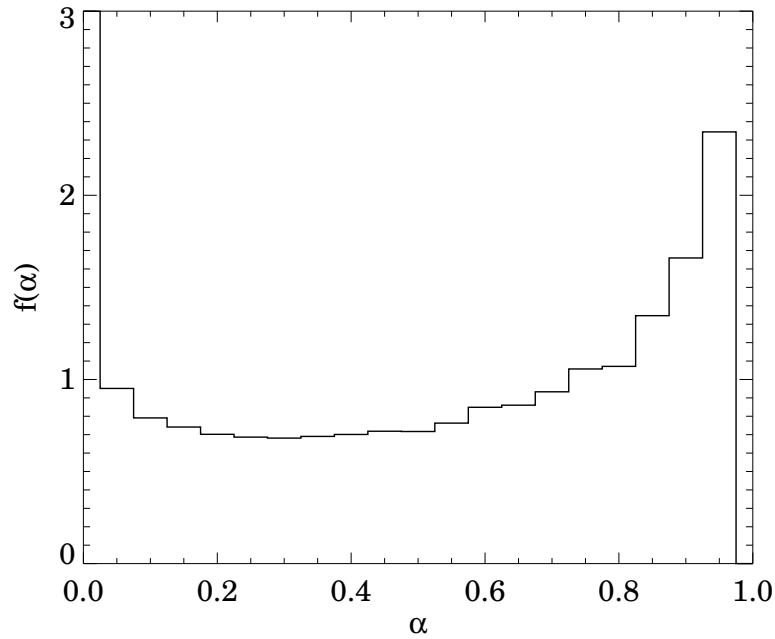


Figure 5.11: Simulated distribution for the geometric amplitude dilution factor $\alpha = A(i, \lambda)/A(90, 0)$ for a single spot with a 10° radius and input distributions $f(i) \propto \sin i$ and $f(\lambda) \propto \cos(\lambda)$.

$$F_{\text{sens}}^0(A_0) = \frac{1}{N} \sum_{i=1}^N f_{\text{sens},i}^0[\sigma_{a,i}, \Delta t_i; A_0] \quad (5.5)$$

The survey completeness as a function of A and A_0 , for both “short” and “long” period distributions is shown in figure 5.12.

5.5 Variability Statistics

In this section we aim to answer two questions. First, is there statistical evidence for an increase in variability within the L/T transition? And second, given the survey detection limits, what fraction of L/T transition objects will be variable from *some* observer’s vantage point? Although we have 62 unique target light curves, the statistical sample is reduced to 57. Recall that the targets SDSS1416, 2M0559, and DEN0817 were eliminated due to having more than 4 non-linear pixels in their PSF

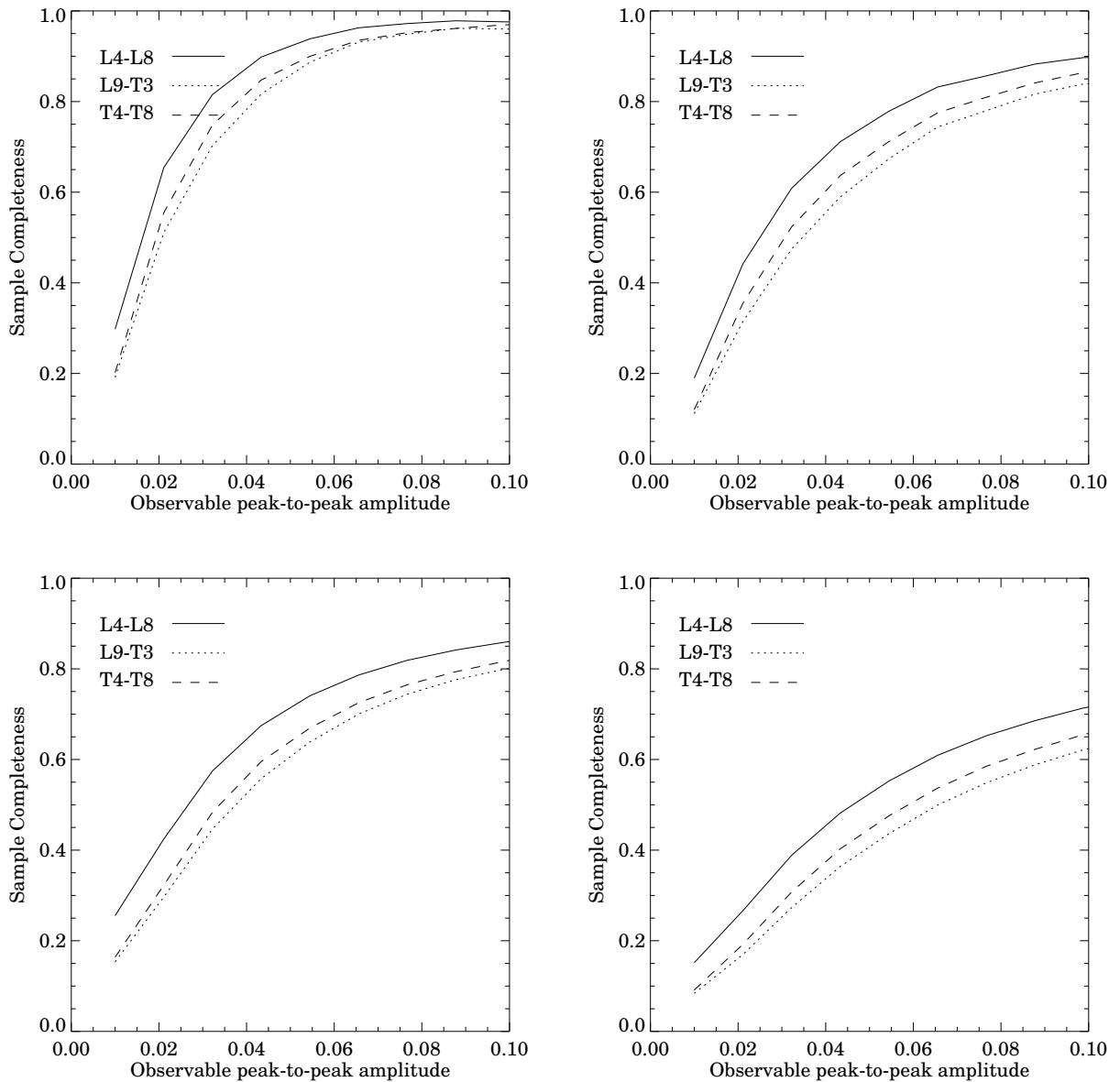


Figure 5.12: Survey completeness to sinusoidal variability signals as a function of peak-to-peak amplitude for the “short” (left) and “long” (right) period distributions. The top panels show completeness to observed amplitudes, A , whereas the bottom panels show completeness to maximum intrinsic amplitudes, A_0 (see text for explanation). The sample has been divided into three spectral type bins. The survey is slightly more complete (by 10-20%) for the brighter L4-L7 targets, in comparison to later spectral types surveyed.

cores. The targets SDSS0423¹, 2M0518, and 2M1404 are removed from the sample because they are known binaries, and hence different detection limits for the individual components apply. In addition, if determined to be variable it would be impossible to tell which component was responsible. All other targets from table 5.2 are considered for the analysis in the following section.

5.5.1 Testing the cloud “hole” hypothesis: does variability increase at the L/T Transition?

The original goal of the variability survey was to test whether or not cloud holes can explain the rapid decline in dust opacity and corresponding J -band brightening observed to occur across the L/T transition. The cloud-hole hypothesis predicts that L/T transition BDs in particular should be variable due to their patchy surfaces. In figure 5.13 the detected variability is shown as a function of spectral type and 2MASS $J - K_s$ color, with symbol radius scaling proportionately to the observed amplitude (in the original observing sequence).

There appears to be an increase in the frequency and/or amplitude of variability observed within the L/T transition regime, defined here as L9-T3.5 spectral types (see the dashed lines in figure 5.13). It is worth noting that the L/T transition is often defined to encompass L8-T5 spectral types. The more narrow range used here is motivated by the natural groupings in color vs. SpT space of our sample in figure 5.13. If we consider only detections with amplitudes above 2%, then variability is detected exclusively in the L/T transition: 4/17 targets within the transition are high amplitude variables, compared to 0/40 outside. To assess the probability of such a discrepancy occurring entirely by chance we construct probability distributions for the observed variability frequencies inside and outside the L/T transition. The probability of n detections in N trials for some frequency ν_{obs} is given by the Binomial distribution. This

¹SDSS0423 is also flagged for having a noisy pixel in its photometry aperture

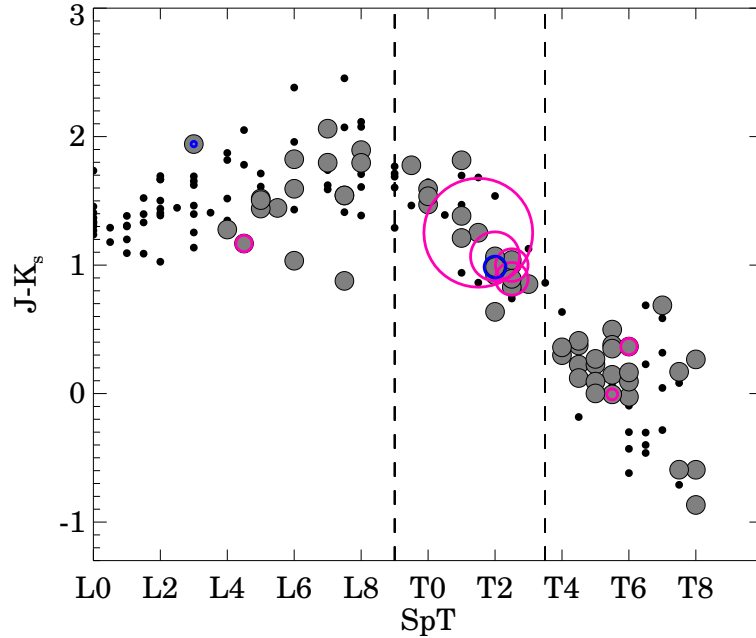


Figure 5.13: $J - K_s$ color as a function of spectral type for all known BDs with $J < 17$ (black points). The survey targets are over plotted as filled grey circles. Detections of variability are circled in pink, with symbol radius corresponding linearly to the peak-to-peak amplitude of variability observed. Marginal detections of variability are overplotted by blue open circles (also reflecting the peak-to-peak amplitude detected in the symbol size).

can be inverted using Baye’s Law to infer $P(\nu_{obs}|n, N) \propto P(n|N, \nu_{obs})P(\nu_{obs})$, where we have assumed a flat (most ignorant) prior probability distribution of $P(\nu_{obs}) = 1$. The probability distributions for ν_{obs} inside and outside the transition region (and with amplitudes above 2%) are shown in figure 5.14. While there will be some completeness correction that converts observed frequencies to “true” frequencies, for our comparison we assume this scaling factor to be similar for both samples, which is supported by figure 5.12 in section 5.4. In order to quantify the difference between $P(\nu_{out})$ and $P(\nu_{in})$, a new distribution $P(\Delta\nu)$ was constructed according to

$$P(\Delta\nu) = \int_{-1}^{+1} P(\nu_{out})P(\nu_{out} + \Delta\nu)d\nu_{out} \quad (5.6)$$

where ν_{out} refers to the observed variability frequency outside the transition, and

the frequency inside is given by $\nu_{in} = \nu_{out} + \Delta\nu$. Distribution for $P(\nu_{in})$, $P(\nu_{out})$, and $P(\Delta\nu)$ are shown in figure 5.14. We find that $\Delta\nu = 0$ lies just outside of the 95% credible interval for $P(\Delta\nu)$. We can therefore state with 95% confidence that the frequency of high amplitude variables increases inside the L/T transition.

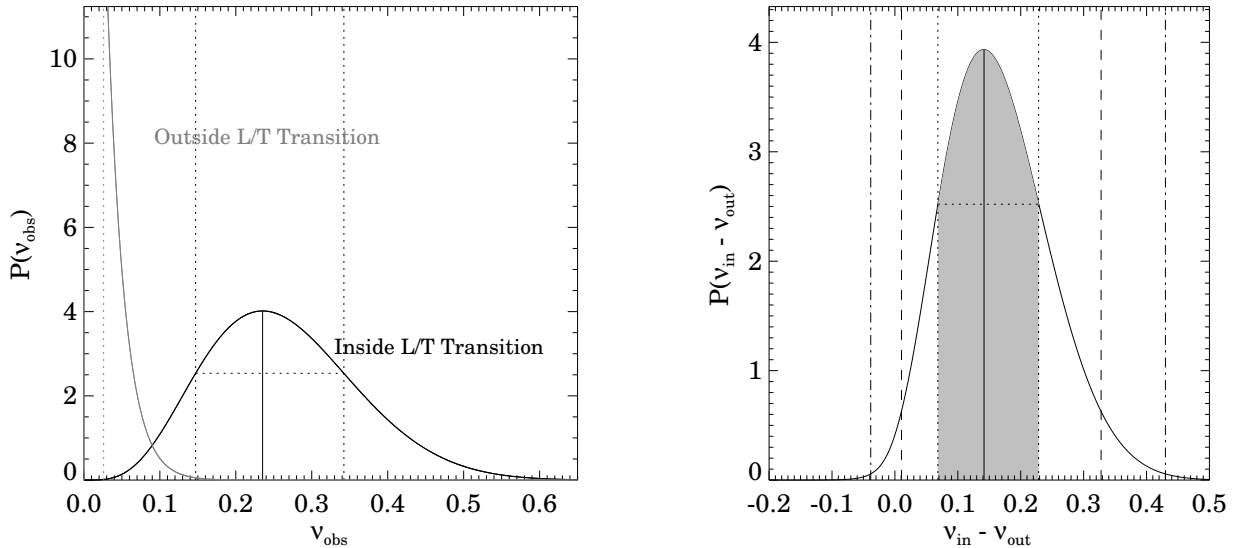


Figure 5.14: *Left*: Probability distributions for the observed frequencies of high amplitude ($>2\%$ peak-to-peak) variability for objects inside (solid black line) and out of (solid grey line) the L/T transition (defined here as L9-T3.5 spectral types). *Right*: Probability distribution for the difference in observed frequency inside and outside of the transition. This distribution is obtained by integrating over the two distributions on the left according to equation 5.6.

5.6 The Frequency of Variability at the L/T Transition

In total we observed 20 targets with spectral types of L9-T3.5, which we consider here as the L/T transition (see figure 5.13). Of these targets we eliminated three from the statistical sample due to known binarity: 2M0423, 2M0518 and 2M1404, leaving 17 objects. Of these 17 objects, 4 show evidence of significant variability: 2M2139, SIMP0136, 2M0758, and SIMP1629 (another object, SDSS1750+42, shows marginal

evidence for variability). The probability distribution for the observed variability frequency, uncorrected for observational biases, was determined in the previous section and is shown in figure 5.14. From this distribution we find an observed variability fraction of $23_{-8}^{+11}\%$. If we include the marginally variable SDSS1750+42 we obtain a fraction of $29_{-9}^{+11}\%$. Thus while we observed a significant increase in variability at the L/T transition, we still find the majority of objects—71-77%—to be non-variable in this regime.

To obtain the “true” fraction of L/T transition objects that are variable (or that would be variable from some observer’s vantage point) we consider our completeness to signals of a given amplitude taking into account our observational sensitivity and a distribution of periods and inclinations of our targets.

To do this we use the sensitivity curve, $F_{\text{sens}}^0(A_0)$, determined from simulations in section 5.4 for L/T transition objects (see figure 5.12). It is important to note that $F_{\text{sens}}^0(A_0)$, as constructed from simulations, accounts not only for objects where variability is missed due to unfavorable inclinations, but also for objects that are not highly variable due to unfavorable latitudes of spot features.

The completeness to amplitudes similar to those detected is estimated as:

$$C \approx \frac{1}{N_v} \sum_{i=1}^{N_v} F_{\text{sens}}^0(A_i) \quad (5.7)$$

where we have summed over $N_v = 4$ targets with amplitudes $>2\%$. Dividing the observed variability fraction by C should result in an estimate of the true fraction.

In the case of the “short” period distribution we find $C = 0.63$, while for the “long” period distribution we obtain $C=0.46$. These sensitivities imply that the true fraction of L/T transition objects with cloud features/asymmetries capable of producing large variability (for favorable geometries) is $\sim 37\%-50\%$ depending on assumptions made about the underlying period distribution of L and T dwarfs. Below, three additional corrections that may increase this fraction are considered.

Binarity

As discussed in chapter 4, it has been suggested that binaries may be more frequent among objects with unresolved L/T transition spectral types. Binarity confuses the analysis because (i) the component spectral types can be significantly different than the unresolved spectral type, allowing components straddling the L/T transition to masquerade as a bonafide transition object and hence dilute the sample, and (ii) even if one component is an L/T transition object, the flux contribution of the companion will diminish the strength of any variability signal, causing our presumed detection limits to be inaccurate. Therefore, it is important to understand what contribution binaries make to our sample. In chapter 4 the most recent estimate of the resolved binary fraction in the L/T transition was determined to be $14_{-5}^{+7}\%$. If the spectroscopic binary fraction is as high as the resolved binary fraction, as has been suggested by radial velocity surveys of young BDs (Maxted & Jeffries 2005; Joergens 2008), then up to 30% of our L/T transition sample may be binaries. Since 3 binaries were already excluded from the sample (2M1404, 2M0518, and 2M0423), the pre-exclusion expectation would be to find at most $0.3 \times 20 \approx 6$ binaries in our sample. Thus, we may reasonably expect up to three more, which would increase our estimated variable fraction to 41-65%.

Colors and spectral types of variable objects

An additional possibility is that the color and spectral type range where variability is observed is more narrow than the broadly defined L9-T3.5 range used here. The onset of this region should correspond with the development of cloud holes in the atmosphere, but the endpoint need not correspond with their disappearance. As cloud holes develop and the underlying atmosphere is allowed to cool, the temperature (and hence flux) contrast between the cloud tops and clearings will decrease. In addition, since high temperature regions quickly dominate the total flux, the contrast between clouds and clearings is greatest (and the size of cloud features required

to produce a given amplitude of variability smallest) when clouds cover a larger fraction of the atmosphere (e.g., see figure 3.10 in chapter 3). Therefore it would not be surprising if amplitudes of variability become much smaller before clouds have completely dissipated. The idea that the observed properties of highly variable objects may fall into a very specific region of color space is supported by the narrow range in $J - K_s$ (0.89-1.3) and NIR spectral types (11.5-12.5) of our four strong detections. If we confine our sample to only objects with $1.4 < J - K < 0.7$ and T1-T3 spectral types we are left with 13 objects-, or a 23% reduction in the sample size, which would suggest true variability fractions as high as 54 – 85% for the subsample. Therefore, while we only observe large amplitude variability for $\sim 20\%$ of our L/T transition sample, it is possible that patchy, asymmetric cloud structures responsible for causing such variability exist for majority of T1-T3 objects with $1.4 < J - K < 0.7$.

Symmetric patches and the variability duty cycle

Finally, it is possible that some L/T transition objects possess cloud patches or holes that are azimuthally symmetric (e.g., bands or small-scale structures) that do not give rise to variability. Furthermore, the evolution of cloud features may lead to different levels of asymmetry and variability at different epochs. For instance, SIMP0136 was observed to have an amplitude of variability as high as $\sim 5\text{-}8\%$ in September 2008 (Artigau et al. 2009), but went through a quiescent phase (amplitude $< 1\%$) in February 2010 before returning to full strength in November 2011 (see E. Artigau’s contribution to the *Clouds in Brown Dwarfs and Giant Planets* Splinter Session of the Cool Stars 17 Meeting in Barcelona, 2012, Metchev et al. in Press). Therefore a variable fraction < 1 may in part reflect a duty cycle for cloud and weather related variability in any given L/T transition atmosphere.

5.7 Discussion and Conclusions

In this chapter the results of a large survey for variability of late-L and T BDs was presented, with the aim of testing the cloud-hole hypothesis: if the development of cloud holes is responsible for the rapid decline in condensate opacity across \sim L9-T4 spectral types, then these objects should be variable on rotational timescales. To test this hypothesis we obtained continuous light curves over 1.5 hr-6 hr baselines for 62 unique targets spanning mid L to T spectral types, 57 of which were considered in our statistical sample. Our major result is summarized in figure 5.13: large-amplitude variability (peak-to-peak amplitudes $>2\%$) are observed exclusively within the L/T transition, with an observed variability fraction of $\nu_{obs} = 23_{-8}^{+11}\%$ for L9-T3.5 spectral types. We rule out with 95% confidence that high amplitude variability can be observed with a similar frequency outside the L/T transition.

There are two different interpretations of these results that should be considered. The first is that clouds are significantly disrupted at the L/T transition, leading to large variability (the cloud hole hypothesis of the L/T transition; Ackerman & Marley 2001; Burgasser et al. 2002). This interpretation is attractive because it naturally explains the sudden decrease in cloud opacity at the L/T transition and the corresponding J band brightening. In addition, this behavior was predicted nearly a decade before it was observed. However, if cloud holes are responsible for observed properties of the L/T transition, then most L/T transition objects should be variable. The main detraction from this interpretation is that aggressive completion corrections (assuming a period distribution skewed toward long periods, a 30% binary fraction in our sample, and a narrow spectral type and color range for cloud dissipation) are required in order for the inferred fraction of objects with cloud features capable of producing large amplitude variability approaches unity. However, axisymmetric clearings cloud also explain a lack of variability in some L/T transition objects with patchy cloud coverage. The second interpretation is that discrete and persistent high

altitude cloud features (e.g., cyclonic storms) exist in the atmospheres of most L dwarfs, and the contrast of these features against a thinner cloud layer increases at the L/T transition. This interpretation suggests that low amplitude variables outside the transition become large amplitude variables inside the transition, and does not require that all L/T transition objects are variable. The drawback of this scenario is that another mechanism is still needed to explain features of the L/T transition such as *J* band brightening.

Targeted observations in the future can be used to shed light on which interpretation is correct. If cloud disruption is responsible for observed properties of the L/T transition, then nearly all L/T transition objects should display some evidence for patchy clouds when observed at high enough precision and over long enough baselines. Alternatively, if the cloud features responsible are mostly high altitude storms that are equally present in L and T dwarf atmospheres, then frequencies of low amplitude variability outside the transition should be approximately the same as frequencies of high amplitude variability inside the transition (i.e., only the size, not the frequency of variability changes). Additionally, if the cloud features responsible are mostly high-altitude storms, then long-term monitoring should reveal stable features that persist over long timescales (where significant light curve evolution as seen for SIMP0136 and 2M2139 may be explained by differential rotation between stable features). Further monitoring of BDs over a wide range of spectral types at even higher precision (e.g., from space) should reveal whether the overall fraction of variable objects at any amplitude is similar inside and outside the L/T transition and whether the mechanisms involved are fundamentally similar or different in each regime.

Table 5.1. Observing Log

Name	Ref ^a	Camera	Date	Δt	t_{exp}	N_{obs}	Median FWHM	σ_{raw}^b	Type ^c
2MASSW J0030300-145033	2	WIRC	2009-09-26T04:24:40	4.49	60.0	188	0.99	0.01	D
2MASS J00501994-3322402	3	WIRC	2009-08-02T07:37:18	3.26	60.0	175	0.73	0.10	S
SIMP J013656.57+093347.3	4	WIRC	2009-07-31T08:44:56	2.32	40.0	177	1.42	0.03	S
SDSS J015141.69+124429.6	5	WIRCam	2009-12-30T04:57:02	3.72	40.0	270	0.65	0.01	S
SDSS J020742.48+000056.2	5	WIRC	2009-09-25T06:02:03	3.97	60.0	166	1.20	0.02	D
2MASS J0243137-245329	6	WIRC	2009-08-10T07:36:13	3.16	40.0	184	1.21	0.02	D
2MASS J02572581-3105523	7	WIRC	2009-09-30T05:49:55	3.93	30.0	379	1.19	0.01	S
2MASS J03185403-3421292	7	WIRC	2009-09-24T05:55:46	4.28	60.0	179	0.74	0.02	D
2MASS J0328426+230205	2	WIRCam	2009-12-26T05:14:20	3.69	40.0	270	0.38	0.02	S
2MASS J0415195-093506	6	WIRC	2009-09-23T06:07:36	3.79	60.0	203	0.84	0.01	S
SDSSp J042348.57-041403.5	5	WIRC	2009-10-02T06:26:36	3.57	45.0	241	1.12	0.02	S
2MASS J05103520-4208140	8	WIRC	2010-02-04T00:46:13	3.33	60.0	172	0.99	0.03	D
2MASS J05160945-0445499	9	WIRC	2009-09-22T06:11:15	3.99	60.0	171	1.10	0.01	D
2MASS J05185995-2828372	10	WIRC	2010-02-03T00:08:53	3.79	60.0	178	0.88	0.02	S
SDSSp J053951.99-005902.0	11	WIRC	2010-02-07T00:27:30	1.72	45.0	119	1.29	0.01	S

Table 5.1 (cont'd)

Name	Ref ^a	Camera	Date	Δt	t_{exp}	N_{obs}	Median FWHM	σ_{raw}^b	Type ^c
2MASS J05591914-1404488	12	WIRC	2010-02-01T00:31:38	3.52	45.0	242	1.03	0.07	S
UGPS J072227.51-054031.2	13	WIRC	2010-04-22T23:24:07	1.74	60.0	71	1.05	0.02	D
2MASS J07290002-3954043	8	WIRC	2010-02-02T01:02:15	3.13	60.0	138	0.82	0.26	D
SDSS J074201.41+205520.5	1	WIRCam	2009-12-27T10:47:08	3.72	40.0	270	0.57	0.01	S
SDSS J075840.33+324723.4	1	WIRCam	2009-12-26T10:15:20	3.54	15.0	476	2.31	0.00	S
DENIS J081730.0-615520	14	WIRC	2010-04-23T23:25:45	3.99	45.0	215	0.77	0.04	D
SDSS J083048.80+012831.1	1	WIRC	2010-02-08T00:24:18	3.75	60.0	166	1.13	0.01	D
SDSS J093109.56+032732.5	1	WIRC	2010-03-30T00:05:51	4.43	60.0	197	0.82	0.02	D
2MASS J09393548-2448279	3	WIRC	2010-04-02T23:29:53	5.92	60.0	262	0.79	0.07	D
2MASS J09490860-1545485	3	WIRC	2010-03-26T01:04:35	4.48	40.0	333	0.83	0.02	S
2MASS J10073369-4555147	8	WIRC	2010-01-31T03:34:10	3.56	30.0	244	0.76	0.02	D
2MASSW J1036530-344138	15	WIRC	2010-03-28T01:43:22	4.52	60.0	179	1.05	0.02	D
SDSS J104829.21+091937.8	16	WIRC	2010-03-31T01:14:03	4.14	60.0	184	0.78	0.02	D
SDSSp J111010.01+011613.1	5	WIRC	2010-04-03T23:46:45	5.72	60.0	244	0.84	0.01	D
2MASS J11145133-2618235	3	WIRC	2010-03-29T03:03:22	3.13	60.0	140	0.99	0.02	D

Table 5.1 (cont'd)

Name	Ref ^a	Camera	Date	Δt	t_{exp}	N_{obs}	Median FWHM	σ_{raw}^b	Type ^c
2MASS J11220826-3512363	3	WIRC	2010-02-01T06:07:16	2.76	60.0	122	0.73	0.02	D
2MASS J11263991-5003550	17	WIRC	2010-04-26T23:20:23	4.91	45.0	338	1.24	0.02	S
SDSS J115553.86+055957.5	1	WIRC	2010-05-04T23:32:28	4.57	60.0	196	1.01	0.04	D
SDSS J120747.17+024424.8	18	WIRC	2010-02-08T04:55:18	3.84	60.0	181	1.23	0.01	S
2MASS J12095613-1004008	19	WIRC	2010-02-07T05:31:00	3.13	60.0	168	1.21	0.02	S
2MASS J12154432-3420591	8	WIRC	2010-03-27T03:57:43	3.42	60.0	143	0.87	0.03	D
2MASS J1217110-031113	20	WIRC	2010-04-23T01:28:51	3.18	60.0	140	0.73	0.07	D
2MASS J12314753+0847331	19	WIRC	2010-02-09T05:39:00	3.16	60.0	139	1.35	0.02	D
SDSSp J125453.90-012247.4	21	WIRC	2010-02-02T05:43:40	3.10	45.0	143	0.95	0.45	D
SDSSp J132629.82-003831.5	11	WIRC	2010-04-02T06:08:34	2.60	60.0	108	0.64	0.03	D
SDSS J140255.66+080055.2	16	WIRC	2010-03-30T04:53:38	3.19	60.0	143	0.99	0.01	D
2MASS J14044941-3159329	8	WIRC	2010-03-28T06:32:51	4.02	60.0	178	1.09	0.03	D
SDSS J141624.08+134826.7	22	WIRC	2010-05-04T03:28:04	3.24	30.0	218	0.98	0.02	D
DENIS-P J142527.97-365023.4	23	WIRC	2010-04-25T04:25:08	2.98	45.0	161	0.86	0.02	D
2MASSW J1507476-162738	24	WIRC	2010-04-06T05:22:58	5.24	40.0	427	0.72	0.14	D

Table 5.1 (cont'd)

Name	Ref ^a	Camera	Date	Δt	t_{exp}	N_{obs}	Median FWHM	σ_{raw}^b	Type ^c
SDSS J151114.66+060742.9	16	WIRC	2010-03-26T07:12:40	2.92	60.0	157	0.86	0.02	S
SDSS J152103.24+013142.7	1	WIRC	2010-03-27T07:38:15	2.91	60.0	120	1.19	0.02	D
2MASS J1546291-332511	6	WIRC	2009-07-29T00:44:34	3.79	60.0	203	0.97	0.02	S
SDSSp J162414.37+002915.6	25	WIRC	2009-08-09T23:33:14	3.58	60.0	192	1.38	0.20	S
SIMP J162918.41+033537.0	29	WIRC	2009-07-29T23:47:39	4.03	60.0	216	0.96	0.01	S
SDSS J163359.23-064056.5	16	WIRC	2010-04-22T05:13:23	5.44	60.0	249	0.86	0.01	D
DENIS-P J170548.38-051645.7	23	WIRC	2010-04-25T07:47:48	3.04	25.0	235	0.90	0.02	D
SDSS J175024.01+422237.8	1	WIRCam	2009-08-09T07:53:44	2.63	40.0	224	0.96	0.03	S
2MASS J17502484-0016151	26	WIRC	2010-05-01T06:05:06	2.63	30.0	250	1.70	0.03	S
2MASS J18283572-4849046	19	WIRC	2009-08-11T00:55:16	4.13	40.0	314	0.90	0.04	S
2MASS J19360187-5502322	27	WIRC	2010-05-04T07:00:42	3.73	45.0	195	0.90	0.01	D
SDSS J205235.31-160929.8	16	WIRC	2009-07-30T04:41:41	3.69	60.0	198	0.89	0.01	S
2MASS J21392676+0220226	27	WIRC	2009-08-02T04:38:41	2.50	40.0	140	0.71	0.05	D
2MASS J21513839-4853542	28	WIRC	2009-07-29T05:34:29	4.28	60.0	229	0.96	0.01	S
2MASS J22282889-4310262	9	WIRC	2009-08-01T05:03:12	5.73	60.0	307	1.49	0.01	S

Table 5.1 (cont'd)

Name	Ref ^a	Camera	Date	Δt	t_{exp}	N_{obs}	Median FWHM	σ_{raw}^b	Type ^c
2MASS J2254188+312349	6	WIRCam	2009-11-03T05:28:16	3.37	40.0	231	1.60	0.01	S
2MASS J23312378-4718274	19	WIRC	2009-09-30T00:02:44	4.09	60.0	212	1.31	0.02	S

^aDiscovery references

^bRMS deviations of the normalized, raw light curves. Large values indicate variable or cloudy observing conditions.

^cMethod used to obtain light curve. D="dithered", S="staring"

References. — (1)Knapp et al. (2004) (2)Kirkpatrick et al. (2000) (3)Tinney et al. (2005) (4)Artigau et al. (2006) (5)Geballe et al. (2002) (6)Burgasser et al. (2002) (7)Kirkpatrick et al. (2008) (8)Looper, Kirkpatrick, & Burgasser (2007) (9)Burgasser, McElwain, & Kirkpatrick (2003) (10)Cruz et al. (2004) (11)Fan et al. (2000) (12)Burgasser et al. (2000)b (13)Lucas et al. (2010) (14)Artigau et al. (2010) (15)Gizis (2002) (16)Chiu et al. (2006) (17)Folkes et al. (2007) (18)Hawley et al. (2002) (19)Burgasser et al. (2004) (20)Burgasser et al. (1999) (21)Leggett et al. (2000) (22)Bowler, Liu, & Dupuy (23)Kendall et al. (2004) (24)Reid et al. (2000) (25)Strauss et al. (1999) (26)Kendall et al. (2007) (27)Reid et al. (2008) (28)Ellis et al. (2005) (29)Artigau et al., in prep

Table 5.2. Target Information

Name	SpT	Ref ^a	J	$J - K_s$	σ_n	β	$A(f_{det} = 0.5)$
2MASSW J0030300-145033	L7	2	16.28±0.11	1.80±0.15	0.0213478	0.689049	0.015
2MASS J00501994-3322402	T7	1	15.93±0.07	0.69±0.20	0.0108944	0.582236	0.01
SIMP J013656.57+093347.3	T2.5	3	13.45±0.03	0.89±0.04	0.00842237	3.68826	0.0125
SDSS J015141.69+124429.6	T1	1	16.57±0.13	1.38±0.23	0.00649816	0.613666	0.0075
SDSS J020742.48+000056.2	T4.5	1	16.80±0.16	0.41±0.19	0.0459007	0.583418	0.0225
2MASS J0243137-245329	T6	1	15.38±0.05	0.16±0.18	0.0113388	0.402831	0.0125
2MASS J02572581-3105523	L8	4	14.67±0.04	1.80±0.05	0.00617618	0.839165	0.0075
2MASS J03185403-3421292	L7	4	15.57±0.05	2.06±0.07	0.0119432	0.485385	0.01
2MASS J0328426+230205	L9.5	5	16.69±0.14	1.78±0.18	0.00598806	0.542144	0.0075
2MASS J0415195-093506	T8	1	15.69±0.06	0.27±0.21	0.00680025	0.666069	0.0075
SDSSp J042348.57-041403.5	T0	1	14.47±0.03	1.54±0.04	0.00550973	1.76033	0.0075
2MASS J05103520-4208140	T5	6	16.22±0.09	0.23±0.30	0.0188281	0.143519	0.0175
2MASS J05160945-0445499	T5.5	1	15.98±0.08	0.50±0.22	0.0141805	0.282821	0.01
2MASS J05185995-2828372	T1p	1	15.98±0.10	1.82±0.12	0.0138961	0.729296	0.01
SDSSp J053951.99-005902.0	L5	7	14.03±0.03	1.51±0.04	0.00411029	0.599209	0.01
2MASS J05591914-1404488	T4.5	1	13.80±0.02	0.23±0.06	0.0035923	2.14758	0.0075
UGPS J072227.51-054031.2	T9	8	16.49±0.13	16.49±0.13	0.0395804	0.35192	0.0475

Table 5.2 (cont'd)

Name	SpT	Ref ^a	J	$J - K_s$	σ_a	β	$A(f_{det} = 0.5)$
2MASS J07290002-3954043	T8pec	6	15.92±0.08	-0.59±0.13	0.0179608	0.292615	0.0175
SDSS J074201.41+205520.5	T5	1	16.19±0.09	0.00±0.14	0.0039772	0.85264	0.0075
SDSS J075840.33+324723.4	T2	1	14.95±0.04	1.07±0.07	0.00673976	11.7344	0.0075
DENIS J081730.0-615520	T6	9	13.61±0.02	0.09±0.05	0.00479058	1.92507	0.0075
SDSS J083048.80+012831.1	T4.5	1	16.29±0.11	0.12±0.15	0.0220512	0.39159	0.0175
SDSS J093109.56+032732.5	L7.5±1.5	5	16.61±0.14	0.88±0.14	0.0357241	0.473958	0.0225
2MASS J09393548-2448279	T8	1	15.98±0.11	-0.87±0.15	0.0145961	0.610793	0.01
2MASS J09490860-1545485	T2	1	16.15±0.12	0.92±0.20	0.0120732	0.66844	0.01
2MASS J10073369-4555147	T5	6	15.65±0.07	0.09±0.24	0.0112904	0.728856	0.01
2MASSW J1036530-344138	L6	10	15.62±0.05	1.82±0.06	0.0112607	0.5562	0.0075
SDSS J104829.21+091937.8	T2.5	11	16.59±0.15	0.83±0.18	0.0363438	0.32673	0.0225
SDSSp J111010.01+011613.1	T5.5	1	16.34±0.12	0.38±0.15	0.0203048	0.568172	0.0125
2MASS J11145133-2618235	T7.5	1	15.86±0.08	-0.59±0.13	0.0176909	0.454421	0.0175
2MASS J11220826-3512363	T2	1	15.02±0.04	0.64±0.08	0.008463	0.316188	0.01
2MASS J11263991-5003550	L4.5	12	14.00±0.03	1.17±0.04	0.0045686	4.77132	0.005
SDSS J115553.86+055957.5	L7.5	5	15.66±0.08	1.54±0.11	0.0129667	0.25051	0.015
SDSS J120747.17+024424.8	T0	1	15.58±0.07	1.59±0.09	0.0156794	0.306641	0.0125

Table 5.2 (cont'd)

Name	SpT	Ref ^a	J	$J - K_s$	σ_a	β	$A(f_{det} = 0.5)$
2MASS J12095613-1004008	T3	1	15.91±0.07	0.85±0.16	0.0139965	0.372624	0.015
2MASS J12154432-3420591	T4.5	6	16.24±0.13	0.37±0.17	0.0172968	0.471379	0.015
2MASS J1217110-031113	T7.5	1	15.86±0.06	0.17±0.12	0.0171376	0.478372	0.015
2MASS J12314753+0847331	T5.5	1	15.57±0.07	0.35±0.21	0.0141144	0.700769	0.015
SDSSp J125453.90-012247.4	T2	1	14.89±0.04	1.05±0.06	0.0207109	0.1875	0.02
SDSSp J132629.82-003831.5	L8	7	16.10±0.07	1.90±0.10	0.021919	0.443988	0.025
SDSS J140255.66+080055.2	T1.5	11	16.84±0.18	1.25±0.31	0.0462038	0.226435	0.0275
2MASS J14044941-3159329	T2.5	6	15.58±0.06	1.04±0.11	0.0150924	0.316022	0.0125
SDSS J141624.08+134826.7	L6	13	13.15±0.03	1.03±0.03	0.00728502	1.39056	0.01
DENIS-P J142527.97-365023.4	L3	14	13.75±0.03	1.94±0.04	0.00494556	1.33823	0.0075
2MASSW J1507476-162738	L5	2	12.83±0.03	1.52±0.04	0.00595229	0.458516	0.005
SDSS J151114.66+060742.9	T0±2	11	16.02±0.08	1.47±0.13	0.0135246	0.511835	0.015
SDSS J152103.24+013142.7	T2	1	16.40±0.10	1.05±0.20	0.0276994	0.374618	0.0275
2MASS J1546291-332511	T5.5	1	15.63±0.05	0.15±0.19	0.00837629	0.491749	0.0075
SDSSp J162414.37+002915.6	T6	1	15.49±0.05	-0.03±0.11	0.0170824	0.449016	0.015
SIMP J162918.41+033537.0	T2.5		15.29±0.04	1.06±0.07	0.0084	3.5139	0.0075
SDSS J163359.23-064056.5	L6	11	16.14±0.09	1.59±0.13	0.014591	0.52824	0.01

Table 5.2 (cont'd)

Name	SpT	Ref ^a	J	$J - K_s$	σ_a	β	$A(f_{det} = 0.5)$
DENIS-P J170548.38-051645.7	L4	15	13.31±0.03	1.28±0.04	0.00768815	0.305532	0.01
SDSS J175024.01+422237.8	T2	1	16.47±0.10	0.98±0.20	0.0129167	1.37535	0.01
2MASS J17502484-0016151	L5.5	16	13.29±0.02	1.44±0.03	0.00480147	0.989332	0.01
2MASS J18283572-4849046	T5.5	1	15.18±0.06	-0.01±0.15	0.00632607	2.3048	0.0075
2MASS J19360187-5502322	L5	14	14.49±0.04	1.44±0.05	0.00733857	1.08872	0.0075
SDSS J205235.31-160929.8	T1±1	11	16.33±0.12	1.21±0.19	0.0114658	0.688075	0.01
2MASS J21392676+0220226	T1.5	1	15.26±0.05	1.68±0.07	0.0117246	5.22856	0.015
2MASS J21513839-4853542	T4	1	15.73±0.07	0.30±0.20	0.00924446	0.837887	0.0075
2MASS J22282889-4310262	T6	1	15.66±0.07	0.37±0.22	0.0138886	2.33914	0.0075
2MASS J2254188+312349	T4	1	15.26±0.05	0.36±0.15	0.00761563	0.389159	0.01
2MASS J23312378-4718274	T5	1	15.66±0.07	0.27±0.21	0.0177453	0.576966	0.0125

^aSpectral type references

References. — (1)Burgasser et al. (2006) (2)Kirkpatrick et al. (2000) (3)Artigau et al. (2006) (4)Kirkpatrick et al. (2008) (5)Knapp et al. (2004) (6)Looper, Kirkpatrick, & Burgasser (2007) (7)Fan et al. (2000) (8)Lucas et al. (2010) (9)Artigau et al. (2010) (10)Gizis (2002) (11)Chiu et al. (2006) (12)Burgasser et al. (2008) (13)Bowler, Liu, & Dupuy (2014) (14)Reid et al. (2008) (15)Kendall et al. (2004) (16)Kendall et al. (2007) (17)Artigau et al. in prep

Table 5.3. Detections

Name	SpT	J	$J - K_s$	A (%)	P (hr)	Notes
SIMP J013656.57+093347.3	T2.5	13.45	0.89	3	2.4 ^a	First reported by (1)
SDSS J075840.33+324723.4	T2	14.95	1.07	4.5	5 ^b	New detection
2MASS J11263991-5003550	L4.5pec	14.00	1.17	1.5	3.6	New detection
SIMP J162918.41+033537.0	T2.5	15.06	1.06	3 ^d	6 ^b	New detection
2MASS J18283572-4849046	T5.5	15.18	0.	1	...	Suspicious; similar trend in comparison star.
2MASS J21392676+0220226	T1.5	15.26	1.27	9	7.72 ^c	New Detection
2MASS J22282889-4310262	T6	15.66	0.37	1.5	1.43	First reported by (2)

^aPeriod measurement from (Artigau et al. 2009)

^bPeriod measurement from Spitzer program 80213 (PI: Radigan), courtesy of Dr. Nick Cowan

^cPeriod measurement from chapter 3; potentially twice as long (15.44 hr)

^dAn amplitude of 5% was observed at a later epoch for this target)

References. — (1)Artigau et al. (2009); (2)Clarke et al. (2008)

Chapter 6

Summary, Conclusions & Future Work

6.1 Summary and Conclusions

Understanding condensate clouds in substellar atmospheres is a challenging yet important problem. The derivation of key parameters such as masses, temperatures, and compositions for both brown dwarfs and giant planets depend strongly on model assumptions made about the vertical location, scale height, and surface distribution of dust clouds (e.g., Skemer et al. 2011; Barman et al. 2011). The work presented in this Thesis has contributed to understanding the role dust clouds play in determining the spectral energy distributions of L dwarfs (chapter 2) as well as their role in mediating the L-dwarf/T-dwarf transition (chapters 3-5), with a particular focus on surface heterogeneities.

In chapter 2 the discovery of an L-dwarf companion (2MASS J17114559+4028578) to a nearby M dwarf was described. The potential to constrain properties of the BD using properties of the main sequence primary makes this system a rare benchmark for understanding the relative role of clouds, gravity, and metallicity in the emergent colors of L dwarfs. With a $J - K_s$ color of 1.28, 2MASS J17114559+4028578 is unusually blue for its spectral type. While extreme blue colors are often attributed to low-metallicity, the M-dwarf primary G 203–50 showed no evidence of being metal poor.

Furthermore, the 656 nm $H\alpha$ feature in its spectrum may be a sign of moderate youth ($t \lesssim 5$ Gyr). It was therefore argued that its unusually blue colors must be caused by abnormally thin or patchy condensate clouds. This result suggests that clouds play a leading role in determining the colors of L dwarfs within a given spectral type. By chapter 5 this hypothesis finds additional support with a strong detection of variability in another unusually blue L dwarf, 2M1126-50, which may be direct evidence for patchy clouds in its atmosphere, and potentially the cause of its unusually blue colors.

In chapter 3 the discovery of large-amplitude variability for the T1.5 dwarf 2MASS J21392676+0220226 was presented, and high precision, multi-color JHK_s light curves of its variability were analyzed and compared to the predictions of model atmospheres. This object was the second brown dwarf after SIMP 0136 (Artigau et al. 2009) reported to display significant and repeatable variability in the NIR. It not only demonstrated that SIMP 0136 wasn't an oddball, but also conformed to our suspicions that variability would be found in the L/T transition. With absolute variations as high as 26% in the J band and color variations as large as $\Delta J - K_s = 0.15$, these observations show that clouds alone can alter the brightness and colors of BDs, without variations in surface gravity or metallicity. Comparisons to model atmospheres revealed that regions of differing cloud thickness *and* effective temperatures are responsible for the variations, with thick cloud regions being cooler by ~ 250 -400 K. Two distinct solutions emerged. The best model fit corresponded to an atmosphere with a moderately thin cloud layer and thick cloud features (possibly high altitude storms) occupying $\sim 25\%$ of the visible disk. The second best model fit consisted of an atmosphere composed of very thick and thin cloud regions in a $\sim 60:40$ ratio, and with a $\sim 12\%$ asymmetry between the brightest and darkest hemispheres. Notably, models of true clearings (i.e., zero condensate regions) in an otherwise cloudy atmosphere did not fit the data, leading us to speculate that "clearings" may retain some degree of condensate opacity. It is interesting that the two best-fitting surface models for 2M2139 mirror the two

possible interpretations of the L/T transition variability found in chapter 5 (i.e., increasing contrast of pre-existing high-altitude cloud features, versus the development of cloud holes, at the L/T transition).

In chapter 4, a Keck LGS AO mini survey of L/T transition objects for binarity was presented with the motivation of understanding the contribution of binaries to our unresolved L/T transition sample surveyed for variability. Combining our results with those from other observational surveys we determined an L/T transition resolved binary fraction of $14_{-6}^{+7}\%$, consistent with the binary fraction found for the brown dwarf population in general (Burgasser et al. 2003a; 2006b; Reid et al. 2008; Bouy et al. 2003). We did not find binaries to be overabundant in this regime, which implies that our L/T transition sample surveyed for variability in chapter 5 is no more likely to be contaminated by binaries than the non-L/T transition sample. In addition, these observations fortuitously revealed the first *visual* brown dwarf triple system, 2M0838+15ABC, and properties of this system are also reported. Resolved OSIRIS spectra revealed component spectral types of T3-T3.5, placing all components in the L/T transition regime. Surprisingly, the more massive component appears to be furthest evolved along the L/T transition sequence on a color magnitude diagram. Since the inferred surface gravities between components differ by no more than ~ 0.1 dex according to evolutionary models, we argue that differing fractional cloud coverage (possibly due to different viewing angles) is responsible. With the possibility of a dynamical mass measurement for the tight BC components, in the future this system can (i) be used to constrain evolutionary and atmosphere models in the puzzling L/T transition, and (ii) act as a gravity benchmark to constrain the influence of surface gravity on condensate cloud structure. In addition to pursuing a dynamical mass, it will be interesting to monitor this system for variability.

Despite the suggestion made over a decade ago that the disruption of a homogeneous cloud layer may be responsible for key observed properties of the L/T transition

(Ackerman & Marley 2001; Burgasser et al. 2002), until the present work, no link between variability and spectral type has been established. This Thesis, for the first time, demonstrates a connection between large amplitude variability indicative of patchy clouds, and L/T transition spectral types. In chapter 5 results were presented from a *J* band variability survey of 62 objects spanning mid-L to late-T spectral types, representing the most comprehensive search to date. Large amplitude variability (defined here as peak-to-peak amplitudes $>2\%$) were found exclusively in the L/T transition (4 of 17 objects in the statistical sample, or $23_{-8}^{+11}\%$) while no variability of similar amplitude was found for 40 non-L/T transition objects. Equal rates of high amplitude variability both inside and out of the L/T transition regime were excluded with 95% confidence. Taking completeness corrections into account it was argued that the majority of L/T transition objects with T1-T3 spectral types and $0.7 < J - K_s < 1.4$ possess discrete cloud holes or patches required to produce such variability. There are two possible interpretations of these results. The first, is that cloud holes and patches develop at the L/T transition and are directly responsible for observed properties such as *J*-band brightening. The second is that cloud heterogeneities or discrete features exist for all spectral types, and their contrast against the underlying atmosphere simply increases in the L/T transition. In the latter case another mechanism is still required to explain *J*-band brightening.

Although the present work demonstrates the first significant link between variability and L/T transition spectral types, the causal nature of the relationship remains unclear, and is a question to be addressed in future work. Does cloud disruption cause the L/T transition, or does the L/T transition cause pre-existing cloud patches to be more easily observed? Continued monitoring efforts of cool BDs at higher precision, over longer timescales, and with increased wavelength coverage will further constrain the physical nature of the variability. Such observations should test whether the features responsible are predominantly warm clearings (as opposed to cool, high

altitude cloud features), and furthermore, whether the development of such cloud holes at the L/T transition is a sufficient explanation for key features such as *J*-band brightening.

Beyond understanding the L/T transition, the identification of a population of variable BDs with patchy clouds provides two novel opportunities to study substellar atmospheres in unprecedented depth. First, the presence of discrete cloud features provides a means of visualizing atmospheric flows, via the mapping of brightness changes as contrasting cloud features rotate in and out of sight. Second, holes in the cloud layer act as windows to deeper regions of the photosphere, providing a unique probe of the vertical structure of condensates relative to other gaseous absorbers. Thus future observations of variable BDs can and should be leveraged to better understand the atmospheric structure and dynamics of substellar objects in general.

Appendices

Appendix A

Chapter 3 Appendix

A.1 Relative Flux Calibration of SpeX Prism Library Spectra and Synthetic 2MASS Colors

The relative flux calibration between J , H , and K_s bands for M, L, and T dwarf sources in the SpeX Prism Library was investigated by determining synthetic 2MASS colors from the SpeX spectra and comparing them to reported values from the 2MASS catalog. Synthetic 2MASS colors were found using the relative spectral response curves and zero-magnitude fluxes provided by Cohen et al. (2003). The error estimates, σ_{SpeX} are the sum of a random error component determined from the measurement uncertainties associated with individual wavelength bins (typically small), and an additional 0.07 mag corresponding to the average difference in synthetic $J - K_s$ colors computed for (presumed non-variable) targets which have been observed at two epochs within the SpeX Prism Libraries.

Differences between 2MASS colors and SpeX synthetic colors were determined for all M, L and T dwarf sources from the SpeX Prism Library that also had moderate to high quality detections in 2MASS (2MASS catalog QFLG of at least 'C'). For each BD meeting these requirements, the difference between the 2MASS and synthetic SpeX

colors, $\Delta(J - K_s)$, was computed and assigned an uncertainty of

$$\sigma_{\Delta(J-K_s)} = \sqrt{\sigma_J^2 + \sigma_{K_s}^2 + \sigma_{SpeX}^2} \quad (\text{A.1})$$

where σ_J and σ_K are the photometric errors taken directly from the 2MASS catalog. The resultant $\Delta(J - K_s)/\sigma_{J-K_s}$ for all BDs considered is plotted in figure A.1, and shows that 2M2139 is a 4σ outlier. If we consider only L and T-dwarfs the match between 2MASS and SpeX colors is surprisingly good; a gaussian fit to a histogram of $\Delta(J - K_s)/\sigma_{J-K_s}$, also shown in figure A.1, has width of $\sigma \sim 1$ and is roughly centered about zero ($\mu = -0.14$). While differences in $J - K_s$ color are roughly symmetric about zero for L and T dwarfs, there appears to be a small systematic offset for M dwarfs, the origin of which is not clear.

Therefore, uncertainties in synthetic $J - K_s$ colors for SpeX Prism Library L and T dwarf spectra are well estimated by propagating the standard errors reported for each wavelength bin, and then adding to this 0.07 mag.

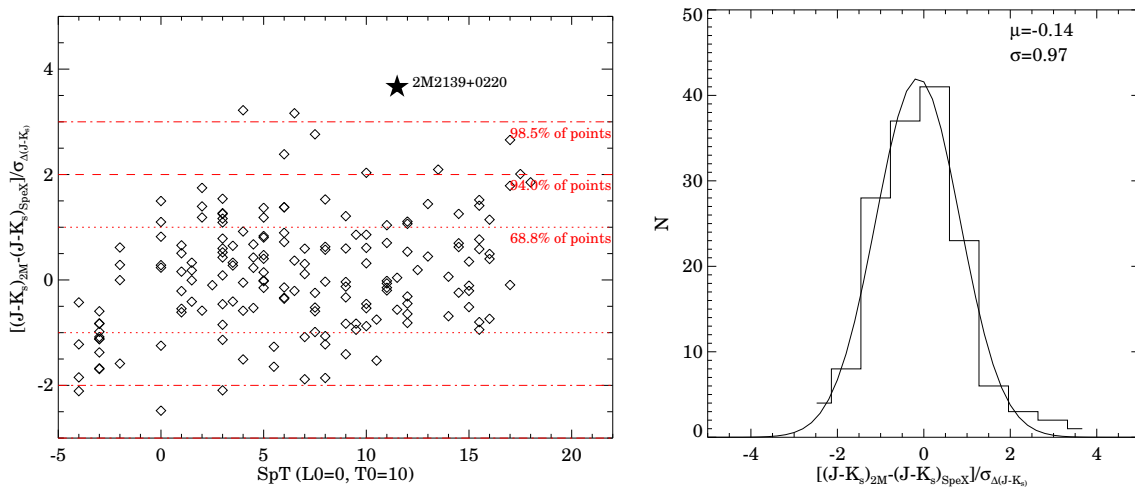


Figure A.1: Comparison between 2MASS photometry and synthetic 2MASS colors derived from SpeX prism spectra for all L and T dwarfs in the SpeX prism library. Sources flagged in the prism library as having a poor SNR, or those with poor quality J and/or K_s 2MASS photometry (Point Source Catalog quality flag not equal to 'A', 'B', or 'C'), were omitted.

A.2 Models for 2M2139's Variability at Additional Epochs

In section 3.6.1 we presented simultaneous model fits to both the NIR spectrum and multi-color variability of 2M2139. The model fits presented were constrained using A_H/A_J and A_{K_s}/A_J amplitude ratios measured from the simultaneous JHK_s light curves obtained on 30 Sep 2009 (figure 3.12). Here we provide equivalent model fits constrained using amplitude ratios measured from the other two epochs for which we obtained simultaneous JHK_s light curves: 26 Sep 2009 (figure A.2), and 01 Oct 2009 (figure A.3).

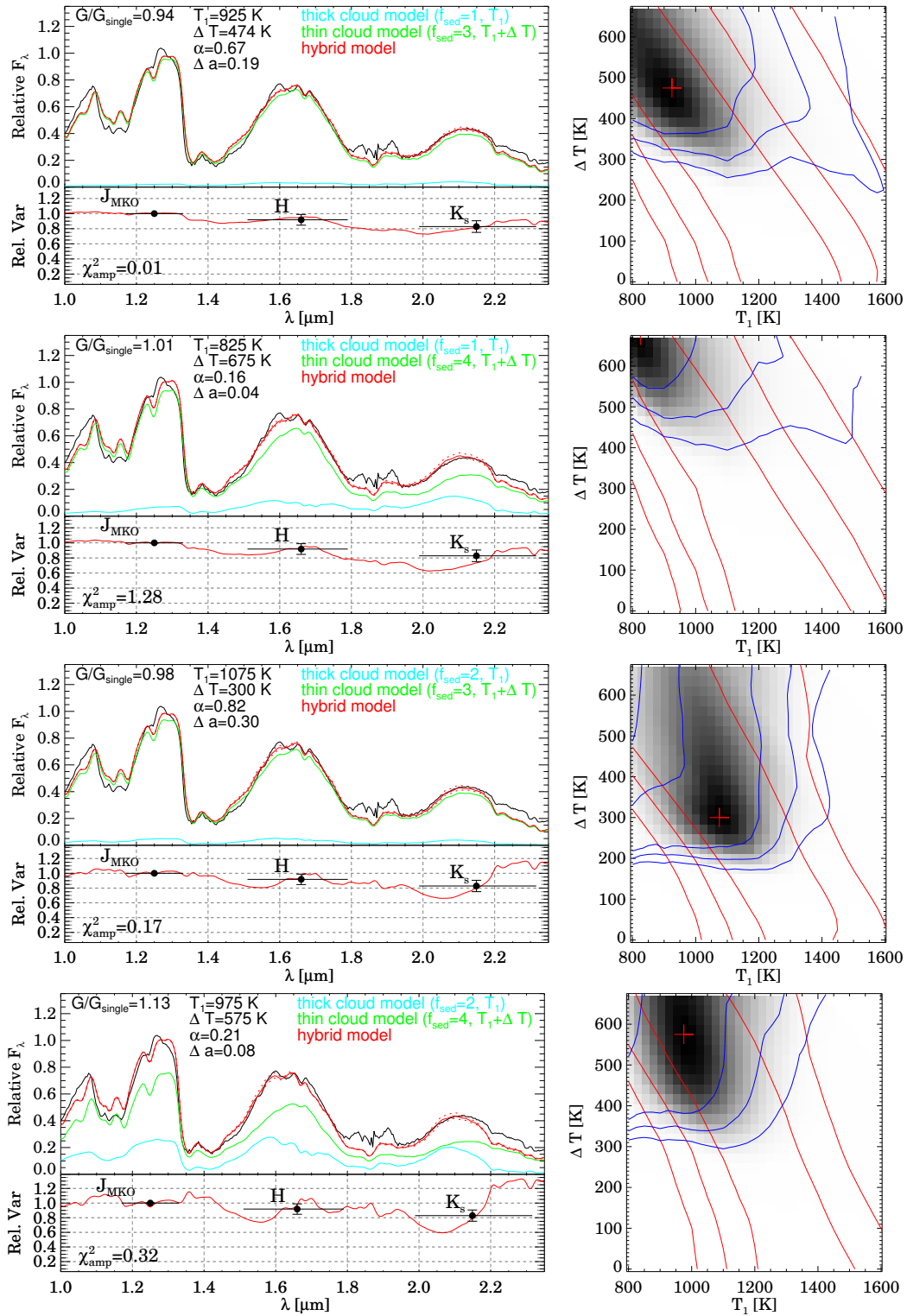


Figure A.2: Same as figure 3.12, but with amplitude ratios constrained using data from the 26 Sep 2009 epoch.

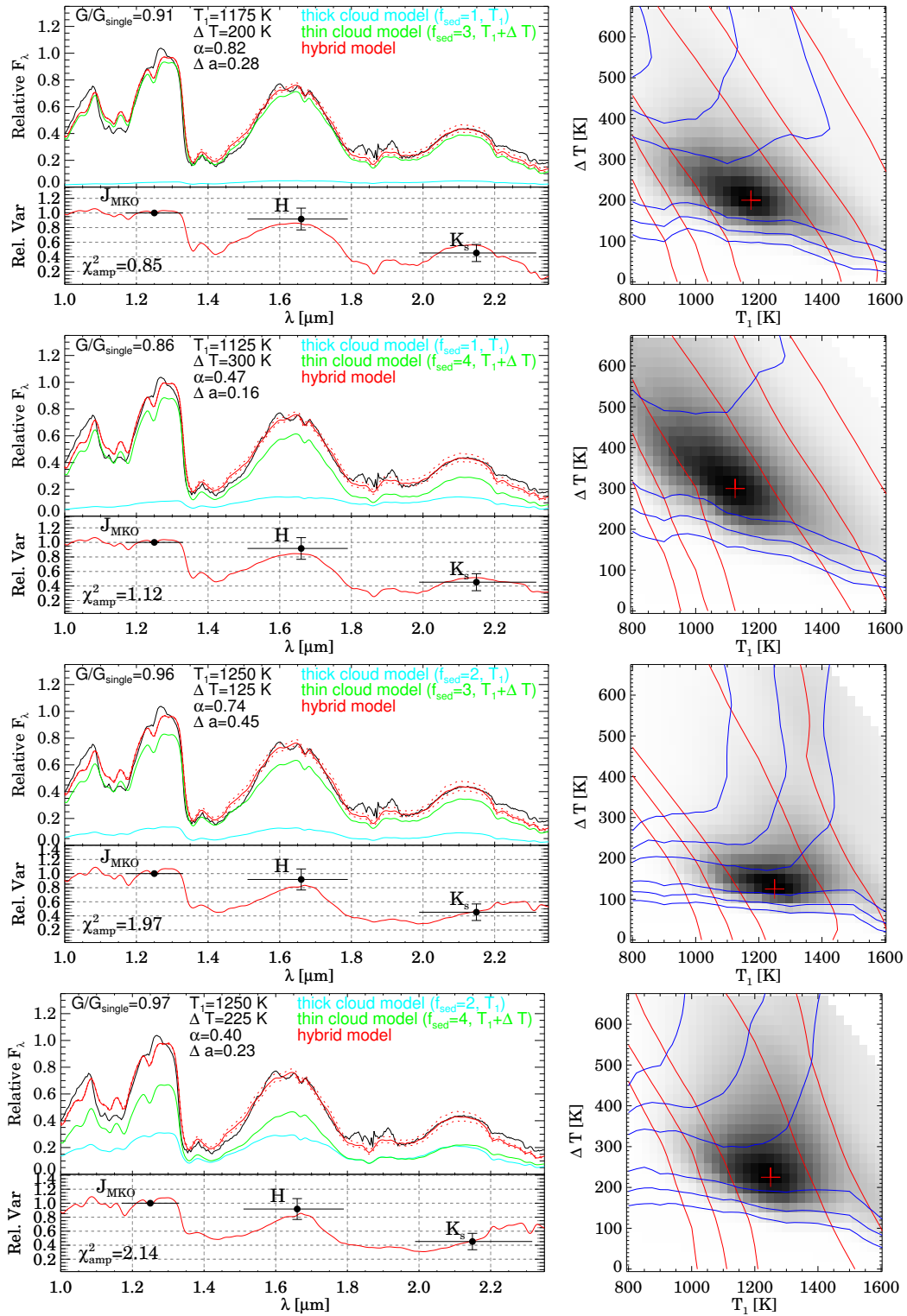


Figure A.3: Same as figure 3.12, but with amplitude ratios constrained using data from the 01 Oct 2009 epoch.

Appendix B

Chapter 4 Appendix

B.1 The Empirical Flux Ratio Distribution of Resolved L and T Dwarf Binaries

In order to convert the observed binary fraction into a volume-corrected binary frequency using equation 4.4 we needed to compute the ratio of volume searched for binaries over single objects, $\alpha = (d_{\text{bin}}/d_{\text{single}})^3$. To do this we used equation 4.5 which is originally given in Burgasser et al. (2003a), and depends on the distribution of flux ratios for resolved binaries, (f_2/f_1) . The contrasts, Δm for known binaries reported by Burgasser et al. (2003a); Bouy et al. (2003); Burgasser et al. (2006a); Reid et al. (2006; 2008) are given in table B.1. We converted these contrasts to flux ratios according to $f_2/f_1 = 10^{-0.4*\Delta m}$. This empirical flux ratio distribution is shown in figure B.1. Integrating directly over this empirical distribution in equation 4.4 we found $\alpha = 1.87$, which is almost identical to the value obtained for a flat flux ratio distribution of $\alpha = 1.86$.

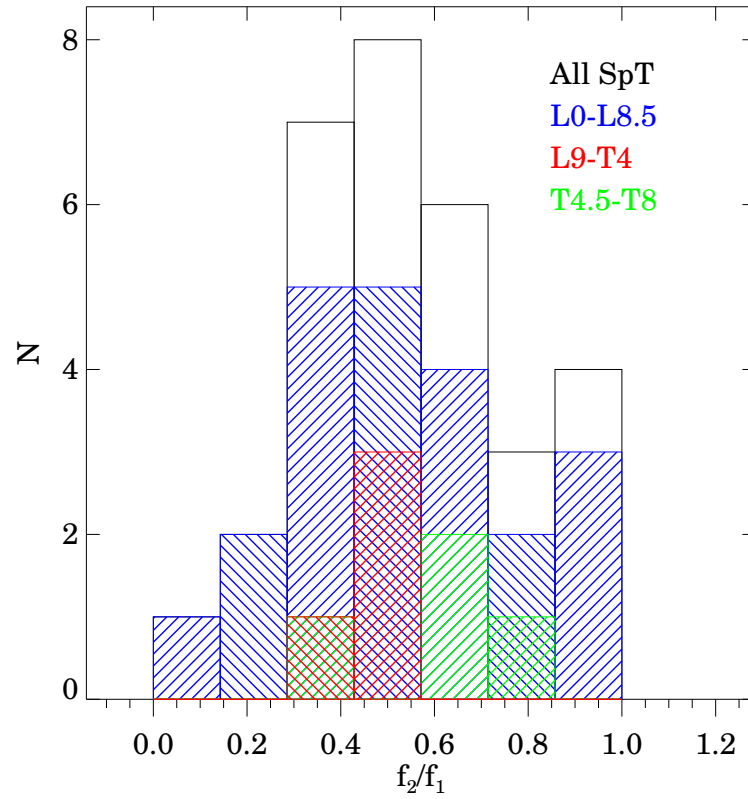


Figure B.1: The distribution of flux ratios for resolved L and T dwarf binaries in table B.1 (black histogram). Colored bars show how the sample subdivides by unresolved spectral type. Integrating over this empirical distribution using equation 4.5, we find $\alpha=1.87$, which is equivalent to the value for for a flat distribution, and strongly differs from the value found by assuming flux ratios peak at 1

Table B.1. Flux ratios of resolved binaries

2MASS ID	SpT ^a	SpT A	SpT B	Δm	f_2/f_1	Filter	Ref. 1 ^b	Ref. 2 ^c
2MASS J00043484–4044058	L5	L5	L5	0.10	0.91	F110W	1	5
2MASS J00250365+4759191	L4	L4	L4	0.17	0.86	F110W	1	1
2MASS J02052940–1159296	L7	L7	L7	0.63	0.56	F814W	2	6
2MASS J03572695–4417305	L0	M9	L1.5	1.50	0.25	F814W	2	7
2MASS J04234858–0414035	T0	L6.5	T2	0.82	0.47	F170M	3	5
2MASS J05185995–2828372	T1	L6	T4	0.90	0.44	F170M	3	5
2MASS J07003664+3157266	L3.5	L3	L6.5	1.20	0.33	F110W	1	5
2MASS J07464256+2000321	L0.5	L0	L1.5	1.00	0.40	F814W	2	5
2MASS J08503593+1057156	L6	L6.5	L8.5	1.47	0.26	F814W	2	5
2MASS J08564793+2235182	L3	L3	L9.5	2.76	0.08	F814W	2	6
2MASS J09153413+0422045	L7	L7	L7.5	0.12	0.90	F110W	1	6
2MASS J09201223+3517429	T0p	L5.5	L9	0.88	0.44	F814W	2	5
2MASS J09261537+5847212	T4.5	T3.5	T5	0.40	0.69	F170M	3	5
2MASS J10170754+1308398	L2	L1.5	L3	0.74	0.51	F1042	2	5
2MASS J10210969–0304197	T3	T0	T5	1.03	0.39	F170M	3	5
2MASS J11122567+3548131	L4.5	L4.5	L6	1.04	0.38	F1042	2	5
2MASS J11463449+2230527	L3	L3	L3	0.75	0.50	F814W	2	5
2MASS J12255432–2739466	T6	T6	T8	1.05	0.38	F1042	4	3
2MASS J12281523–1547342	L5	L5.5	L5.5	0.40	0.69	F814W	2	5
2MASS J12392727+5515371	L5	L5	L6	0.54	0.61	F1042	2	6
2MASS J14304358+2915405	L2	L2	L3.5	0.45	0.66	F1042	2	6
2MASS J14413716–0945590	L0.5	L0.5	L1	0.34	0.73	F814W	2	6

Table B.1 (cont'd)

2MASS ID	SpT ^a	SpT A	SpT B	Δm	f_2/f_1	Filter	Ref. 1 ^b	Ref. 2 ^c
2MASS J14493784+2355378	L0	L0	L3	1.08	0.37	F1042	2	6
2MASS J15344984−2952274	T5.5	T5.5	T5.5	0.20	0.83	F1042	4	3
2MASS J15530228+1532369	T7	T6.5	T7.5	0.46	0.65	F170M	3	5
2MASS J16000548+1708328	L1.5	L1.5	L1.5	0.69	0.53	F814W	2	6
2MASS J17281150+3948593	L7	L5	L7	0.66	0.54	F814W	2	5
2MASS J21011544+1756586	L7.5	L7	L8	0.59	0.58	F814W	2	5
2MASS J21522609+0937575	L6	L6	L6	0.15	0.87	F110W	1	6
2MASS J22521073−1730134	L7.5	L4.5	T3.5	1.12	0.36	F110W	1	5

^aUnresolved Spectral Type

^bSurvey References

^cResolved spectral type references.

References. — (1)Reid et al. (2006) (2)Bouy et al. (2003) (3)Burgasser et al. (2003a) (4)Burgasser et al. (2006a) (5)Dupuy & Liu (2012) (6)Trent J. Dupuy, Private Comm. (7)Martín et al. (2006)

Appendix C

Chapter 5 Appendix

C.1 Detrended lightcurves for all targets

Caption for figures C.1-C.63:

Light curve of target (top left) and up to 7 reference stars observed simultaneously (below). See section 5.3 for a complete description. All light curves have been binned by a factor of 3. A finding chart is shown in the top right with the target and reference stars labelled by number (associated with the “ID” field given with each light curve). The target always has an ID of 0 and is circled. In the lower right are diagnostic plots from top to bottom of: the sky brightness, median FWHM of all reference stars, first order variations of all stars on the chip (e.g. due to changing atmosphere, instrumental, and procedural effects) and the relative light curve RMS deviations as a function of magnitude. In the latter plot the target is indicated by a black filled circle, while “good” reference stars used to build the 1st order calibration curve are shown as open circles. Reference stars flagged for quality or excluded for having a large RMS are shown in grey (see section 5.3 for the specific criteria used). **Finding charts for the WIRCam targets are omitted due to their large size.** Sharps dips in the first order variations curves (i.e., those labelled “atmosphere plus detector”) typically arise due to frames where the telescope moved during the exposure (for instance, to reposition

the target away from a hot pixel without having to abort the sequence). These highly deviant frames are automatically clipped before the light curves are analyzed.

Figure C.1: As described in section C.1: 2MASSW J0030300-145033 (2009-09-26T04:24:40)

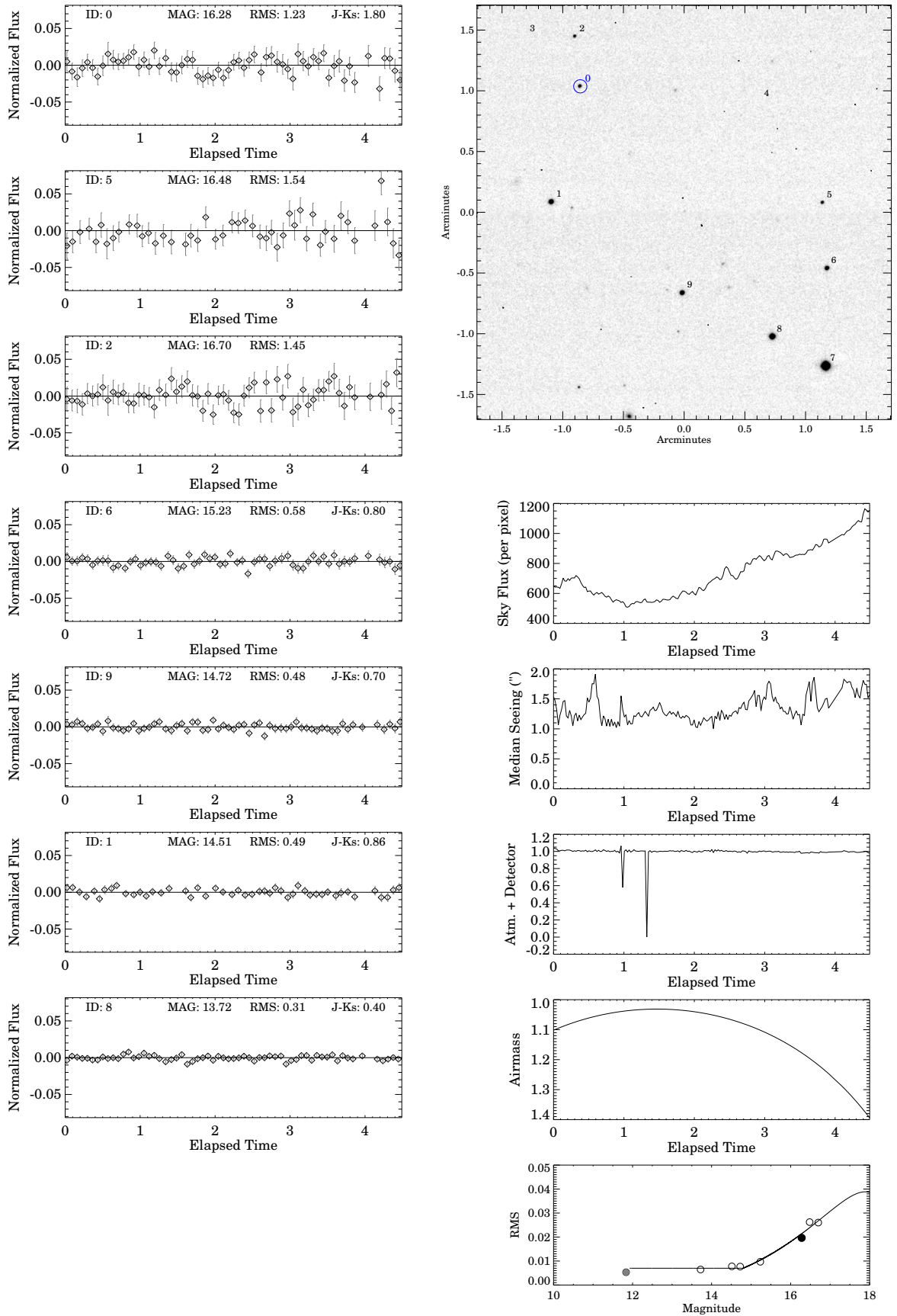


Figure C.2: As described in section C.1: 2MASS J00501994-3322402 (2009-08-02T07:37:18)

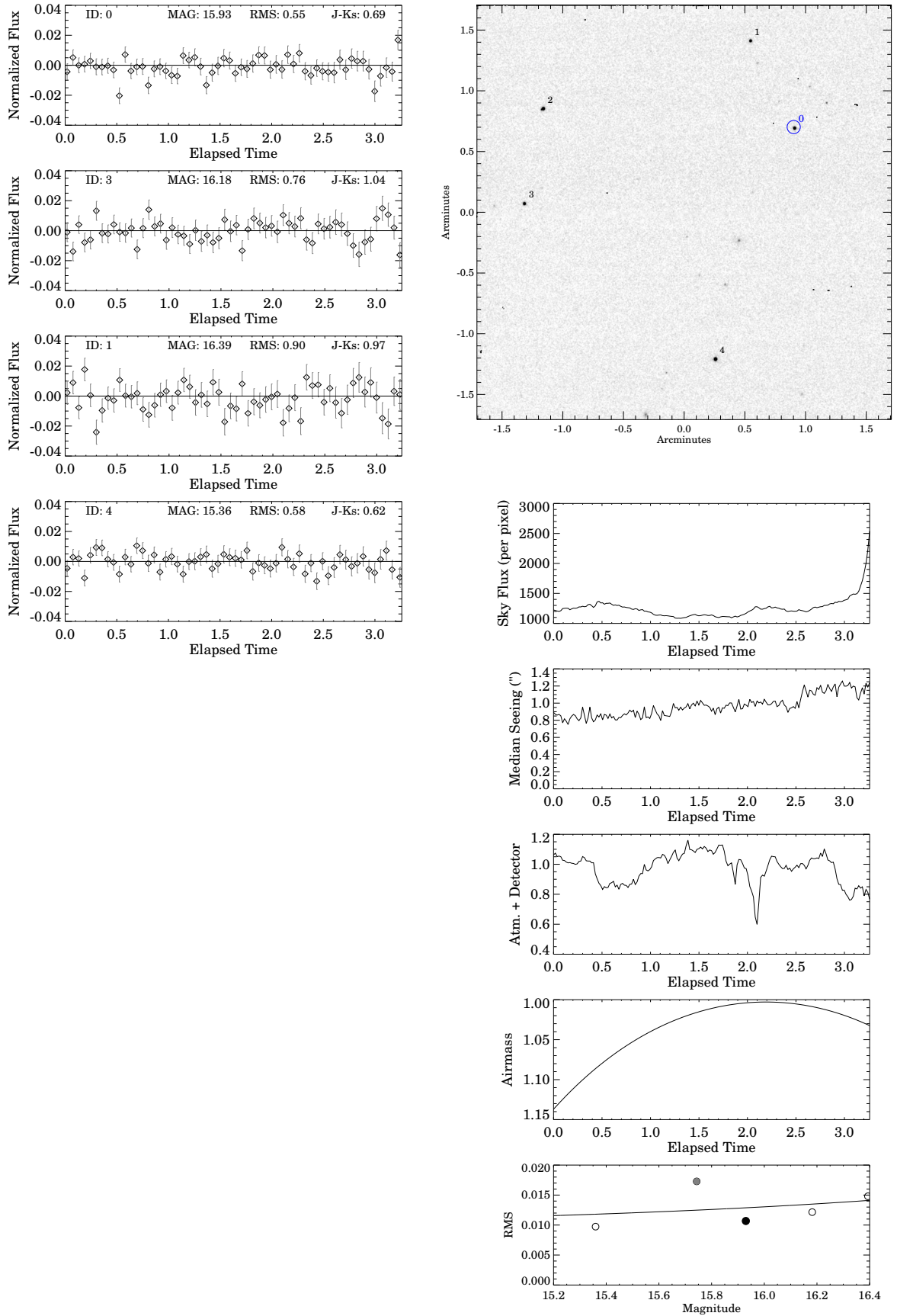


Figure C.3: As described in section C.1: SIMP J013656.57+093347.3 (2009-07-31T08:44:56)

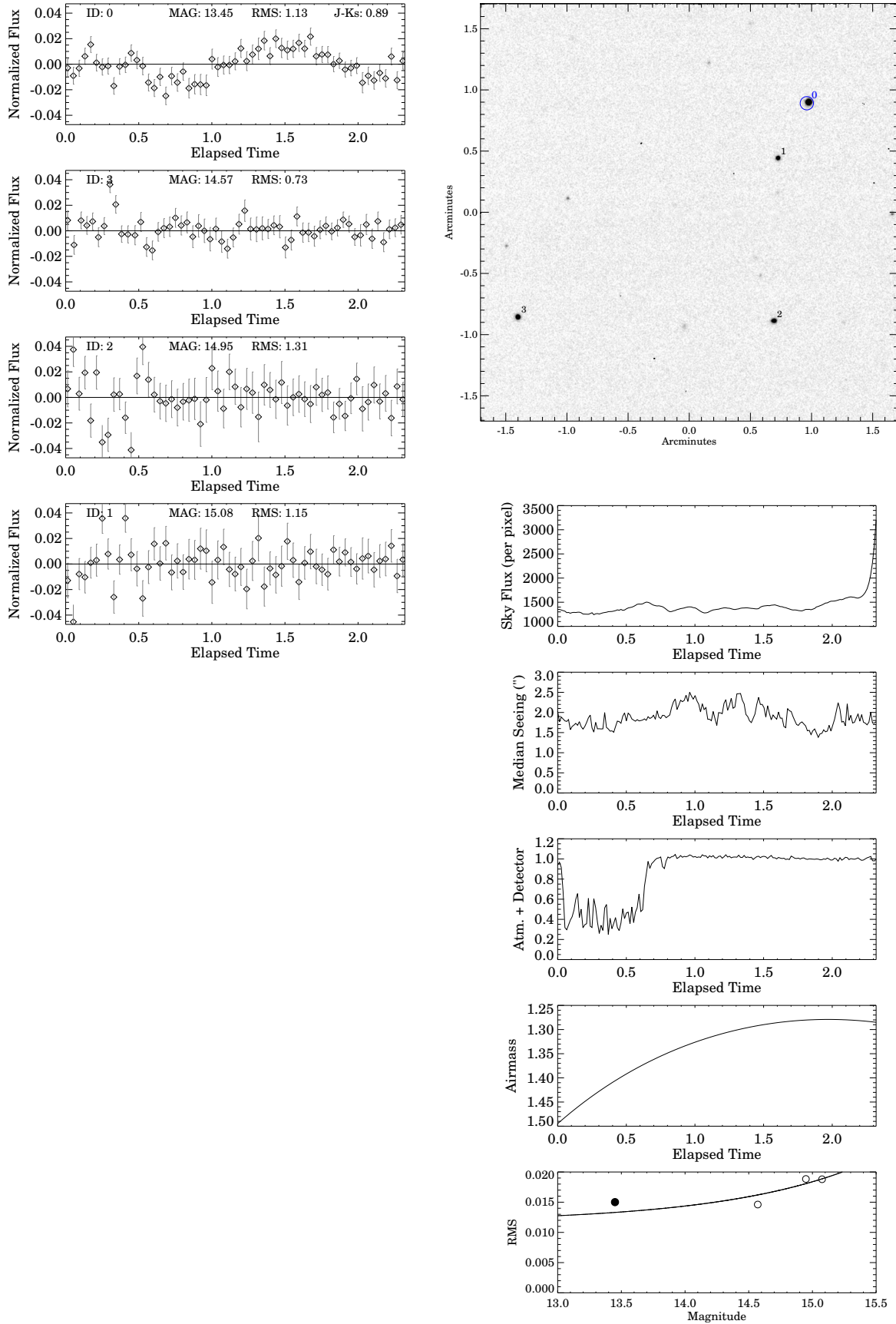


Figure C.4: As described in section C.1: SDSS J015141.69+124429.6 (2009-12-30)

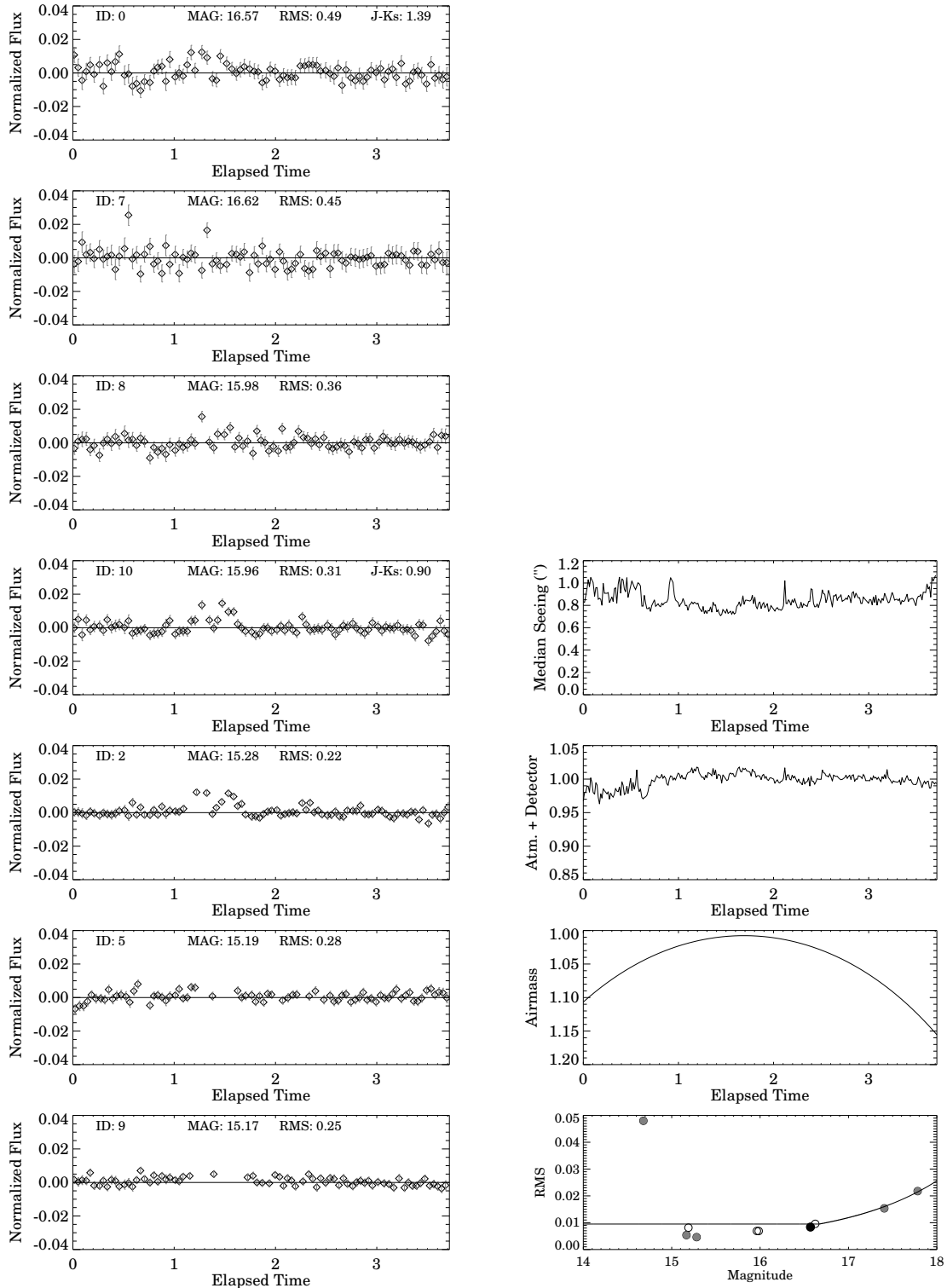


Figure C.5: As described in section C.1: SDSS J020742.48+000056.2 (2009-09-25T06:02:03)

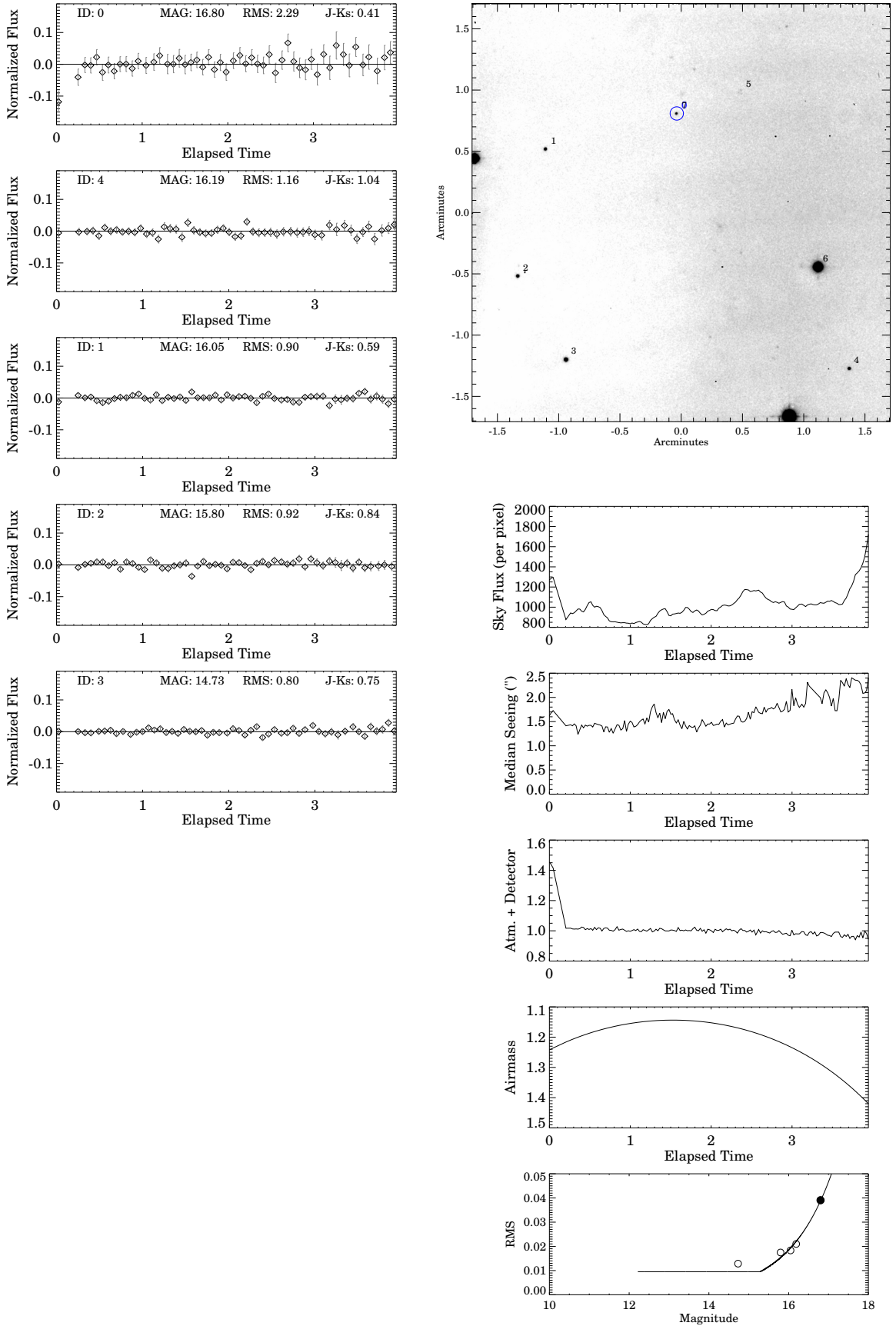


Figure C.6: As described in section C.1: 2MASS J0243137-245329 (2009-08-10T07:36:13)

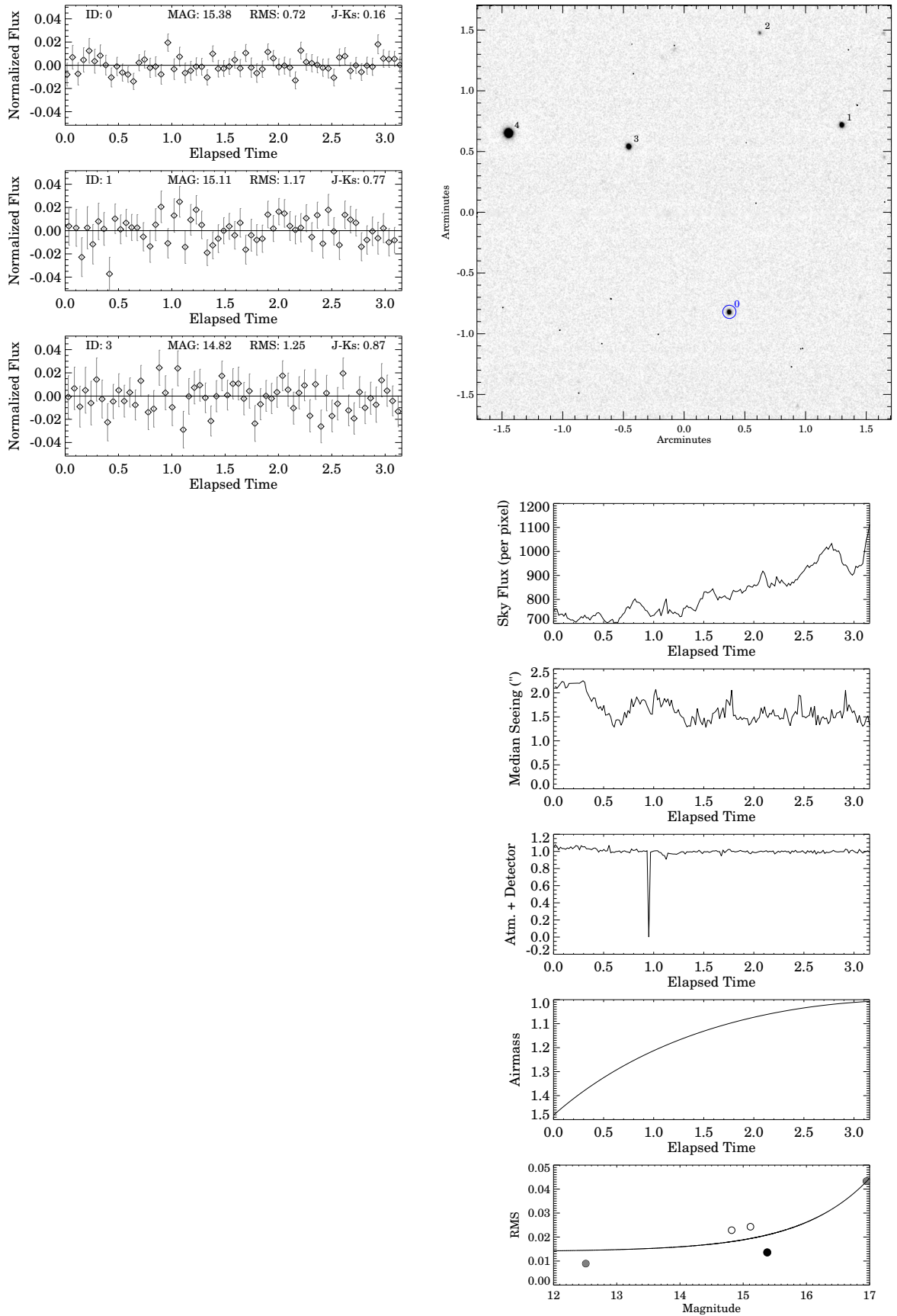


Figure C.7: As described in section C.1: 2MASS J02572581-3105523 (2009-09-30T05:49:55)

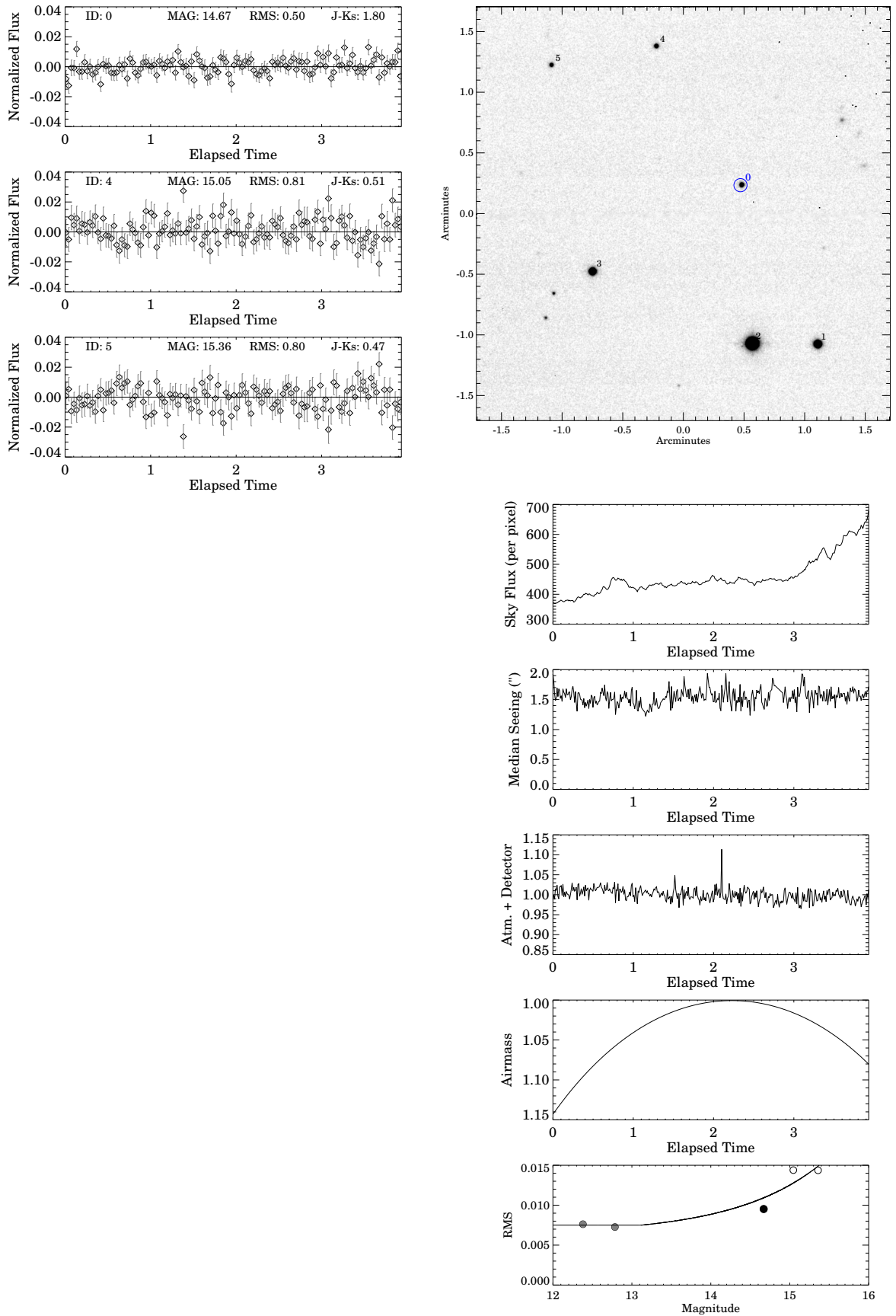


Figure C.8: As described in section C.1: 2MASS J03185403-3421292 (2009-09-24T05:55:46)

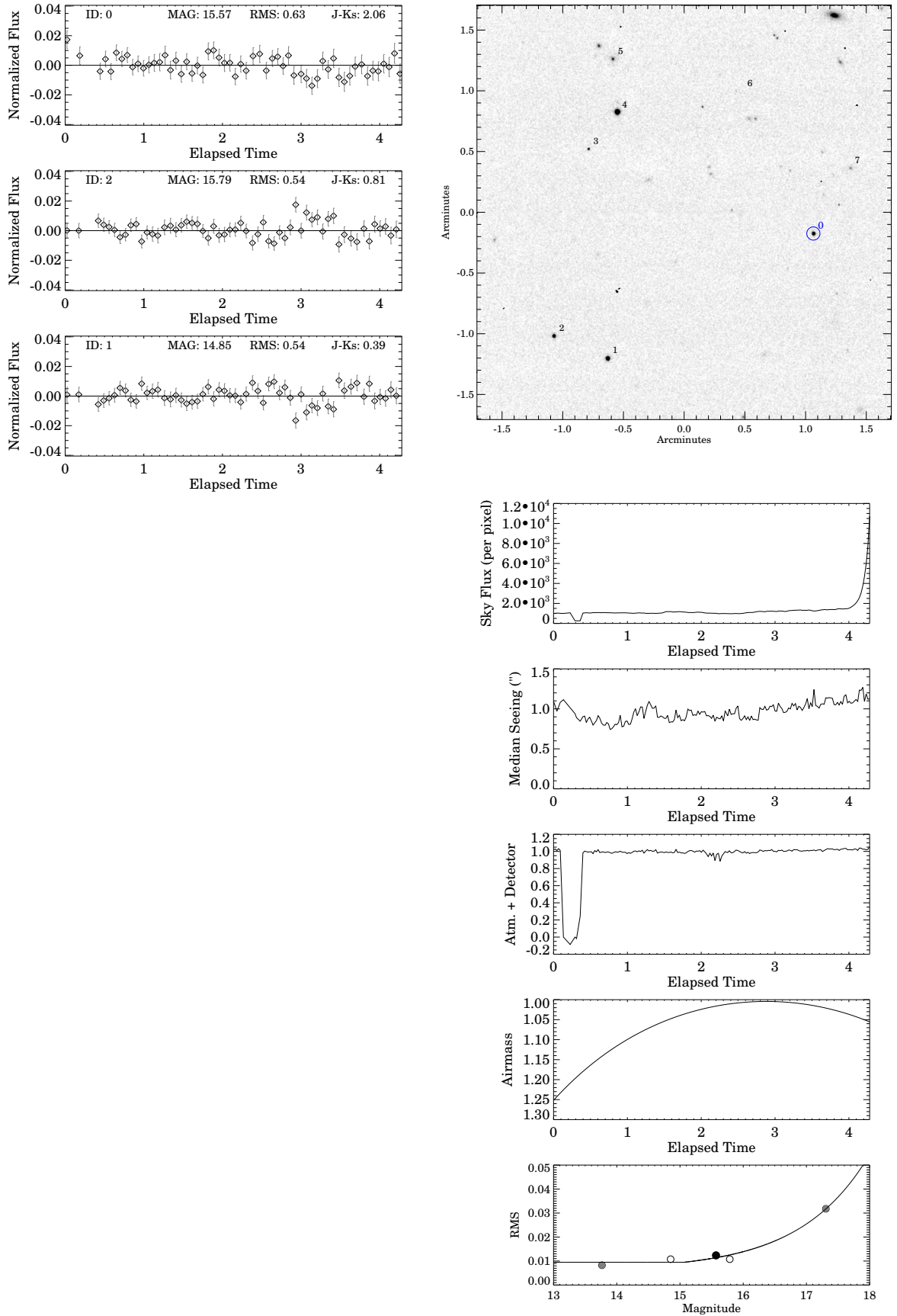


Figure C.9: As described in section C.1: 2MASS J0328426+230205 (2009-12-26)

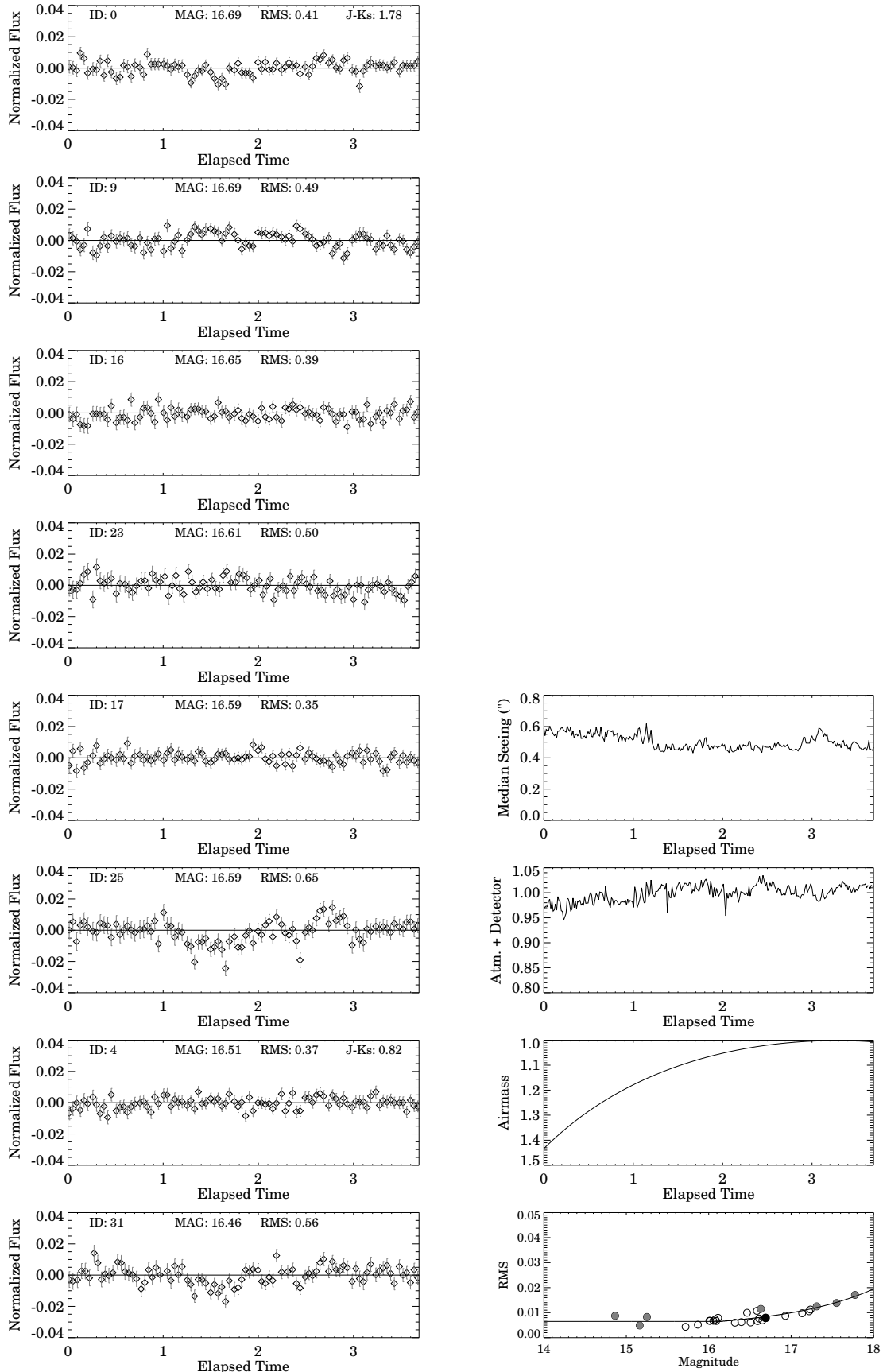


Figure C.10: As described in section C.1: 2MASS J0415195-093506 (2010-02-05T23:34:30)

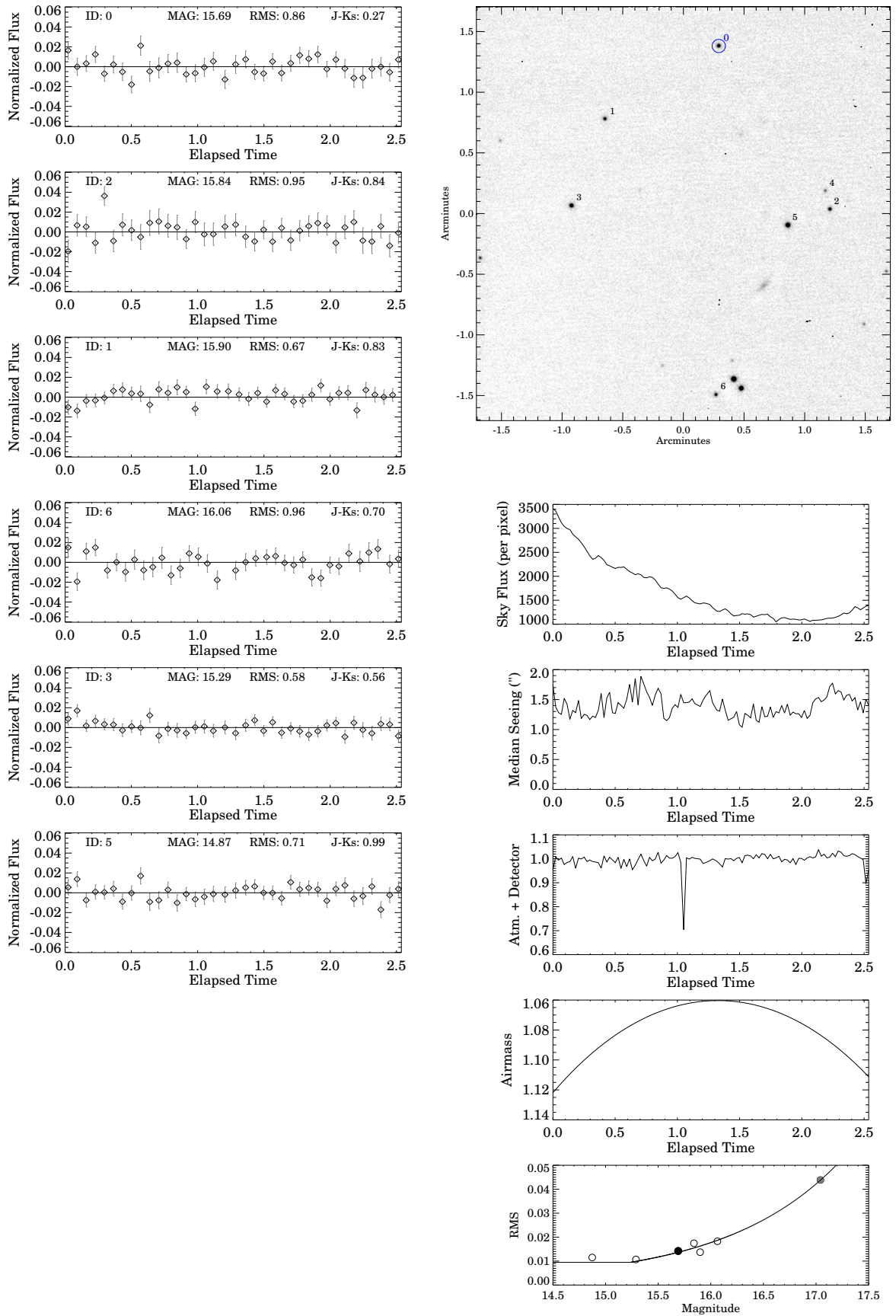


Figure C.11: As described in section C.1: 2MASS J0415195-093506 (2009-09-23T06:07:36)

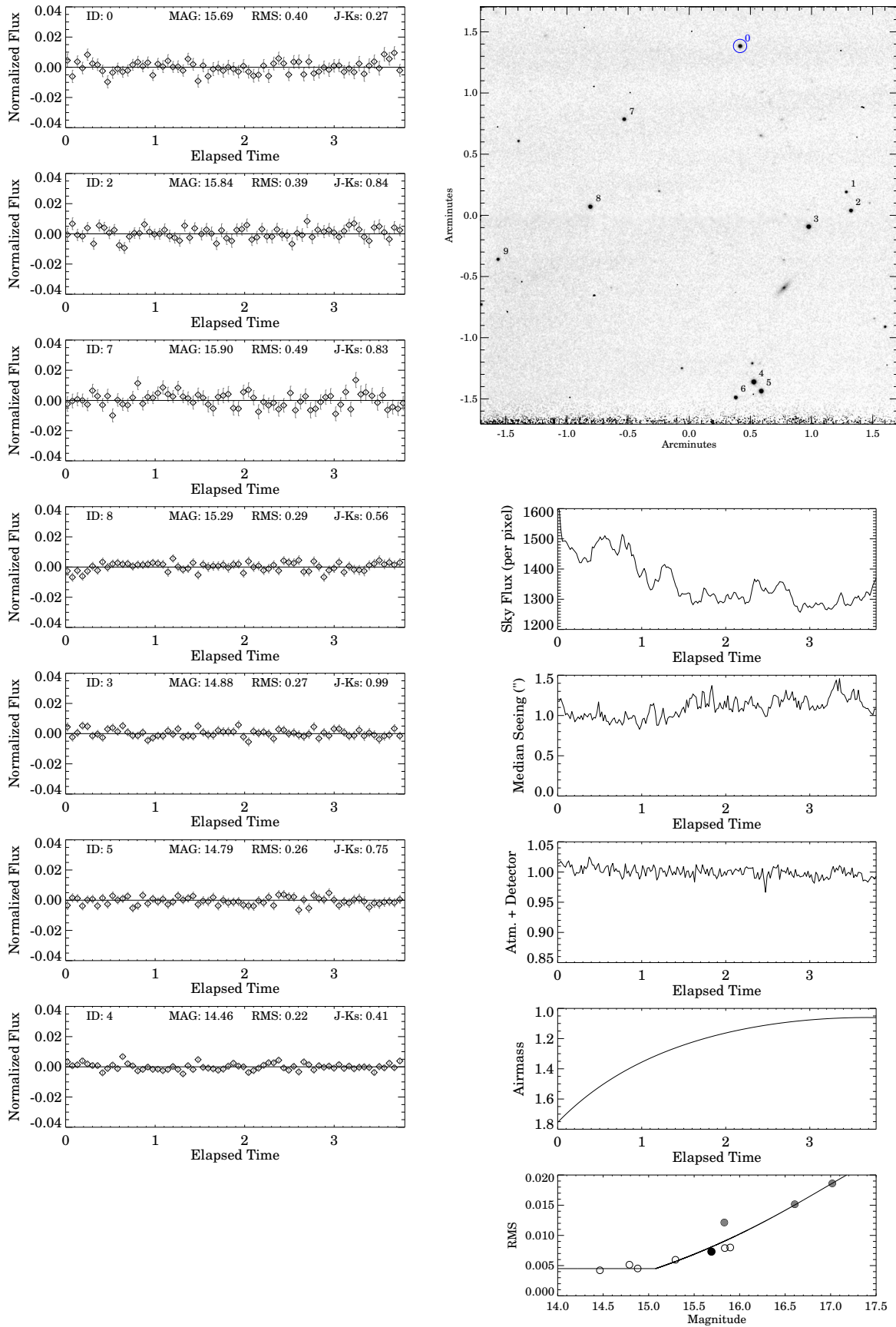


Figure C.12: As described in section C.1: SDSSp J042348.57-041403.5 (2009-10-02T06:26:36)

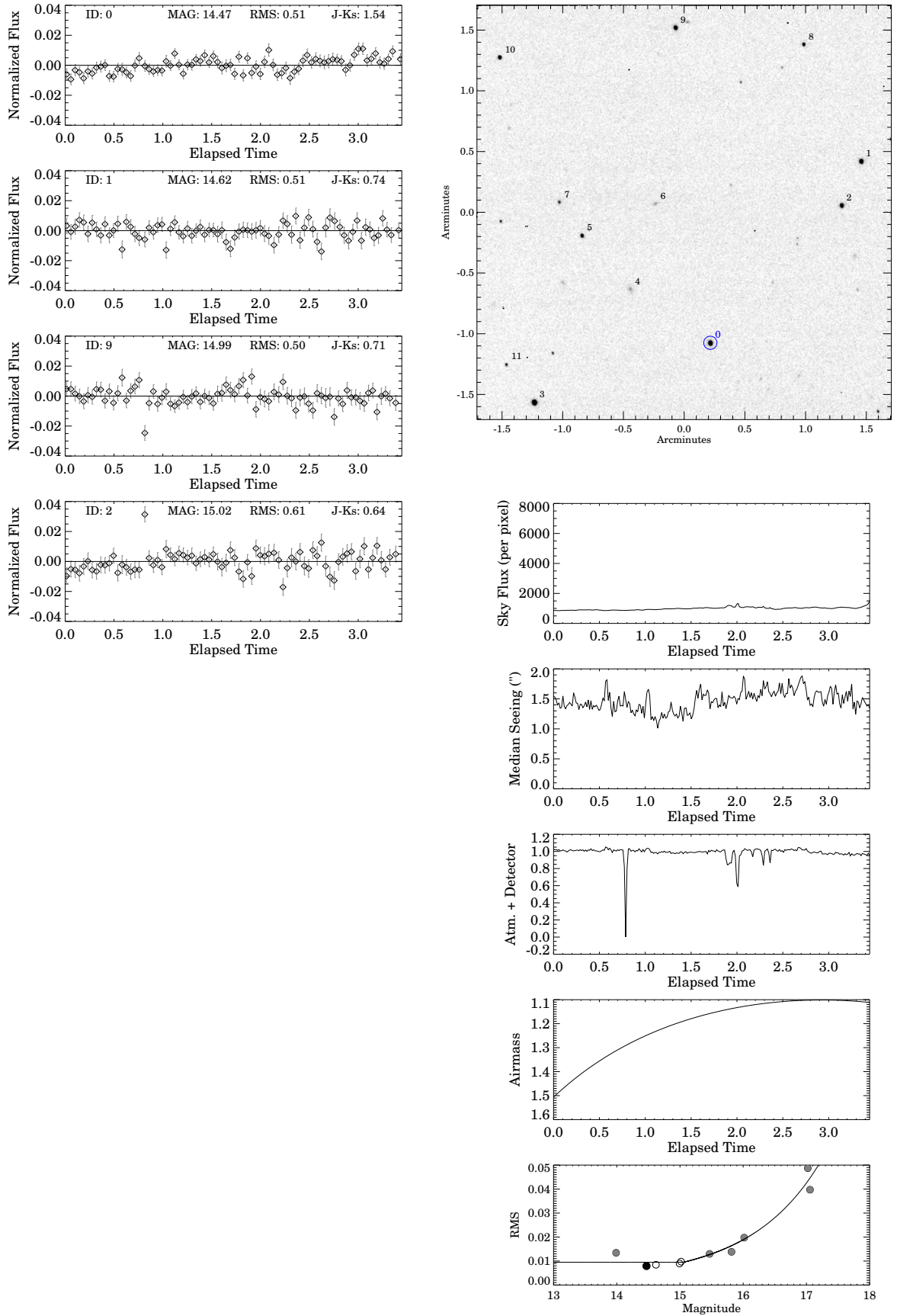


Figure C.13: As described in section C.1: 2MASS J05103520-4208140 (2010-02-04T00:46:13)

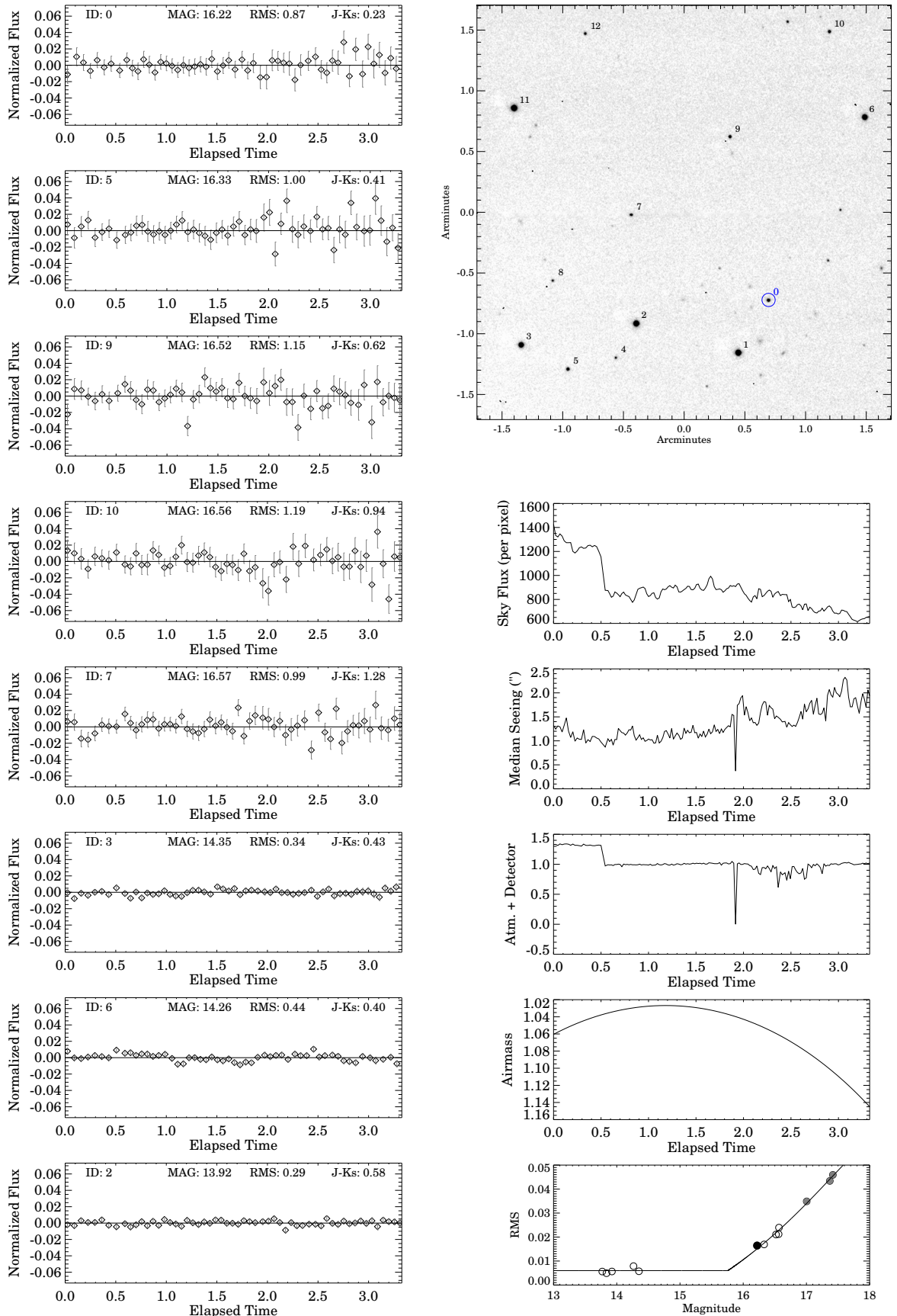


Figure C.14: As described in section C.1: 2MASS J05160945-0445499 (2009-09-22T06:11:15)

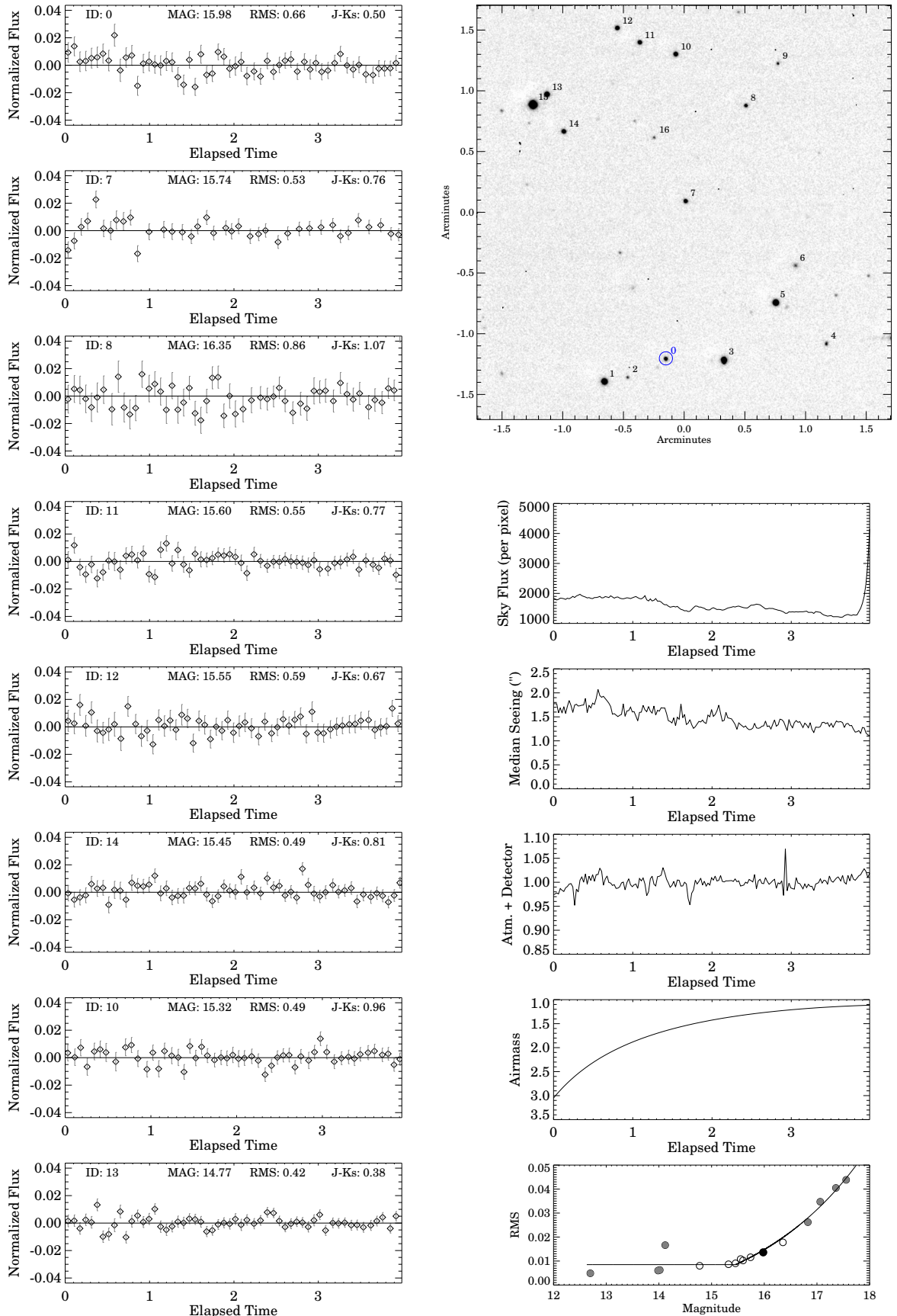


Figure C.15: As described in section C.1: 2MASS J05185995-2828372 (2010-02-03T00:08:53)

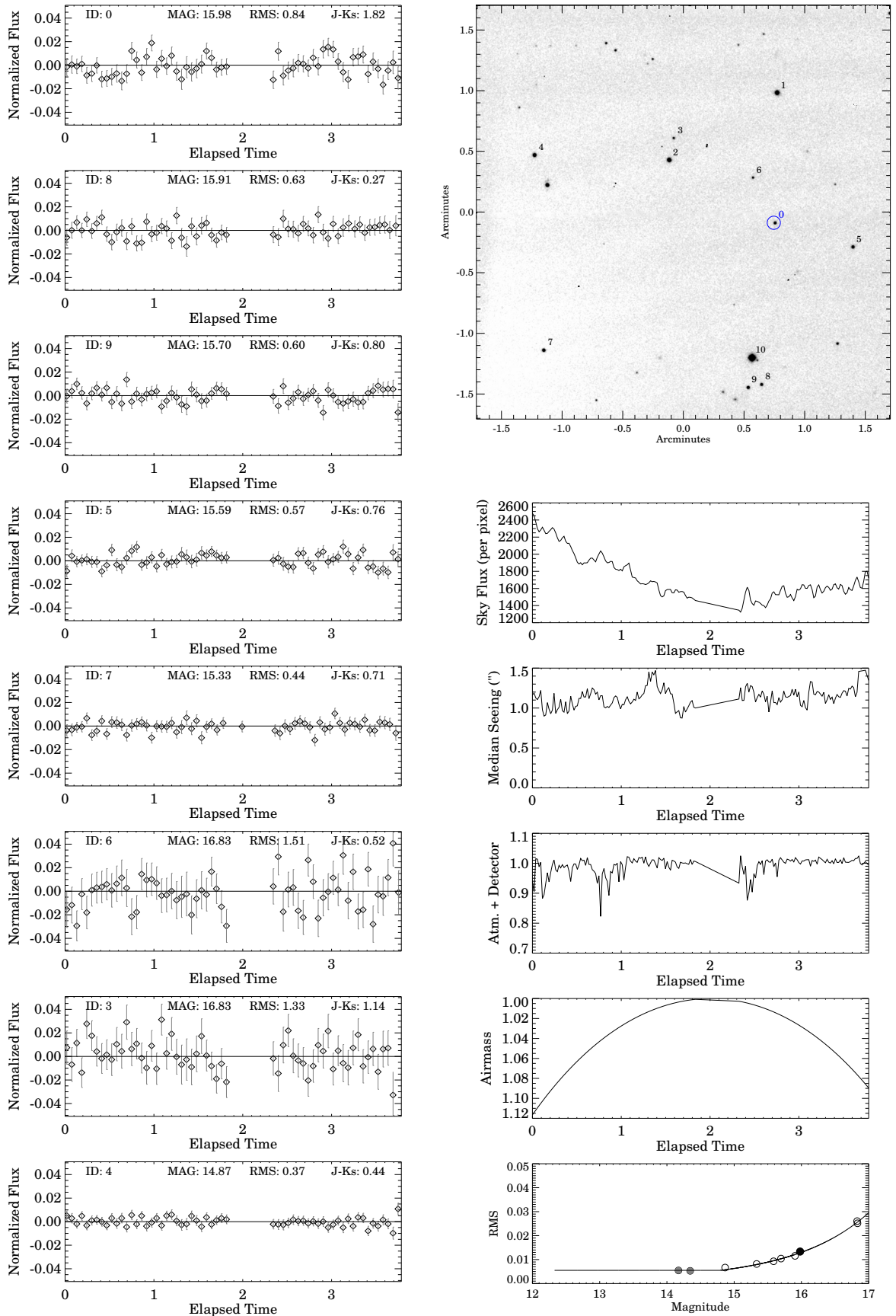


Figure C.16: As described in section C.1: 2MASS J05395200-0059019 (2010-02-07T00:27:30)

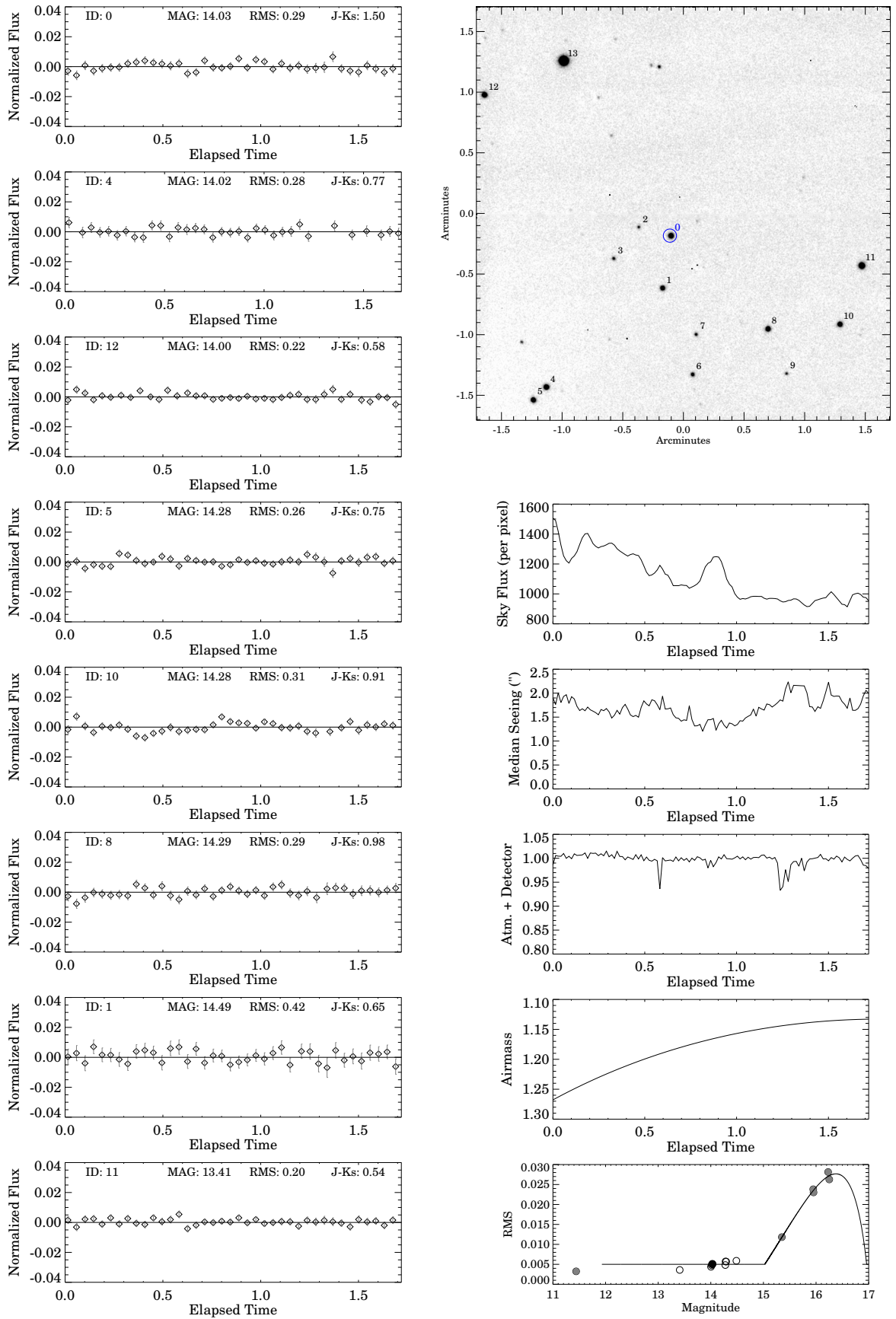


Figure C.17: As described in section C.1: 2MASS J05591914-1404488 (2010-02-01T00:31:38)

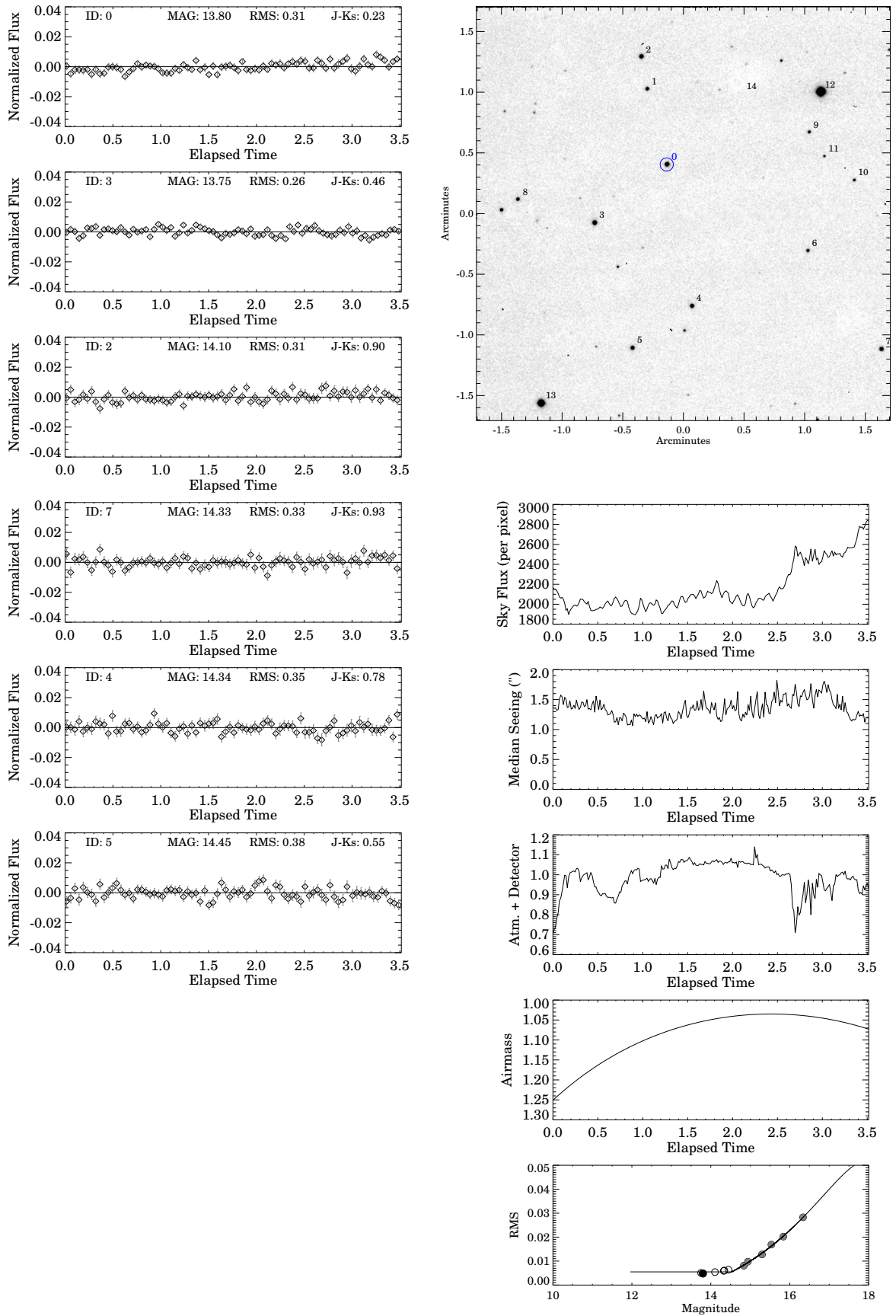


Figure C.18: As described in section C.1: 2MASS J07222760-0540384 (2010-04-22T23:24:07)

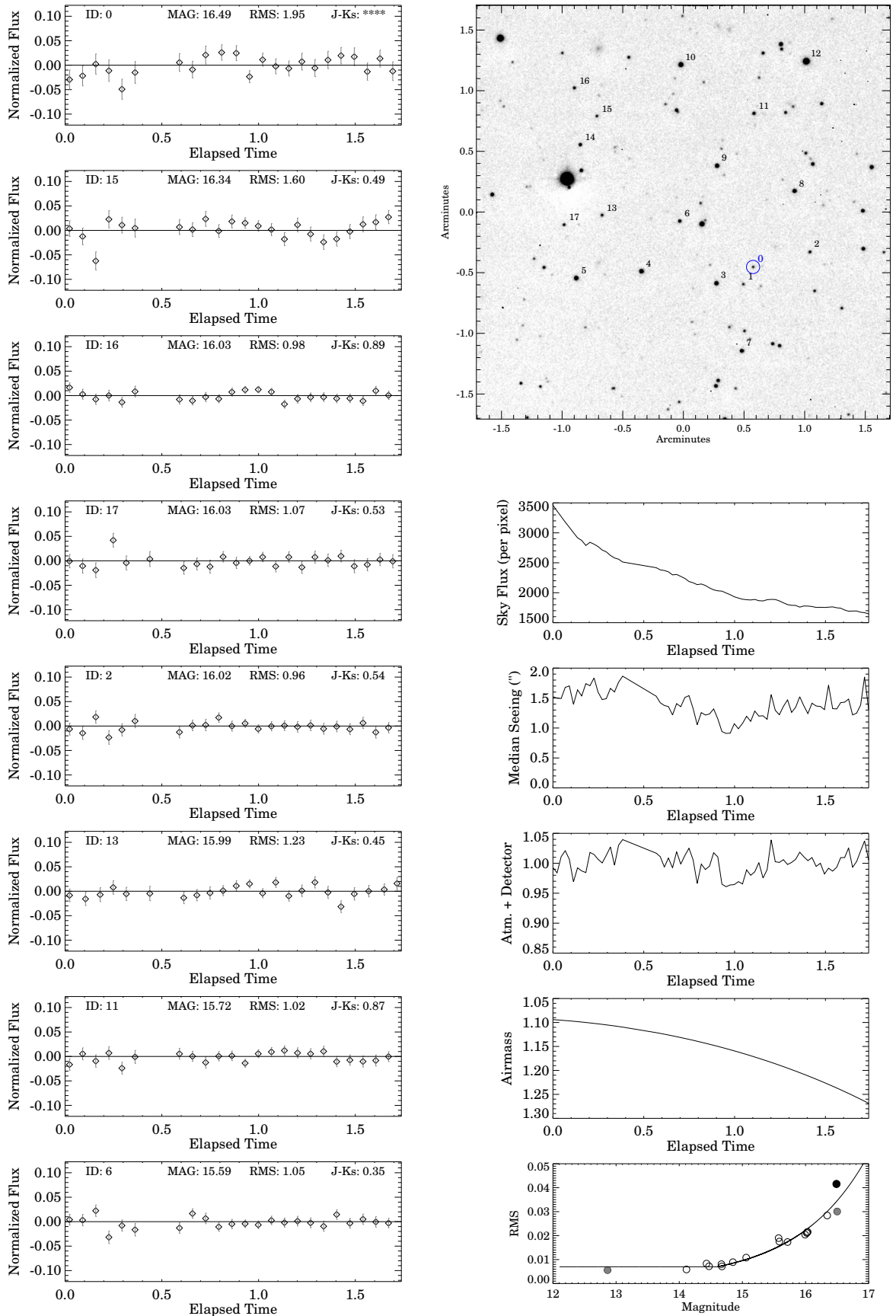


Figure C.19: As described in section C.1: 2MASS J07290002-3954043 (2010-02-02T01:02:15)

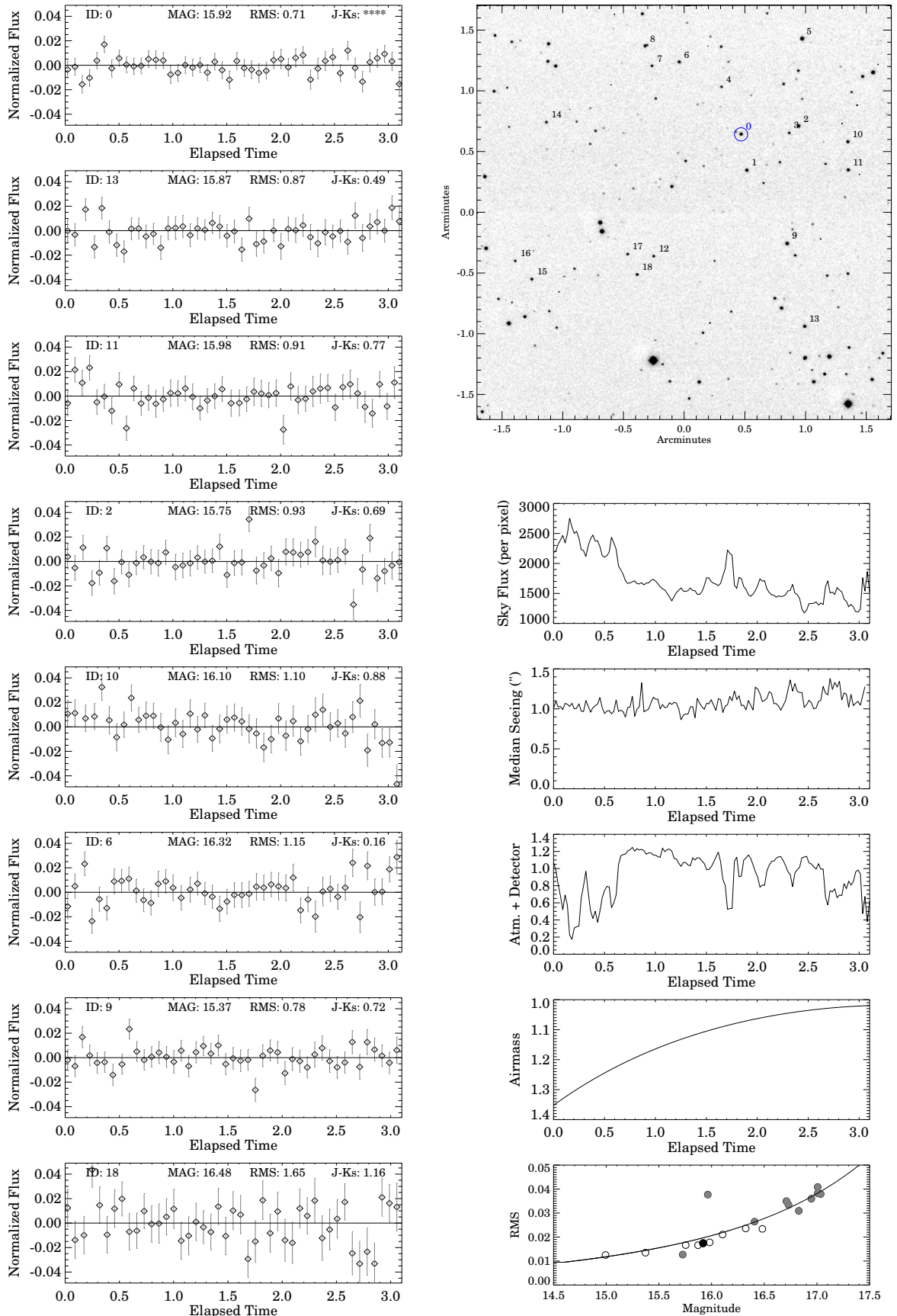


Figure C.20: As described in section C.1: SDSS J074201.41+205520.5 (2009-12-27)

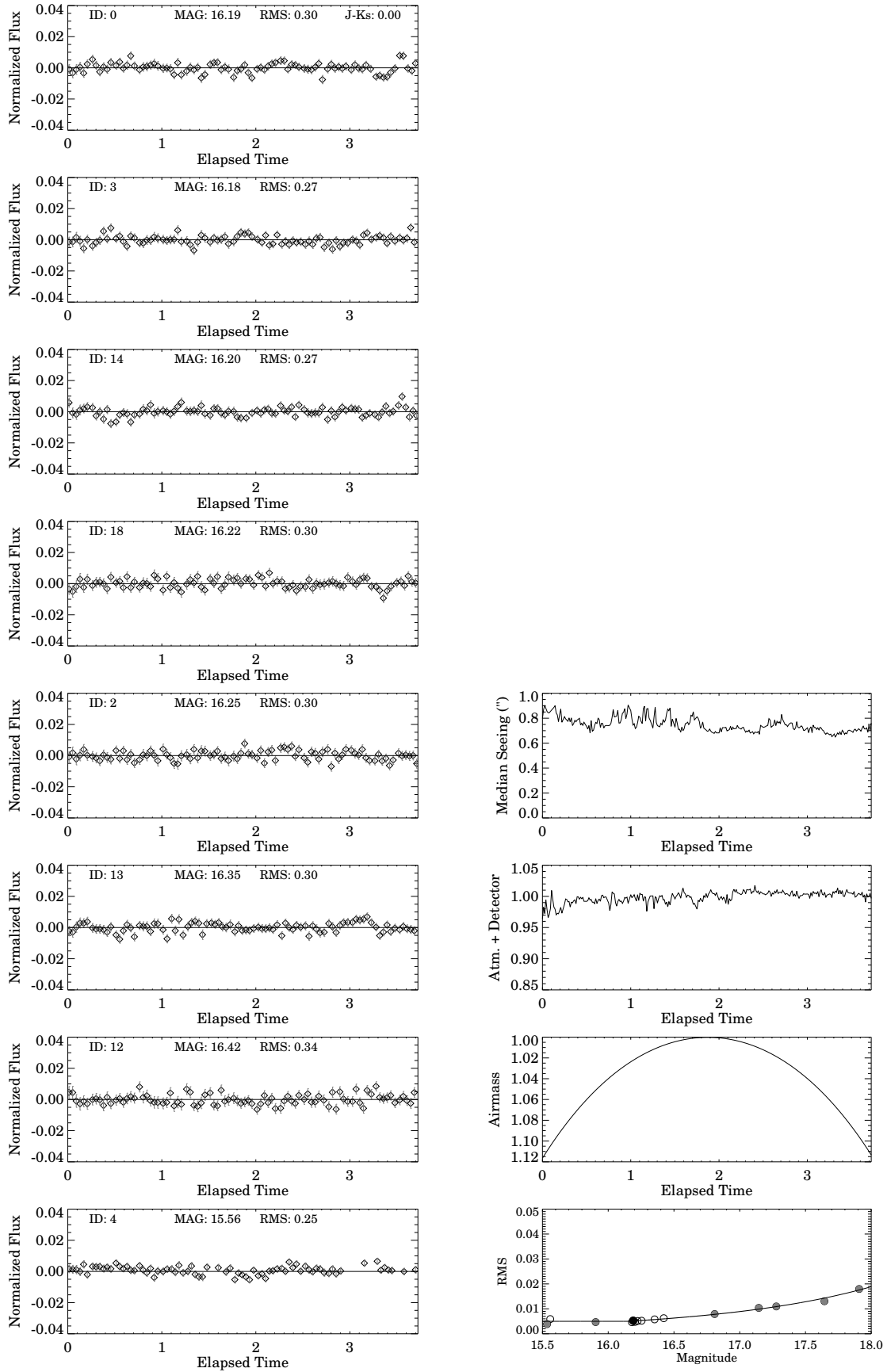


Figure C.21: As described in section C.1: SDSS J075840.33+324723.4 (2009-12-26)

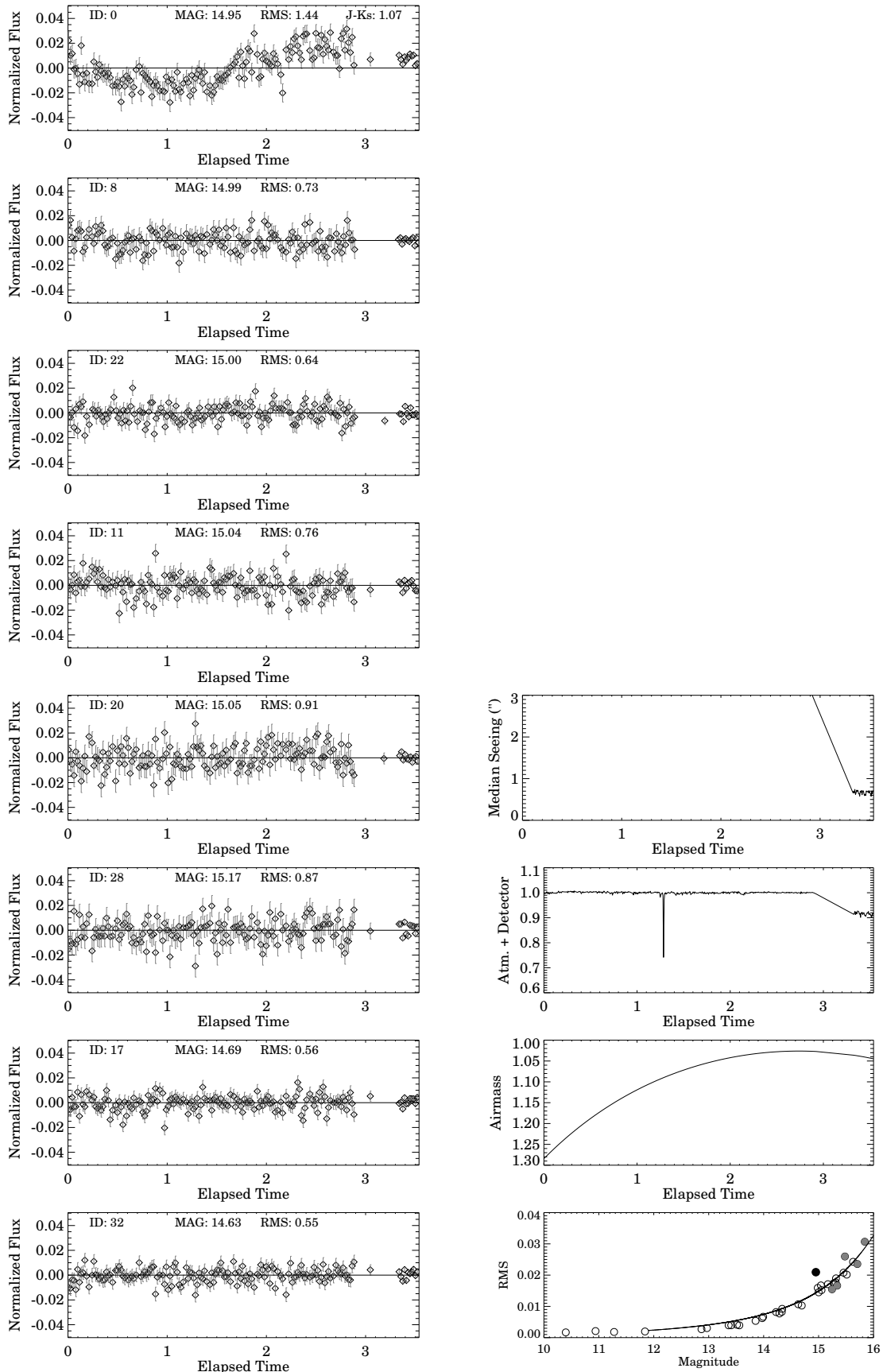


Figure C.22: As described in section C.1: DENIS J081730.0-615520 (2010-04-23T23:25:45)

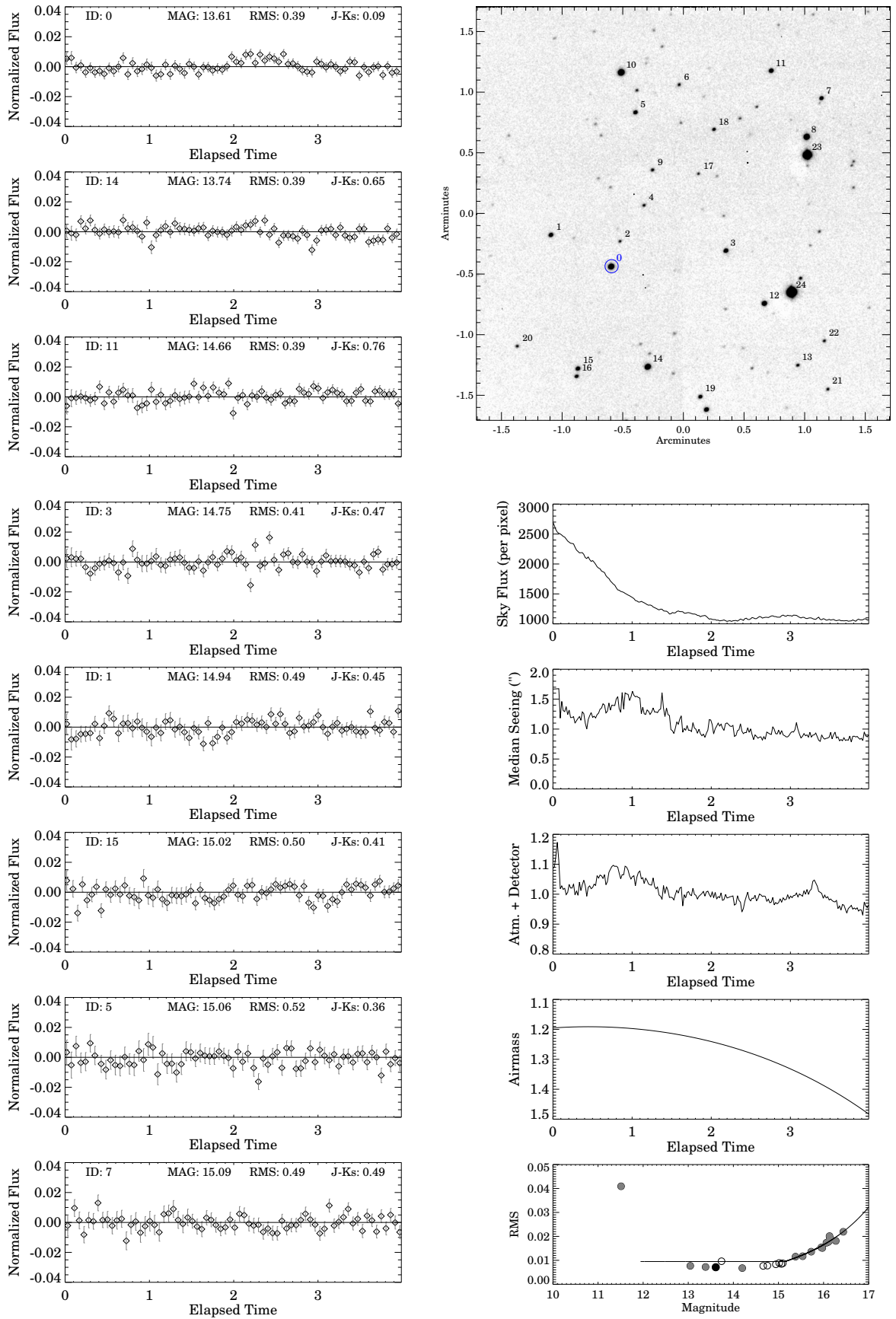


Figure C.23: As described in section C.1: SDSS J083048.80+012831.1 (2010-04-25T04:25:08)

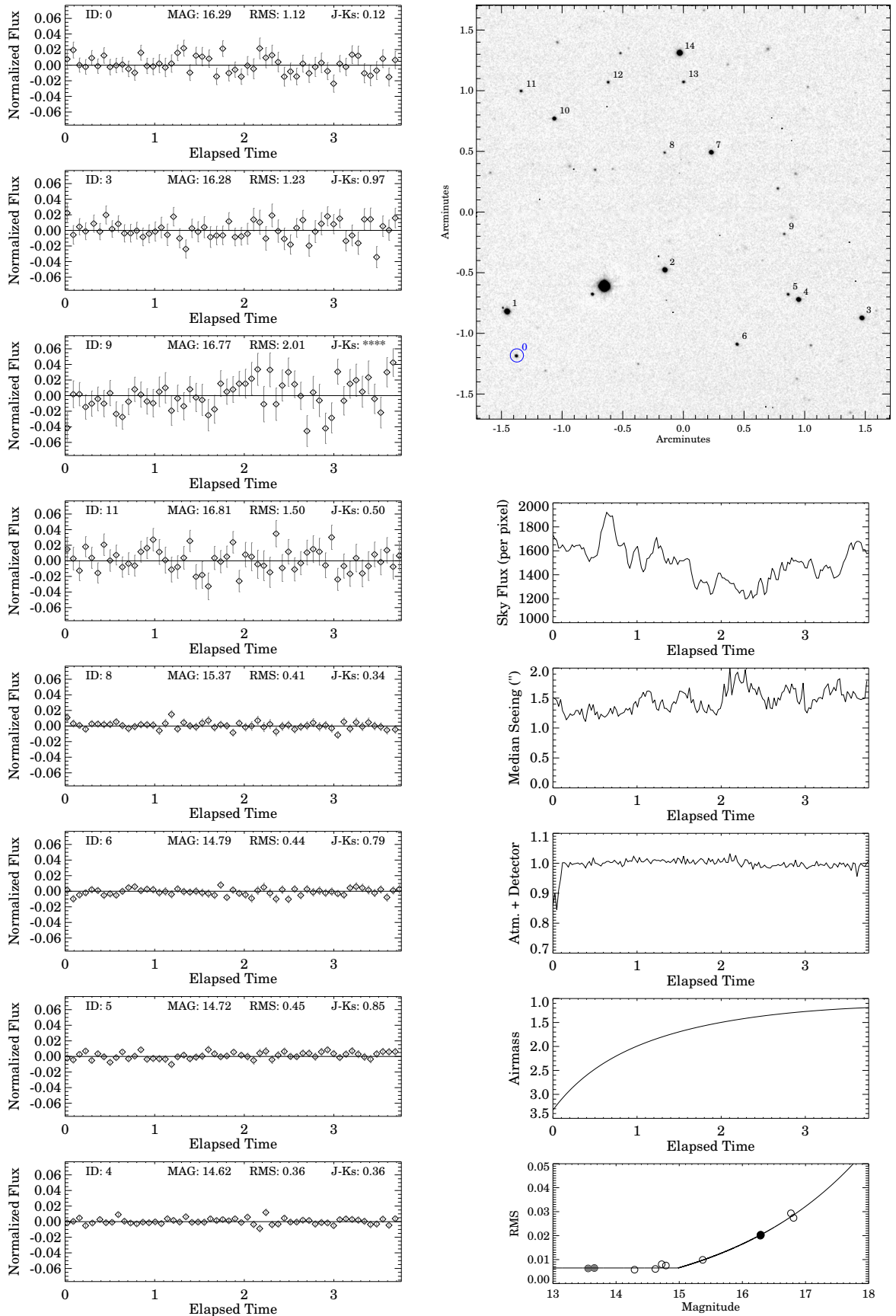


Figure C.24: As described in section C.1: 2MASS J09310955+0327331 (2010-03-30T00:05:51)

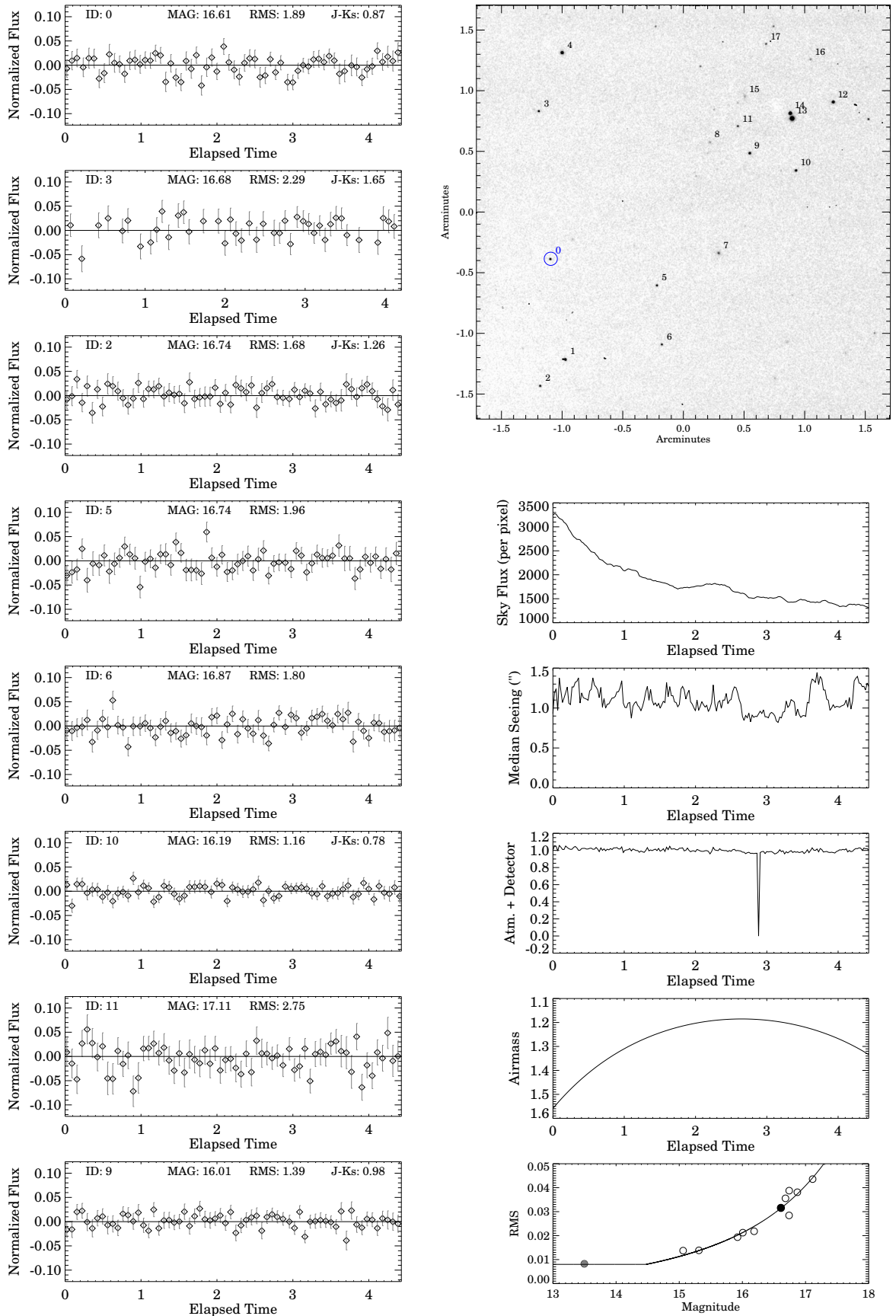


Figure C.25: As described in section C.1: 2MASS J09393548-2448279 (2010-04-02T23:29:53)

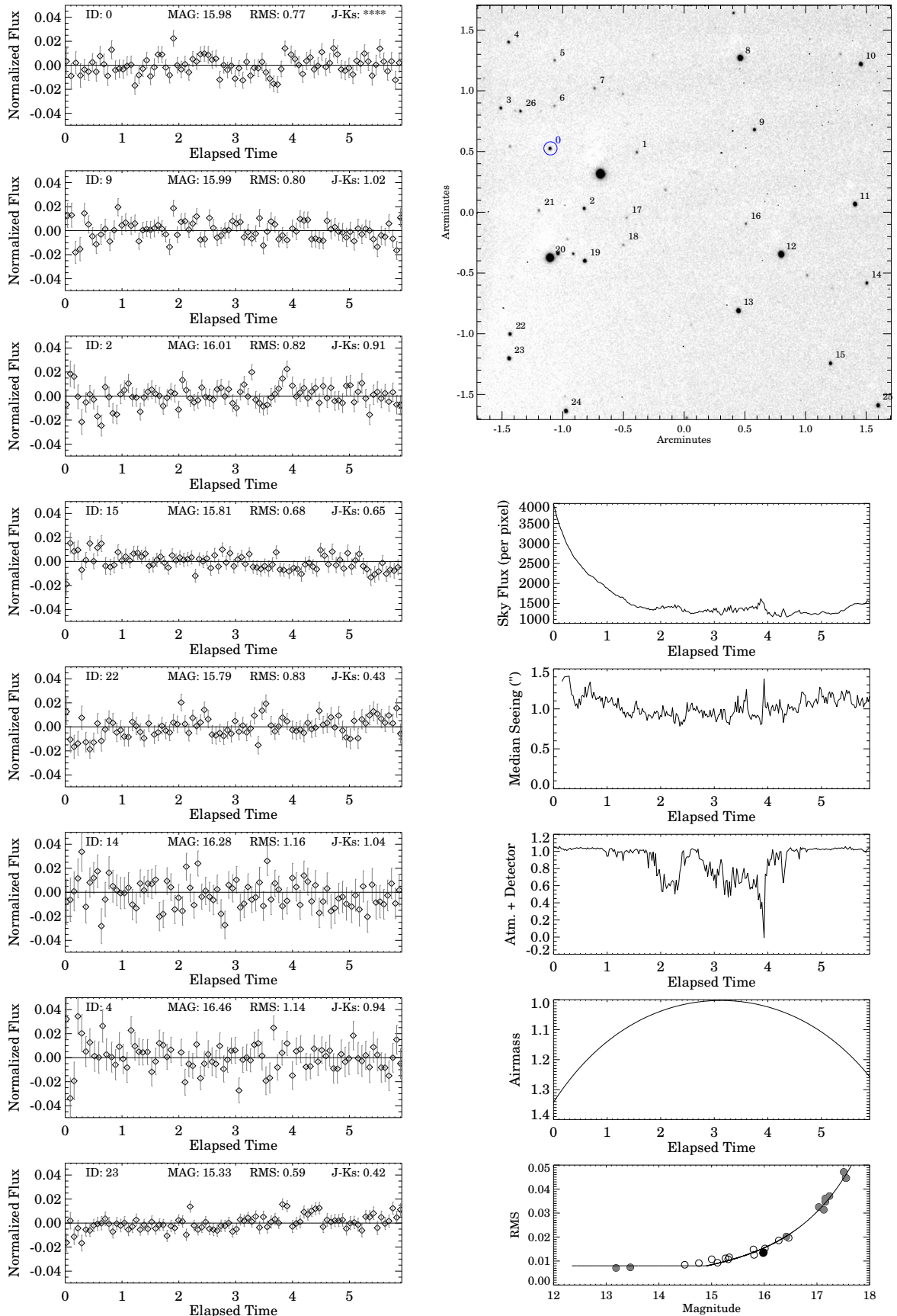


Figure C.26: As described in section C.1: 2MASS J09490860-1545485 (2010-03-26T01:04:35)

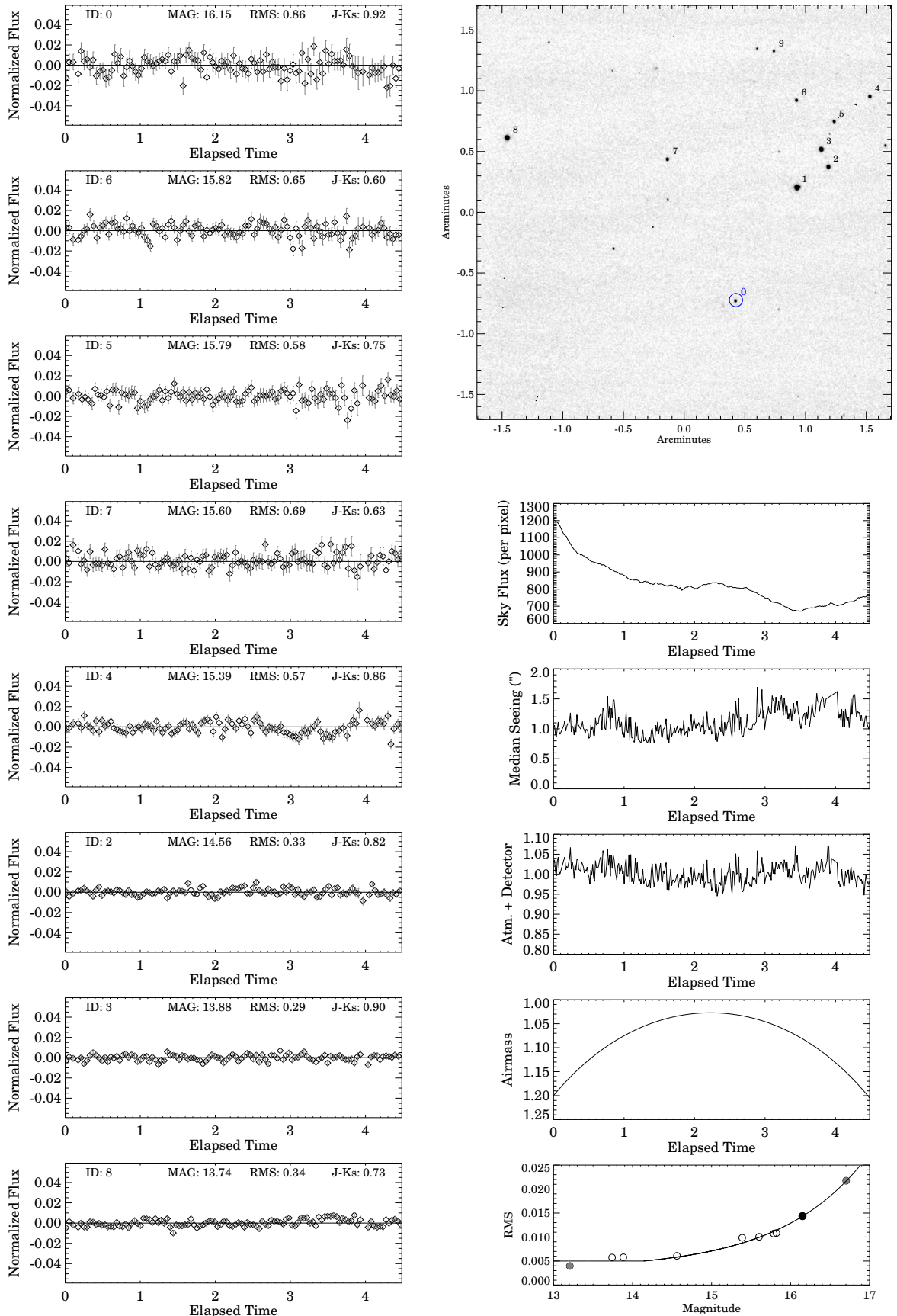


Figure C.27: As described in section C.1: 2MASS J10073369-4555147 (2010-01-31T03:34:10)

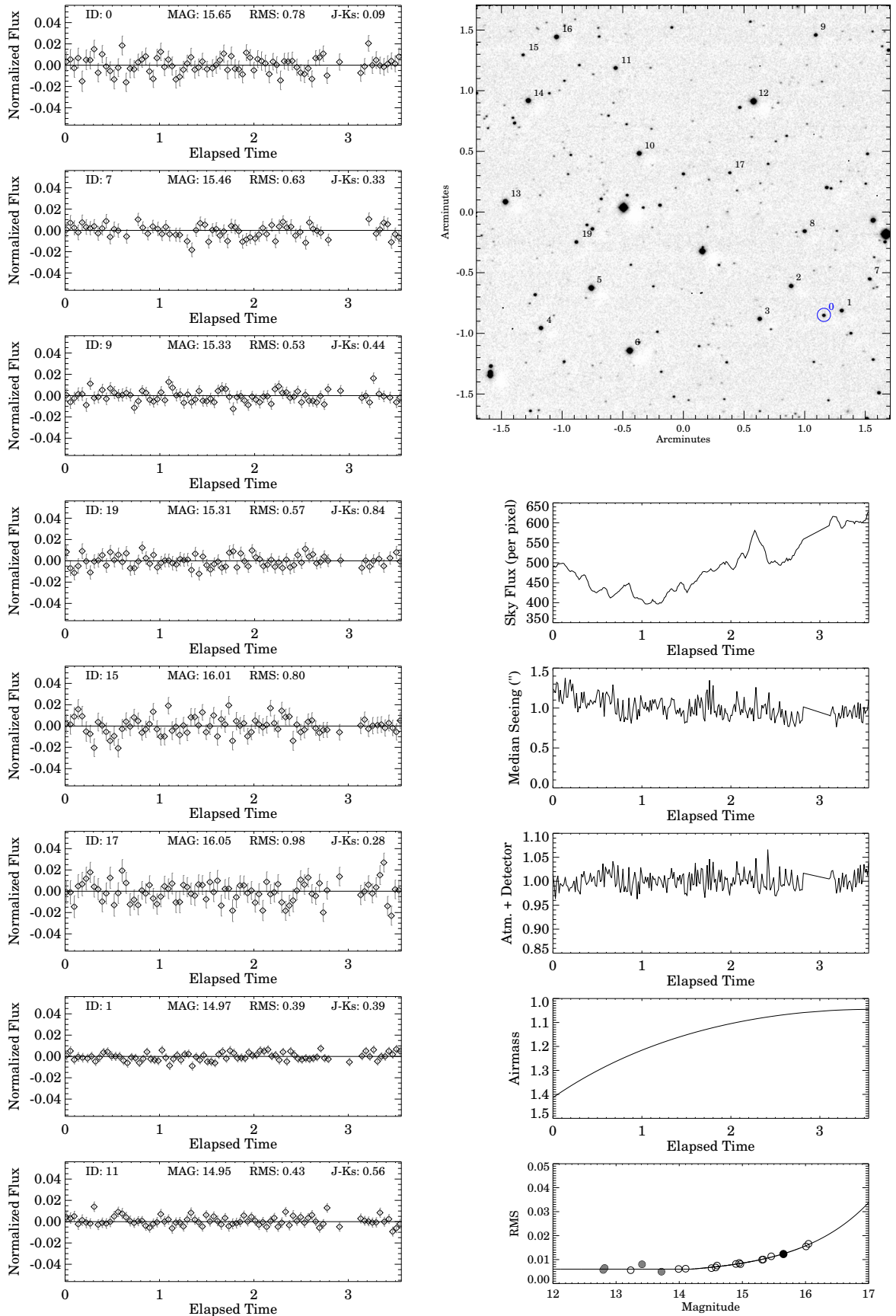


Figure C.28: As described in section C.1: 2MASS J10365305-3441380 (2010-03-28T01:43:22)

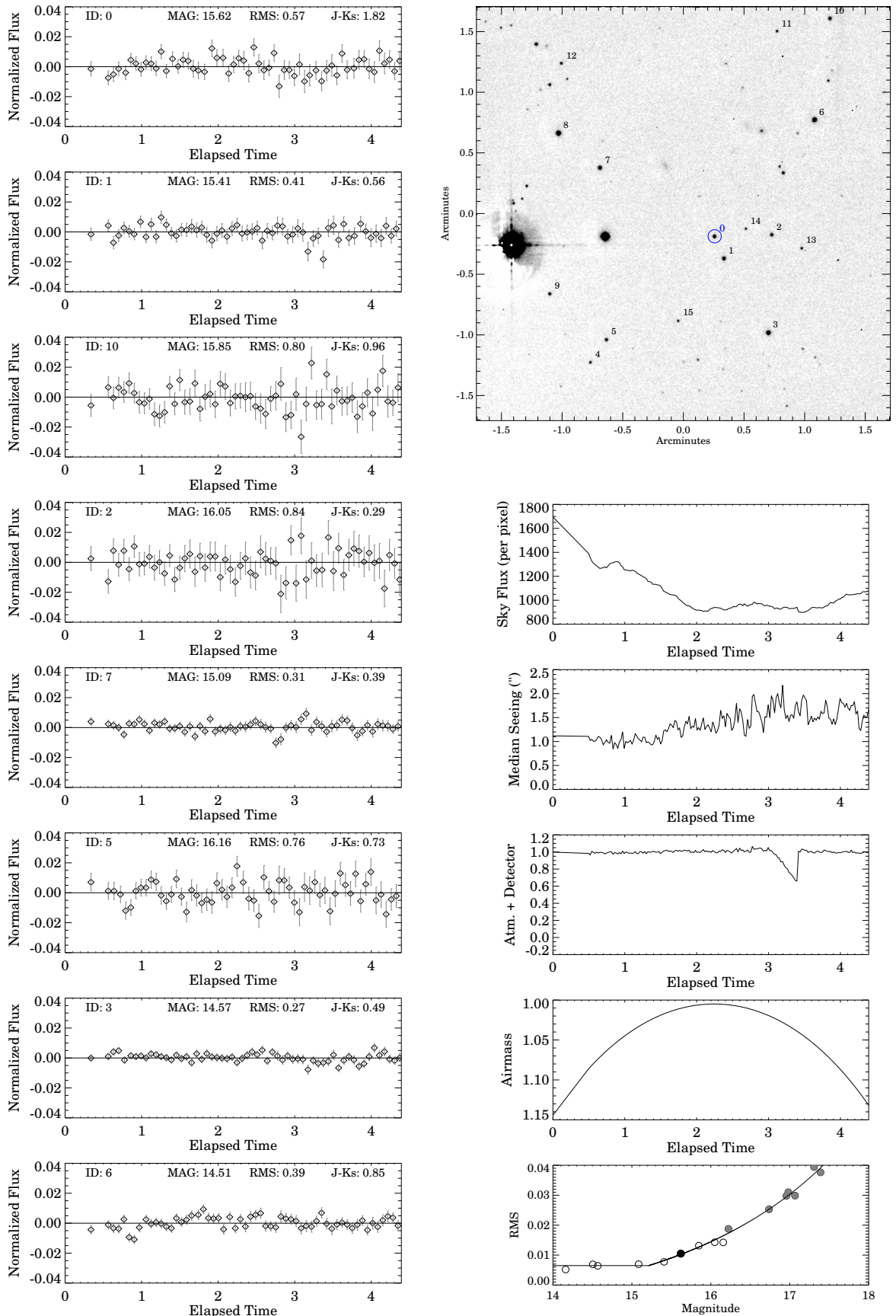


Figure C.29: As described in section C.1: SDSS J104829.21+091937.8 (2010-03-31T01:14:03)

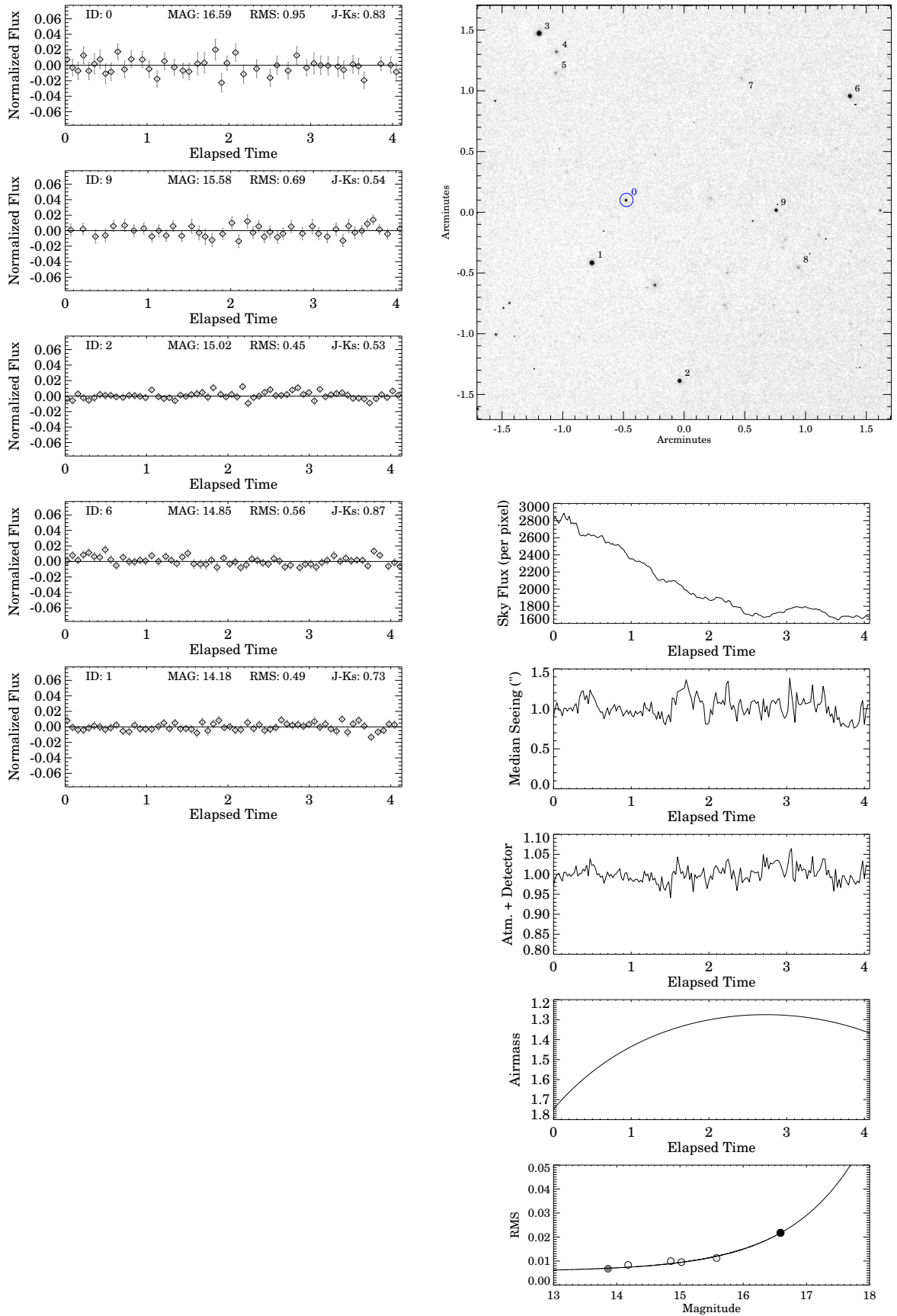


Figure C.30: As described in section C.1: SDSSp J111010.01+011613.1 (2010-04-03T23:46:45)

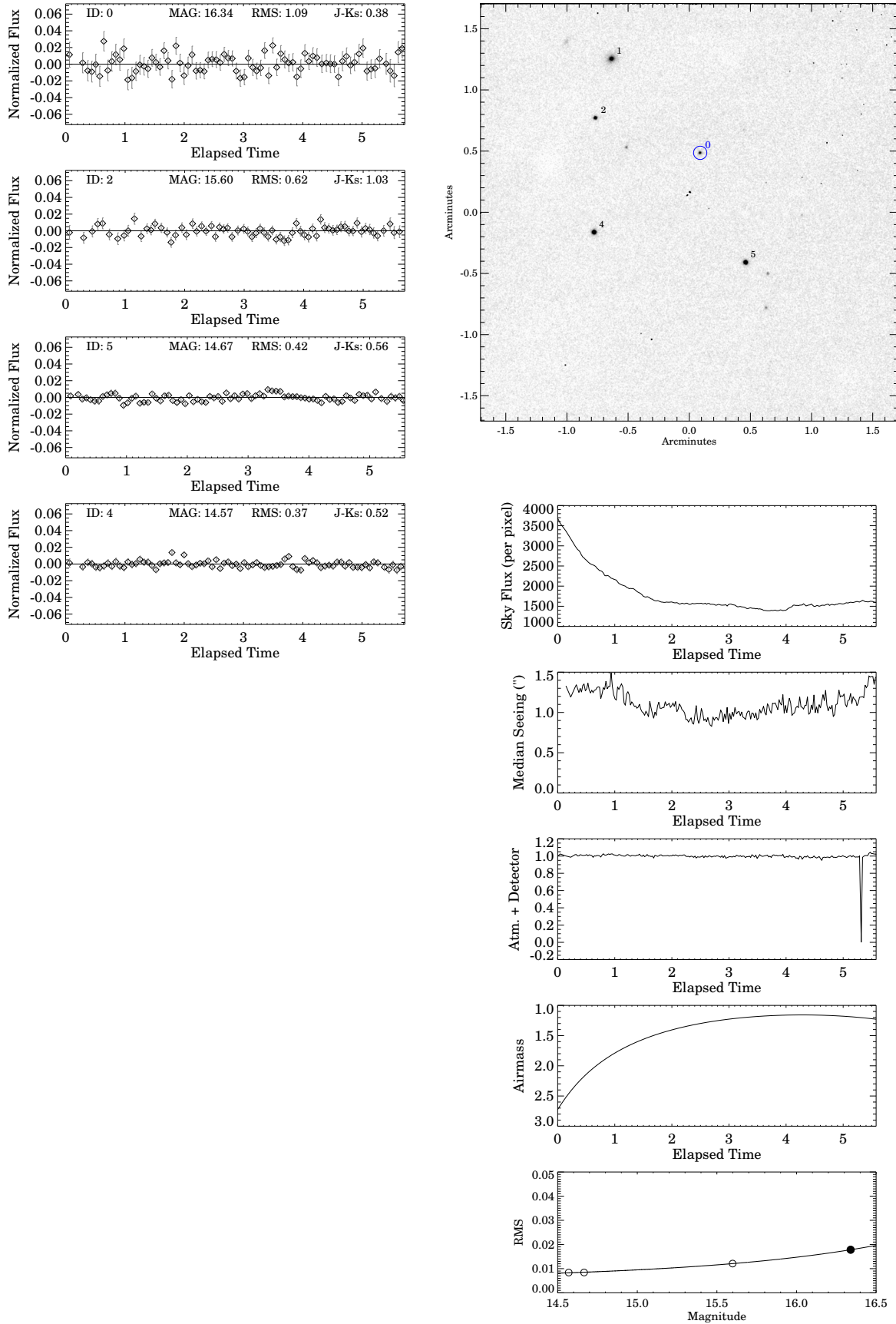


Figure C.31: As described in section C.1: 2MASS J11145133-2618235 (2010-03-29T03:03:22)

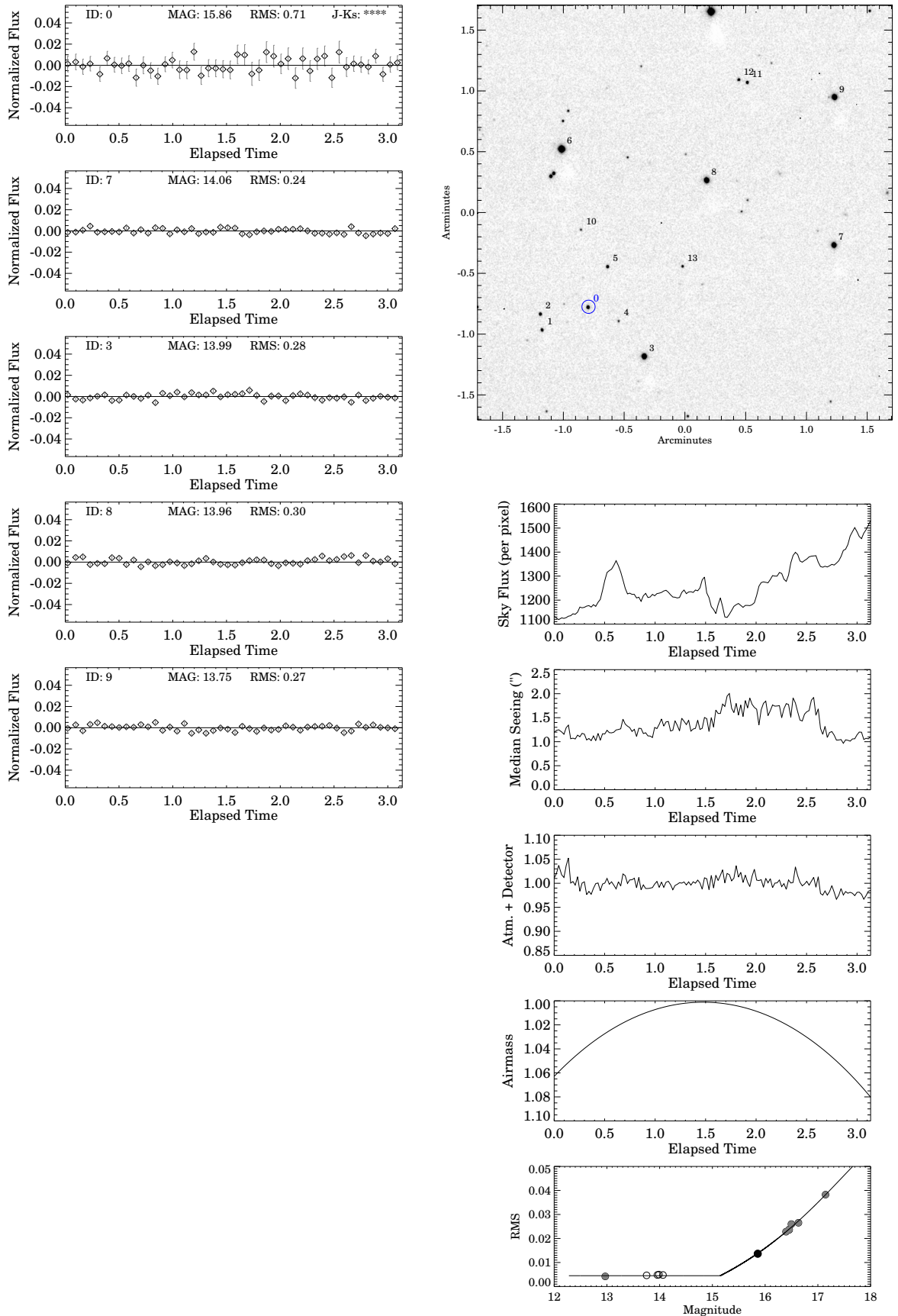


Figure C.32: As described in section C.1: 2MASS J11220826-3512363 (2010-02-01T06:07:16)

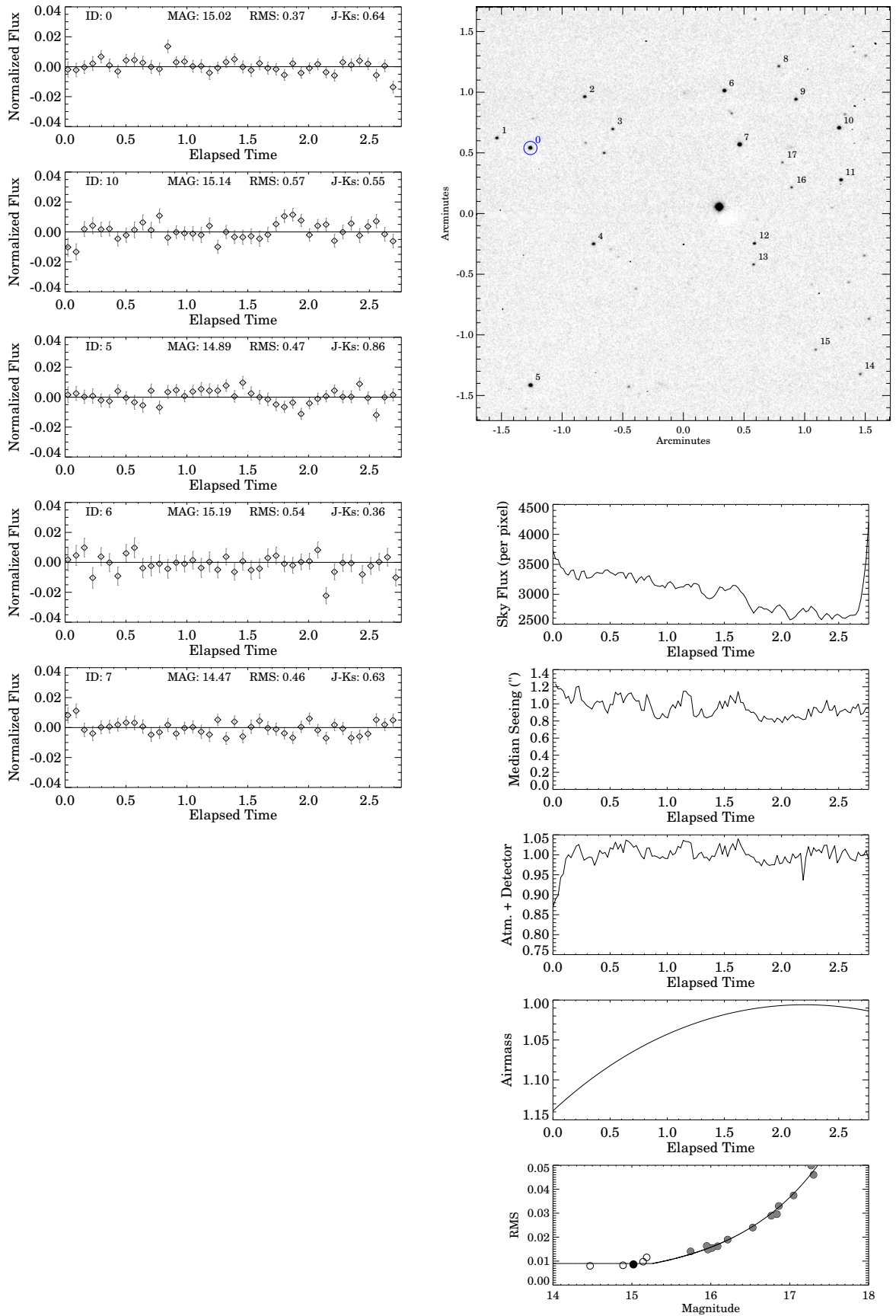


Figure C.33: As described in section C.1: 2MASS J11263991-5003550 (2010-04-26T23:20:23)

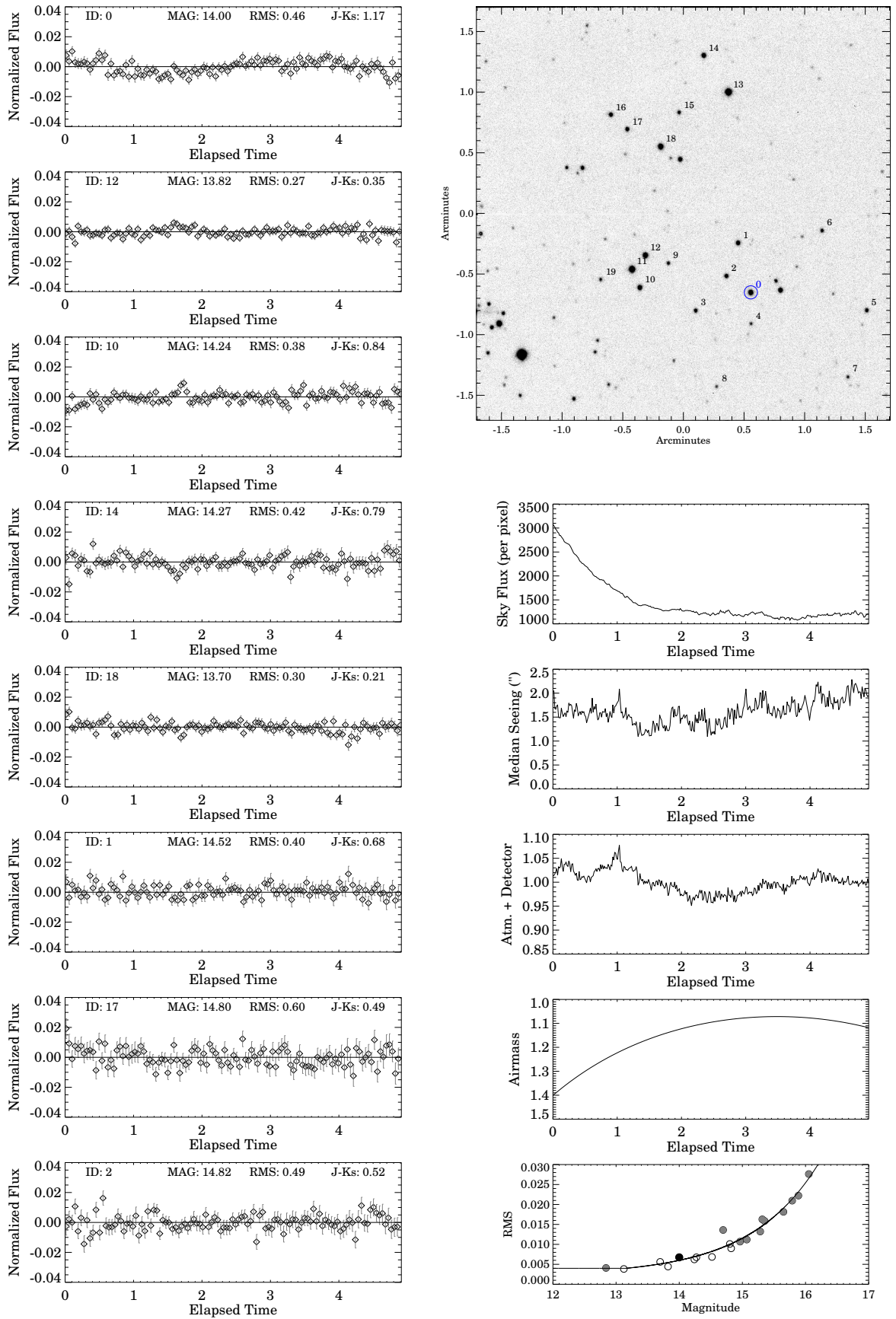


Figure C.34: As described in section C.1: 2MASS J11555389+0559577 (2010-04-22T02:07:39)

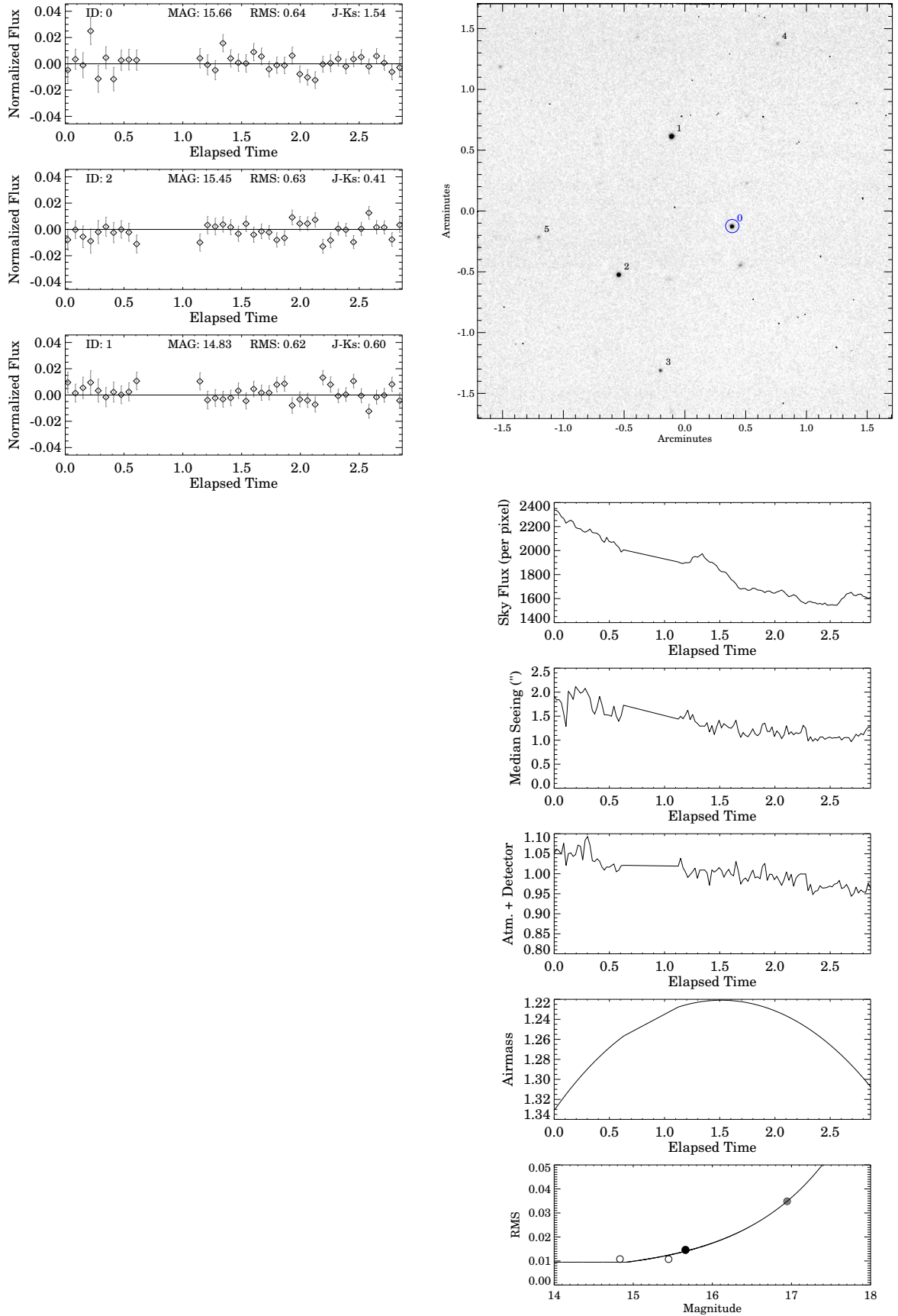


Figure C.35: As described in section C.1: SDSS J120747.17+024424.8 (2010-02-08T04:55:18)

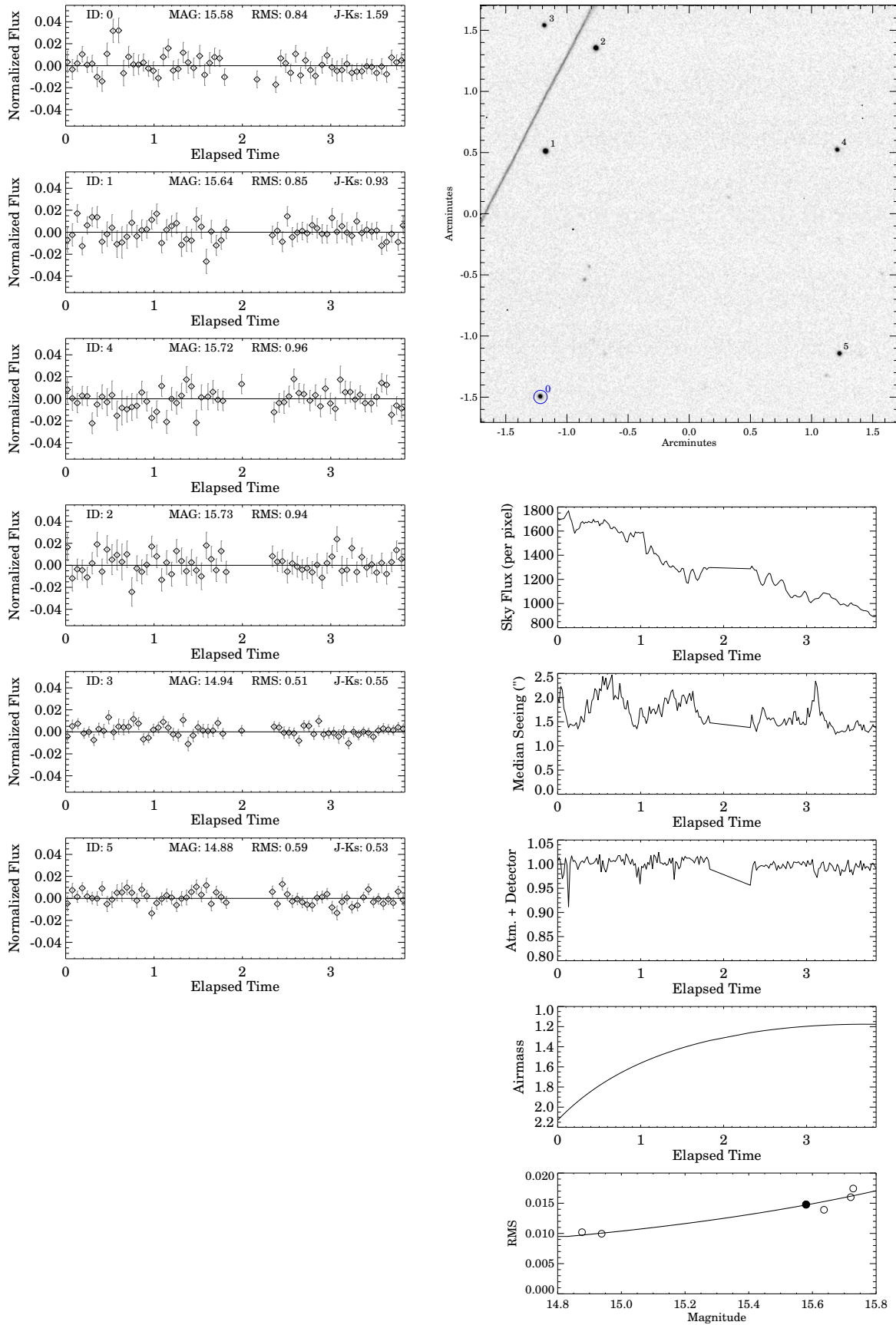


Figure C.36: As described in section C.1: 2MASS J12095613-1004008 (2010-02-07T05:31:00)

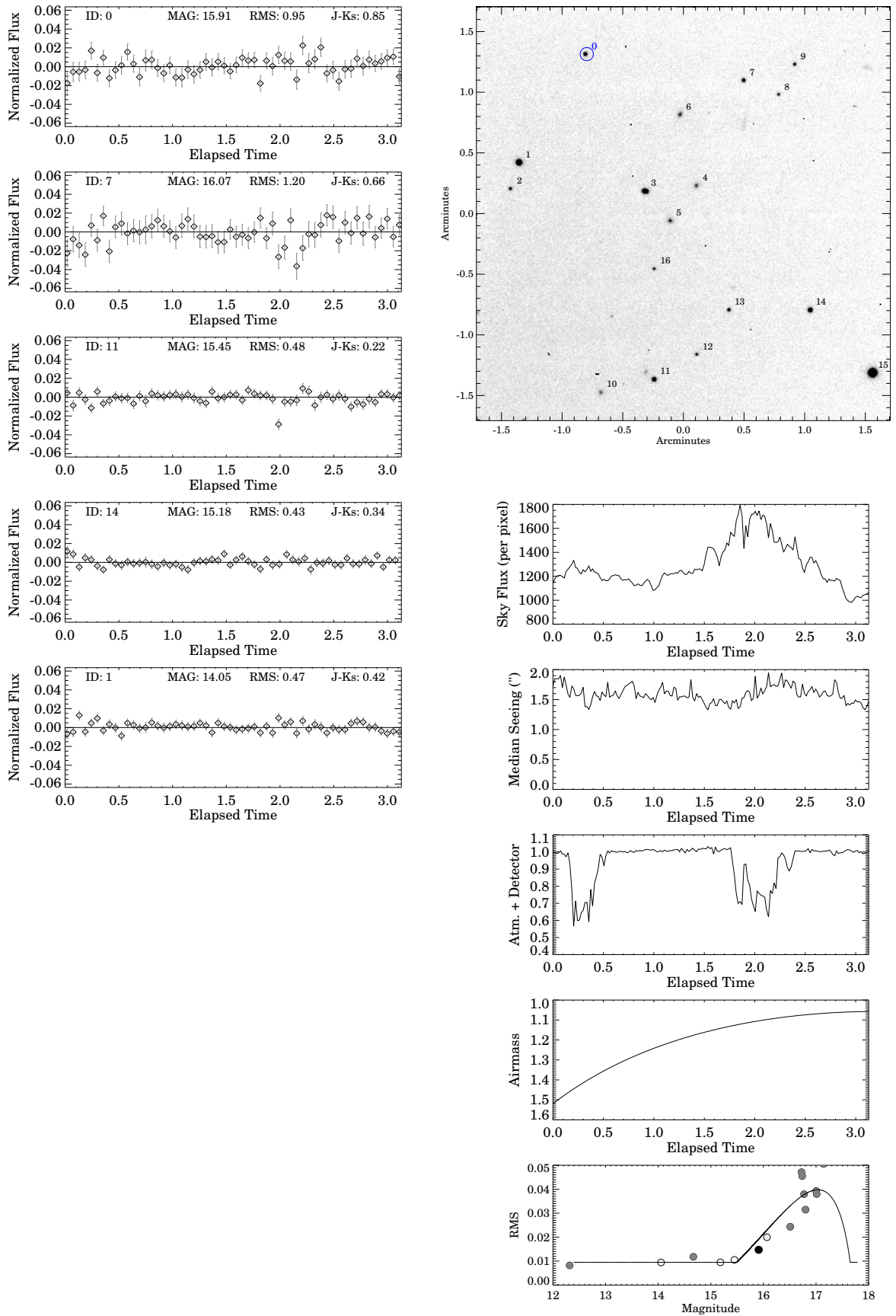


Figure C.37: As described in section C.1: 2MASS J12154432-3420591 (2010-03-27T03:57:43)

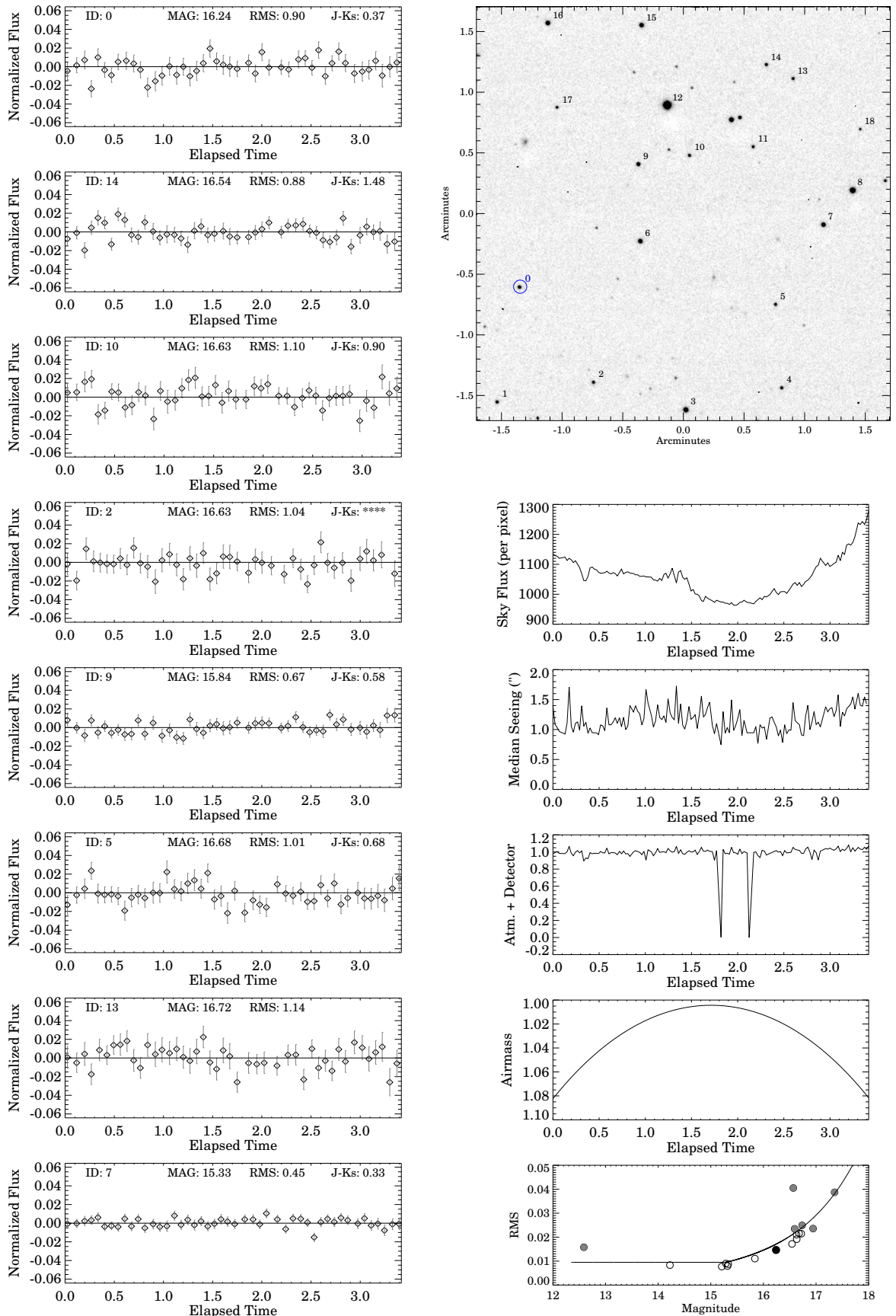


Figure C.38: As described in section C.1: 2MASS J1217110-031113 (2010-04-23T01:28:51)

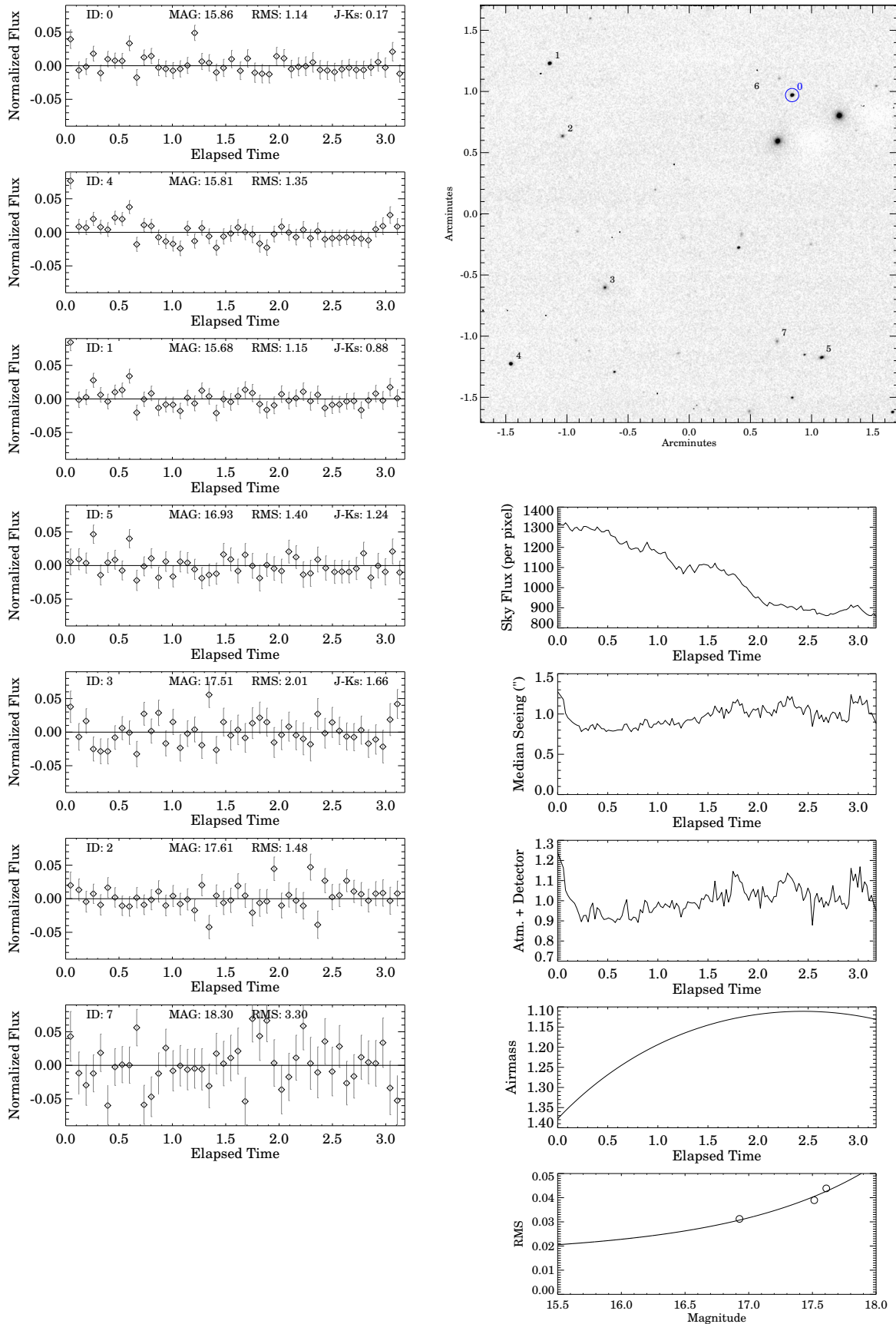


Figure C.39: As described in section C.1: 2MASS J12314753+0847331 (2010-02-09T05:39:00)

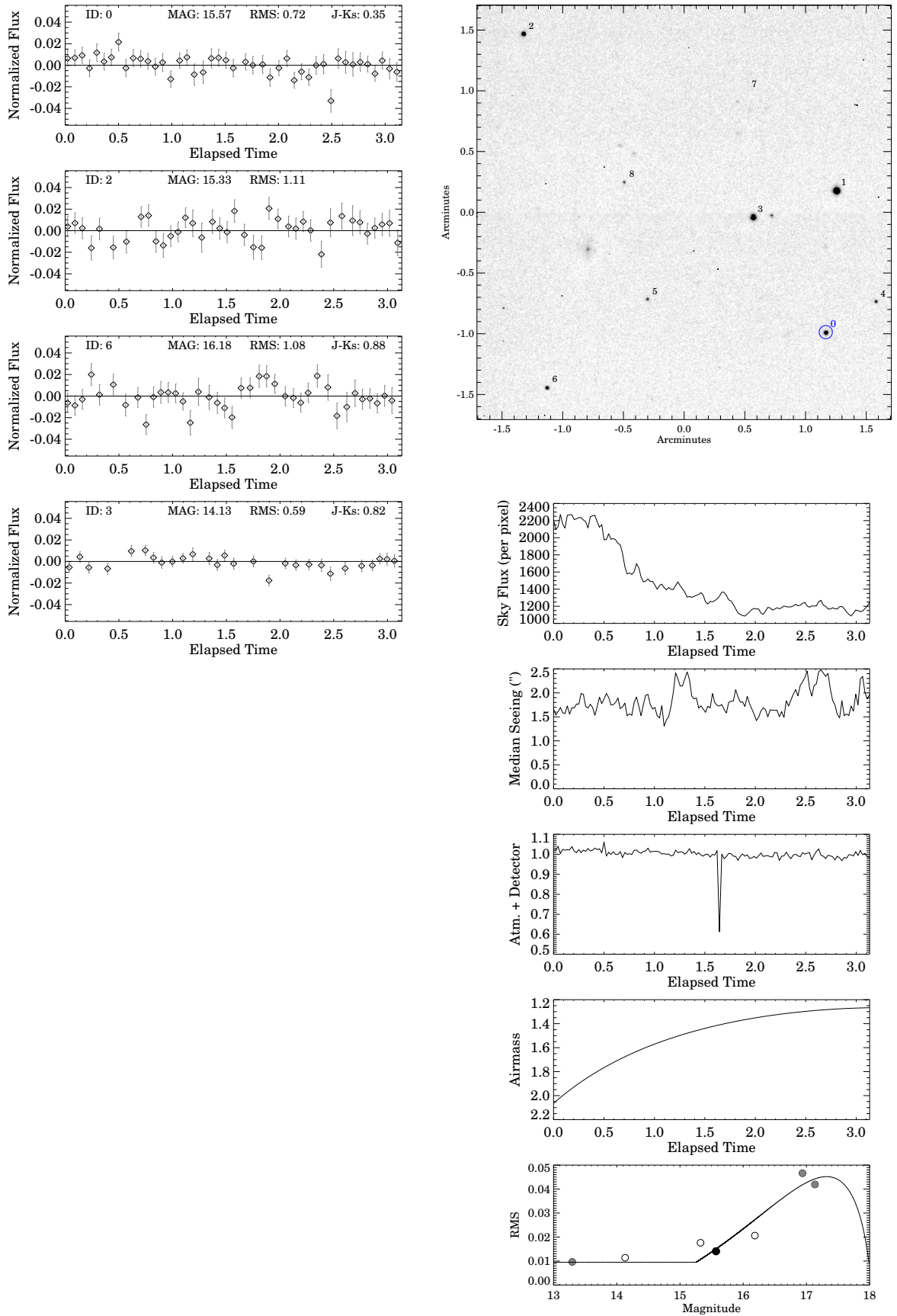


Figure C.40: As described in section C.1: SDSSp J125453.90-012247.4 (2010-02-02T05:43:40)

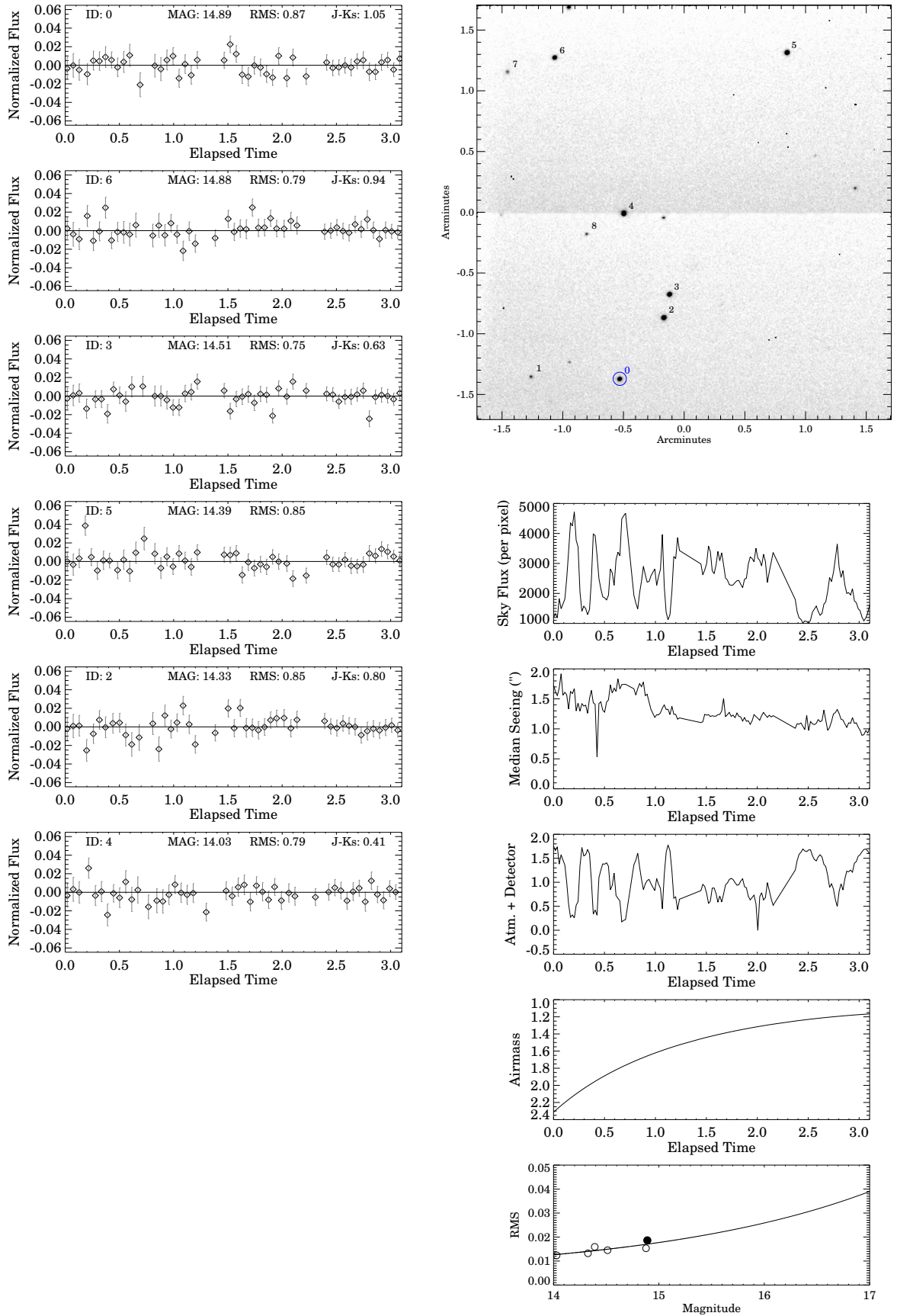


Figure C.41: As described in section C.1: SDSSp J132629.82-003831.5 (2010-04-02T06:08:34)

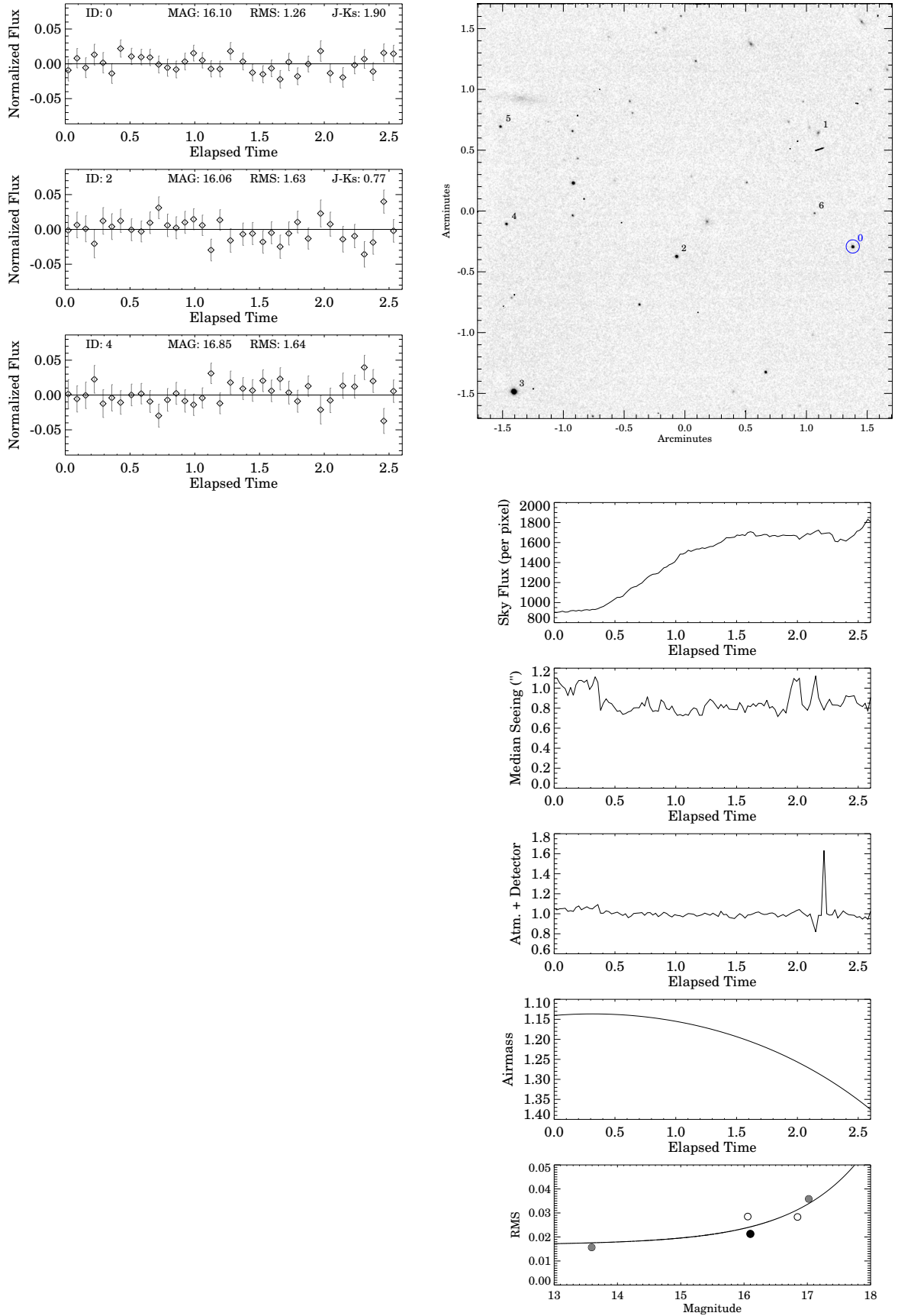


Figure C.42: As described in section C.1: SDSS J140255.66+080055.2 (2010-03-30T04:53:38)

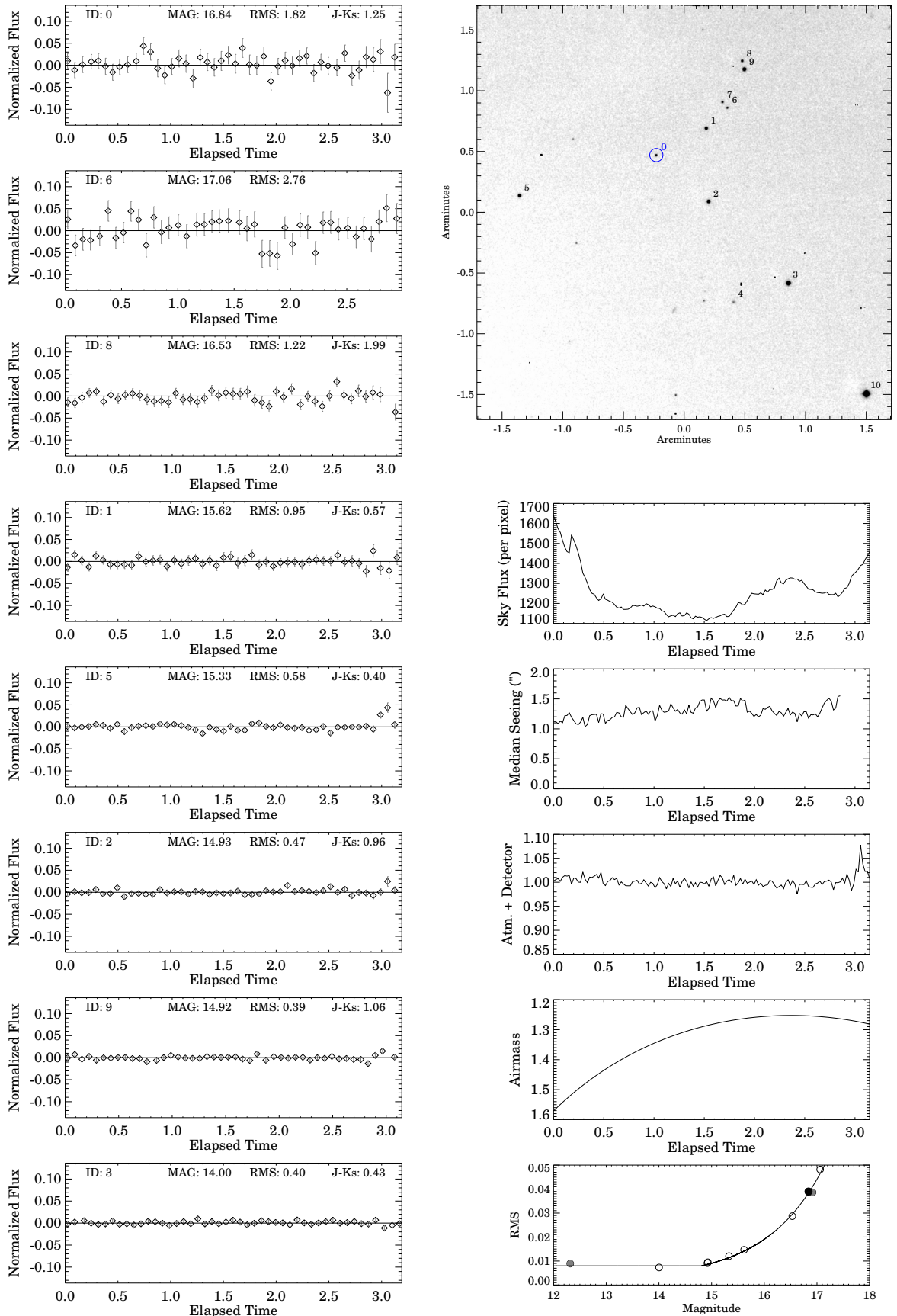


Figure C.43: As described in section C.1: 2MASS J14044941-3159329 (2010-03-28T06:32:51)

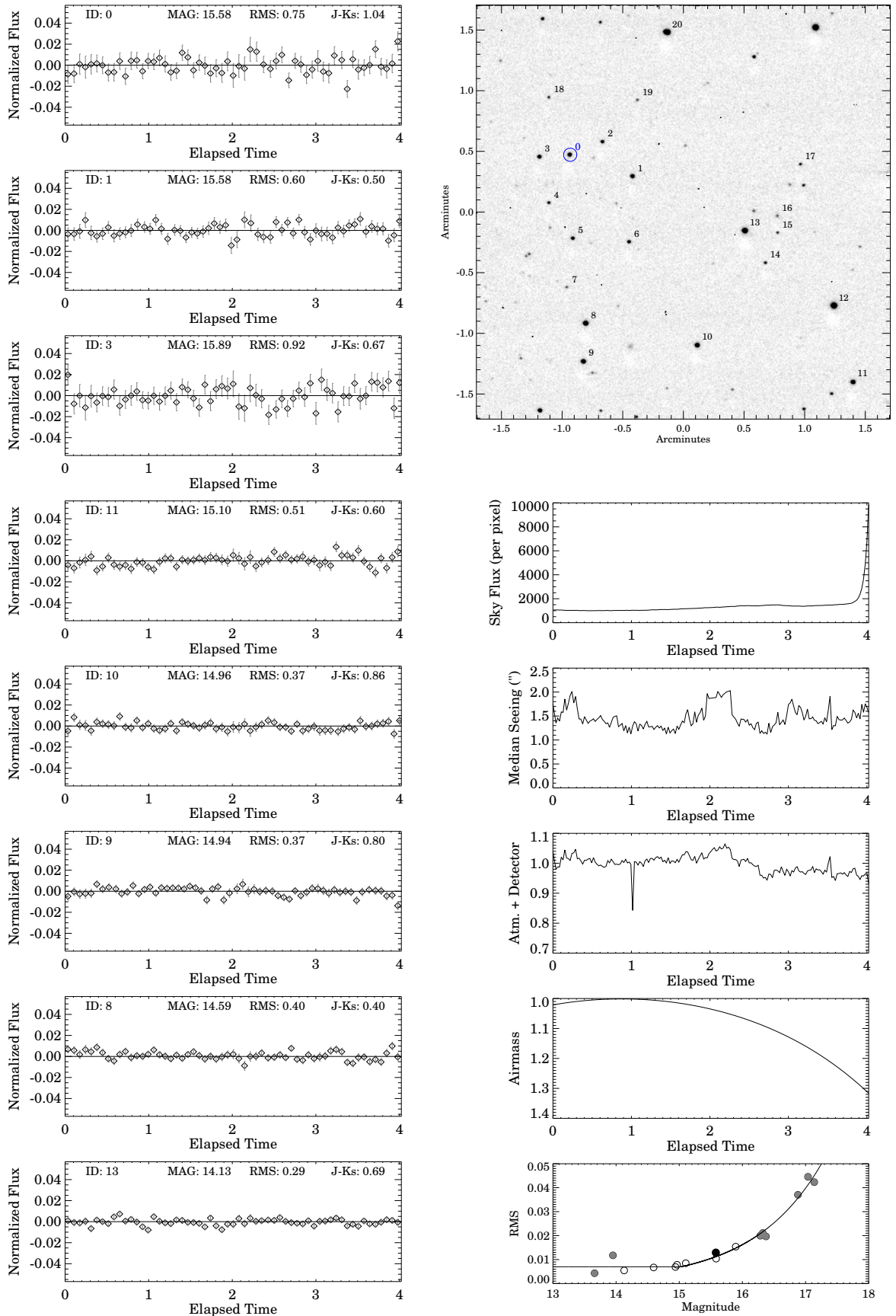


Figure C.44: As described in section C.1: SDSS J141624.08+134826.7 (2010-05-04T03:28:04)

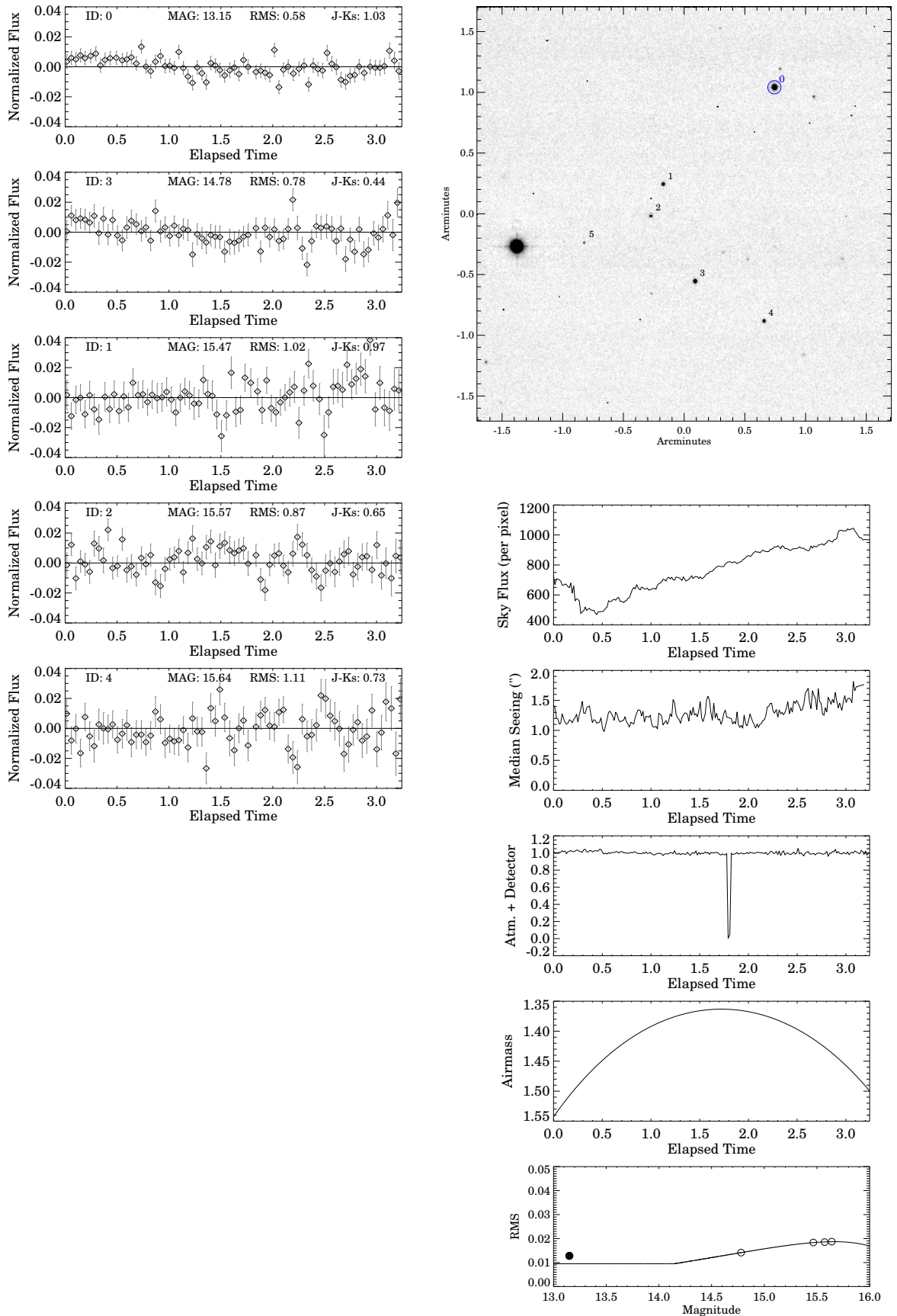


Figure C.45: As described in section C.1: DENIS-P J142527.97-365023.4 (2010-04-25T04:25:08)

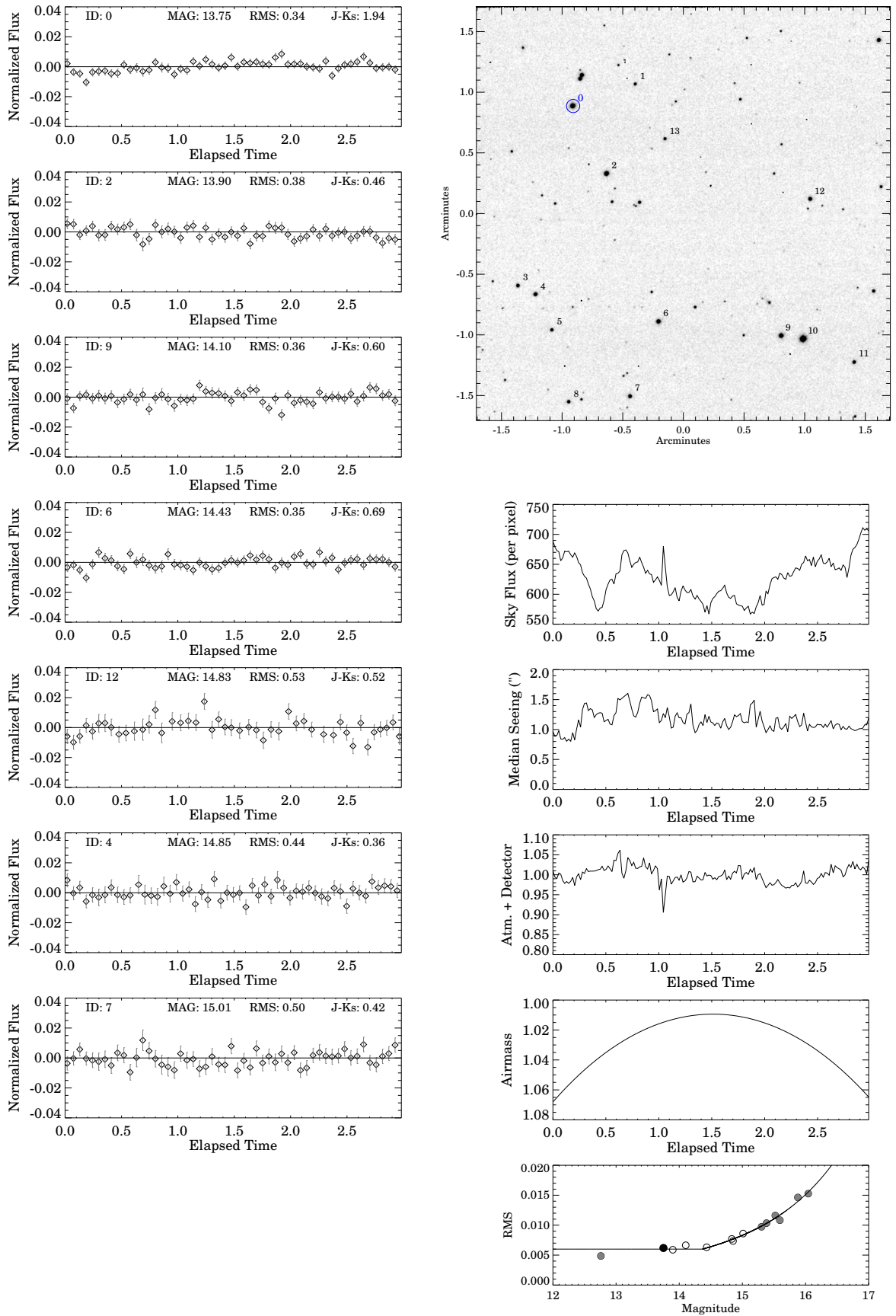


Figure C.46: As described in section C.1: 2MASS J15074769-1627386 (2010-04-06T05:22:58)

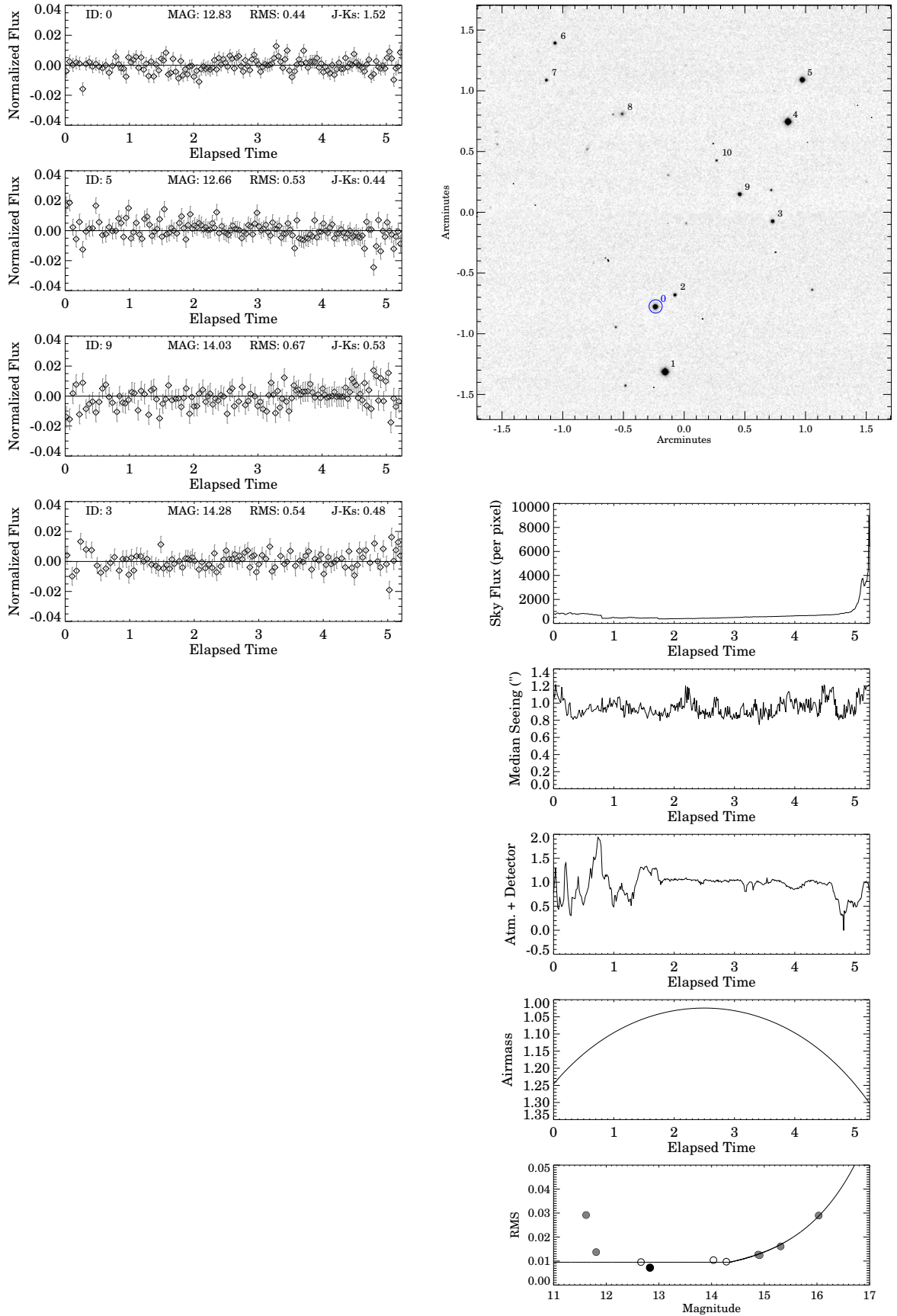


Figure C.47: As described in section C.1: SDSS J151114.66+060742.9 (2010-03-26T07:12:40)

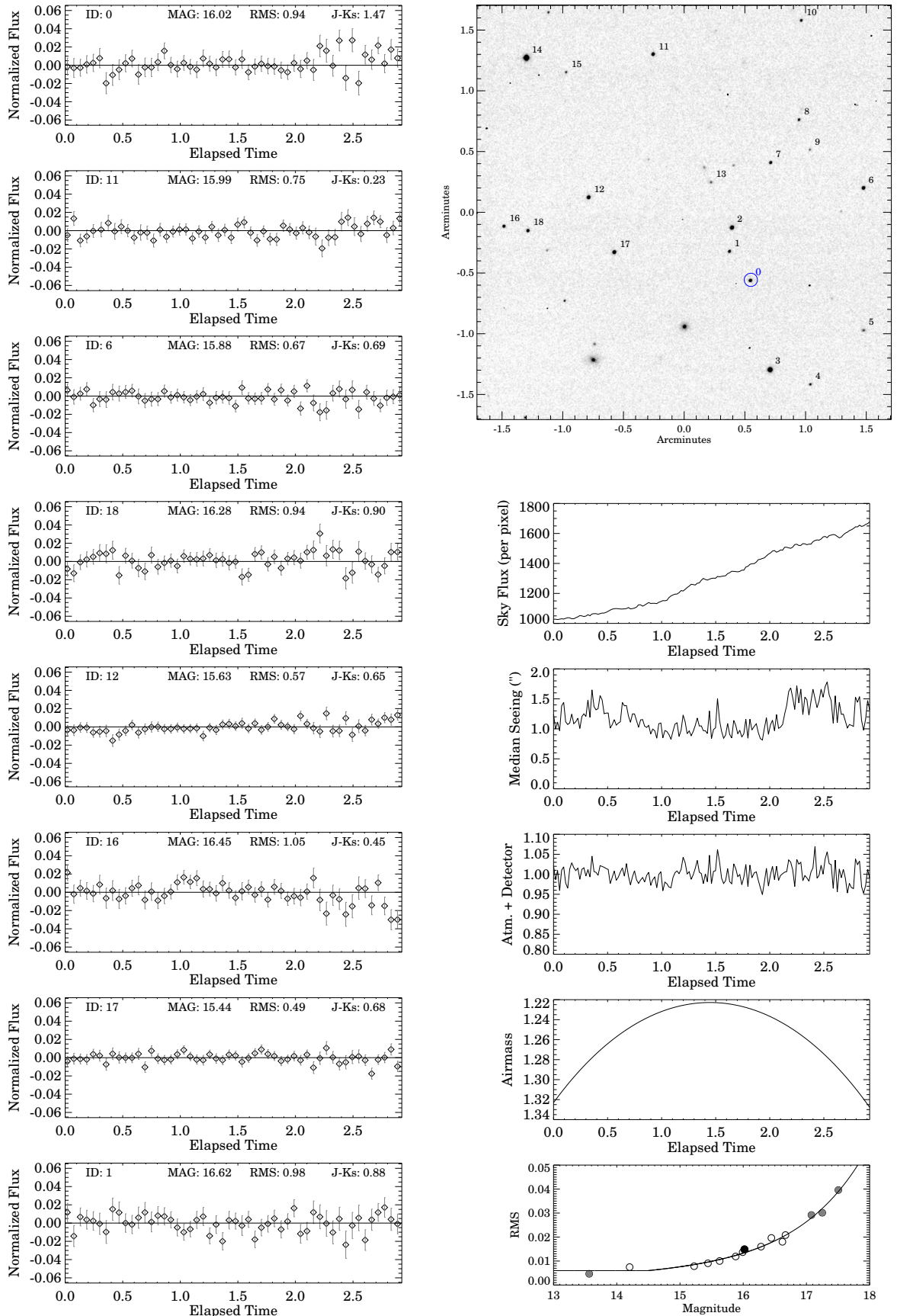


Figure C.48: As described in section C.1: SDSS J152103.24+013142.7 (2010-03-27T07:38:15)

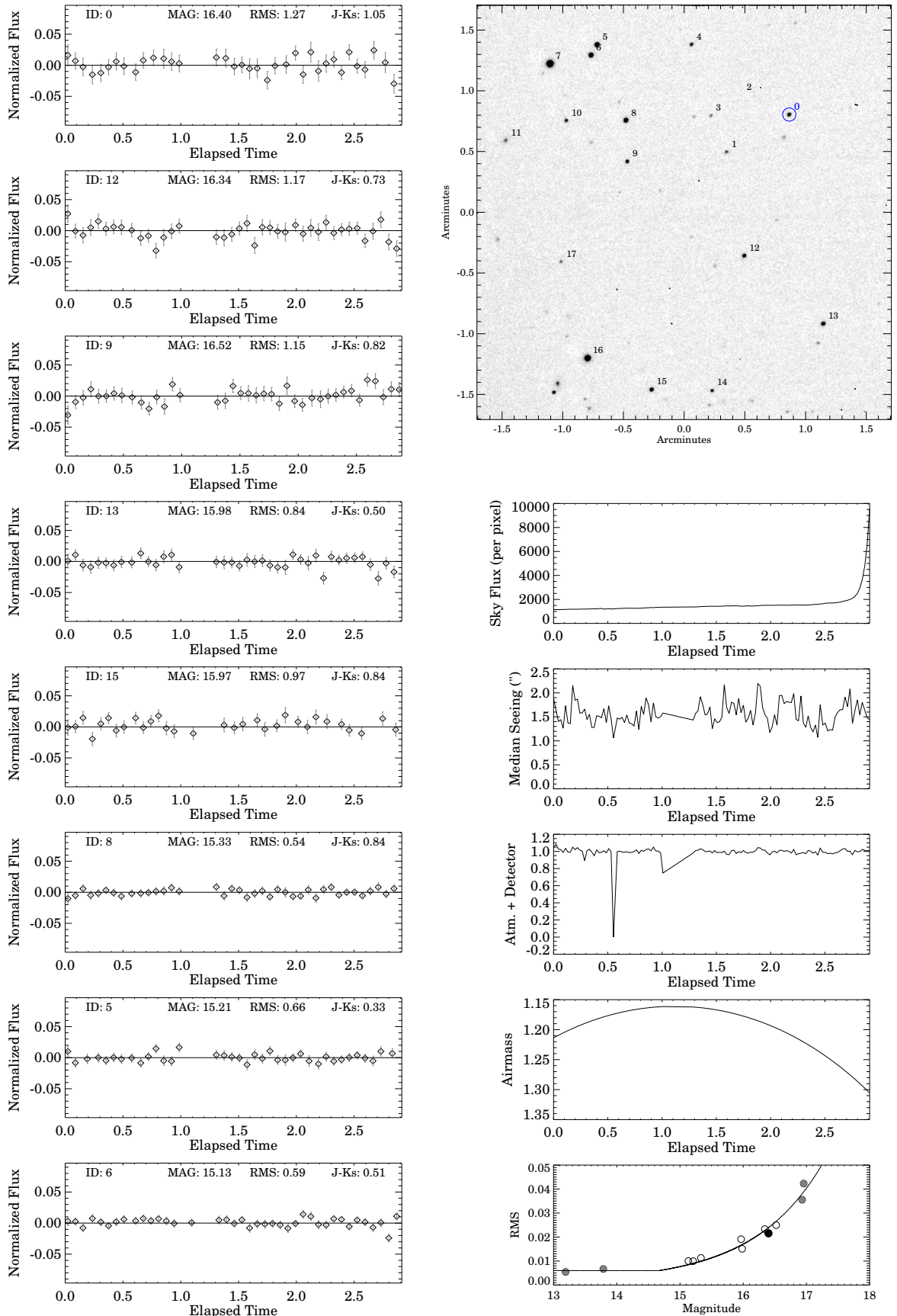


Figure C.49: As described in section C.1: 2MASS J1546271-332511 (2009-07-29T00:44:34)

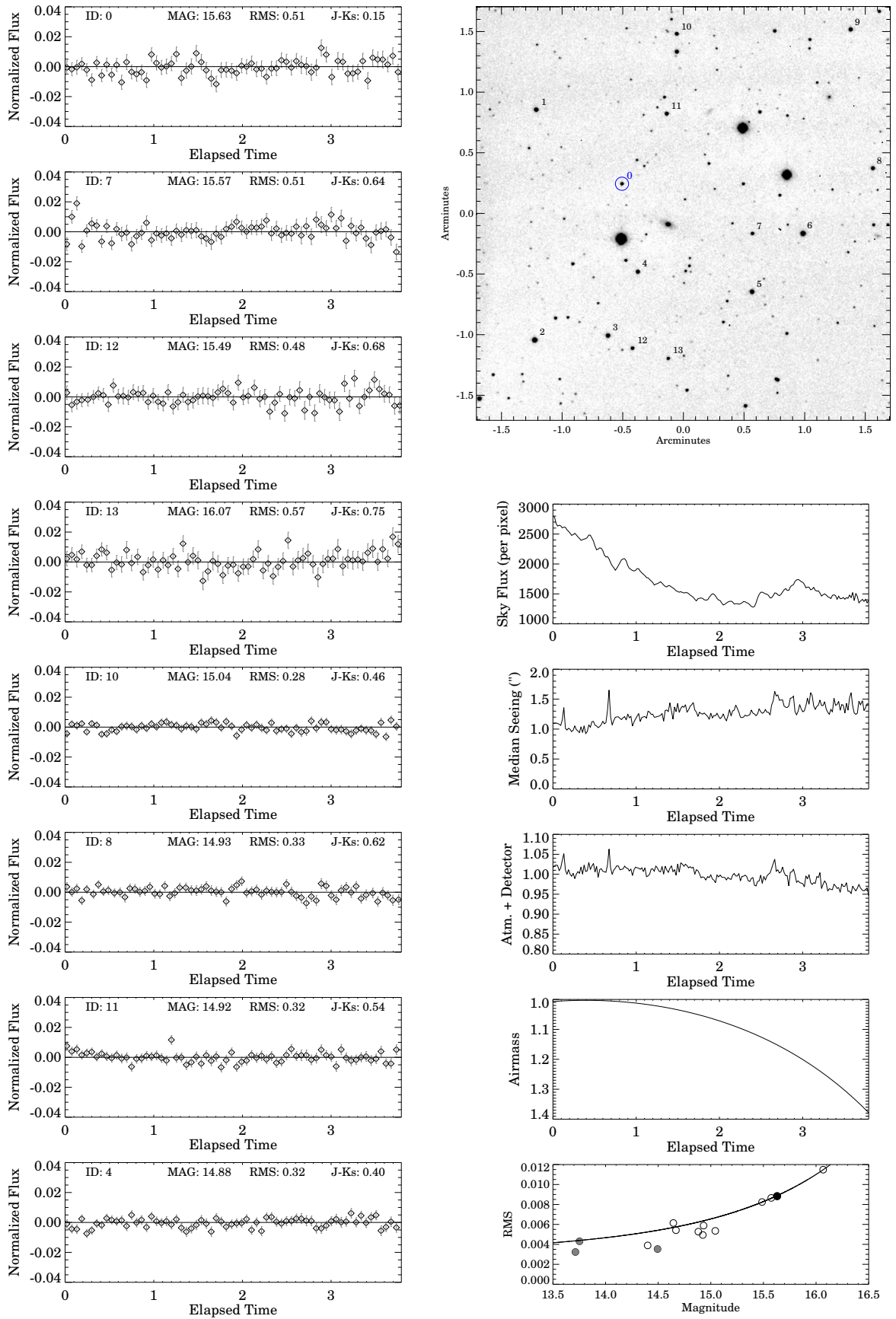


Figure C.50: As described in section C.1: SIMP J162918.41+033537.0 (2009-07-29T23:47:39)

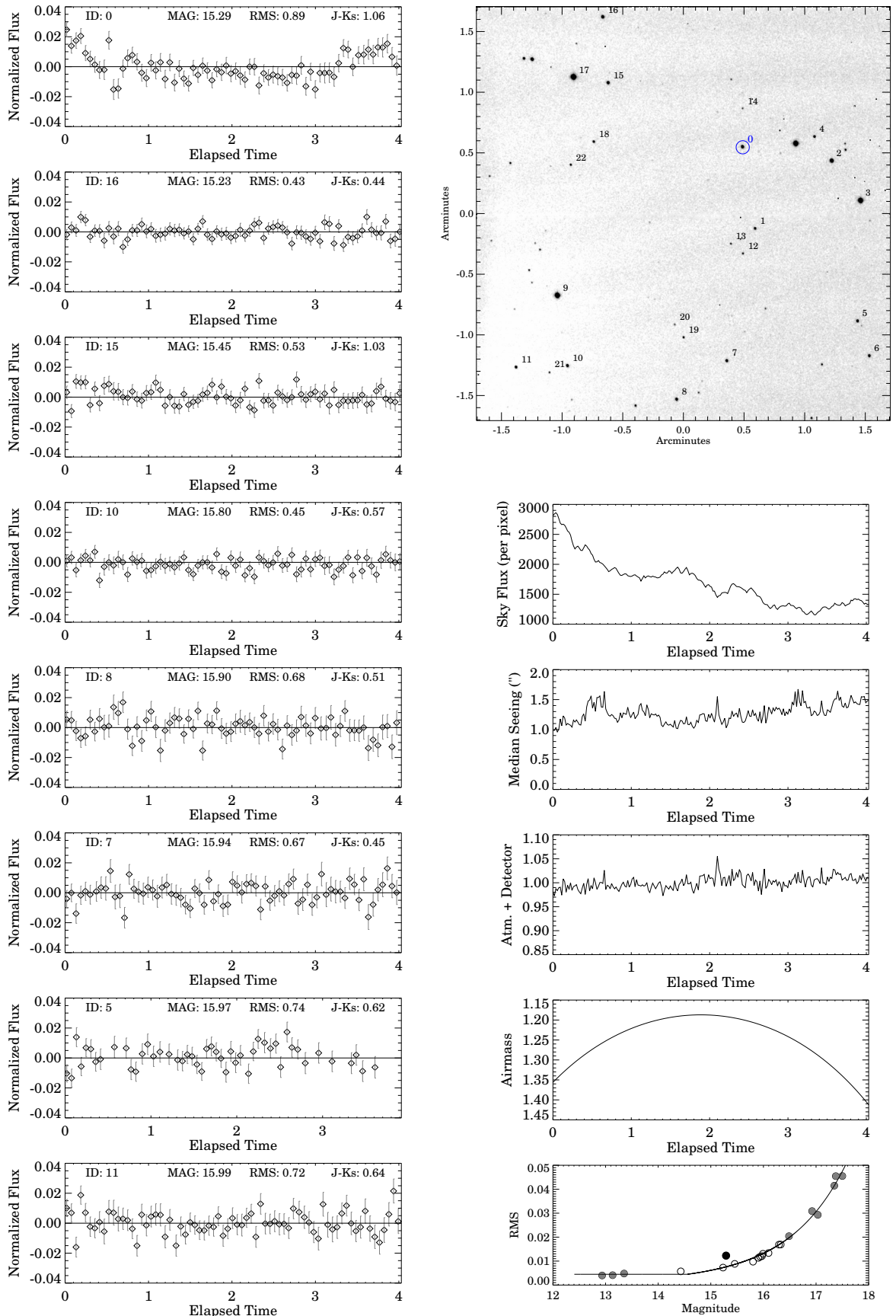


Figure C.51: As described in section C.1: 2MASS J16241436+0029158 (2009-08-09T23:33:14)

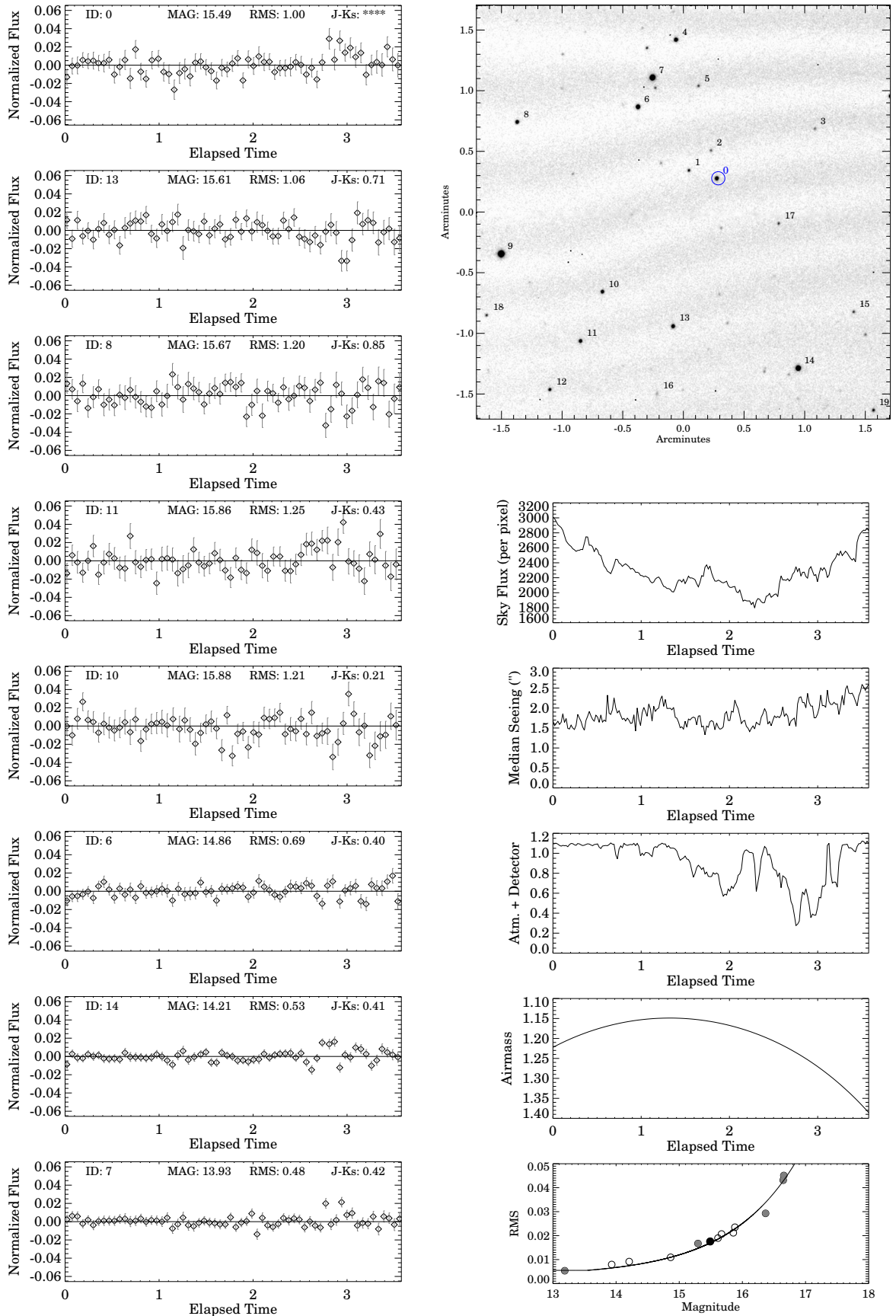


Figure C.52: As described in section C.1: SDSS J163359.23-064056.5 (2010-04-22T05:13:23)

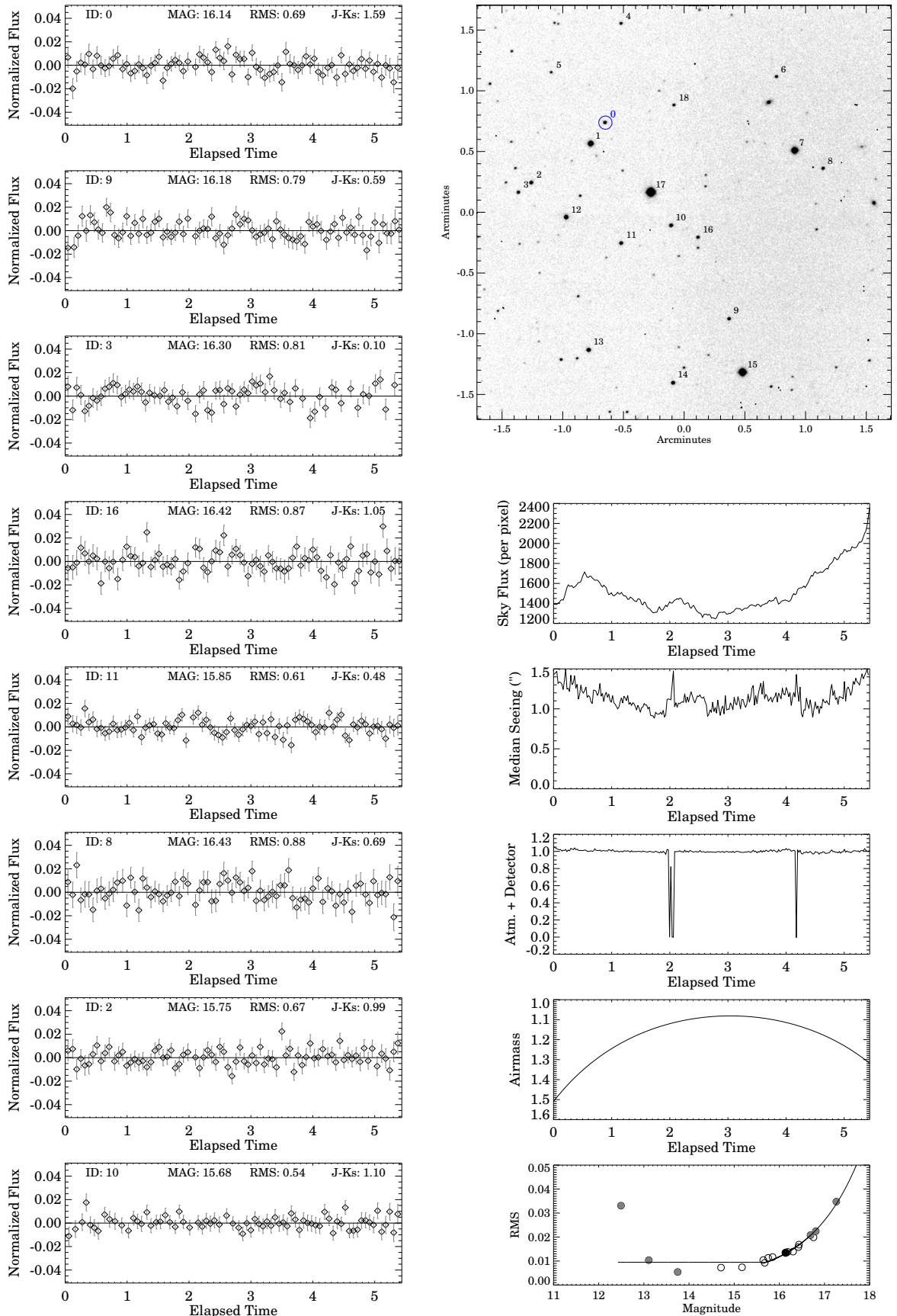


Figure C.53: As described in section C.1: DENIS-P J170548.38-051645.7 (2010-04-25T07:47:48)

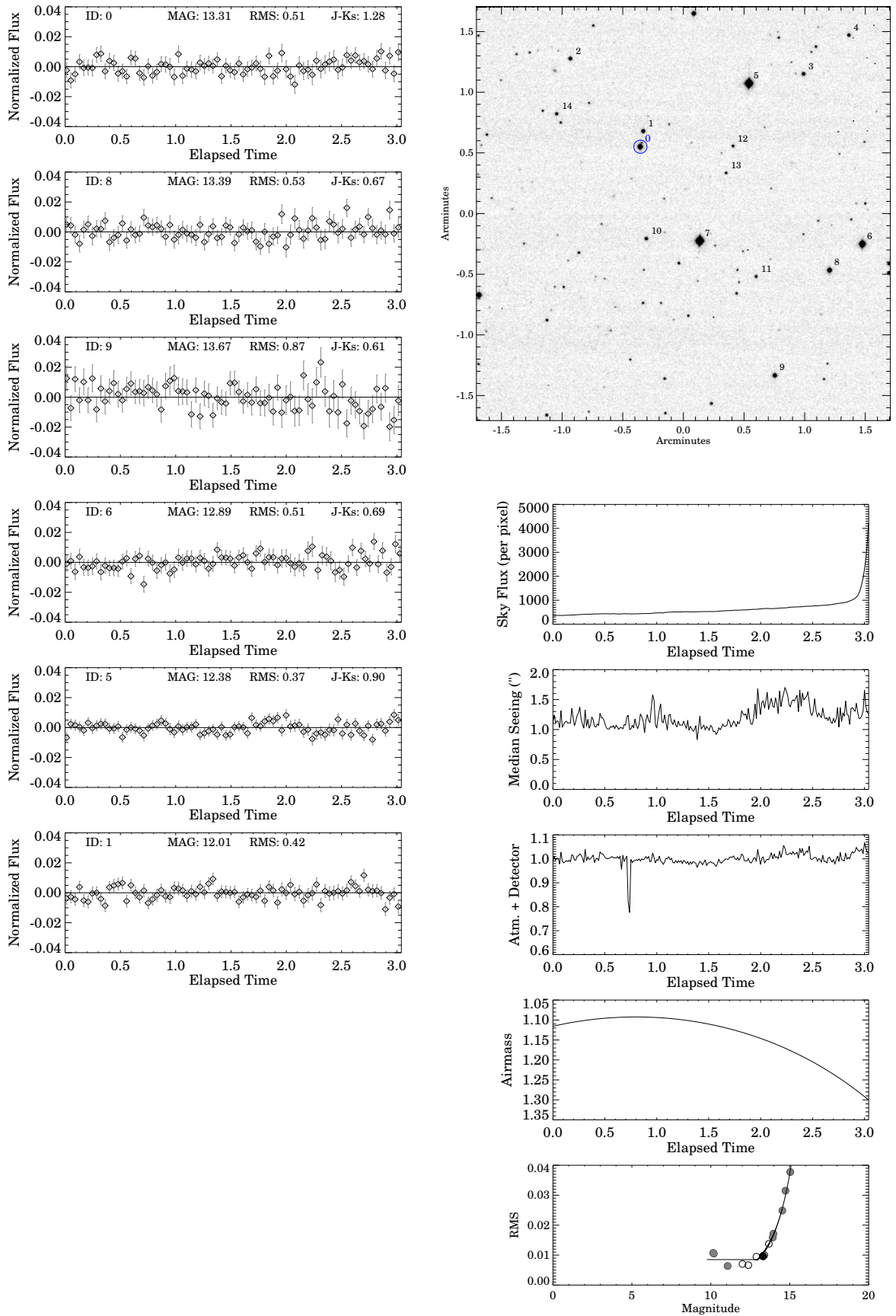


Figure C.54: As described in section C.1: 2MASS J17502484-0016151 (2010-05-01T06:05:06)

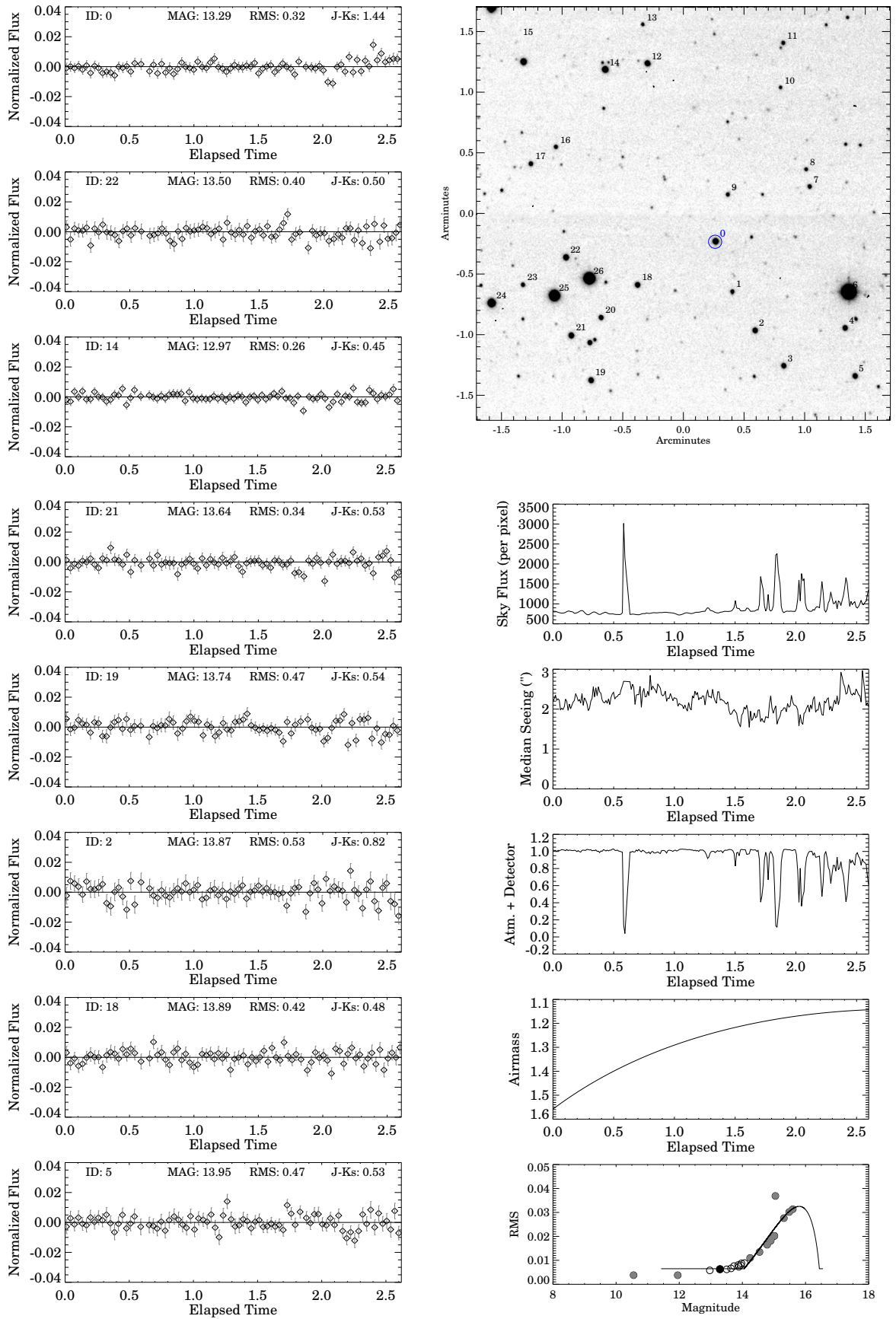


Figure C.55: As described in section C.1: SDSS J175024.01+422237.8 (2009-08-09)

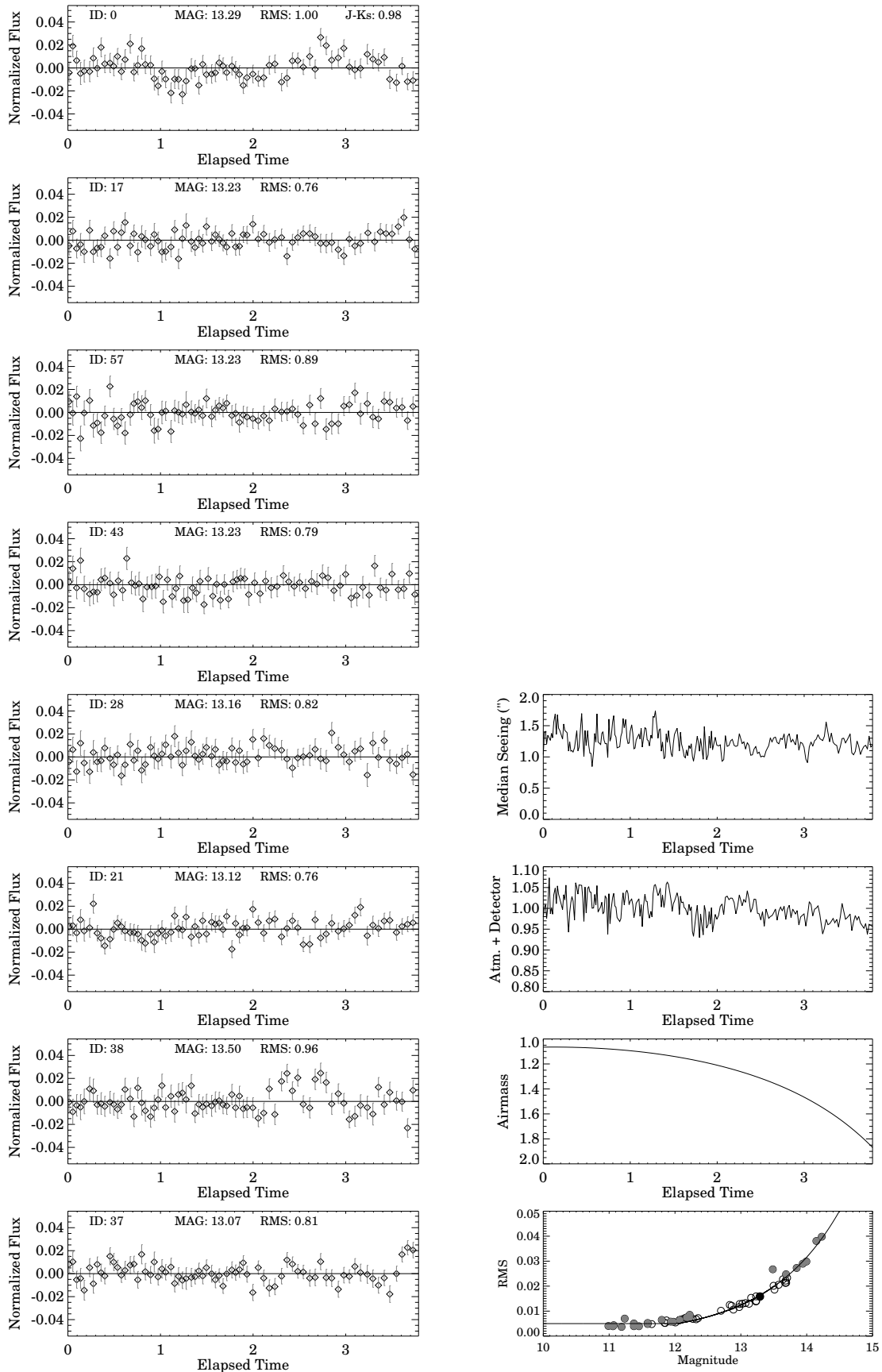


Figure C.56: As described in section C.1: 2MASS J18283572-4849046 (2009-08-11T00:55:16)

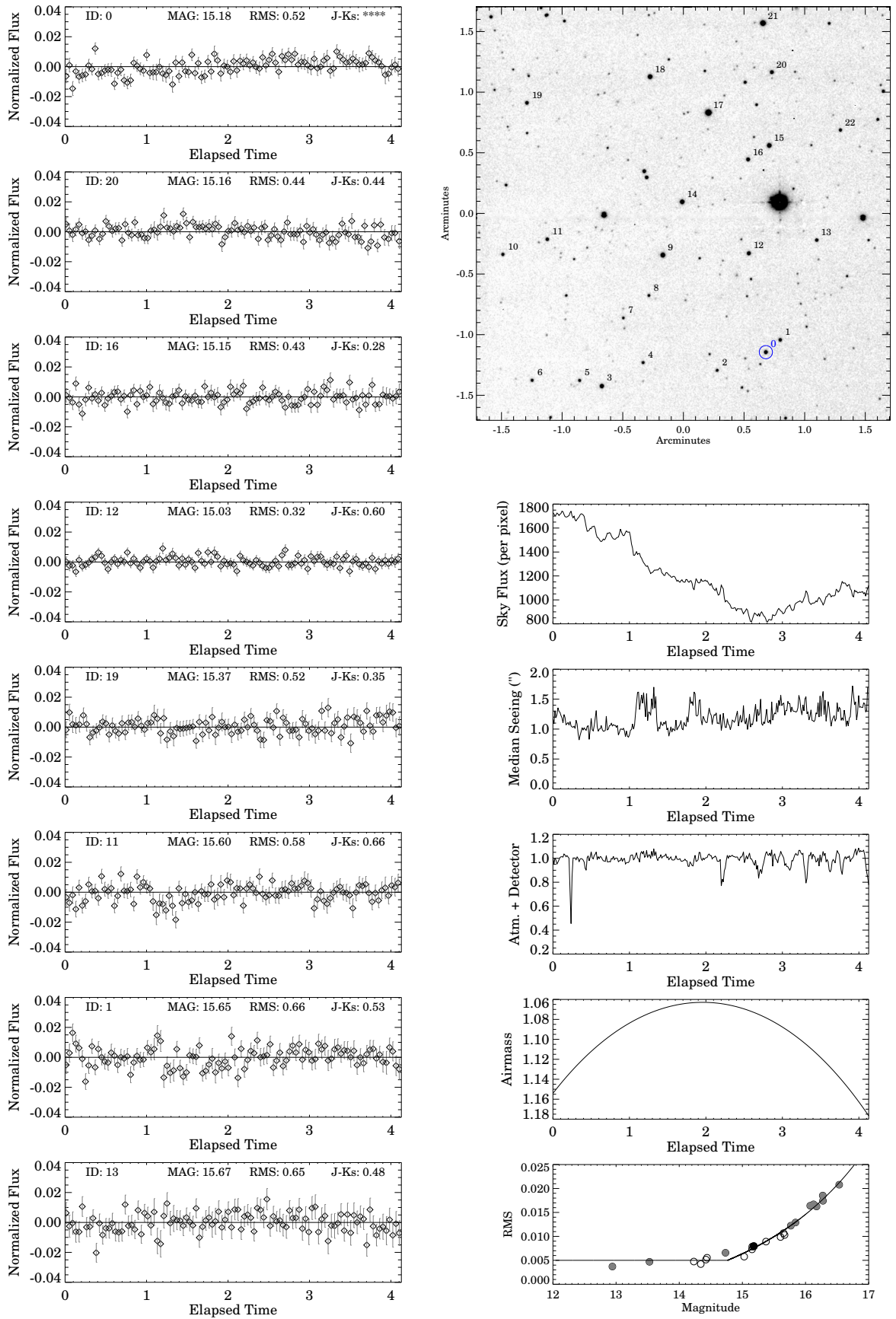


Figure C.57: As described in section C.1: 2MASS J19360187-5502322 (2010-05-04T07:00:42)

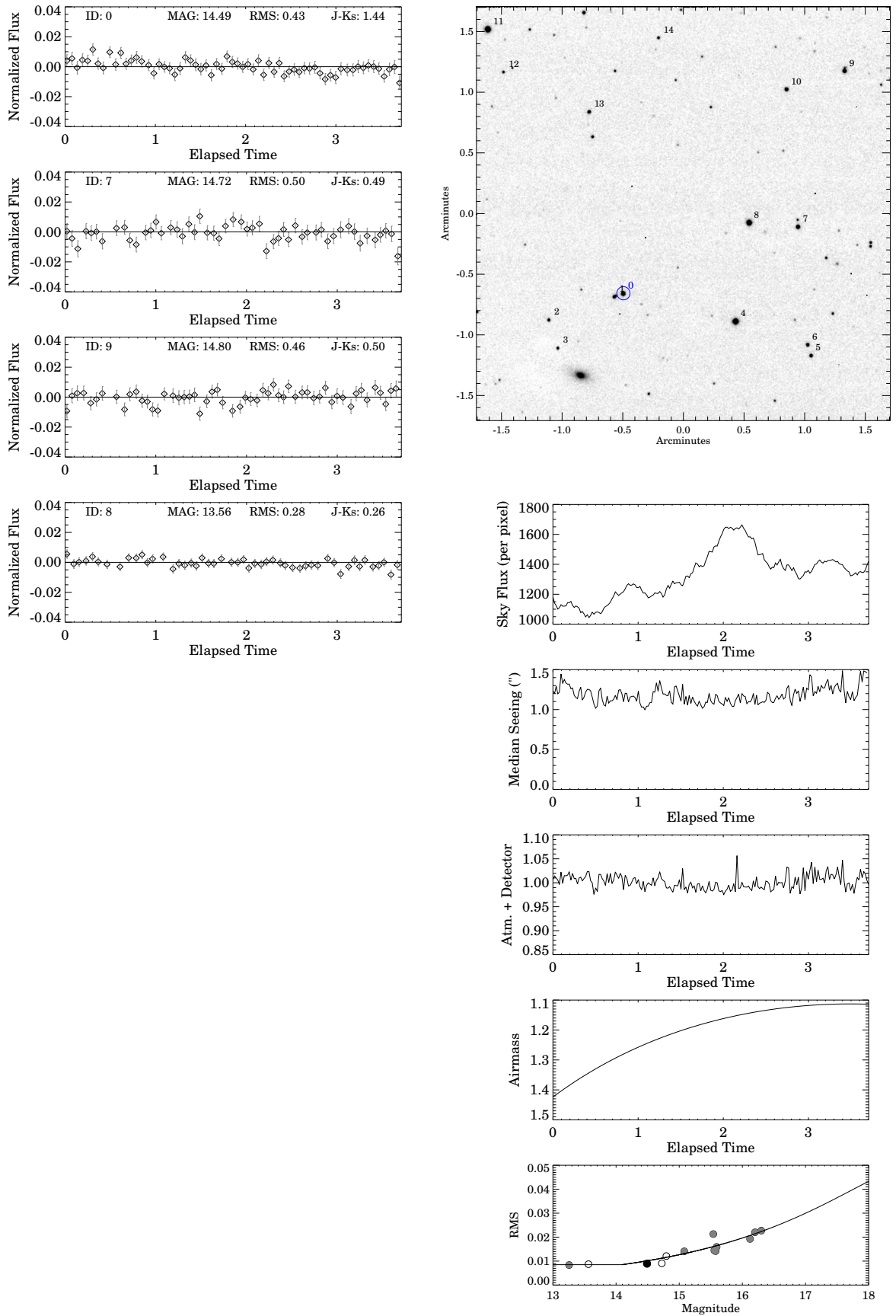


Figure C.58: As described in section C.1: SDSS J205235.31-160929.8 (2009-07-30T04:41:41)

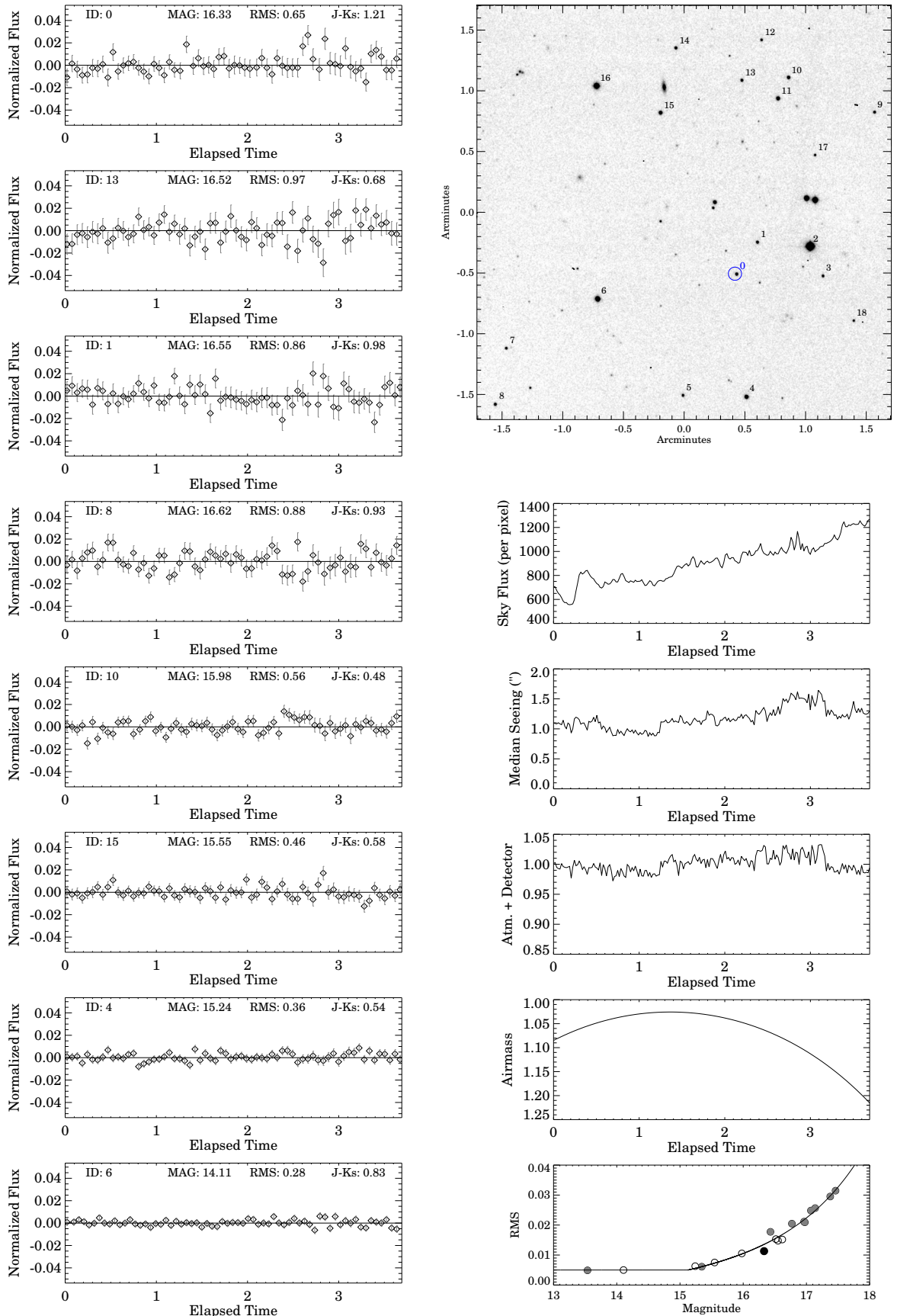


Figure C.59: As described in section C.1: 2MASS J21392676+0220226 (2009-08-02T04:38:41)

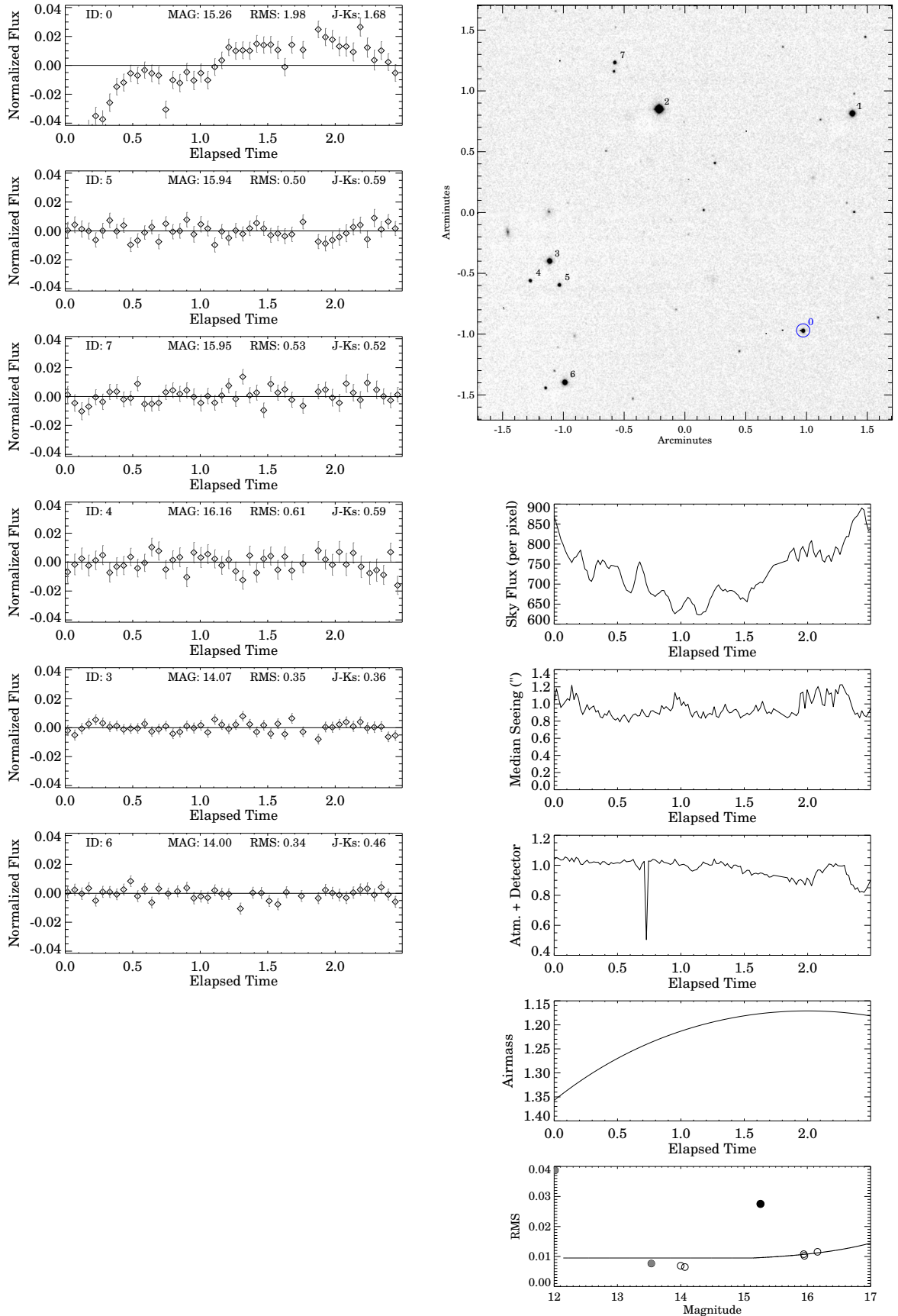


Figure C.60: As described in section C.1: 2MASS J21513839-4853542 (2009-07-29T05:34:29)

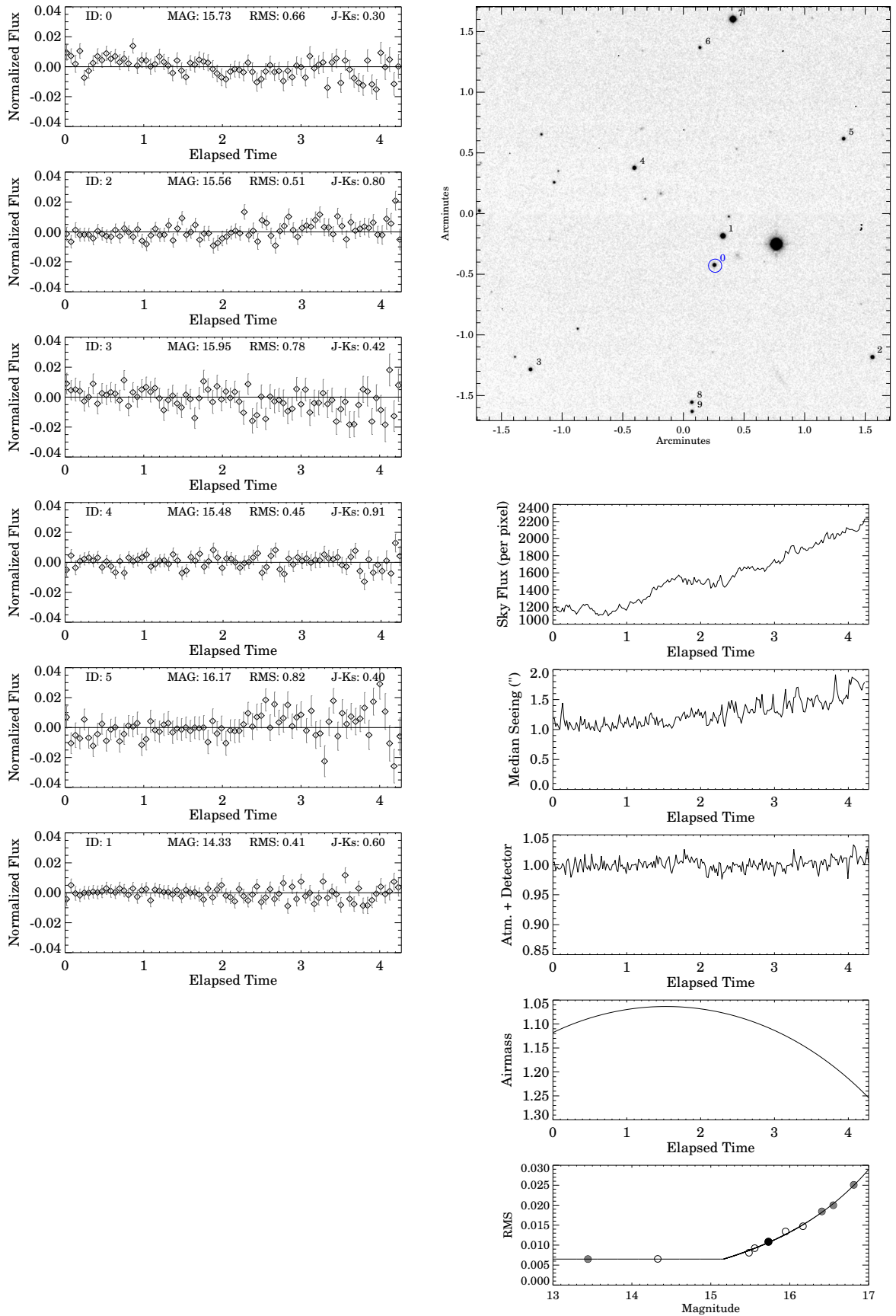


Figure C.61: As described in section C.1: 2MASS J22282889-4310262 (2009-08-01T05:03:12)

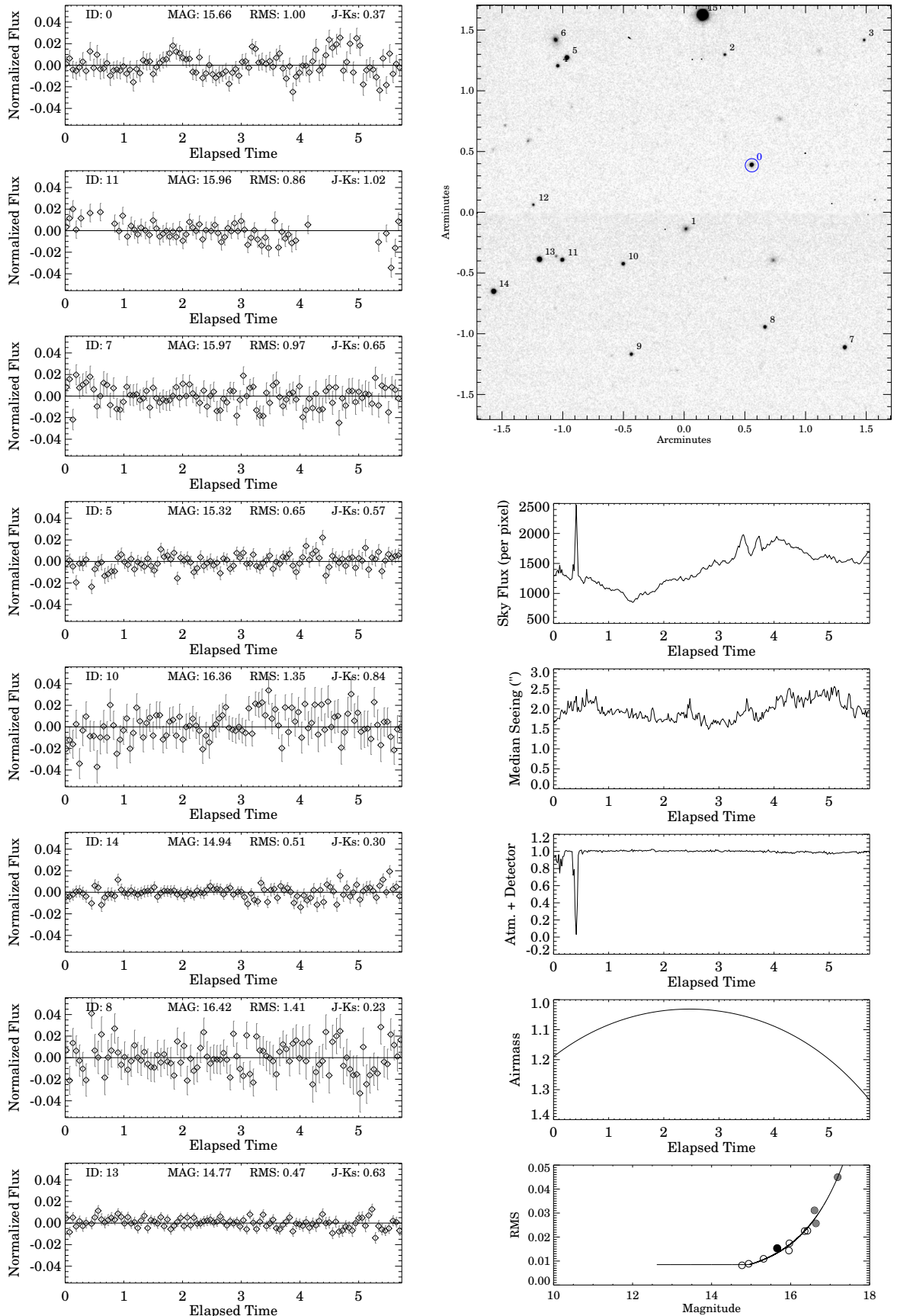


Figure C.62: As described in section C.1: 2MASS J2254188+312349 (2009-11-03)

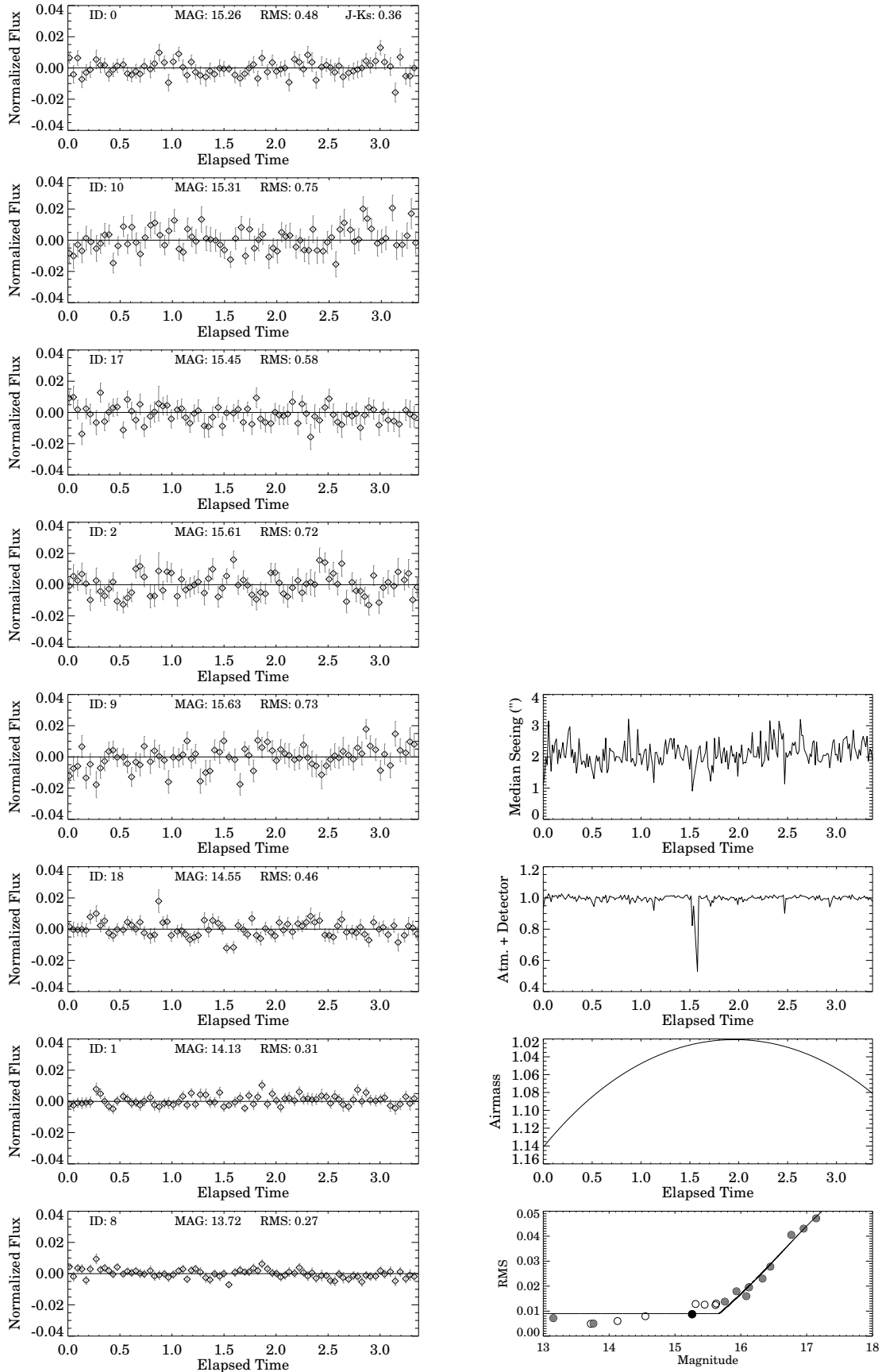
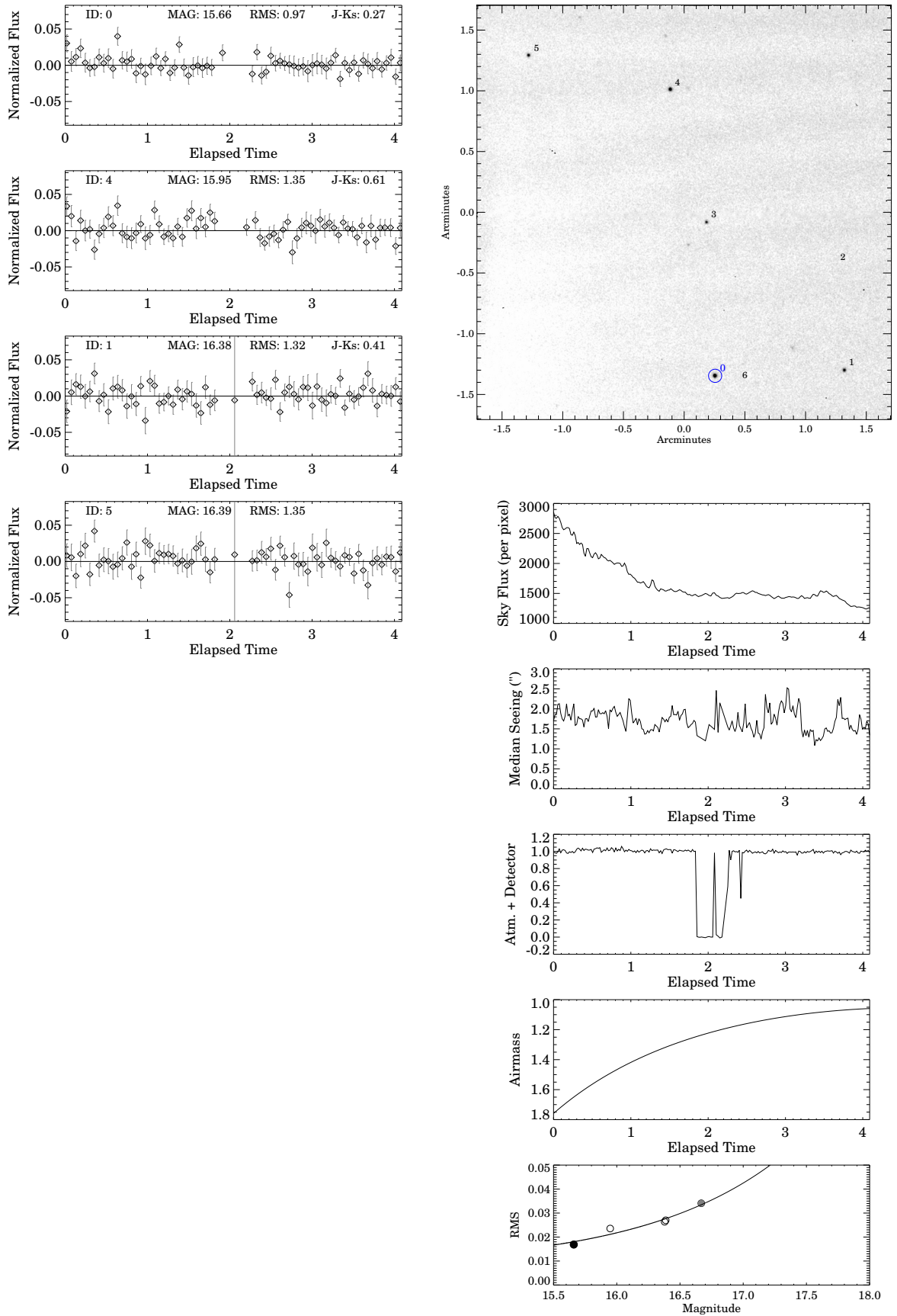


Figure C.63: As described in section C.1: 2MASS J23312378-4718274 (2009-09-30T00:02:44)



C.2 Lomb-Scargle Periodograms for all targets

Caption for figures C.64-C.65

Lomb-Scargle Periodograms for all detrended light curves. The target is shown using a solid black line, while reference stars are shown using solid grey lines. In cases where the target itself is flagged for quality the flagged reference stars are also shown as dashed grey lines to make a fair comparison. Note that flagged targets were not considered in the statistical analysis. The 0.01 FAP from simulations is shown for the target as a dashed horizontal line. A detection was claimed when the target's peak power was found to be 1.4 times greater than the 0.01 FAP power, *and* the if target's light curve was not flagged for quality issues. The following light curves are flagged for poor quality: DENIS J081730.0-615520, 2MASS J05591914-1404488, SDSSp J042348.57-041403.5, SDSS J141624.08+134826.7.

Figure C.64: As described in section C.2

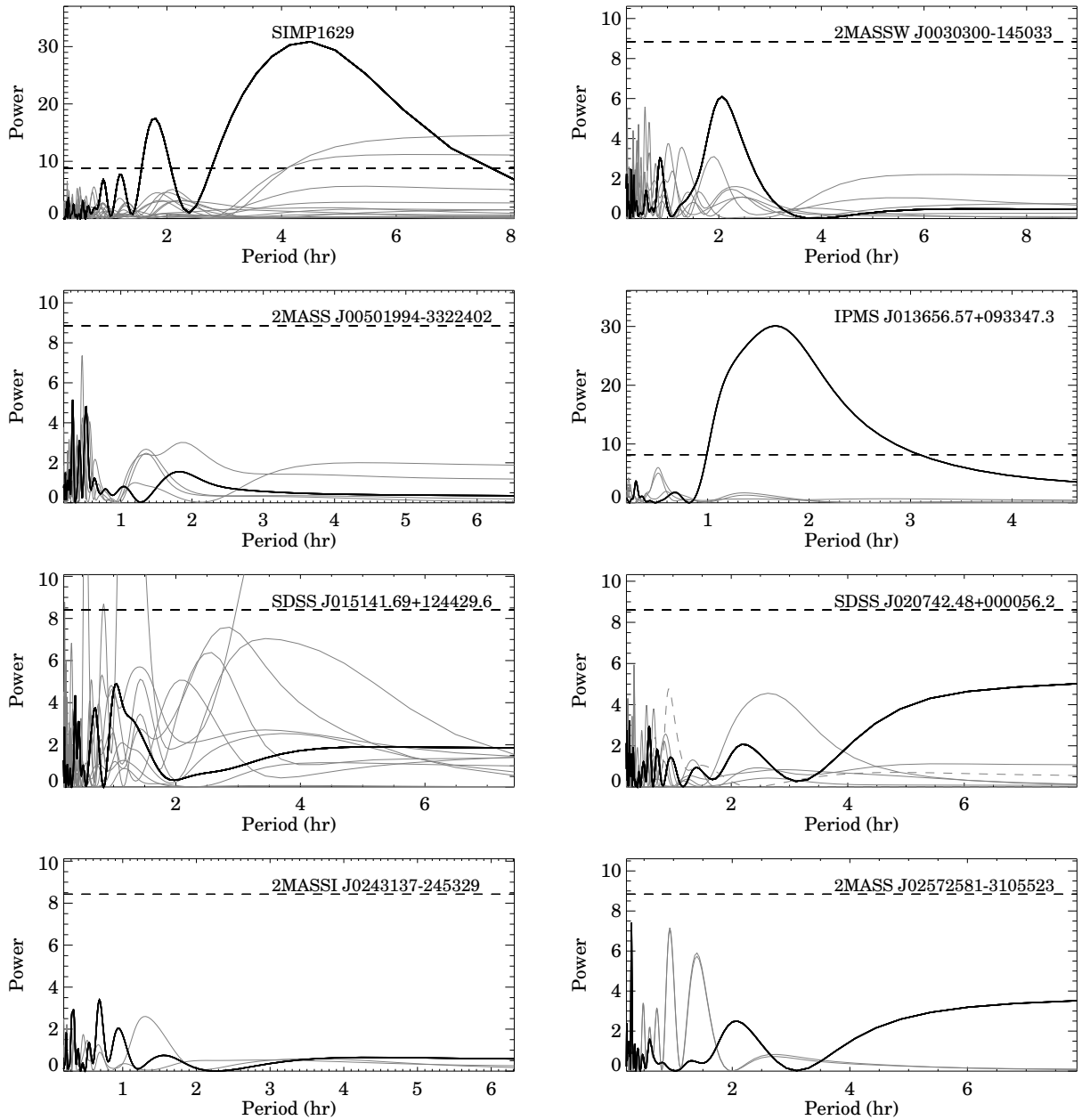


Figure C.65: As described in section C.2

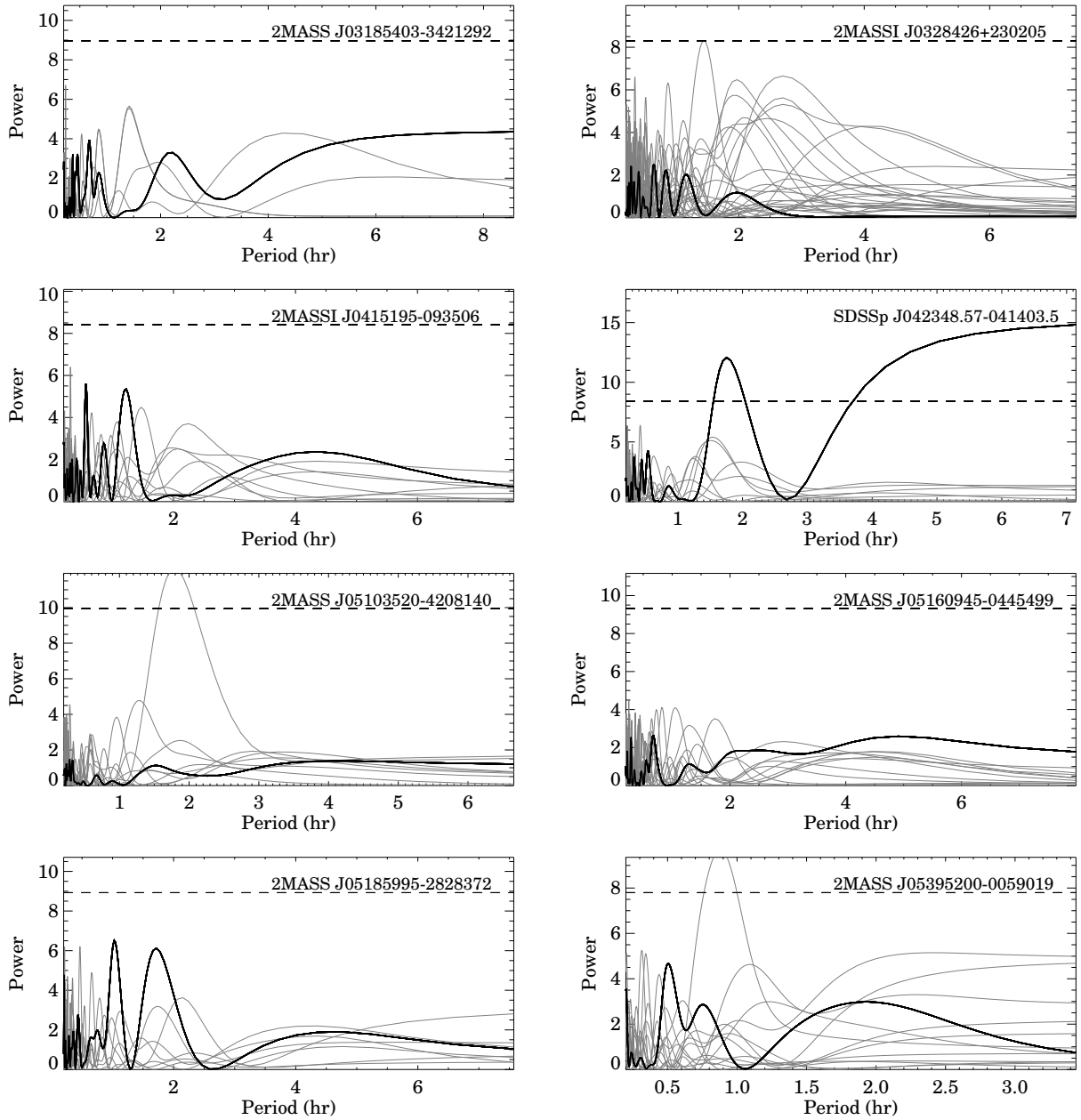


Figure C.66: As described in section C.2

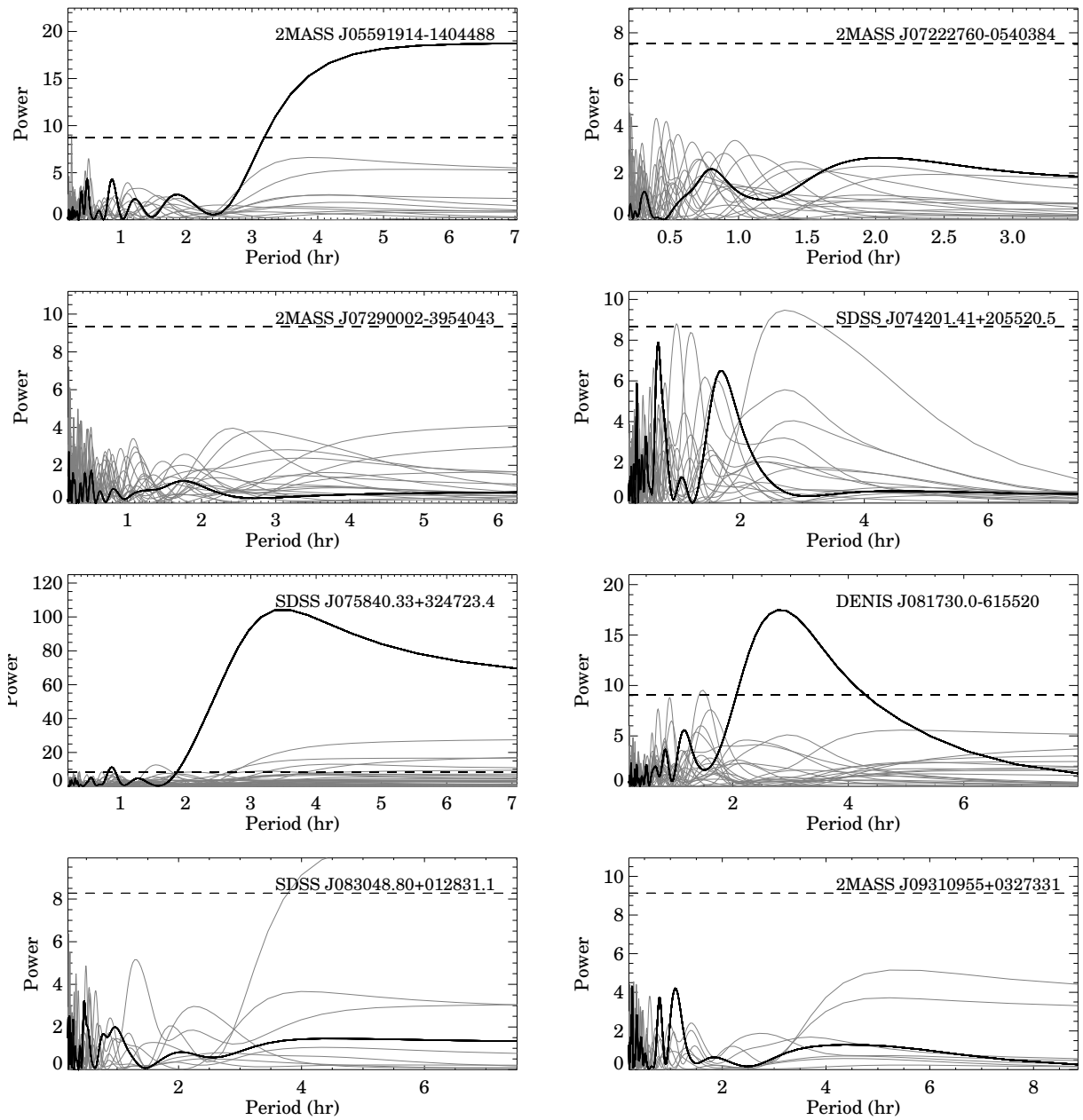


Figure C.67: As described in section C.2

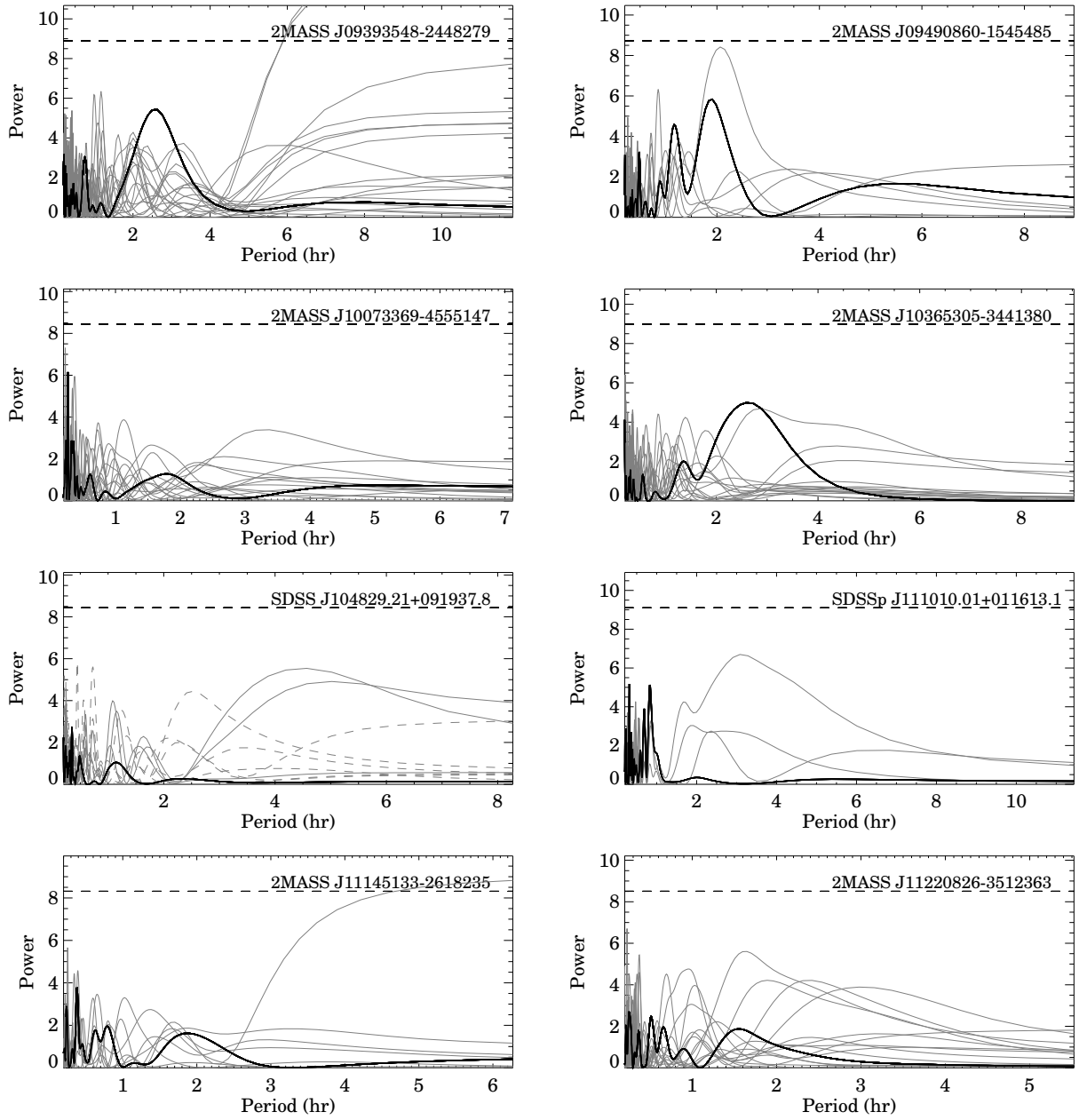


Figure C.68: As described in section C.2

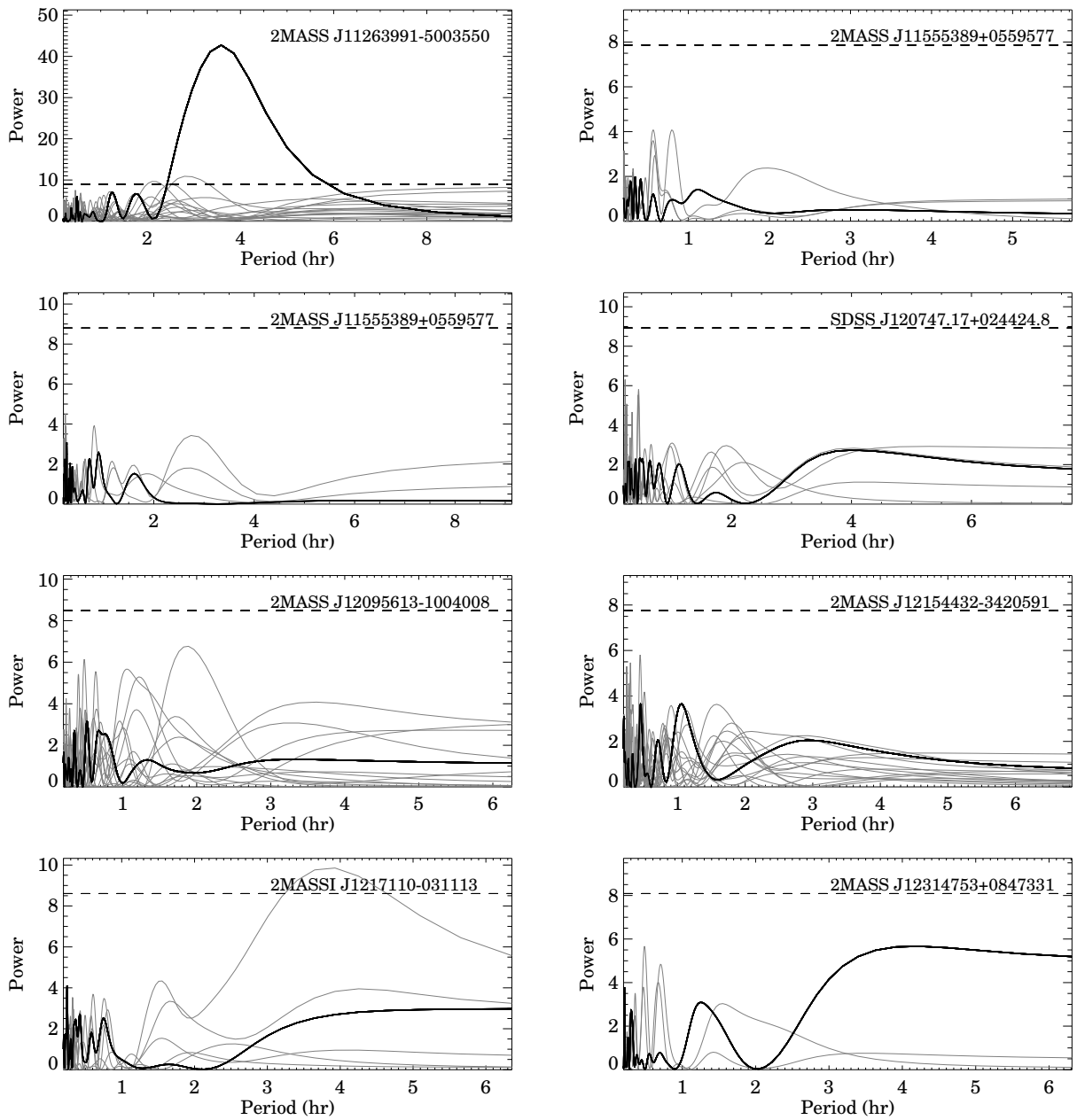


Figure C.69: As described in section C.2

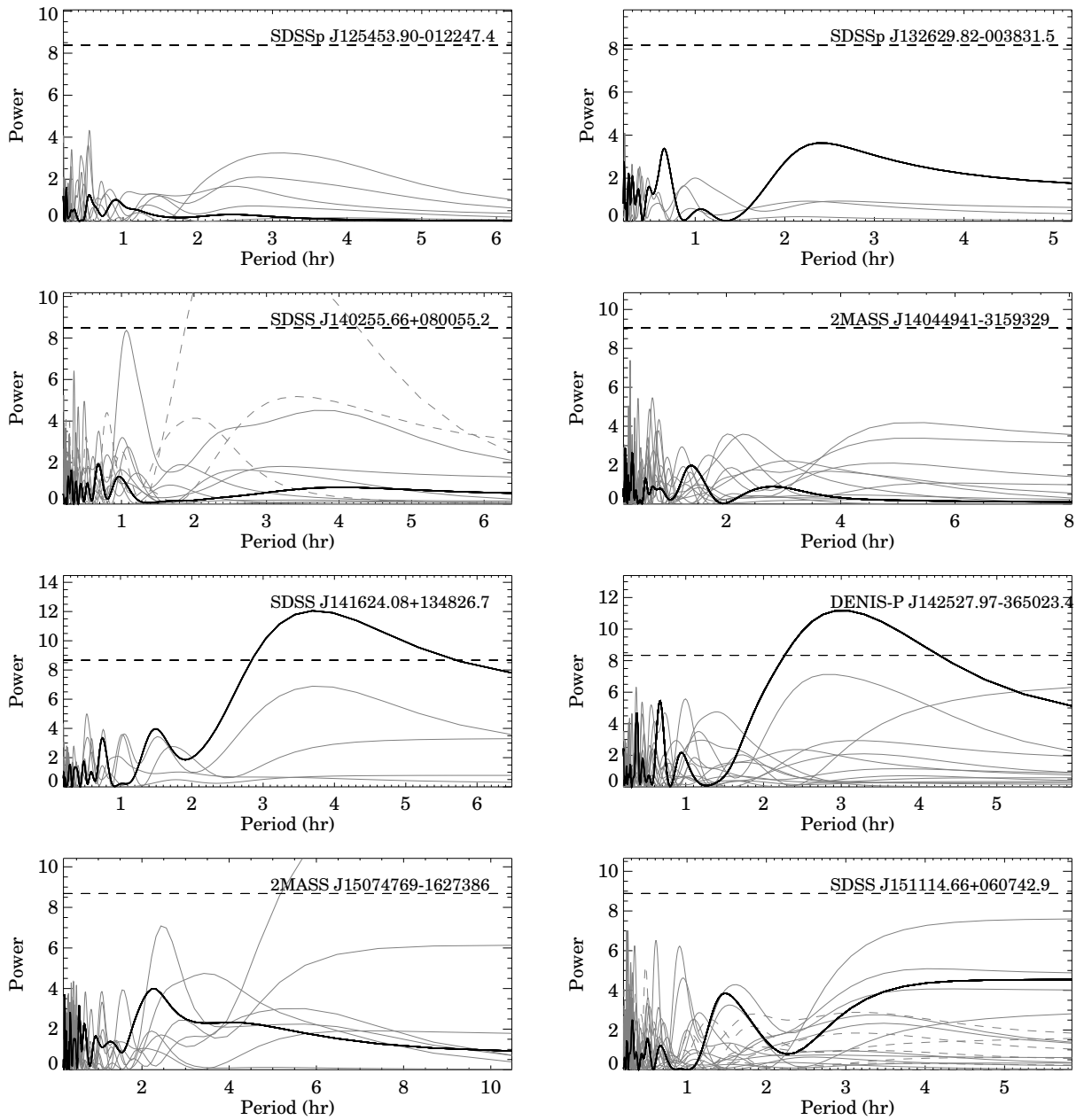


Figure C.70: As described in section C.2

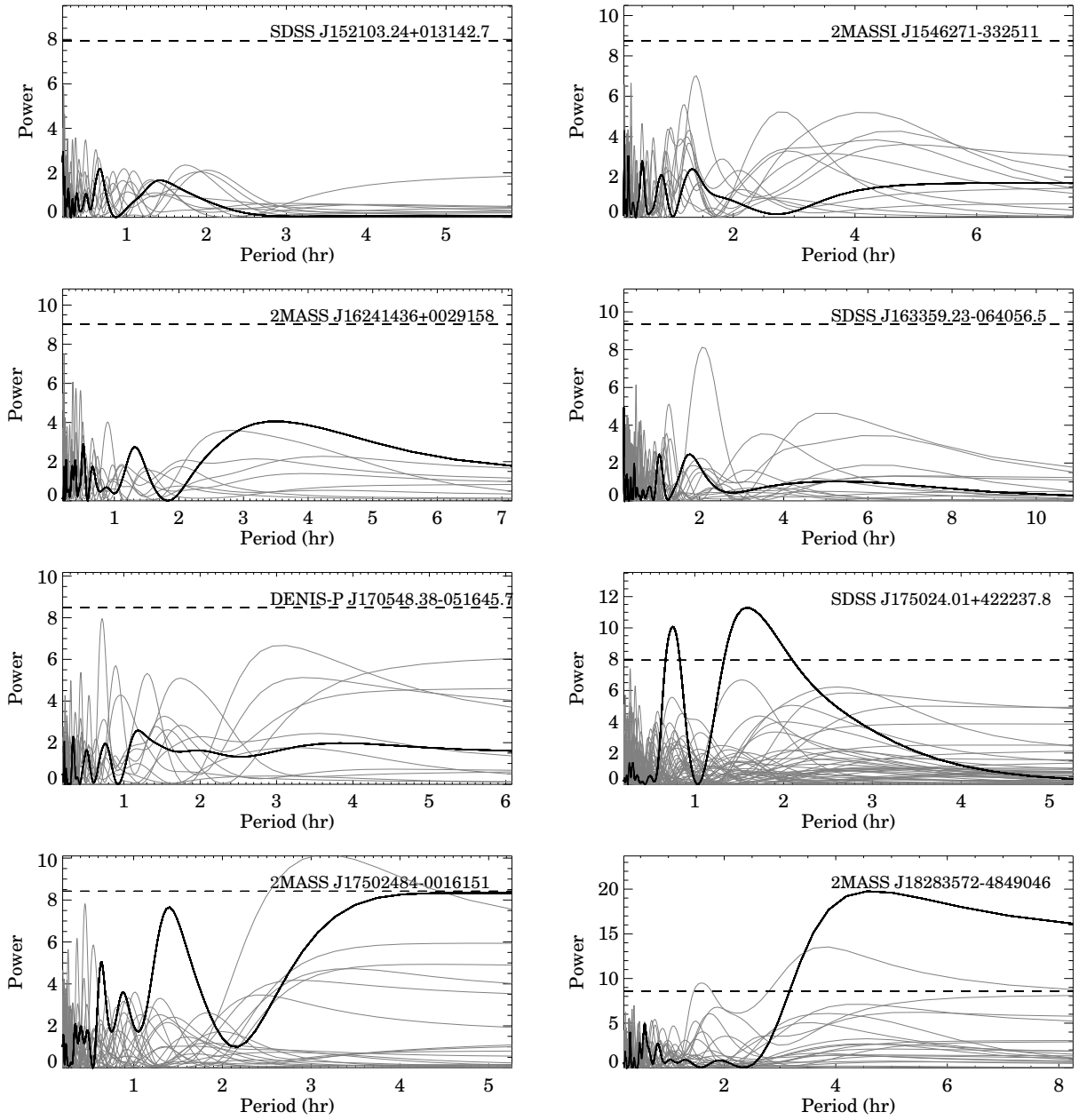
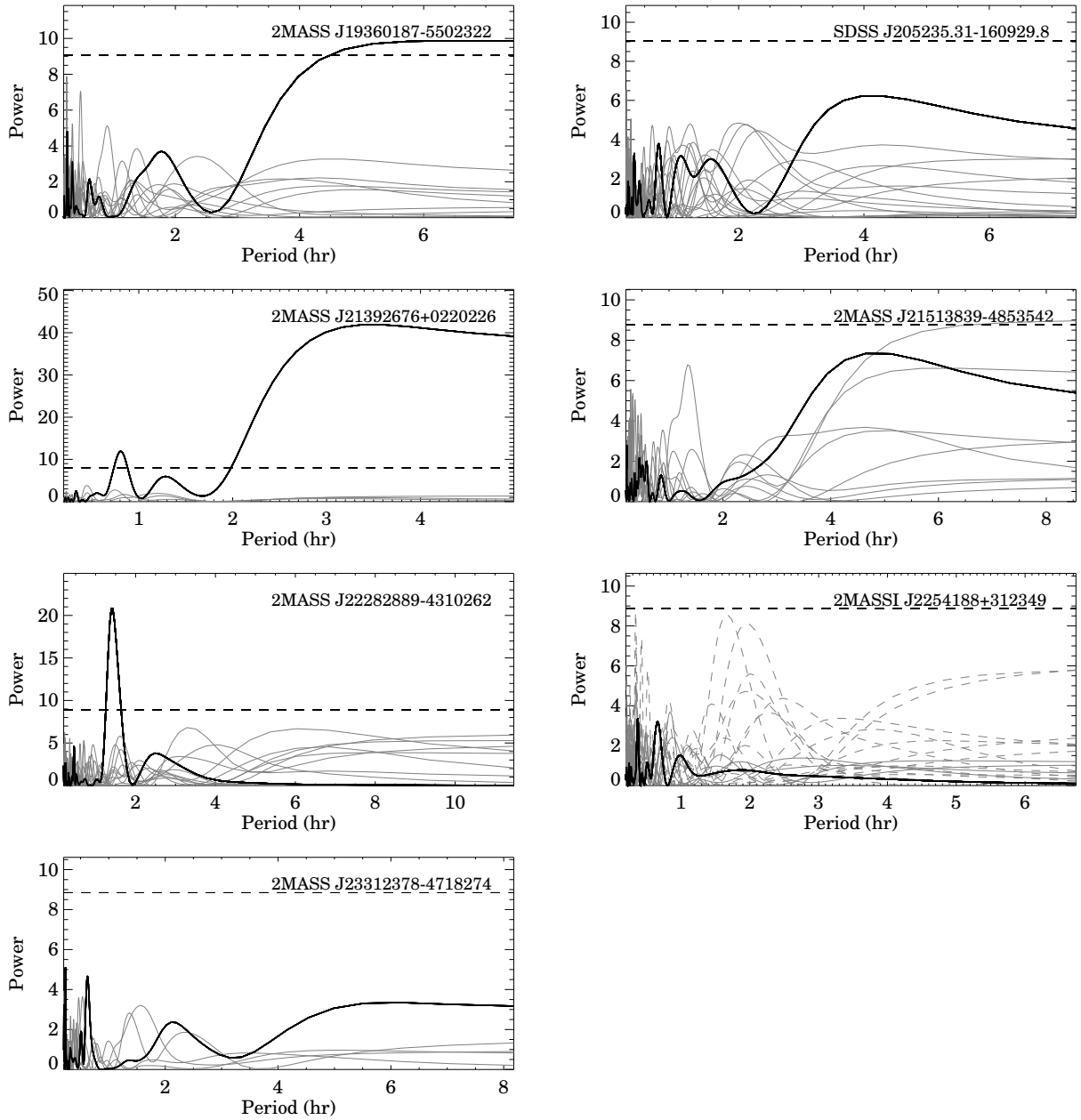


Figure C.71: As described in section C.2



Bibliography

Aberasturi, M., Solano, E., & Martín, E. L. 2011, *A&A*, 534, L7

Ackerman, A. S., & Marley, M. S. 2001, *ApJ*, 556, 872

Adelman-McCarthy, J. K., et al. 2008, *ApJS*, 175, 297

Allard, F., Guillot, T., Ludwig, H., Hauschildt, P. H., Schweitzer, A., Alexander, D. R., & Ferguson, J. W. 2003, in *IAU Symposium*, Vol. 211, *Brown Dwarfs*, ed. E. Martín, 325–+

Allard, F., Hauschildt, P. H., Alexander, D. R., Tamanai, A., & Schweitzer, A. 2001, *ApJ*, 556, 357

Allen, P. R. 2007, *ApJ*, 668, 492

Allen, P. R., & Reid, I. N. 2008, *AJ*, 135, 2024

Artigau, E. 2006, PhD thesis, Université de Montréal (Canada)

Artigau, É., Bouchard, S., Doyon, R., & Lafrenière, D. 2009, *ApJ*, 701, 1534

Artigau, É., Doyon, R., Lafrenière, D., Nadeau, D., Robert, J., & Albert, L. 2006, *ApJ*, 651, L57

Artigau, E., Doyon, R., Vallee, P., Riopel, M., & Nadeau, D. 2004, in *Presented at the Society of Photo-Optical Instrumentation Engineers (SPIE) Conference*, Vol. 5492,

- Society of Photo-Optical Instrumentation Engineers (SPIE) Conference Series, ed. A. F. M. Moorwood & M. Iye, 1479–1486
- Artigau, E., Nadeau, D., & Doyon, R. 2003, in IAU Symposium, Vol. 211, *Brown Dwarfs*, ed. E. Martín, 451–+
- Artigau, É., et al. 2011, *ApJ*, 739, 48
- Bailer-Jones, C. A. L. 2002, *A&A*, 389, 963
- . 2004, *A&A*, 419, 703
- . 2008, *MNRAS*, 384, 1145
- Bailer-Jones, C. A. L., & Lamm, M. 2003, *MNRAS*, 339, 477
- Bailer-Jones, C. A. L., & Mundt, R. 1999, *A&A*, 348, 800
- . 2001, *A&A*, 367, 218
- Baraffe, I., Chabrier, G., Allard, F., & Hauschildt, P. H. 1998, *A&A*, 337, 403
- Barman, T. S., Macintosh, B., Konopacky, Q. M., & Marois, C. 2011, *ApJ*, 733, 65
- Basri, G., & Reiners, A. 2006, *AJ*, 132, 663
- Bate, M. R. 2000, *MNRAS*, 314, 33
- . 2009, *MNRAS*, 392, 590
- . 2012, *MNRAS*, 419, 3115
- Bate, M. R., & Bonnell, I. A. 2005, *MNRAS*, 356, 1201
- Bate, M. R., Bonnell, I. A., & Bromm, V. 2002a, *MNRAS*, 332, L65
- . 2002b, *MNRAS*, 336, 705

—. 2003, *MNRAS*, 339, 577

Bean, J. L., Sneden, C., Hauschildt, P. H., Johns-Krull, C. M., & Benedict, G. F. 2006, *ApJ*, 652, 1604

Beers, T. C., Flynn, K., & Gebhardt, K. 1990, *AJ*, 100, 32

Berger, E., et al. 2001, *Nature*, 410, 338

Boss, A. P. 2000, *ApJ*, 536, L101

Bouy, H., Brandner, W., Martín, E. L., Delfosse, X., Allard, F., & Basri, G. 2003, *AJ*, 126, 1526

Bouy, H., Martín, E. L., Brandner, W., & Bouvier, J. 2005, *AJ*, 129, 511

Bowler, B. P., Liu, M. C., Dupuy, T. J., & Cushing, M. C. 2010, *ApJ*, 723, 850

Burgasser, A. J. 2007, *ApJ*, 659, 655

Burgasser, A. J., Cruz, K. L., Cushing, M., Gelino, C. R., Looper, D. L., Faherty, J. K., Kirkpatrick, J. D., & Reid, I. N. 2010, *ApJ*, 710, 1142

Burgasser, A. J., Geballe, T. R., Leggett, S. K., Kirkpatrick, J. D., & Golimowski, D. A. 2006a, *ApJ*, 637, 1067

Burgasser, A. J., Kirkpatrick, J. D., Cruz, K. L., Reid, I. N., Leggett, S. K., Liebert, J., Burrows, A., & Brown, M. E. 2006b, *ApJS*, 166, 585

Burgasser, A. J., Kirkpatrick, J. D., & Lowrance, P. J. 2005, *AJ*, 129, 2849

Burgasser, A. J., Kirkpatrick, J. D., Reid, I. N., Brown, M. E., Miskay, C. L., & Gizis, J. E. 2003a, *ApJ*, 586, 512

Burgasser, A. J., Looper, D. L., Kirkpatrick, J. D., Cruz, K. L., & Swift, B. J. 2008, *ApJ*, 674, 451

- Burgasser, A. J., Luk, C., Dhital, S., Bardalez Gagliuffi, D., Nicholls, C. P., Prato, L., West, A. A., & Lepine, S. 2012, ArXiv e-prints
- Burgasser, A. J., Marley, M. S., Ackerman, A. S., Saumon, D., Lodders, K., Dahn, C. C., Harris, H. C., & Kirkpatrick, J. D. 2002, *ApJ*, 571, L151
- Burgasser, A. J., McElwain, M. W., & Kirkpatrick, J. D. 2003b, *AJ*, 126, 2487
- Burgasser, A. J., Reid, I. N., Siegler, N., Close, L., Allen, P., Lowrance, P., & Gizis, J. 2007, *Protostars and Planets V*, 427
- Burrows, A., Heng, K., & Nampaisarn, T. 2011, ArXiv e-prints
- Burrows, A., Hubbard, W. B., Lunine, J. I., & Liebert, J. 2001, *Reviews of Modern Physics*, 73, 719
- Burrows, A., & Sharp, C. M. 1999, *ApJ*, 512, 843
- Burrows, A., Sudarsky, D., & Hubeny, I. 2006, *ApJ*, 640, 1063
- Burrows, A., et al. 1997, *ApJ*, 491, 856
- Caballero, J. A., Martín, E. L., Dobbie, P. D., & Barrado Y Navascués, D. 2006, *A&A*, 460, 635
- Chabrier, G., Baraffe, I., Allard, F., & Hauschildt, P. 2000, *ApJ*, 542, 464
- Chiu, K., Fan, X., Leggett, S. K., Golimowski, D. A., Zheng, W., Geballe, T. R., Schneider, D. P., & Brinkmann, J. 2006, *AJ*, 131, 2722
- Clarke, F. J., Hodgkin, S. T., Oppenheimer, B. R., Robertson, J., & Haubois, X. 2008, *MNRAS*, 386, 2009
- Clarke, F. J., Oppenheimer, B. R., & Tinney, C. G. 2002a, *MNRAS*, 335, 1158
- Clarke, F. J., Tinney, C. G., & Covey, K. R. 2002b, *MNRAS*, 332, 361

- Clarke, F. J., Tinney, C. G., & Hodgkin, S. T. 2003, *MNRAS*, 341, 239
- Close, L. M., Richer, H. B., & Crabtree, D. R. 1990, *AJ*, 100, 1968
- Close, L. M., Siegler, N., Freed, M., & Biller, B. 2003, *ApJ*, 587, 407
- Cohen, M., Wheaton, W. A., & Megeath, S. T. 2003, *AJ*, 126, 1090
- Cruz, K. L., & Reid, I. N. 2002, *AJ*, 123, 2828
- Cushing, M. C., Vacca, W. D., & Rayner, J. T. 2004, *PASP*, 116, 362
- Cushing, M. C., et al. 2008, *ApJ*, 678, 1372
- Daemgen, S., Siegler, N., Reid, I. N., & Close, L. M. 2007, *ApJ*, 654, 558
- Dahn, C. C., et al. 2002, *AJ*, 124, 1170
- Delfosse, X., Forveille, T., Ségransan, D., Beuzit, J.-L., Udry, S., Perrier, C., & Mayor, M. 2000, *A&A*, 364, 217
- Delfosse, X., et al. 1997, *A&A*, 327, L25
- Dorren, J. D. 1987, *ApJ*, 320, 756
- Dupuy, T. J., & Liu, M. C. 2012, *ArXiv e-prints*
- Dupuy, T. J., Liu, M. C., & Ireland, M. J. 2011, *ArXiv e-prints*
- Eggleton, P., & Kiseleva, L. 1995, *ApJ*, 455, 640
- Eggleton, P. P. 1983, *ApJ*, 268, 368
- Enoch, M. L., Brown, M. E., & Burgasser, A. J. 2003, *AJ*, 126, 1006
- EROS Collaboration et al. 1999, *A&A*, 351, L5
- Fabrycky, D., & Tremaine, S. 2007, *ApJ*, 669, 1298

- Faherty, J. K., Burgasser, A. J., West, A. A., Bochanski, J. J., Cruz, K. L., Shara, M. M., & Walter, F. M. 2010, *AJ*, 139, 176
- Faherty, J. K., et al. 2012, *ArXiv e-prints*
- Fan, X., et al. 2000, *AJ*, 119, 928
- Fischer, D. A., & Marcy, G. W. 1992, *ApJ*, 396, 178
- Folkes, S. L., Pinfield, D. J., Kendall, T. R., & Jones, H. R. A. 2007, *MNRAS*, 378, 901
- Geballe, T. R., et al. 2002, *ApJ*, 564, 466
- Gelino, C., & Marley, M. 2000, in *Astronomical Society of the Pacific Conference Series*, Vol. 212, *From Giant Planets to Cool Stars*, ed. C. A. Griffith & M. S. Marley, 322–+
- Gelino, C. R., Marley, M. S., Holtzman, J. A., Ackerman, A. S., & Lodders, K. 2002, *ApJ*, 577, 433
- Ghez, A. M., et al. 2008, *ApJ*, 689, 1044
- Gizis, J. E. 1997, *AJ*, 113, 806
- Gizis, J. E., Reid, I. N., Knapp, G. R., Liebert, J., Kirkpatrick, J. D., Koerner, D. W., & Burgasser, A. J. 2003, *AJ*, 125, 3302
- Goldman, B., et al. 2008, *A&A*, 487, 277
- Golimowski, D. A., et al. 2004, *AJ*, 127, 3516
- Goodwin, S. P., Whitworth, A. P., & Ward-Thompson, D. 2004, *A&A*, 414, 633
- Guenther, E. W., Zapatero Osorio, M. R., Mehner, A., & Martín, E. L. 2009, *A&A*, 498, 281
- Hale, A. 1994, *AJ*, 107, 306

- Harding, L. K., Hallinan, G., Boyle, R. P., Butler, R. F., Sheehan, B., & Golden, A. 2011, in *Astronomical Society of the Pacific Conference Series*, Vol. 448, 16th Cambridge Workshop on Cool Stars, Stellar Systems, and the Sun, ed. C. Johns-Krull, M. K. Browning, & A. A. West, 219
- Hastings, W. K. 1970, *Biometrika*, 57(1), 97
- Hauschildt, P. H., Allard, F., & Baron, E. 1999, *ApJ*, 512, 377
- Hinz, J. L., McCarthy, Jr., D. W., Simons, D. A., Henry, T. J., Kirkpatrick, J. D., & McGuire, P. C. 2002, *AJ*, 123, 2027
- Horne, J. H., & Baliunas, S. L. 1986, *ApJ*, 302, 757
- Joergens, V. 2008, *A&A*, 492, 545
- Kirkpatrick, J. D. 2008, in *Astronomical Society of the Pacific Conference Series*, Vol. 384, 14th Cambridge Workshop on Cool Stars, Stellar Systems, and the Sun, ed. G. van Belle, 85
- Kirkpatrick, J. D., Henry, T. J., & McCarthy, Jr., D. W. 1991, *ApJS*, 77, 417
- Kirkpatrick, J. D., et al. 1999, *ApJ*, 519, 802
- . 2000, *AJ*, 120, 447
- Knapp, G. R., et al. 2004, *AJ*, 127, 3553
- Koen, C. 2003, *MNRAS*, 346, 473
- . 2004, *MNRAS*, 354, 378
- . 2005a, *MNRAS*, 360, 1132
- . 2005b, *MNRAS*, 357, 1151

—. 2006, *MNRAS*, 367, 1735

Koen, C., Matsunaga, N., & Menzies, J. 2004, *MNRAS*, 354, 466

Koen, C., Tanabé, T., Tamura, M., & Kusakabe, N. 2005, *MNRAS*, 362, 727

Koerner, D. W., Kirkpatrick, J. D., McElwain, M. W., & Bonaventura, N. R. 1999, *ApJ*, 526, L25

Konopacky, Q. M., et al. 2012, *ApJ*, 750, 79

Kozai, Y. 1962, *AJ*, 67, 591

Kraus, A. L., & Hillenbrand, L. A. 2007, *ApJ*, 664, 1167

Krist, J. 1993, in *Astronomical Society of the Pacific Conference Series*, Vol. 52, *Astronomical Data Analysis Software and Systems II*, ed. R. J. Hanisch, R. J. V. Brissenden, & J. Barnes, 536–+

Kurucz, R. L. 1979, *ApJS*, 40, 1

—. 1993, *VizieR Online Data Catalog*, 6039, 0

Lane, C., et al. 2007, *ApJ*, 668, L163

Leggett, S. K., Allard, F., Geballe, T. R., Hauschildt, P. H., & Schweitzer, A. 2001a, *ApJ*, 548, 908

—. 2001b, *ApJ*, 548, 908

Leggett, S. K., et al. 2006, *MNRAS*, 373, 781

—. 2008, *ApJ*, 682, 1256

Leinert, C., Jahreiß, H., Woitas, J., Zucker, S., Mazeh, T., Eckart, A., & Köhler, R. 2001, *A&A*, 367, 183

Lépine, S., Rich, R. M., & Shara, M. M. 2007, *ApJ*, 669, 1235

Lewis, A., & Bridle, S. 2002, *Phys. Rev. D*, 66, 103511

Littlefair, S. P., Dhillon, V. S., Marsh, T. R., Shahbaz, T., & Martín, E. L. 2006, *MNRAS*, 370, 1208

Littlefair, S. P., Dhillon, V. S., Marsh, T. R., Shahbaz, T., Martín, E. L., & Copperwheat, C. 2008, *MNRAS*, 391, L88

Liu, M. C., Dupuy, T. J., & Ireland, M. J. 2008, *ApJ*, 689, 436

Liu, M. C., Dupuy, T. J., & Leggett, S. K. 2010, *ApJ*, 722, 311

Liu, M. C., & Leggett, S. K. 2005, *ApJ*, 634, 616

Liu, M. C., Leggett, S. K., Golimowski, D. A., Chiu, K., Fan, X., Geballe, T. R., Schneider, D. P., & Brinkmann, J. 2006, *ApJ*, 647, 1393

Lodders, K. 1999, *ApJ*, 519, 793

Lodders, K., & Fegley, Jr., B. 2006, *Chemistry of Low Mass Substellar Objects*, ed. Mason, J. W. (Springer Verlag), 1

Looper, D. L., Gelino, C. R., Burgasser, A. J., & Kirkpatrick, J. D. 2008, *ApJ*, 685, 1183

Looper, D. L., Kirkpatrick, J. D., & Burgasser, A. J. 2007, *AJ*, 134, 1162

Lowrance, P. J., et al. 1999, *ApJ*, 512, L69

Luhman, K. L., Mamajek, E. E., Allen, P. R., Muench, A. A., & Finkbeiner, D. P. 2009, *ApJ*, 691, 1265

Maiti, M. 2007, *AJ*, 133, 1633

Maiti, M., Sengupta, S., Parihar, P. S., & Anupama, G. C. 2005, *ApJ*, 619, L183

- Marcy, G. W., & Butler, R. P. 2000, *PASP*, 112, 137
- Marley, M. S., Saumon, D., & Goldblatt, C. 2010, *ApJ*, 723, L117
- Marley, M. S., Seager, S., Saumon, D., Lodders, K., Ackerman, A. S., Freedman, R. S., & Fan, X. 2002, *ApJ*, 568, 335
- Marocco, F., et al. 2010, *A&A*, 524, A38
- Martín, E. L., Brandner, W., Bouy, H., Basri, G., Davis, J., Deshpande, R., & Montgomery, M. M. 2006, *A&A*, 456, 253
- Martín, E. L., Zapatero Osorio, M. R., & Lehto, H. J. 2001, *ApJ*, 557, 822
- Maxted, P. F. L., & Jeffries, R. D. 2005, *MNRAS*, 362, L45
- McCarthy, C., & Zuckerman, B. 2004, *AJ*, 127, 2871
- McLean, I. S., McGovern, M. R., Burgasser, A. J., Kirkpatrick, J. D., Prato, L., & Kim, S. S. 2003, *ApJ*, 596, 561
- Metchev, S. A., & Hillenbrand, L. A. 2005, in *Protostars and Planets V*, 8635
- Metchev, S. A., & Hillenbrand, L. A. 2006, *ApJ*, 651, 1166
- Metropolis, N., Rosenbluth, A. W., Rosenbluth, M. N., Teller, A. H., & Teller, E. 1953, *J. Chem. Phys.*, 21, 1087
- Mohanty, S., & Basri, G. 2003, *ApJ*, 583, 451
- Mohanty, S., Basri, G., Shu, F., Allard, F., & Chabrier, G. 2002, *ApJ*, 571, 469
- Morales-Calderón, M., et al. 2006, *ApJ*, 653, 1454
- Murakawa, K., et al. 2004, *PASJ*, 56, 509

- Nakajima, T., Oppenheimer, B. R., Kulkarni, S. R., Golimowski, D. A., Matthews, K., & Durrance, S. T. 1995, *Nature*, 378, 463
- Nakajima, T., et al. 2000, *PASJ*, 52, 87
- Oppenheimer, B. R., Golimowski, D. A., Kulkarni, S. R., Matthews, K., Nakajima, T., Creech-Eakman, M., & Durrance, S. T. 2001, *AJ*, 121, 2189
- Padoan, P., & Nordlund, Å. 2002, *ApJ*, 576, 870
- Persson, S. E., Murphy, D. C., Gunnels, S. M., Birk, C., Bagish, A., & Koch, E. 2002, *AJ*, 124, 619
- Pickles, A. J. 1998, *PASP*, 110, 863
- Pinfield, D. J., Jones, H. R. A., Lucas, P. W., Kendall, T. R., Folkes, S. L., Day-Jones, A. C., Chappelle, R. J., & Steele, I. A. 2006, *MNRAS*, 368, 1281
- Radigan, J., Jayawardhana, R., Lafrenière, D., & Artigau, É. 2011, in *Astronomical Society of the Pacific Conference Series*, Vol. 448, 16th Cambridge Workshop on Cool Stars, Stellar Systems, and the Sun, ed. C. Johns-Krull, M. K. Browning, & A. A. West, 187
- Radigan, J., Jayawardhana, R., Lafrenière, D., Artigau, É., Marley, M., & Saumon, D. 2012, *ApJ*, 750, 105
- Radigan, J., Lafrenière, D., Jayawardhana, R., & Doyon, R. 2008, *ApJ*, 689, 471
- Ragozzine, D., & Wolf, A. S. 2009, *ApJ*, 698, 1778
- Rayner, J. T., Toomey, D. W., Onaka, P. M., Denault, A. J., Stahlberger, W. E., Vacca, W. D., Cushing, M. C., & Wang, S. 2003, *PASP*, 115, 362
- Rebolo, R., Zapatero Osorio, M. R., Madruga, S., Bejar, V. J. S., Arribas, S., & Licandro, J. 1998, *Science*, 282, 1309

- Reid, I. N., Burgasser, A. J., Cruz, K. L., Kirkpatrick, J. D., & Gizis, J. E. 2001a, *AJ*, 121, 1710
- . 2001b, *AJ*, 121, 1710
- Reid, I. N., Cruz, K. L., Kirkpatrick, J. D., Allen, P. R., Mungall, F., Liebert, J., Lowrance, P., & Sweet, A. 2008, *AJ*, 136, 1290
- Reid, I. N., & Gizis, J. E. 1997a, *AJ*, 113, 2246
- . 1997b, *AJ*, 114, 1992
- Reid, I. N., Gizis, J. E., & Hawley, S. L. 2002, *AJ*, 124, 2721
- Reid, I. N., Gizis, J. E., Kirkpatrick, J. D., & Koerner, D. W. 2001c, *AJ*, 121, 489
- Reid, I. N., Kirkpatrick, J. D., Gizis, J. E., Dahn, C. C., Monet, D. G., Williams, R. J., Liebert, J., & Burgasser, A. J. 2000, *AJ*, 119, 369
- Reid, I. N., Lewitus, E., Allen, P. R., Cruz, K. L., & Burgasser, A. J. 2006, *AJ*, 132, 891
- Reid, I. N., et al. 2003, *AJ*, 126, 3007
- Reiners, A., & Basri, G. 2008, *ApJ*, 684, 1390
- Reipurth, B., & Clarke, C. 2001, *AJ*, 122, 432
- Rockenfeller, B., Bailer-Jones, C. A. L., & Mundt, R. 2006, *A&A*, 448, 1111
- Ruiz, M. T., Leggett, S. K., & Allard, F. 1997, *ApJ*, 491, L107
- Rutledge, R. E., Basri, G., Martín, E. L., & Bildsten, L. 2000, *ApJ*, 538, L141
- Salim, S., & Gould, A. 2003, *ApJ*, 582, 1011
- Saumon, D., & Marley, M. S. 2008, *ApJ*, 689, 1327

Scargle, J. D. 1982, *ApJ*, 263, 835

Schmidt, S. J., Cruz, K. L., Bongiorno, B. J., Liebert, J., & Reid, I. N. 2007, *AJ*, 133, 2258

Scholz, A., & Eislöffel, J. 2004, *A&A*, 421, 259

Scholz, A., Eislöffel, J., & Mundt, R. 2009, *MNRAS*, 400, 1548

Scholz, A., Jayawardhana, R., & Wood, K. 2006, *ApJ*, 645, 1498

Seifahrt, A., Röhl, T., Neuhäuser, R., Reiners, A., Kerber, F., Käufl, H. U., Siebenmorgen, R., & Smette, A. 2008, *A&A*, 484, 429

Skemer, A. J., Close, L. M., Szűcs, L., Apai, D., Pascucci, I., & Biller, B. A. 2011, *ApJ*, 732, 107

Skrutskie, M. F., et al. 2006, *AJ*, 131, 1163

Smith, B. A., et al. 1989, *Science*, 246, 1422

Stamatellos, D., Hubber, D. A., & Whitworth, A. P. 2007, *MNRAS*, 382, L30

Stassun, K. G., Mathieu, R. D., & Valenti, J. A. 2007, *ApJ*, 664, 1154

Stephens, D. C., & Leggett, S. K. 2004, *PASP*, 116, 9

Stephens, D. C., et al. 2009, *ApJ*, 702, 154

Sterzik, M. F., & Durisen, R. H. 2003, *A&A*, 400, 1031

Stumpf, M. B., Brandner, W., Henning, T., Bouy, H., Koehler, R., Hormuth, F., Joergens, V., & Kasper, M. 2008, *ArXiv e-prints*

Takami, H., et al. 2004, *PASJ*, 56, 225

Terndrup, D. M., Krishnamurthi, A., Pinsonneault, M. H., & Stauffer, J. R. 1999, *AJ*, 118, 1814

- Tinney, C. G., & Tolley, A. J. 1999, *MNRAS*, 304, 119
- Tokovinin, A. 2004, in *Revista Mexicana de Astronomia y Astrofisica Conference Series*, Vol. 21, *Revista Mexicana de Astronomia y Astrofisica Conference Series*, ed. C. Allen & C. Scarfe, 7–14
- Tokovinin, A. 2008, *MNRAS*, 389, 925
- Tokovinin, A. A. 1997, *A&AS*, 124, 75
- Tokunaga, A. T., & Kobayashi, N. 1999, *AJ*, 117, 1010
- Tokunaga, A. T., & Vacca, W. D. 2005, *PASP*, 117, 421
- Tsuji, T. 2002, *ApJ*, 575, 264
- Tsuji, T., & Nakajima, T. 2003, *ApJ*, 585, L151
- Vacca, W. D., Cushing, M. C., & Rayner, J. T. 2003, *PASP*, 115, 389
- Vasavada, A. R., et al. 1998, *Icarus*, 135, 265
- Vrba, F. J., et al. 2004, *AJ*, 127, 2948
- West, A. A., Hawley, S. L., Bochanski, J. J., Covey, K. R., Reid, I. N., Dhital, S., Hilton, E. J., & Masuda, M. 2008, *AJ*, 135, 785
- Wilson, J. C., Kirkpatrick, J. D., Gizis, J. E., Skrutskie, M. F., Monet, D. G., & Houck, J. R. 2001, *AJ*, 122, 1989
- Witte, S., Helling, C., Barman, T., Heidrich, N., & Hauschildt, P. H. 2011, *A&A*, 529, A44+
- Woitke, P., & Helling, C. 2003, *A&A*, 399, 297
- Yelda, S., Lu, J. R., Ghez, A. M., Clarkson, W., Anderson, J., Do, T., & Matthews, K. 2010, *ApJ*, 725, 331

Zapatero Osorio, M. R., Martín, E. L., Béjar, V. J. S., Bouy, H., Deshpande, R., & Wainscoat, R. J. 2007, *ApJ*, 666, 1205

Zapatero Osorio, M. R., Martín, E. L., Bouy, H., Tata, R., Deshpande, R., & Wainscoat, R. J. 2006, *ApJ*, 647, 1405

Zuckerman, B., & Song, I. 2004, *ARA&A*, 42, 685